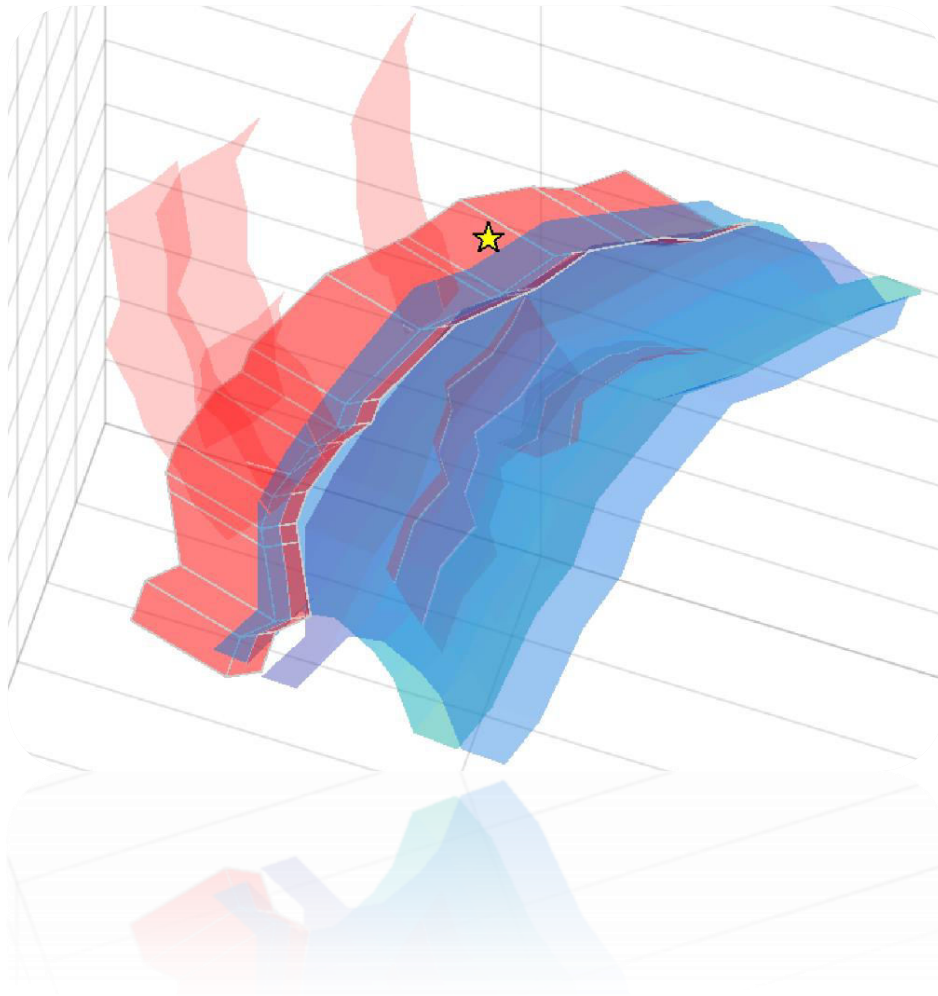




UNIVERSITAT POLITÈCNICA
DE CATALUNYA
BARCELONATECH

Master programme in Geotechnical
and Earthquake Engineering



Improving the knowledge of the 2013 Castor UGS (Spain) seismic sequence from a seismological and geomechanical standpoint

Lluís Saló Salgado

Master final thesis
June 2016

Improving the knowledge of the 2013 Castor UGS (Spain) seismic sequence from a seismological and geomechanical standpoint

Cover Illustration: Excerpt from a simplified 3D fault model of the area of study. See annex E for further information.



Escola de Camins
Escola Tècnica Superior d'Enginyeria de Camins, Canals i Ports
UPC BARCELONATECH

Improving the knowledge of the 2013 Castor UGS (Spain) seismic sequence from a seismological and geomechanical standpoint

Final Thesis developed by:
Lluís Saló Salgado

Directed by:
Dra. Tànit Frontera Genovard
Dr. Xavier Goula Suriñach
Dr. Lluís G. Pujades Beneit

Master in:
Geotechnical and Earthquake Engineering

Barcelona, **June 23rd** 2016

Department of Civil and Environmental Engineering

MASTERFINAL THESIS

My most sincere thanks,

To the Institut Cartografic i Geologic de Catalunya (ICGC), for giving me the opportunity to enroll myself in their Geophysics and Seismology group, as a result of a collaboration agreement scholarship with the Universitat Politecnica de Catalunya (UPC).

To my supervisors:

Tanit Frontera, for her guidance, support and dedication throughout the whole year. For transmitting to me the importance of thinking outside the box too, which has helped me addressing more than one difficult situation during the project.

Xavier Goula and Lluís Pujades, for their expertise and passion to advance in scientific knowledge, as well as the interest they have placed in the project.

To the other seismologists and interns at ICGC. Specially to Josep Batllo for his seismological knowledge and help with Posido software, to Mar Tapia for introducing me to GMT, and to Guillem Piris, another research fellow at ICGC, for his constructive comments.

To William Ellsworth and Martin Schoenball, for their remarks on how to properly address a case of induced seismicity, and on computing Coulomb stress changes respectively.

To the Civil and Environmental Engineering department of the Barcelona School of Civil Engineering (UPC), for their scientific rigor and competence. Particularly to Alberto Ledesma for his assistance and attention in the topic of static stress transfer.

To Milford Edge, for helping me improve writing in English.

Finally, to my family and friends, for their unconditional support.

ABSTRACT

The injection of fluids into the crust can modify the governing stress state and therefore generate seismic activity. The 2013 seismic sequence which took place in the area around the Castor offshore underground gas storage facility in northeastern Spain is studied here; the project aims to assess the anthropogenic seismicity problem. Location of a dataset of 50 earthquakes which are interpreted jointly with the largest 45, and a focal mechanism computation of the 8 strongest events were performed; seismological aspects were completed by studying the frequency-magnitude relationship. The final part of the study focused on earthquake static stress transfer as a trigger, which was quantified through Coulomb stress changes.

Results show that relating earthquakes and faults from earthquake location is difficult, but focal mechanism solutions indicate that both NE-SW to NNE-SSW and NW-SE oriented planes could have hosted the earthquakes. Seismicity could have taken place at greater depths than the reservoir bottom. Frequency-magnitude distribution points towards a first phase of the sequence exhibiting a b value of around 1.5, higher than expected for tectonic earthquakes, but lower than the usually reported values for induced seismicity; afterwards, the b parameter drops towards likely values for slip in active fault systems (near to 1.0), although the linearity of the distribution should be argued. Computed static stress transfer due to the 8 largest earthquakes is consistent with the activation of an east-dipping, NE-SW-striking fault, and it should not have significantly altered return periods of characteristic tremors in the area. The question regarding the origin of seismicity cannot be rigorously addressed unless a quantitative model which considers gas injections and fluid diffusion throughout the fracture network, as well as other earthquake-triggering mechanisms, is made.

RESUM

Injectar fluids a l'interior de l'escorça terrestre pot modificar l'estat d'esforços dominant i conseqüentment generar activitat sísmica. Aquest treball estudia la seqüència sísmica de 2013 en l'àrea al voltant del magatzem de gas subterrani Castor al nord-est d'Espanya; l'objectiu és avaluar la problemàtica en relació a la sismicitat antropogènica. Es van realitzar localitzacions d'un grup de 50 terratrèmols que s'interpreten en conjunt amb els 45 de major magnitud, així com el càlcul dels mecanismes focals pels 8 més grans; els aspectes sismològics es van completar a partir de l'estudi de la distribució magnitud-freqüència. La part final de l'estudi es concentra en la transferència d'esforç estàtic per terratrèmols propers com a mecanisme físic desestabilitzant, que es quantifica a partir de canvis d'esforç de Coulomb.

Els resultats mostren que relacionar terratrèmols i falles a partir de les localitzacions és difícil, però les solucions dels mecanismes focals indiquen que tant falles amb orientació NE-SW a NNE-SSW com NW-SE podrien haver generat els terratrèmols. La sismicitat podria ser més profunda que la base del reservori. La distribució magnitud-freqüència suggereix una primera fase de la seqüència amb valors del paràmetre b al voltant de 1.5, més alts que el que s'espera per terratrèmols tectònics, però inferiors que els valors normalment trobats per projectes que generen sismicitat induïda; posteriorment, el valor de b cau fins a valors normals en el context de terratrèmols tectònics (al voltant de 1.0), tot i que la linealitat de la relació és discutible. Els valors obtinguts a partir de la transferència d'esforç estàtic degut als 8 terratrèmols de major magnitud és consistent amb l'activació d'una falla d'orientació NE-SW que cabussa cap a l'est, i no hauria d'haver modificat de manera rellevant els períodes de retorn de terratrèmols característics en la zona. La qüestió en referència a l'origen de la sismicitat no es pot discutir de manera rigorosa sense un model que permeti quantificar les injeccions de gas i la difusió del fluid a través de la xarxa de fractures presents, així com altres mecanismes que poden desencadenar terratrèmols.

TABLE OF CONTENTS

ABSTRACT.....	IX
RESUM	XI
LIST OF FIGURES.....	XVII
LIST OF TABLES	XXII
LIST OF ABBREVIATIONS	XXIII
1. INTRODUCTION AND OBJECTIVES	1
1.1 Motivation.....	1
1.2 Objective and scope.....	2
1.3 Outline.....	3
2. INDUCED SEISMICITY: FUNDAMENTALS AND STATE OF ART	4
2.1 Induced and triggered events	4
2.2 Physical mechanisms of injection-induced seismicity.....	5
2.2.1 Pore pressure increase.....	6
2.2.2 Poroelastic stress changes.....	7
2.2.3 Differential compaction	8
2.2.4 Thermal stress change.....	8
2.2.5 Mass change	9
2.2.6 Stress transfer by nearby earthquakes	10
2.2.7 Chemical reactions	10
2.2.8 Extraction-induced seismicity	10
2.3 Man-induced seismicity and energy technologies.....	10
2.3.1 Highlighted cases	11
2.3.2 Maximum magnitude constraints.....	13
2.4 UGS and induced seismicity.....	13
2.4.1 Current technological situation.....	14
2.4.2 Injection-related seismic activity and UGS projects.....	15
2.4.3 Summing up	17
3. THE CASTOR UGS AND THE 2013 SEISMIC SEQUENCE: PRIOR CONSIDERATIONS.....	18
3.1 The UGS project – historical summary	18
3.2 Geographical and geological context	19
3.2.1 Geographical location	19
3.2.2 Geological context (regional)	20
3.3 Castor's seismic sequence	21
3.3.1 Chronology and first interpretations.....	21

Table of contents

3.3.2 Injection activities and seismicity	23
3.4 Preliminary review of potentially present destabilizing factors	25
3.4.1 Seismic activity triggers.....	25
3.4.2 Geological unknowns	27
3.5 Seismicity's origin: A case of triggered seismicity?.....	28
3.6 Approach of the present study	30
4. HYPOCENTRAL LOCATIONS	33
4.1 Location method	33
4.1.1 Overview of location methods	33
4.1.2 HYPOCENTER routine	34
4.1.3 Input parameters	36
4.2 Event data	37
4.2.1 Data selection	37
4.2.2 Data treatment: Posido v1.5.15	39
4.2.3 Data conditions and quality of the locations	43
4.3 Location results.....	43
4.3.1 Hypocentral locations	43
4.3.2 Magnitude analysis	51
4.4 Discussion: Interpretation of obtained locations. Implications for Castor's anthropogenic seismicity assumption	53
4.4.1 Depth analysis	53
4.4.3 Spatiotemporal evolution of seismicity	57
5. MOMENT TENSOR.....	62
5.1 Method	62
5.1.1 Introduction	62
5.1.2 FMNEAR routine	63
5.2 Event data	67
5.2.1 Data selection	67
5.2.2 Velocity models.....	67
5.3 Results	68
5.3.1 Focal mechanism solutions	71
5.3.2 Nodal plane orientation, dip and depth	71
5.3.3 Magnitudes	72
5.3.4 Quality assessment	73
5.3.5 Model assessment.....	74
5.4 Discussion: Tectonic interpretation. Implications in relation to Castor's anthropogenic seismicity assumption	75

Table of contents

6. STATISTIC ANALYSIS OF SEISMICITY: THE FREQUENCY-MAGNITUDE RELATION.....	80
6.1 Method	80
6.1.1 GR law determination	80
6.1.2 b value evaluation on the context of induced seismicity.....	83
6.2 Earthquake catalog.....	85
6.3 Natural seismicity in the area	85
6.4 Results	86
6.5 Discussion: FMR and the b parameter. Implications for the anthropogenic seismicity assumption	88
7. EARTHQUAKE STATIC STRESS TRANSFER	91
7.1 Fundamental concepts.....	91
7.1.1 Stress and strain.....	91
7.1.2 Stress on a plane	92
7.1.3 Principal angles	93
7.1.4 The Mohr-Coulomb failure criterion and Coulomb stress	94
7.2 Method	95
7.2.1 Stress propagation	96
7.2.2 Coulomb stress changes computation.....	97
7.2.3 The role of the background stress.....	98
7.2.4 Layered half-space	99
7.2.5 Acceleration of the seismic cycle	101
7.2.6 Parameter selection.....	102
7.3 Results.....	103
7.3.1 Coulomb stress change on the source fault planes.....	103
7.3.2 Coulomb stress change on the mapped fault planes.....	106
7.3.3 Optimally oriented faults	109
7.3.4 Acceleration of the seismic cycle on the main fault.....	112
7.4 Discussion: Coulomb stress variations and the occurrence of earthquakes in the case of study	114
8. FINAL REMARKS	116
8.1 Integrated discussion	116
8.2 Conclusions	120
8.3 Recommendations on the context of fluid injection activities	121
8.3.1 Geological model.....	121
8.3.2 Operation practice.....	121
8.3.3 Other aspects	122
8.4 The Castor's case: Future prospects to be expected	122

Table of contents

9. REFERENCES.....	123
ANNEX A: ADDITIONAL BACKGROUND INFORMATION	iv
ANNEX B: SERIANEX STUDY SUMMARY. AP2000, AP3000 AND AP4000	xxiii
ANNEX C: MAXIMUM REGISTERED MAGNITUDES AND PARAMETERS.....	lxxvii
ANNEX D: HYPOCENTRAL LOCATION DATA	cviii
ANNEX E: WORKING 3D FAULT MODEL	clv
ANNEX F: FM SOLUTIONS	clxiv
ANNEX G: EARTHQUAKE RECURRENCE STUDY CATALOG.....	ccxliii
ANNEX H: PLANE STRESS TRANSFORMATION EQUATIONS	cclvi
ANNEX I: COULOMB STRESS CHANGES COMPUTATION. CODA AND INPUT FILE.....	cclxi
ANNEX J: ADDITIONAL FIGURES	cclxxx

LIST OF FIGURES

Figure 1: Representation of the acceleration of the seismic cycle due to a perturbation which could be man-caused. In this case the perturbation is of positive nature (it accelerates the seismic cycle on the fault), but could as well be of negative nature. The latter is obviously not concerning. Modified from Baisch et al. (2009).	4
Figure 2: Stress path during fluid injection into an open fault in a relatively impermeable reservoir (i.e. no poroelastic effects in the matrix) – the stress path of a fracture with optimal orientation for reactivation is given by the movement of the black dot. In this case the stress path during injection always converges onto failure envelope and injection leads to less stable conditions. Source: TNO (2014).	6
Figure 3: Combined effect of poroelastic stressing and pore pressure increase during injection on fault stability. In the case presented here, poroelastic stress changes during injection are destabilizing the fault (continuous red circle). The effect of the pore pressure increase in the faults (dashed red circle) brings the fault to failure. Source: TNO (2014).	8
Figure 4: Stress path due to cooling of the reservoir rocks. αT is volumetric thermal expansion coefficient, K is rock bulk modulus, ΔT is temperature change. The stress path is representative for a laterally extended, uniformly cooling reservoir. Horizontal effective stresses are reduced due to contraction of the reservoir rocks; vertical effective stresses are determined by the weight of the overburden and pore pressure. In a tectonic normal faulting regime the Mohr circle grows and cooling is destabilizing the faults. Source: TNO (2014).	9
Figure 5: Maximum magnitude of events reported to have been caused by or likely related to human activity worldwide. Extracted from NRC, 2012.	12
Figure 6: Main types of UGS. Source: Belcher (2004).	14
Figure 7: Castor's platform south of Ebro Delta, off the eastern coast of Spain.	19
Figure 8: Scheme of representative regional tectonic and sedimentary contexts, in which the structure of the Amposta field and subsequent Castor reservoir is exemplified. Source: ICGC, 2013 (reportedly extracted from an Escal UGS exposition).	20
Figure 9: Histogram of Castor's seismic sequence, showing the number of earthquakes per day and their magnitudes. Two separate phases can be distinguished in this sequence. The first one would last until September 19th, just two days after injections were stopped, and maximum magnitudes did not surpass M 3. After four days of almost no seismicity, the first felt earthquake took place on September 24th (M 3.7), and high levels of seismicity with three M 4 earthquakes were registered during the two following weeks. Source: ICGC (2013).	21
Figure 10: Castor seismic sequence. Source: IGME (2013).	22
Figure 11: Absolute location results for the largest events in the sequence, and faults in the epicentral area. Circles: epicentral locations, with colour corresponding to the timescale on the right side; the prior 2012 April 8 event is also shown. White square: location of the Castor platform. Coloured lines: faults in the proximity of the injection site (faults further away are omitted). In the largest map, the rough locations of the Amposta fault strands (redlines) and a different mapped fault (blue line) are plotted according to Garcia-Mayordomo et al.(2012). The small panel shows a more detailed view of the epicentral region: more detailed digitalized faults are shown (green lines), according to Geostock (2010). These include the Eastern Amposta fault, striking NNE–SSW below the platform, different steep subparallel faults striking NW–SE on the NW side of the Amposta fault, and few subfaults on the opposite side of the Amposta fault striking NE–SW but with different dip angles. Source: Cesca et al. (2014).	24

List of figures

Figure 12: Locations obtained using the 3D shear wave velocity model developed in Gaite et al. (2016). Faults are plotted according to Garcia-Mayordomo et al. (2012). Source: Gaite et al. (2016).	24
Figure 13: Top: Energy released by seismic waves compared to energy introduced to the system. 5% and 0.05% limits, as well as 1 to 1 limits are shown. Bottom: Total energy of the earthquakes (Seismic Moment) compared to energy introduced to the system.	29
Figure 14: Workflow to reach objectives a) and b), the latter subdivided into b.1, b.2 and b.3, according to the unknown aspects from a scientific point of view. The numbers in the yellow (seismological topic) and light brown (geological - geomechanical topic) filled rectangles refer to chapter numeration. Discontinuously contoured boxes indicate that data input or methodology was insufficient to include (red) or properly assess them (black). In the uncertainties box, grey refers to errors that involve both the method applied and input data, black refers to limiting factors associated with current knowledge, and blue indicates that more information is known but was not available to the author.	32
Figure 15: HYPOCENTER routine flowchart. Extracted from Lienert and Havskov (1995).	34
Figure 16: Catalan seismic network and main stations around the Castor platform. ALCN and ALCX waveforms were not available for the dataset located here (<i>loc</i>), nor E301 (Columbretes; since it became permanent named ECOL), which was installed during the seismic sequence. Study area shows the region in which earthquakes were selected. Red discontinuous traces indicate Quaternary Active Faults of Iberia (QAFI; IGME, 2015a), and Castor Platform is also plotted.	38
Figure 17: Schematic dataset selection workflow.	39
Figure 18: CMAS Z, N and E components' waveform showing the M_L 2.1 of September 9 th 05:37:42. The blue vertical line is the P wave, while pink corresponds to the S. Light green shows other phase picks not considered (obviously, just one arrival time of each phase-type can be used).	40
Figure 19: CMAS Z, N and E components' waveform showing the M_L 4.2 of October 1 st 03:32:45. Apart from the P and S wave, light brown shows amplitude picks of the S wave, which are used to calculate the magnitude.	41
Figure 20: Location result as shown in Posido (event of M_L 4.2 occurred on October 1 st 03:32:45).	41
Figure 21: Wood-Anderson seismogram response for a certain earthquake. Light brown represents the maximum peak to peak amplitudes of the S wave.	42
Figure 22: Magnitude result window as shown in Posido event of M_L 4.2 occurred on October 1 st 03:32:45.	43
Figure 23: Earthquake locations with main alignment direction. Light brown indicates shallower than 1.5 km, green between 1.5 and 2.5 (reservoir depths) and blue deeper than 2.5. The yellow star indicates the platform location.	44
Figure 24: Depth distribution along the A-B profile.	45
Figure 25: Gap as a function of magnitudes and number of phases used, for each location. Note how it inversely relates with the number of phases used.	45
Figure 26: Number of phases vs. Magnitude in each single location. Grey line indicates the minimum number of phases used in pub events' locations.	46
Figure 27: Maximum residual (station-hypocenter) vs. magnitude for each location.	47
Figure 28: RMS of each location vs. magnitude.	47
Figure 29: RMS vs. minimum epicentral distance. It can be seen how for those locations with the nearest station at 40 km or farther, RMS starts to increase.	47

List of figures

Figure 30: Horizontal error and magnitudes. Clearly, pub events (ML 2.5 and above) are more reliably located.	48
Figure 31: Volume of the error ellipsoids.	48
Figure 32: Error ellipsoids (pub dataset) displayed on the horizontal (above) and on an E-W depth profile. The yellow star represents the Castor Platform. Negative depths (height above surface) do not have physical meaning, but they are needed to show the whole error ellipsoids.	49
Figure 33: Error ellipsoids (loc dataset) displayed on the horizontal (above) and on an E-W depth profile. The yellow star represents the Castor Platform. Negative depths (height above surface) do not have physical meaning, but they are needed to show the whole error ellipsoids.	50
Figure 34: Depth and magnitude comparison. Horizontal lines indicate average depths of the pub and loc datasets, respectively.	51
Figure 35: Primary magnitude determination parameters, plotted against magnitude and against each other. Note that while standard deviation does not vary, the number of components is systematically higher for the pub dataset.	52
Figure 36: Magnitude comparison. The line adjust is the one in Equation (16).	52
Figure 37: Earthquake locations. Seismic stations are plotted in different color depending on the agency to which they belong. The detailed fault system in the zoom view (black lines) is shown at an approximate depth of 1.7 km, near the reservoir top, and according to Cesca et al. (2014). The Amposta Eastern trace from the QAFI v3 (the composition of Montsia W7, Montsia W7B and Amposta South, see chapter 2 and annex A.4 for further information) is plotted near surface depth. Latitudes and longitudes are shown in degrees.	54
Figure 38: Absolute location results for the largest events in the sequence without using the seismic station COBS, according to Cesca et al. (2014). The red fault traces in the largest map are plotted based on Garcia-Mayordomo et al. (2012), whereas the green ones in the zoom accord to Geostock (2010). Source: Cesca et al. (2014).	55
Figure 39: Fault model slice at depth 1.7 km. Earthquakes' color accords to Figure 37 apart from those in purple, which are the ones which happened inside or just around the boundaries of the reservoir. The main and East 4 faults are represented using thicker and discontinuous lines, respectively. The East 4 fault is the only one dipping towards the East . All earthquakes shallower than 2 km are shown, as well as a simple reservoir surface approximation. While faults dip to the W, the reservoir plunges to the E (review figure 8).	55
Figure 40: Fault model slice near reservoir base depth (around 2.5 km deep) . Earthquakes' color accords to Figure 37 apart from those in purple, which are the ones which happened inside or just around the boundaries of the reservoir. The main fault is represented using a thicker line. The rough base of the reservoir is shown, as well as those events in between 1.7 and 3.5 km deep.	56
Figure 41: Fault model slice at an approximate depth of 3 km. Earthquakes' color accords to Figure 37, and earthquakes between 3 and 7 km are shown.	56
Figure 42: Time evolution of all earthquakes from the <i>pub</i> and <i>loc</i> datasets. Plan view, size of circles indicates magnitude according to figure legend and color indicates time according to colorbar.	58
Figure 43: Histogram of the pub and loc datasets divided in four phases. The first one refers to the swarm during injections. The second one comprises a decreasing of seismicity after injections were stopped. The third phase includes the days with strongest shaking (up to M 4.3), and the fourth is the gradual return to base levels.	58
Figure 44: Plan view of the earthquakes in each of the four phases described in the text. Here, the focus is plenty on time and location, so size of the earthquakes is not distinguished.	59

Figure 45: Strike slip fault and body force descriptions of the double couple. Each force couple can be formed by two forces offset a determinate distance (left double couple, generates torque) or dipoles (right, does not introduce torque). Modified from Stein and Wysession (2009).	62
Figure 46: (a) The 24 fault planes tested in the coarse search, with strike, dip and central rake values tested. (b) exploration of obliquity in the focal mechanisms when the rake is modified to $\pm 50^\circ$ around the central value. In (a) and (b), the fault plane is represented by a heavier black line. Extracted from Delouis (2014).	65
Figure 47: Cyclographic projections of nodal planes on a polar sphere. 0.5 and 1 indicate dips of 45° and 0° respectively.	71
Figure 48: Left: FM solution depth for each of the 8 events, considering the default or the Castor model. Right: FM solution depth compared to input (location) depth.	72
Figure 49: Depth difference between input (location) and output (FM).	72
Figure 50: $M_L - M_w$ comparison and adjust.	73
Figure 51: Quality analysis for solutions obtained using both models.	74
Figure 52: Left: General map of the area with FM solutions. Seismic station colors accord to Figure 16 (chapter 4). The black rectangle shows the rough zoomed area. Right: Solutions using the default or Castor model in a detailed map of the Amposta E fault system, plotted near reservoir top depth. The yellow star represents the Castor Platform. In the legend, NS (Normal-Strike slip) is used for those solutions whose rake indicates relevant normal component, whereas SS is used for the others (strike slip).	76
Figure 53: Rose diagram highlighting nodal plane orientations.	77
Figure 54: Dip and depth of each FM (note that for each FM there are two different nodal planes). The ellipse highlights the steepest planes.	77
Figure 55: Seismogenic zonation of the Iberian peninsula and its seismicity. The black star shows the platform location. Modified from the ZESIS database (IGME, 2015).	85
Figure 56: Cumulative FMR. Blue dots and grey lines show the observed distribution, while the black and red lines indicate the fit (LSE) to the GR distribution and the value of the b parameter. On the right panel, the sequence is divided between the events up to the last day of injections (phase 1), and events afterwards (phase 2).	87
Figure 57: Cumulative seismic moment release of the earthquakes, as obtained from the IGN catalogue.	87
Figure 58: Moving-window calculation of b parameter for the studied catalog, divided according to indications in the figure. The central b value and standard deviations are shown according to indications, as obtained using the LSE. The red discontinuous line represents the tempting interpretation, with two significant drops. In between groups 2 (September 12 th to 17 th) and 4 (September 17 th to 29 th) the parameter value falls from 1.55 to 0.95, whereas between 7 (September 30 th to October 2 nd) and 8 (October 2 nd to 4 th) changes from 0.85 to 0.7.	88
Figure 59: Stresses on a cube, using engineering notation. Source: Schofield and Wroth (1968).	92
Figure 60: Axis system, principal stresses (σ_1 and σ_3) and a failure plane. Modified from King et al. (1994).	93
Figure 61: Schematic representation of the Mohr's circle, which stands for the stress conditions, and the Mohr-Coulomb failure envelope. The red dot marks the intersection of the circle and the failure envelope.	94

List of figures

Figure 62: Convention used in focal mechanisms and Coulomb's software. Source: Toda et al., 2011.	96
Figure 63: Scheme of two axes systems.....	97
Figure 64: <i>edcmp_cou2.m</i> flowchart. Main steps are shown in yellow highlighted boxes. Subroutines and their input parameters or calculation basis are shown in light blue, while light grey shows user-defined parameters or information needed to compute CSC in function <i>compcou2.m</i> .	100
Figure 65: Location of the 8 strongest events of the seismic sequence, numbered in chronological order (first to last). Fault's trace at an approximate depth of 1.7 km is also depicted (according to Geostock, 2010), as well as the Castor platform location (yellow square).	103
Figure 66: Coulomb stress resolved on the nodal planes. Each subplot shows the CSC due to the nodal plane of the previous earthquake slipping, on both the nodal planes of the old and the upcoming event. Past nodal planes are shown as red rectangles, whereas the new ones are directly represented onto the beach ball plot (pink line). The last subplot shows as well the faults' trace at a depth of 1.7 km, to better picture locations. Note that colorbar changes scale as sequence evolves. $\mu' = 0.6$.	104
Figure 67: Time series of CSC on the source fault planes. Each line color represents one different plane, with empty circle markers being the state before the quake and filled markers afterwards. The black box in the left subplot limits the zoomed area on the right. $\mu' = 0.4$.	105
Figure 68: Time series of CSC on the source fault planes. $\mu' = 0.6$.	105
Figure 69: Time series of CSC on the receiver fault planes. The discontinuous vertical lines indicate the occurrence of an earthquake (note that days 267 and 277 also have earthquakes). Colors are used to better distinct faults, and do not accord with CS being positive or negative (which is represented on the vertical scale). $\mu' = 0.4$.	106
Figure 70: Time series of CSC on the receiver fault planes, divided each one into various patches. $\mu' = 0.4$.	107
Figure 71: CSC on modeled fault planes, using single patches (above), and multiple patches (below). Deeper dark blue patches are the source faults, corresponding to those in Figure 66. $\mu' = 0.4$. The orientation of the plot view was chosen so that all faults were visible, although no perfect solution which shows all fault areas at once is possible.	108
Figure 72: Coulomb stress changes computed at each point of the grid for a fixed depth of 1.7 km, where the fault traces (main black lines) are plotted. S_H strike is varied from 9 to 37 ° ($S_h = S_H + 90$). The three panels above show as well the OOF (strike-slip) orientations, left lateral in grey and right lateral in black. Red rectangles represent the hosting planes, although they are deeper than the map plot. $\mu' = 0.6$.	110
Figure 73: Coulomb stress changes computed at each point of the grid for a fixed depth of 5.0 km, according to figure indications.	111
Figure 74: Coulomb stress changes resolved on cross sections indicated in the left panels. The map view is plotted at the depth indicated by the discontinuous line. $\mu' = 0.6$.	112

LIST OF TABLES

Table 1: Summary of world's induced seismicity cases (caused by or likely related to human activities). The first known, best documented or considered as most relevant are the cases featured here. Sources: Talwani, 1997; Baisch et al., 2009; NRC, 2012.	11
Table 2: VG model specifications. The flat layer assumption considers constant values in any point inside the layer. Source: ICGC (2013).	37
Table 3: FMNEAR webservice speed model. Q_p , Q_s are the seismic attenuation coefficients (Higher Q means lower attenuation).	67
Table 4: Castor velocity model. Q_p and Q_s are the seismic attenuation coefficients (Higher Q means lower attenuation).	67
Table 5: FMs solutions summary table – default model. Sorted by input magnitude (highest to lowest). Solutions obtained by Frontera et al. (2013), IGN (2013) and Cesca et al. (2014) are also shown to ease comparison. Frontera's et al. (2013) solutions were obtained using the same method (FMNEAR) and model (default).	69
Table 6: FMs solutions summary table – Castor model. According to other indications given for the previous table.	70
Table 7: Values of the b parameter of the GR law and differences according to analysis group and method used. The standard deviation is also indicated for the LSE case.	86
Table 8: Stress and strain notations.	92
Table 9: Direction cosines (simplified notation) of the angles between the old and new axes.	97
Table 10: Relative magnitudes of the commonly assumed background stresses depending on the faulting regime. S_H and S_h are the maximum and minimum horizontal stresses, whereas S_v is the vertical.	98
Table 11: Parameter selection and variations in order to compute Coulomb stress changes and acceleration of the seismic cycle.	102
Table 12: Acceleration of the seismic cycle (%), assuming three different magnitude cases and two effective friction values, and according to stress drops indicated in the tables and ds in the stress drop boxes refer to strike slip and dip slip respectively, while min and max are the assumed threshold values.	113
Table 13: Acceleration of the seismic cycle (years), assuming three different magnitude cases, according to stress drops and T_r indicated in the table. Note that Standard Deviation (SD) is higher than the $T_r, \mu' = 0.4$	113

LIST OF ABBREVIATIONS

- ACS – [Company]: Actividades de Construcción y Servicios. <http://www.grupoacs.com/>
- BU – [University]: Boston University. <http://www.bu.edu>
- CCS – [Term]: Carbon Capture and Storage
- CEDIGAZ – [Non profit Association]: The international association for natural gas. UGS worldwide database. <http://www.cedigaz.org/>
- CI – [Term]: Confidence Index. See Delouis (2014).
- CIS – [Term]: Commonwealth of Independent States (Russia and some former Soviet Republics).
- CLP – [Company]: Castor Limited Partnership
- CNIG – [Institute]: Centro Nacional de Información Geográfica. www.cnig.es
- CSC – [Term]: Coulomb Stress Change(s)
- DD – [Term]: Double Difference. See Waldhauser and Ellsworth (2000).
- EIA – [Institution]: U.S. Energy Information Administration. www.eia.gov
- EGR – [Term]: Enhanced Gas Recovery
- EGS – [Term]: Enhanced Geothermal System; also known as Hot Dry Rock (HDR) geothermal system.
- EPA – [Agency]: Environmental Protection Agency (U.S.). www.epa.gov
- EOR – [Term]: Enhanced Oil Recovery
- EPA – [Agency]: Environmental Protection Agency (U.S.). www.epa.gov
- FERC – [Comission]: Federal Energy Regulatory Comission (U.S.). www.ferc.gov
- FM– [Term]: Focal Mechanism
- FMNEAR– [Term]: Focal Mechanism calculation method. See Delouis (2014).
- FMR– [Term]: Frequency Magnitude Relationship
- GR law – [Term]: Gutenberg-Richter law(Frequency-Magnitude relationship).
- GSE– [Research group]: Group of Seismic Experts.
- HF– [Term]: Hydraulic Fracture
- HYC–[Term]: HYPOCENTER. See Lienert and Havskov (1995).
- IEA – [Agency]: International Energy Agency. www.iea.org
- IIE – [Institution]: Instituto de la Ingeniería en España. <http://iies.es/>
- ICGC – [Institution]: Institut Cartogràfic i Geològic de Catalunya. www.icgc.cat
- IGN – [Institution]: Insituto Geográfico Nacional. www.ign.es
- IGME – [Institution]: Instituto Geológico y Minero de España. www.igme.es
- IGU – [Association]: International Gas Union. www.igu.org
- JD– [Term]: Joint Density
- JHD – [Term]: Joint Hypocenter Determination. See Douglas (1967).
- LNG – [Term]: Liquified Natural Gas.
- LSE– [Term]: Least Squares method
- MAXC– [Term]: Maximum Curvature. See Wiemer and Wyss (2000).
- MIT – [University]: Massachusetts Institute of Technology. www.web.mit.edu

List of abbreviations

MLE– [Term]: Maximum Likelihood Estimation method

NAM–[Company]: Nederlandse Aardolie Maatschappij. www.nam.nl

NRC – [Council]: National Research Council. <http://www.nationalacademies.org/nrc/>

OBS –[Term]: Ocean Bottom Seismometer

OOF –[Term]: Optimally Oriented Fault Planes

PDF – [Term]: Probability Density Function

QAFI – [Database]: Quaternary Active Faults of Iberia. <http://info.igme.es/QAFI/>

RMS – [Term]: Root Mean Square error or deviation.

SA – [Term]: Simulated Annealing (probabilistic technique).

SERIANEX - [Research Group]: Trinational SEismic Risk ANALysis EXpert group. See Baisch et al. (2009).

SGC – [Syndicate]: Síndic de Greuges de Catalunya. www.sindic.cat/en/

SMT– [Term]: Seismic Moment Tensor

UA – [University]: Universidad de Alicante. <http://www.ua.es/>

UGS – [Term]: Underground Gas Storage

UNECE – [Comission]: United Nations Economic Comission for Europe

UPC - [University]: Universitat Politècnica de Catalunya. www.upc.edu

UPM- [University]: Universidad Politécnica de Madrid. www.upm.es

USGS – [Institution]: United States Geological Survey. www.usgs.gov

TNO – [Association]: Netherlands Organisation for Applied Scientific Research. www.tno.nl

TTR – [Term]: Travel Time Residuals

VG model– [Term]: Valencia Gulf velocity model.

WCP– [Document]: Watercraft Capital Prospectus

WGV – [Term]: Working Gas Volumes

ZESIS– [Database]: Seismogenic Zones of Iberia. <http://info.igme.es/zesis/>

1. INTRODUCTION AND OBJECTIVES

This document is the result of nine months of work and it presents the findings of research in the topic of induced seismicity in Underground Gas Storage projects (UGS hereafter). Particularly, it comprises the study of the seismicity occurred in the vicinity of the Castor platform, presumably triggered by gas injections in September and October 2013.

The work has been mainly effectuated at the Institut Cartogràfic i Geològic de Catalunya (ICGC), in collaboration with the Universitat Politècnica de Catalunya (UPC). The outcome is this report which constitutes a master's thesis and, although primarily focused on the Castor project, intends to be an introduction to the UGS projects' challenges and general problematic in relation to induced seismicity. It also includes general recommendations when addressing a project of this kind, both to avoid and better monitor induced seismicity.

1.1 Motivation

Energy availability is an unconditional need for our societies and is therefore a priority for any government. The storage of gas may be of interest for most countries, essentially in economic terms. Gas reservoirs can provide secure energetic supply when the market experiences fluctuations, during peak demands, or in occurrence of problems of any kind with the supplier (companies, countries, etc). However, induced seismicity might be a threat for further development of gas reservoirs in some areas, as it has previously happened with other anthropogenic projects worldwide.

The alteration of subsurface conditions (essentially states of stress and pore pressures) can change the earth's crust tectonic regime. Though foreseeable, either the injection or withdrawal of underground fluids may hassle undesirable behavior, especially earthquakes, which are the result of the sudden slip of a fault. This slip results in the release of energy in the form of seismic waves, which can travel large distances through the earth's layers and cause ground shaking at the surface. Structures are built in contact with the ground, and may consequently be damaged by the shaking, the worst case being structural collapse. Hence, earthquakes are and will undeniably be of public concern.

In the second half of the 20th century and the beginning of the 21st, many energy technologies such as geothermal energy, oil and gas production, wastewater injections and gas storage among others have experienced induced seismicity (NRC, 2012). Generally, public awareness in relation to this topic is rising up due to numerous documented cases of seismicity after the development of such projects, as well as growing media coverage. Thus, scientific research oriented to understand and diminish the problematic with induced seismicity must be conducted, as well as the implementation of good practices in terms of communication to the general public. With the current energy demand and complex workflow between governments, companies and public at large, any option to store or obtain control over an energy source should be explored.

1.2 Objective and scope

Published studies in relation to the Castor case have already addressed problems in earthquake locations and focal mechanisms' computation, as well as the frequency-magnitude relationship (ICGC, 2013; IGME, 2013; IGN, 2013; Cesca et al., 2014; Gonzalez, 2014; Gaite et al., 2016; among others). Cesca et al. (2014), include as well some discussion in relation to the mapped faults which would have been more likely to slip based on background stress. However, quantification of the physical mechanisms that may generate earthquakes and its evolution is yet to be published.

The goal of this work is being able to apply a methodologically correct approach to assess induced seismicity due to fluid injections, on a real field case. The scheme is simple, yet it intends to cover all essential aspects of the problem presented by the development of seismicity during and after the gas injection performed in September 2013 near the coast of Castello (NE Spain). In this context, the first immediate goal was improving and incrementing the seismological data stored in ICGC's database. And second, an assessment of seismicity, taking into account the described faults in the area of interest, was performed; for this part, a specific triggering mechanism (earthquake static stress transfer) is quantified by means of Coulomb stress changes.

For such a study, the distribution of the Catalan (surveilled by the ICGC) and Spanish (property of Instituto Geografico Nacional, IGN) networks, as well as other regional stations, is not optimal for earthquakes located in the offshore area of interest. Due to this fact, earthquakes are located within uncertainties of a few kilometers, which means that it is very difficult to directly relate earthquakes and faults, especially when a complex fault network exists. That being said, an important effort has been made to constrain seismological results as much as possible.

Moreover, both the results and ability to develop interpretations which accord with truth is essentially dependent on the quality of the input data. In this case, information regarding geological setting was the one available to any public user. Hence, detailed information in the surroundings of the reservoir had to be deduced, or extrapolated, from other literature that did not necessarily have the same goals, or that did not report obtained results clearly enough so that they could be used in another study. Regarding injection procedures, the available information was very limited.

Though results concerning the evaluation of seismicity are an approximation, the author believes in the opportunity of being able to achieve general-trend valuable results when a coherent methodology and fundamental concepts are applied, and therefore, in this work to add valuable information to the existing studies in relation with the Castor UGS. Escal UGS, the project's responsible company, surely has more precise and extensive data which is to be used in another study with capacity to reveal accurately more facts, especially regarding seismicity's origin.

Specific objectives comprised in the different parts of this report include: Phase arrival picking, hypocentral location determination and magnitude calculation, focal mechanisms computation, earthquake recurrence law study, and implementation of a simplified fault

model around the Castor platform in which Coulomb stress changes and seismic cycle acceleration are evaluated.

1.3 Outline

This project is divided in the following sections:

Fundamentals of induced seismicity and state of the art (chapter 2): Physical mechanisms of induced seismicity and induced seismicity on the context of energy technologies (with focus on UGS).

The Castor project and the 2013 seismic sequence (chapter 3). It includes the essential background information and a preliminary evaluation of the problem. The procedure to be followed is justified.

Hypocentral locations (chapter 4): study of a previously revised dataset by the ICGC, and location of a new one with 50 earthquakes using Lienert and Havskov's (1995), HYPOCENTER. Seismic phase picking, magnitude calculations and analysis of the whole cluster distribution.

Moment tensor (chapter 5): Computation of 8 focal mechanisms via FMNEAR (Delouis, 2014), using two different velocity models, and analysis in relation to known mapped faults.

Seismic recurrence law (chapter 6): Frequency-Magnitude relationship during the seismic sequence, comparison of the b parameter of the Gutenberg-Richter law (GR law from this point) with the value reported for natural seismicity in the area, and evolution during the seismic swarm. Assessment of the information provided by the b parameter in relation to induced seismicity.

Coulomb stresses and seismic cycle (chapter 7): Coulomb stress changes computation as a result of the 8 main events of the sequence using COULOMB 3.4 (Toda et al., 2011), and development of a code which allows obtaining CSC from the strain and stress changes matrix (so as to work with the output given by the ED software by Wang et al., 2003).

Final discussion of the results as a whole, conclusions and recommendations (chapter 8).

2. INDUCED SEISMICITY: FUNDAMENTALS AND STATE OF ART

Even if non desired man induced seismicity is not new, injection induced seismicity, particularly in the UGS context, is a subject yet to cover. The complexity of the topic, which involves various disciplines from both the physics and geology fields, as well as engineering, required a thorough background research. Whereas the specific situation regarding the Castor UGS will be presented in the next chapter, this one aims at providing the following:

1. Physical mechanisms of induced seismicity
2. Energy technologies and induced seismicity cases, with focus on UGS projects.

Though an effort has been made to make these parts as short and reader-friendly as possible, the amount of information needed to contextualize the case of study is notable. Apart from the information in the main text, references to the annexes will be made in case the reader wants to fully grasp the background state.

2.1 Induced and triggered events

First of all, the reader should note that an important distinction is sometimes highlighted in research, when referring to anthropogenic seismicity: Seismicity can be triggered (meaning that its occurrence is anticipated because of a stress perturbation, which is a fraction of the ambient stress) or induced (in this case the seismicity is controlled in nucleation and size by the perturbing stress, and would not take place without it; e.g. McGarr et al., 2002, Cesca et al., 2014)

Induced events are usually of small magnitude, and therefore will not normally cause high-intensity ground shaking. Triggered events, on the other hand, can potentially be much more powerful. This is because the perturbation that causes the shaking is just a little portion of the value of the ambient stress, and so does not control the size of the earthquake itself. In fact, the result is a shortening or acceleration of the seismic cycle, δt_{cycl} (Figure 1). The seismic cycle could be defined as the repetitive or cyclical process of strain accumulation and sudden release on a fault plane, with a recurrence time (T_r).

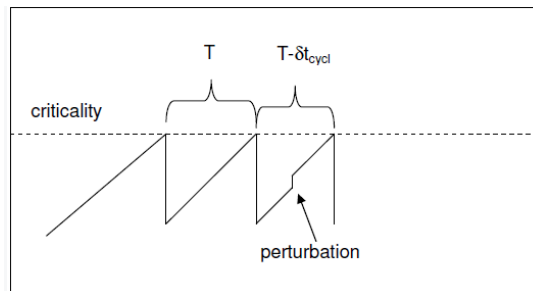


Figure 1: Representation of the acceleration of the seismic cycle due to a perturbation which could be man-caused. In this case the perturbation is of positive nature (it accelerates the seismic cycle on the fault), but could as well be of negative nature. The latter is obviously not concerning. Modified from Baisch et al. (2009).

Henceforth, for reasons of simplicity and most references not distinguishing between induced and triggered events, general terms such as anthropogenic, man-caused or injection-induced will be used for man-originated seismicity without differences in their meaning. Though, when a chapter or a part of it requires discriminating, induced and triggered seismicity terms will come up.

2.2 Physical mechanisms of injection-induced seismicity

Earthquakes occur when a fault slips due to shear stress exceeding its shear strength (also called shear resistance). This condition is usually expressed using the Mohr-Coulomb failure criterion (Jaeger et al., 2007; Ellsworth, 2013), as in Equation (1), which expresses the idea of fault slipping when its friction-based strength is not enough to cope with shear acting on the plane.

$$\tau_{crit} = c_0 + \mu(\sigma_n - u) \quad (1)$$

Where:

τ_{crit}	Critical shear stress for slip to be initiated
c_0	Cohesion. Negligible under normal crustal conditions
μ	Friction coefficient. For the majority of rock types, in between 0.6 and 1.
$\sigma_n - u$	Effective normal stress on the fault (σ_n') expressed as the difference between the total normal stress and the pore pressure (u). Note that the higher the value of u , the lower the value of τ_{crit} .

To account for the perturbation of a local stress field, Coulomb Stress Changes (CSC) as in Equation (2) can be considered (King et al., 1994; Scholz, 2002). Quantifying the Coulomb Stress Change¹ (see chapter 7) allows accounting for the tendency of a certain fault to slip.

$$CSC = \Delta\tau - \mu(\Delta\sigma_n') \quad (2)$$

Where:

CSC	Coulomb Stress Change. Positive values promote fault slip and negative values prevent the fault from slipping.
$\Delta\tau$	Shear stress change
μ	Friction coefficient
$\Delta\sigma_n'$	Effective normal stress change on the fault (σ_n')

There are various physical mechanisms responsible for fault activation. Pore pressure increase, poroelastic stress changes, differential compaction, thermal stress and mass changes, stress transfer by nearby earthquakes and chemical reactions being the most commonly described in literature (e.g. Geertsma, 1973; Segall, 1989; Segall et al., 1998; Stein, 1999; McGarr et al., 2002; Zoback and Zinke, 2002; Mulders, 2003; Bourne et al., 2006; Ellsworth, 2013; Klose, 2013; Orlic et al., 2013). The following mechanisms are detailed next based on TNO (2014), which provides an extensive chapter on this topic.

¹Analytical solutions provided by Okada (1992), are used in order to compute strains. Static strains and associated stress fields can be obtained for different sources, resolved in a particular observation fault with a characteristic location and orientation. These solutions are commonly used in software programs such as COULOMB (developed by the USGS; Toda et al., 2011).

2.2.1 Pore pressure increase

The increasing of pore pressures reduces the effective normal stress and therefore, the shear strength of the fault. Cohesion in a geologic material is due to the contact strength of its mass, which can widely vary depending on the material origin² and structure (fractures, pores, etc). When fluid pressure in the material discontinuities increases, the applied effective stresses may be reduced and, therefore, shear strength diminishes. The extreme would be a case in which pore pressure equals the total normal stress, thus inhibiting any shear strength.

Figure 2 exemplifies this behavior using the Mohr's circle. In the specific case of fluid injection into reservoir rocks, poroelastic effects will have an important influence and the stress paths are likely to change from that figure (see section 2.2.2).

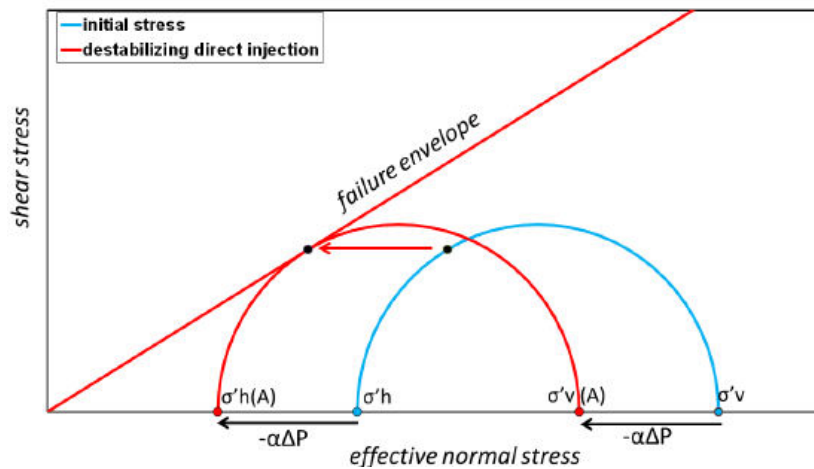


Figure 2: Stress path during fluid injection into an open fault in a relatively impermeable reservoir (i.e. no poroelastic effects in the matrix) – the stress path of a fracture with optimal orientation for reactivation is given by the movement of the black dot. In this case the stress path during injection always converges onto failure envelope and injection leads to less stable conditions. Source: TNO (2014).

Pore pressure increase is usually the dominant factor in injection-induced seismicity. According to NRC (2012), the magnitude of this mechanism, as well as the extent to which this variation affects, depends on:

1. Operation-related parameters: Fluid injection rate, total volume injected, maximum flow reached.
2. Fluid viscosity
3. Rock hydraulic properties: Intrinsic permeability (k) and storage coefficient (S)

Combination of high transmissivity with small storativity and planar faults would lead to pore pressure increase being transmitted over large distances. Any of these factors is, accordingly, essential to consider.

²Soils are formed by particles deposited with enough space between grains for water to flow easily. Rock masses, on the other hand, have followed a different constitutional process and their permeability (assuming intact conditions) is basically due to discontinuities. Source: Hudson & Harrison (1997).

2.2.2 Poroelastic stress changes

Poroelasticity is a branch of continuum mechanics which considers the behavior of a fluid-saturated porous medium. Under loading conditions, the volume fraction of the pores may be affected due to the mechanical stress, and it leads to fluid motion. As a result, the solid mass experiences elastic strain (Multiphysics cyclopedia in www.comsol.es/multiphysics/poroelasticity). By the term elastic strain, it is understood that experienced deformation is not permanent, and, if conditions change, it is possible to return to the original state.

The reservoir rock is subjected to poroelastic behavior, and the change in pore pressure affects the vertical and horizontal effective stresses in a different way, as noted in Equation (3) and (4).

$$\Delta\sigma'_v = -\alpha\Delta u \quad (3)$$

Where:

$\Delta\sigma'_v$	Effective vertical stress change
α	Biot's coefficient. Its range is between 0 and 1
Δu	Pore pressure change

$$\Delta\sigma'_h = -(\alpha - \gamma_h)\Delta u \quad (4)$$

Where:

$\Delta\sigma'_h$	Effective horizontal stress change
$\gamma_h = \alpha \frac{(1 - 2\nu)}{1 - \nu}$	Horizontal stress path coefficient. vis the Poisson ratio ³ . The lower the value of ν , the higher the γ_h , for a constant α value, and the lower the (negative) increment of effective horizontal stress.

It can be noted than the change in horizontal effective stress is smaller than the change in vertical effective stress. This means that changes in poroelastic stress vary the differential of stresses, thus modifying the Mohr's circle and stabilizing or destabilizing a determinate plane; this depends on stress path coefficients. Moreover, depending on the tectonic regime, the maximum stress can be either in the horizontal or vertical direction, consequently determining whether the Mohr's circle grows or shrinks during injection or withdrawal of the reservoir.

Assuming a destabilizing injection, Figure 3 represents the stress paths promoting failure due to poroelastic stress changes and pore pressure changes. The paths followed due to poroelastic stress changes are usually irreversible (e.g. Santarelli et al., 1998; Van der Zee et al., 2011).

³ ν (Poisson ratio), refers to the expansion on the transverse axial. The higher the value, the higher the expansion in the perpendicular direction to the compressing axis. The maximum value, of a perfectly incompressible material, would be 0.5, as it is limited by Young, bulk and shear module which always have to be positive.

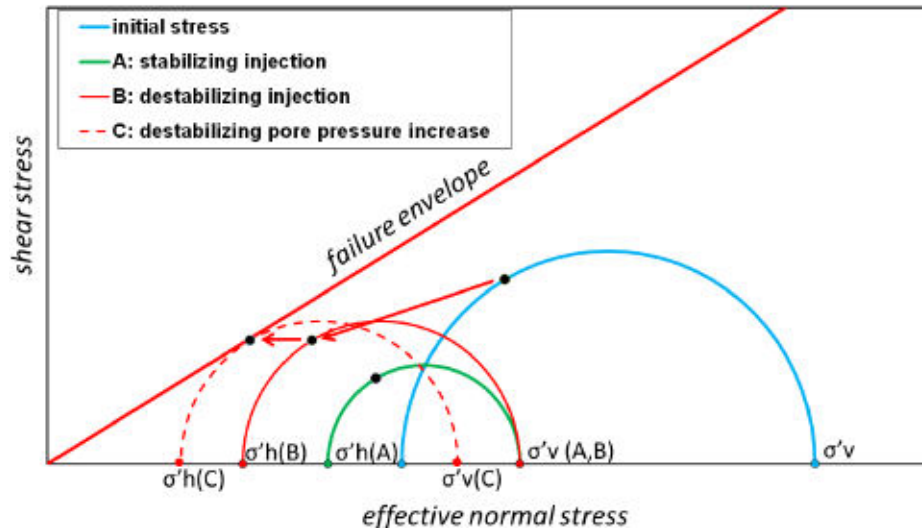


Figure 3: Combined effect of poroelastic stressing and pore pressure increase during injection on fault stability. In the case presented here, poroelastic stress changes during injection are destabilizing the fault (continuous red circle). The effect of the pore pressure increase in the faults (dashed red circle) brings the fault to failure. Source: TNO (2014).

2.2.3 Differential compaction

Reservoir compaction and/or decompaction has been studied in detail by various authors (Segall, 1989; Soltanzadeh & Hawkes, 2008; Van Wees et al., 2014). Distribution of pore pressures, faults, reservoir geometry and geomechanical differences between the reservoir and surrounding rocks are the main factors affecting this topic.

This effect has basically been studied in relation to reservoir depletion, as withdrawal of fluid tends to generate relative compaction in the reservoir, mostly occurring in reservoir boundaries (faults) or edges, with differential pore pressure evolution. Under these conditions, stress paths can vary from the ones shown in 2.2.1. Stress can be generated in places where the fluid volume is not modified.

Segall (1989), notes that under depletion conditions (e.g. producing reservoir), the material below and above the reservoir is decompressed vertically and compressed horizontally, whereas at the flanks it is the opposite. This will have a great influence in the possible activation of neighboring faults; depending on their type, it will promote or disable fault slip.

Modeling studies for an UGS by Orlic et al. (2013), indicated that injection activities (re-pressurization) can produce a similar mechanism due to differential decompaction.

2.2.4 Thermal stress change

Difference of temperatures between the fluid injected and the reservoir induce thermal stresses, not only in the injection area but also in the surrounding rocks, although the significant change is expected near-well. It has been shown (Ghassemi et al., 2007), that thermal contraction of the material can diminish normal stresses (and increase shear stresses) thus promoting fault slip.

Thermal stress changes are of great importance in Enhanced Geothermal Systems, EGS (Segall et al., 1998; Baisch et al., 2009), but also in other projects such as CO₂ storage

where notable differences in temperature are expected. Following Jaeger et al. (2007), for a case of laterally constrained rocks, thermal stress can be expressed as it follows (Equation (5)):

$$\Delta\sigma_T = \alpha_T K \Delta T \quad (5)$$

Where:

$\Delta\sigma_T$	Thermal stress change
α_T	Volumetric thermal expansion coefficient
K	Bulk modulus of the reservoir rocks
ΔT	Temperature change

As an example, with a K of 10 GPa and an α_T of $3\text{E-}5/^{\circ}\text{C}$, a ΔT of 10°C will produce a thermal stress change of 3MPa (relevant near the well). Figure 4 exemplifies the stress path in a laterally extended reservoir with uniform cooling, where the horizontal effective stress decreases and the vertical effective stress remains constant. Figure 4 shows a Mohr's circle with vertical stress greater than horizontal stress, conditions expected in a tectonic context with normal faulting.

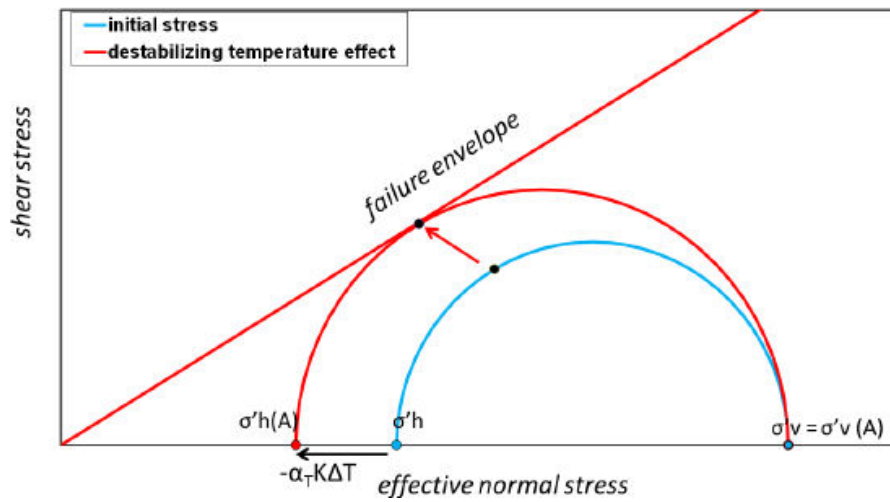


Figure 4: Stress path due to cooling of the reservoir rocks. α_T is volumetric thermal expansion coefficient, K is rock bulk modulus, ΔT is temperature change. The stress path is representative for a laterally extended, uniformly cooling reservoir. Horizontal effective stresses are reduced due to contraction of the reservoir rocks; vertical effective stresses are determined by the weight of the overburden and pore pressure. In a tectonic normal faulting regime the Mohr circle grows and cooling is destabilizing the faults. Source: TNO (2014).

2.2.5 Mass change

Relevant changes in mass, and so stresses at depth, can be produced by fluid injection or withdrawal in the reservoir. Depending on the tectonic regime of the area (e.g. dominant normal faulting, thrusting or strike slipping) positive or negative mass changes will be stabilizing or destabilizing. For example, a positive mass change (which increments vertical stress), will be stabilizing in a thrust fault regime, but it is the opposite in an area dominated by normal faulting. Klose (2013), related moment magnitudes and cumulated mass changes, finding a positive correlation.

2.2.6 Stress transfer by nearby earthquakes

When a fault slips, the stress on the fault itself is reduced due to stress drop after slipping (re-initiation of the seismic cycle). But, the stress redistribution can change conditions on other faults. The provoked stress changes on these called observation faults can be expressed in terms of the CSC (as in Equation (2)). Geological structures near the source can experience an increase or decrease in their potential to be reactivated (Stein, 1999; Baisch et al., 2009). This mechanism will be explored in detail in chapter 7.

2.2.7 Chemical reactions

Geological medium properties can be altered by chemical reactions. The most direct effect would be a modification in the friction coefficient of a fault, expectedly easing fault slip by diminishing it. In literature, stress corrosion is mentioned as the most relevant in relation to induced seismicity topic. (Suckale, 2009).

2.2.8 Extraction-induced seismicity

Although the focus of this chapter and whole document is injection-induced seismicity (due to the fact that the seismic sequence in the Castor UGS is supposed to have been activated by gas injections), fluid withdrawal can as well generate earthquakes. As explained before, pore pressure changes are one of the main factors of (injection) induced seismicity. It is also a key factor in withdrawal induced seismicity. Even if the importance of maintaining balance in the reservoir has long been known by companies carrying out depletion activities, changes in the pore pressure may have been the reason for induced seismicity in this context more than once.

NRC (2012), notes that the diminishment of pore pressure generates contraction of the reservoir, and as explained in part 2.2.3, the horizontal stresses increase both above and below the reservoir, thus promoting reverse faulting (Segall, 1989). Examples of induced seismicity caused by depletion of a reservoir have been reported, for example, in relation to the Lacq gas field, in France (Grasso and Wittlinger, 1990; Segall et al., 1994). Linked factors to extraction-induced seismicity have been reported to be pore pressure decrease due to depletion, the amount of faults above the reservoir, contrasts in stiffness between the reservoir and neighboring rock and reduction of vertical stress below the reservoir (McGarr, 1991; Van Eijs et al., 2006).

Further information on the context of identifying induced events is provided in annex A.1.

2.3 Man-induced seismicity and energy technologies

Processes that involve injection and/or withdrawal of fluids underground (e.g. activity related with energy technologies) can hence cause seismicity⁴ (Kerr, 2012; NRC, 2012), as they can change stress conditions. The number of projects using energy technologies has substantially increased in the last few years, and so have seismic events. For example, just

⁴Although this introductory chapter is just focused on energy technologies because of similarity with the activity at the Castor Reservoir, other processes (man-made) have also been related with induced seismicity (Baisch et al., 2009; NRC, 2012): Underground nuclear tests, controlled explosions related to mining and construction and impoundment of water reservoirs being examples.

within central and eastern United States, more than 300 earthquakes with magnitude⁵ $M \geq 3$ occurred in three years (2010, 2011 and 2012), compared with an average rate of 21 events/year observed from 1967 to 2000 (Ellsworth, 2013).

2.3.1 Highlighted cases

McGarr et al. (2002), indicate that the study of anthropogenic seismicity began when earthquakes were first felt in Johannesburg in 1894. According to NRC (2012), seismicity related to human activity has been documented at least since the 1920's (Pratt and Johnson, 1926), and the number of sites where seismic events ($M \geq 0$) have been related with human activity are listed in Table 1 by technology and represented in Figure 5 by technology and magnitude.

Table 1: Summary of world's induced seismicity cases (caused by or likely related to human activities). The first known, best documented or considered as most relevant are the cases featured here. Sources: Talwani, 1997; Baisch et al., 2009; NRC, 2012.

Type of project	Number of sites with induced seismicity	Highlighted cases
Wastewater injection	11	Denver, CO, United States. (1960's)
Oil and gas withdrawal	38	Lacq Gas Field, France. (1957 - 1980's)
Secondary recovery (water flooding)	27	Rangely, CO, United states. (1957 - 1970's)
Geothermal energy	25	Basel, Switzerland (2006)
Hydraulic fracturing (shale gas)	2	Blackpool, United Kingdom (2011)
Surface water reservoirs (dams)	44	Lake Mead, NV, United States. (1940).
Others-1 (Mining - related activity)	8	Ruhr, Germany (1983 - 2007).
Others-2 (Carbon Capture and Storage)	-	None reported in NRC,2012

One of the first exhaustively documented earthquake cases related with human activity is the case of Lake Mead water reservoir (USA). The area experimented an increase of events in the late 1930's, coinciding with the lake filling, and elevated rates of seismicity continued until the mid 1960's, with maximum magnitudes of $M \sim 5$ (Roger and Lee, 1976; Simpson, 1976). The maximum magnitude of anthropogenic seismic events rarely exceeds $M 5$ (NRC, 2012; McGarr, 2014), although projects such as Denver 1960's (fluid disposal) or the previously cited Lake Mead water reservoir have reported events around or slightly greater than $M 5$. Fluid disposal injection experiments are repetitively reported in literature as the ones inducing events with highest magnitudes. However, events up to $M 7$ have been related with human activity (though not proven to have been caused by it), an example being the Gazli gas field in Uzbekistan (Adushkin et al., 2000; NRC, 2012).

When hydraulic fracturing is related to shale gas projects, it does not pose risk in terms of generating $M > 2$ earthquakes (based on NRC, 2012, only the case of Blackpool in England, 2011, has generated felt episodes, with the greater event of $M 2.3$). On the other hand,

⁵ M refers to the moment magnitude of an earthquake. Today, the magnitude scale used by seismologists to report cases globally is the named moment magnitude scale (M_w or M), which was developed in the 1970's. In the past however, events' magnitudes were calculated at each site using local magnitude scales (M_L), such as the Richter magnitude scale.

Carbon Capture and Storage (CCS) projects remain an unknown risk, as volumes considered for injection in the future may be extremely large and therefore cause big perturbations nearby. At the moment, no harmful events have been related yet with CCS projects (NRC, 2012).

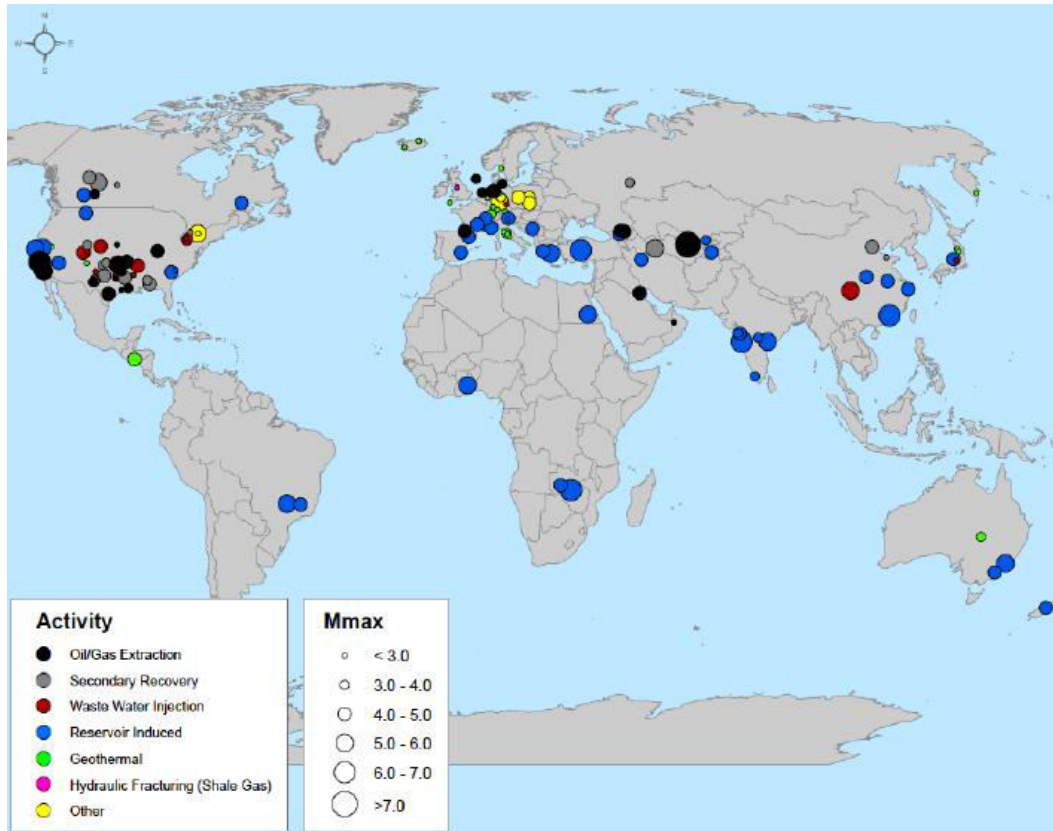


Figure 5: Maximum magnitude of events reported to have been caused by or likely related to human activity worldwide. Extracted from NRC, 2012.

The study elaborated by SERIANEX⁶ (Baisch et al., 2009) in relation to the halted Enhanced Geothermal Project (EGS) at Basel (Switzerland), constitutes a benchmark in the evaluation of seismic risk related to human activity. Basel1 borehole was drilled inside the city of Basel. The geothermal reservoir was at a depth of 5 km and an earthquake of M_L 3.4 was induced on December 8th, 2006, during the stimulation phase of the reservoir. The operator's insurance payment amount, attributed to the earthquake, was of about 7 million CHF. The conducted study developed both local and regional 3D fault models of the area, and afterwards, induced and triggered seismicity studies were carried out.

The goal of the induced seismicity study was to obtain maximum magnitude values and frequencies for further development of the EGS, and they used numerical modeling both with empirical relations using other projects. Triggered seismicity analysis focused on obtaining the variation of T_r of natural characteristic earthquakes in the area. In this case they defined the perturbations introduced by the EGS, and after quantifying them, evaluated their influence in terms of alteration of the seismic cycle in any of the previously defined regional faults. The criterion used is the Coulomb Stress Change (CSC) as defined

⁶SERIANEX's study was commissioned by the Kanton Basel-Stadt and supported by the Swiss federal government, and the collaboration between government and companies was remarkable.

in Scholz, 2002 (see chapter 7). A summary of each of the documents dedicated to the seismicity study, in Baisch et al. (2009), is provided in annex B (in Catalan).

As accounted by the studied cases, the combination of high volumes and rates of injected fluid, continuous operation activity for large periods of time, large pressure differentials between the naturally existing in the reservoir and the one after the activity (e.g. in projects that only extract or inject fluids), and other changes such as temperature of the rock matrix, may change local conditions and therefore generate seismic activity.

2.3.2 Maximum magnitude constraints

As a first step, statistical relations have been done in literature (McGarr, 2002, 2014; Baisch et al., 2009) to obtain constraints of expected maximum magnitudes based on certain parameters (related to operation conditions, geologic material, type of faulting, etc).

The idea behind this approach is being able to predict or limit maximum magnitude values, using information available for any operator in projects of this kind. Nevertheless, it is important to know that:

- a) Uncertainty when adjusting these empirical correlations is high.
- b) They are not necessarily based on any fundamental principle of rock or fluid mechanics and/or stress transfer.

Therefore, such relations should never substitute a wide study focusing on the introduced perturbation, its quantification and its transfer in the geologic structures. Bearing this idea in mind, annex C shows an analysis of how maximum recorded magnitude relates with various parameters, for a data set of different EGS and similar projects provided in Baisch et al. (2009). The Castor UGS was added to the study in annex C, when information regarding a certain parameter was available, in order to explore divergences due to experiments' differences. It was found that the Castor UGS is particular, and should not be modeled with the same relations used for other projects whose data was available, both because of its geology and project's nature.

2.4 UGS and induced seismicity

Injection of fluids into a reservoir has been proven as one of the main causes of induced seismicity, as widely documented in literature (Healy et al., 1968; NRC, 2012; Kim, 2013; Cesca et al., 2014; McGarr, 2014; Dieterich et al., 2015, among many others). Commonly, seismic episodes are related to waste disposal, hydraulic fracturing (popularly known as “fracking”) activities (shale gas operations or EGS) or Enhanced Oil and Gas Recovery (EOR and EGR).

The recent development of gas injection projects, either in the context of a particular gas storage (e.g. CO₂) or gas stored underground (UGS – referred to natural gas⁷ storage) has

⁷Regarding its composition, natural gas is an hydrocarbon which mostly consists of methane (CH₄). It also contains variable proportions of nitrogen, ethane, carbon dioxide, H₂O, butane, propane, mercaptans and other heavier hydrocarbons. Proportions of each gas vary depending on the source, but methane can be up to 97% of the natural gas. Natural gas is an economical and efficient

raised scientific attention, due to their potential to induce seismic activity as it has happened before with other injection experiments. Injected volumes, working pressures and operation times considered in the UGS context can cause earthquakes. Indeed, recent episodes at Bergermeer in the Netherlands (Orlic et al., 2013) or the Castor seismic sequence (events up to M_w 4.3; documented by Cesca et al., 2014) have revealed that UGS related activities have an earthquake triggering potential, and should therefore be treated carefully.

2.4.1 Current technological situation

Present storage options include depleted oil and/or gas reservoirs, (leached) salt caverns, aquifers, and abandoned mines or rock caverns (Bary et al., 2002; Belcher, 2004; Lord, 2009; UNECE 2013).

Depleted oil and gas reservoirs take advantage of existing wells, gathering systems, pipelines and also a good geological knowledge of the area, which makes them the most used storage system. Although reservoir's proven capacity to hold hydrocarbons throughout geological time, gas storage should always be treated carefully. As noted by Lord (2009), loss of gas over geologic time or until certain levels has already occurred.

Natural aquifers can be suitable if the water-bearing formation lies under an impermeable rock, and has high permeability and porosity. Aquifers could be used to reach peak load rates (PB-KBB, 1998), as their withdrawal rate can be enhanced by an active water drive⁸ (Foh et al., 1979). On the other hand, salt caverns main advantage is their high deliverability rate (Belcher, 2004; Lord, 2009). Figure 6 shows the main emplacements of UGSs.

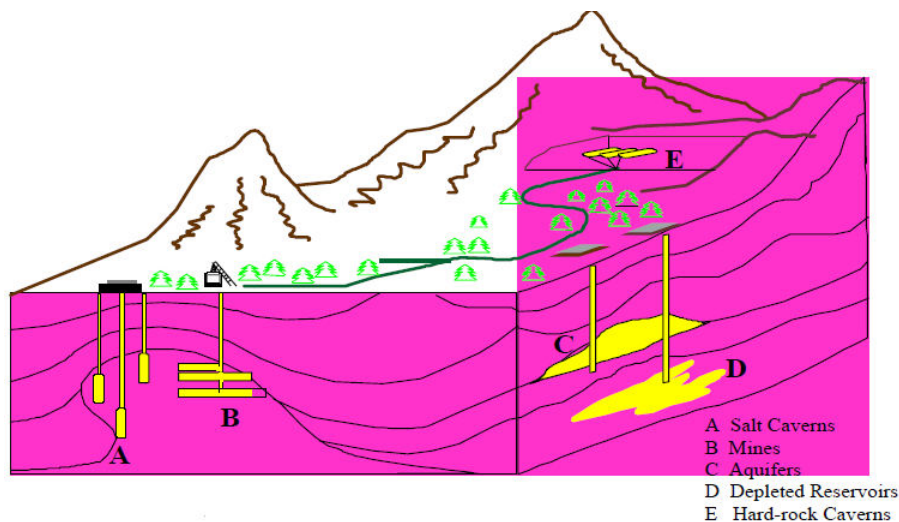


Figure 6: Main types of UGS. Source: Belcher (2004).

In general, UGS technology follows the developments by the oil and gas industry, although particular adaptations are implemented. As reported by UNECE(2013), the number of UGS

energy, as well as environmentally friendly because of its low content in carbon dioxide. Source: www.enagas.es

⁸Water drive is a reservoir-drive mechanism whereby the reservoir fluid is driven by water from an active aquifer. Water fills previously fluid-filled (in the case of UGS, gas) pores and increases its recovery. Source: <http://www.glossary.oilfield.slb.com/>

in abandoned mines and UGS in reservoirs without trap will grow about 50-60% in the future. UGS in fractured aquifers, for associated gas from oil industry and UGS in porous rock-systems will double.

Temperature and pressure are measured at wellhead⁹ for most of the current projects, but monitoring wells with bottom hole pressure only happens at 30-35% of the sites (bottom hole temperature is just monitored for 25% of the projects) (UNECE, 2013). This serves as an example to illustrate that, even in locations with ongoing activity, field-data acquisition at relevant depths is not always possible. This is especially relevant when it comes to the evaluation of potential anthropogenic seismicity risk and the quantification of introduced perturbations by any project of this kind. Without high-quality field data, the development of any numerical model expected to quantify the changes introduced by any project and assess earthquakes' causes becomes unfeasible.

As for the majority of the literature, gas storage industry will remain stable in terms of its technology, although some changes are to be introduced in the near future. A complete database of measurements and variations of key parameters (Pressures, fluid-injection rates, temperatures, etc) is essential. Dense monitoring networks (at surface and depth) are thus important, as well as seismic networks in order to detect and locate precisely any event within the reservoir. In terms of public acceptance, efforts should be aimed towards a secure, effective and rapid gas supply, reducing the cost as much as possible.

Information on the subject of locations of current European and Spanish UGSs is provided in annex A.2.

2.4.2 Injection-related seismic activity and UGS projects

Available information in literature in relation to UGS which have registered seismic activity is very limited. A few cases with existing documentation, such as Bergermeer (The Netherlands) and Castor (Spain), are summarized here in order to provide an introductory overview on the case and on the published studies' focus and goals.

UGS facility in Bergermeer (depleted Rotliegend reservoir), NW-Netherlands

TNO (2014) reports of 3 UGS in The Netherlands which have triggered seismic activity (Bergermeer, Norg and Grijpskerk) but more of them might be related (e.g. Van Wees et al., 2014). In 1994 and 2001, in this case during depletion activities, 4 seismic events with magnitudes between M_L 3 and 3.5 were recorded in a gas field in the Netherlands. Modeling results conducted by Van der Zee et al. (2011) and Orlic et al. (2013), show that stress paths on the fault during injection are not reversible, and also that additional fault slip right at the beginning of the first injection cannot be excluded. However, stress paths reveal that after the first injection phase faults stabilize.

Studies considered here use 3D finite element modeling to infer in faults' proximity to slip and Mohr-Coulomb stress paths (for selected nodes of the modeled mesh) during considered activities (depletion / injection) and scenarios. They investigate how positive and negative pressure variations will affect the modeled fault(s), either bringing them to a

⁹The surface termination of a wellbore that incorporates facilities for installing casing hangers during the well construction phase. Source: <http://www.glossary.oilfield.slb.com/>

more stable situation or vice versa. They can therefore rate beforehand different scenarios based on fault slip probability.

Bergermeer site was equipped with a micro-seismic monitoring array, to track induced events during storage (injection) activity (Kraaijpoel et al., 2012). The largest magnitude reported was of M 0.7 in October 2013.

Offshore UGS facility in Vinaros (Castellon), NE Spain: The Castor Project

The Castor project and its seismicity are described with more detail in the next chapter. Here, the main methods of study up to date and findings regarding seismic activity and its relation to the Castor UGS are summarized.

Cesca et al. (2014) used full waveform techniques to obtain absolute and relative locations, estimate depths and focal mechanisms of the strongest events of the sequence (up to M_w 4.3). Their results show that seismicity is generally characterized by oblique mechanisms with a normal fault component (NNE-SSW and NW-SE planes). Combining information regarding locations of the hypocenters and focal mechanisms, they indicate that the seismic sequence seems to correspond to a rupture of shallow low-dipping structures, which could have been triggered by the gas injections.

Gaite et al. (2016), note that precise locations are a great challenge due to low magnitudes and seismic network distribution. They relocate a subset of 161 events using the NonLinLoc method (Lomax, 2008) and a new 3D shear wave velocity model (developed from surface-wave ambient noise tomography). They obtain a NW-SE alignment of the earthquake cloud and most of the events located at a depth of about 6 km, deeper than what is suggested in Cesca et al. (2014).

Most of the literature seems to point out that the seismic sequence could hardly be expected as the pressure variations introduced in the reservoir were minimal, in an area of low natural seismicity (ICGC, 2013; IGN, 2013; Cesca et al., 2014; del Potro and Diez, 2015). Instituto Geologico y Minero de España (IGME; 2013), note that the swarm-like distribution of seismicity is linked with induced seismicity, and that the second phase of the sequence (with the strongest shakes after the end of injections) is likely to be a case of triggered seismicity.

Another issue worth considering is whether the earthquakes could have been prevented. Doubts arise as to the method used when injecting gas into the geological formation (pressure ramps, ratio of injected volume, total injected volumes, etc), as well as the real capacity of the seal rock (Castello Shale) to prevent gas from escaping. ICGC (2013), rate the Castello Shale as a good seal for heavy oil, but not necessarily for gas, and note the fact that gas leaks into neighboring faults could have increased pore pressures and, consequently, have destabilized them.

Other seismic episodes linked with UGS activity

No other UGS facilities have recorded seismic episodes which could be acceptably correlated with their injection activities. TNO (2014), reports about Gazli former gas field in Uzbekistan, which since 1988 is used as an UGS facility for industrial gas. Based on Plotnikova et al. (1996), a relation between earthquakes recorded and pressure cycles in

the field is discussed. Nevertheless, the mechanisms proposed are not clearly explained and most of the information available to the public is in Russian.

Another example is the monitoring of Collalto Stocaggio UGS in Italy. Mucciarelli et al. (2013), report that events up to M_L 2.3 were recorded during the first year (2012) of monitoring. The updated list (checked October 2015 - www.rete-collalto.crs.inogs.it), shows 4 events above M_L 3 (3.2, 3.6, 3.7, 4.6), but most recent studies (Priolo et al., 2015; Romano et al., 2015), as well as Mucciarelli et al., (2013), do not recall any relation between the UGS and the earthquakes.

The Lacq Gas Field, located in Aquitaine (France), is a natural gas field which is supposed to have registered induced seismicity. However, most of the studies write about extraction-induced seismicity, so its seismicity is beyond scope here (NRC, 2012; TNO, 2014)

2.4.3 Summing up

UGS facilities can cause earthquakes due to their injection (and later extraction) activities. The physical mechanisms that drive man-induced seismicity have been presented in part 2.2 (see also annex A.1) and their discussion will be further addressed. That being said, direct pore pressure increase on faults and changes in solid stress should be mentioned as the main causes (Ellsworth, 2013). The Castor seismic sequence is at the moment the case with strongest shaking clearly related to injection activity in the UGS context.

Due to their resemblances, technology and operation strategy used in UGS is similar to the one in the oil industry. A unified “best practices” protocol in order to minimize UGS’s injection induced seismicity is already available in the U.S. (EPA, 2012), but the analogue in Spain is yet to come. Even if literature record on similar projects and geological particularities at each site should have been important enough, the prospect of obtaining one does not seem an upcoming task. Bearing that in mind, monitoring relevant parameters (temperature, pressure, flow, etc) at reservoir depths, as well as having an adequate seismic network, is the first step to take towards better coverage of the processes happening within the reservoir and, so, wider information and deeper understanding.

The current situation in the world seems to indicate that both U.S. and Europe are already using their most suitable UGS sites, so their growth is going to be more limited than in other countries such as China or the Middle East. Spain is in need of finding new strategies to reduce its energy dependency, and the development of UGS is undoubtedly under the spotlight (see annex A.2). However, seismicity experienced at the Castor reservoir could slow down government and main companies’ ambitions, especially due to public concern.

3. THE CASTOR UGS AND THE 2013 SEISMIC SEQUENCE: PRIOR CONSIDERATIONS

Between the 5th and 8th of September, 2013, the seismicity rate suddenly increased in front of the Castellon coast, in NE Spain (ICGC, 2013; IGME, 2013; Cesca et al., 2014). The sequence peaked with a M_L 4.3 on the 2nd of October (e.g. ICGC, 2015) and high levels of seismicity continued until the end of October.

Intensities up to III-IV were felt by population in the coast of Castellon and neighboring areas, at about 20-30 km from the injection point, and public concern raised up. Injections had actually stopped on September 17th, after at least two events greater than M 2.6 struck on Sept. 12th and 13th (IGME, 2013). Castor UGS is placed in a former oil reservoir (Amposta field), which was operated by Shell until 1989. The main goal of this facility (whose operation is halted, but has not been dismantled¹⁰) was to become the largest UGS in Spain as well as a secure gas source (Escal UGS, 2015). Many questions arise, such as whether the project will ever re-achieve public acceptance after the situation in 2013, if good practices are really going to be implemented in order to control seismicity, or if this was just a strategy to enrich a company(es) on account of their agreements with the Spanish government (SGC, 2014).

To contextualize the study, this chapter is divided in two parts. The first one (3.1 - 3.3) provides the required available background information in relation to the Castor UGS. The second one (3.4 onwards) presents an opening analysis based both on references results and energies comparison (calculated), which will allow justifying the structure of the main parts of this thesis.

3.1 The UGS project – historical summary

The Castor UGS was ideated in 1996, when the Spanish industry ministry gave the hydrocarbon exploration permits to Escal UGS¹¹ (at the time, Spain-Canada Resources Inc.), in order to determine whether the Amposta oil field was suitable for gas storage. Although the ideation took place in a moment of economic growth, the goal was to obtain a strategic storage in case of an energetic crisis or problems with suppliers, as well as an option to meet peak demands in the Spanish natural gas system.

Until 2007, Escal UGS studied the characteristics of the project with the purpose of deciding whether it was both technically and economically feasible. In 2008, they were given green light to start the Castor UGS.

¹⁰Currently, the Massachusetts Institute of Technology (MIT) is developing a study that is supposed to help Spain's next government to decide whether or not the Castor UGS should be definitely suspended. This study should be finished during the second semester of 2016.

¹¹Escal UGS S.L. is the Spanish company responsible for the Castor UGS. As noted by ACS (2007), it is integrated by ACS (66.7 % stake) and CLP (33.3 %). Since the start of operation activities, Enagas was supposed to obtain 50 % of the stake owned by ACS, so each of the three would have a 33.3 %.

In 2010, the company alleged that no study of seismic hazard had been carried out, as both the platform and pipelines were placed in an area of low seismic hazard (see annex A.3). However, as it is stated by IGN (2013), seismic hazard maps do not assess man-induced seismicity problematic, and particular studies should be done at those locations where activities with induced seismicity potential are performed.

Three years later, in September and October 2013, intense seismic activity took place in the area during the third injection phase. Seismicity started on September 8th, and on the 17th operations were halted; studies were officially requested to the IGN and IGME. High levels of seismicity continued until the end of October (Figure 9). The IGME was, at least, partially provided with data from Escal UGS (3D seismic profiles and pressure values in the wells, as well as injected volumes during the 3 injection phases¹²). Unfortunately, Escal UGS has not made public any of this data up to date, thus the only written scientific information available regarding injection operations is the one shown in IGME's (2013), report.

3.2 Geographical and geological context

3.2.1 Geographical location

The Castor UGS is located south of Ebro Delta, in front of the coast of Castellon (NE Spain), at about 22 km offshore. The municipality of Vinaros is the nearest urban nucleus. This area forms part of the Gulf of Valencia (limited by the Ebro Delta at north and Xabia at south), and comprises many highly populated coastal cities, from Castello to the south of Catalonia. Figure 7 shows Castor's platform location.



Figure 7: Castor's platform south of Ebro Delta, off the eastern coast of Spain.

¹²The first phase started on June 14th and lasted until June 27th, the second one from August 19th to 23rd, and the third one from September 2nd to 17th. On each phase, the injected volume was increased using a constant rate, which was the biggest in the third phase. The gas was injected at a depth of about 1800 m.

3.2.2 Geological context (regional)

Geologically, Tarragona's basin comprises a part of the Trough of Valencia, which extends from the north-eastern coast of the Iberian Peninsula to the Balearic Islands. This region is mainly dominated by rifting¹³ structures resulting from Neogene extensional tectonic activity. The evolution of the named trough until present days has resulted in many active quaternary faults (Playa, 2010; ICGC, 2013; IGME, 2012).

According to Fontbote et al. (1990), the Valencia Trough can be divided in the Catalan-Valencian domain (north) and the Betic Balearic domain (south). The Castor is located in the first one, dominated by active extensional tectonics during the whole Neogene, and without the appearance of thrusting along this period.

The rifting structures in the area of study have a predominant NE-SW orientation, where tectonic blocks sink eastwards (Figure 8). These blocks are limited by normal faults which have notorious vertical displacements (about 1000 m) and lengths which can be of tenths of km. The main structure group is the Amposta Fault System (ICGC, 2013).

The hercynian basement is overlain by a wide sedimentary sequence. The Mesozoic and Paleozoic are highly deformed and separated from the Cenozoic cover by an erosive surface. Main reservoir rock in the region is a karstified and fractured limestone (Jurassic and Lower Cretaceous), emplaced at the top of tilted blocks covered by sediments of the Miocene. Certain Miocene sediments, such as clastics and limestone, can also be (sub)economically relevant (Merten, 2006; Playa et al., 2010). More detailed information about the Amposta field (stratigraphy and structure, as well as oil-field history), is provided in annex A.4.

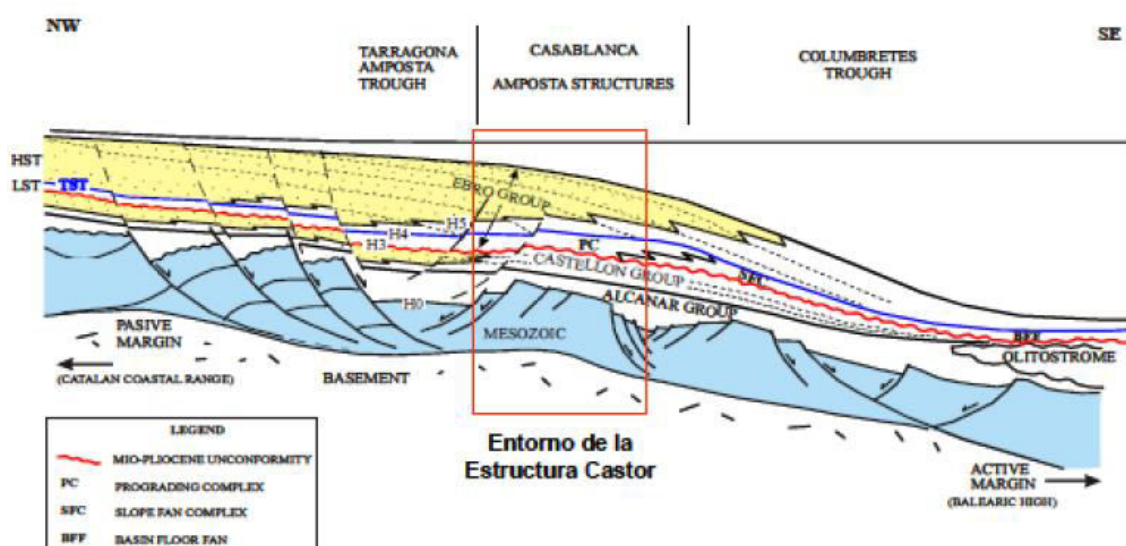


Figure 8: Scheme of representative regional tectonic and sedimentary contexts, in which the structure of the Amposta field and subsequent Castor reservoir is exemplified. Source: ICGC, 2013 (reportedly extracted from an Escal UGS exposition).

¹³In Geology, a rift is a zone where the crust is being torn apart, as a result of extensional tectonics. Main structures associated with rifting processes are the horst (upthrown block) and graben (down-dropped block), as well as normal faulting. Source: <http://earthquake.usgs.gov/learn/glossary>.

3.3 Castor's seismic sequence

3.3.1 Chronology and first interpretations

The seismic sequence started on September 5th, 2013, and it ended the second half of October (Figure 9). In fact, the levels of seismicity from October 9th onwards were really low, without any felt earthquake. In the surroundings of the Castor reservoir (40.150 ° to 40.615 ° latitude N and 0.390 ° to 0.997 ° longitude E, which represents an area of approximately 3500 km²), only 34 earthquakes had been recorded before 2013 (maximum magnitude of 3.3). However, the seismic sequence alone in the vicinity of the UGS built up to more than 900 earthquakes (maximum magnitude of M_w 4.2, and a maximum of 53 earthquakes recorded in only one day) until Oct. 21st (ICGC, 2013; IGN, 2013; IGME, 2013; Cesca et al., 2014).

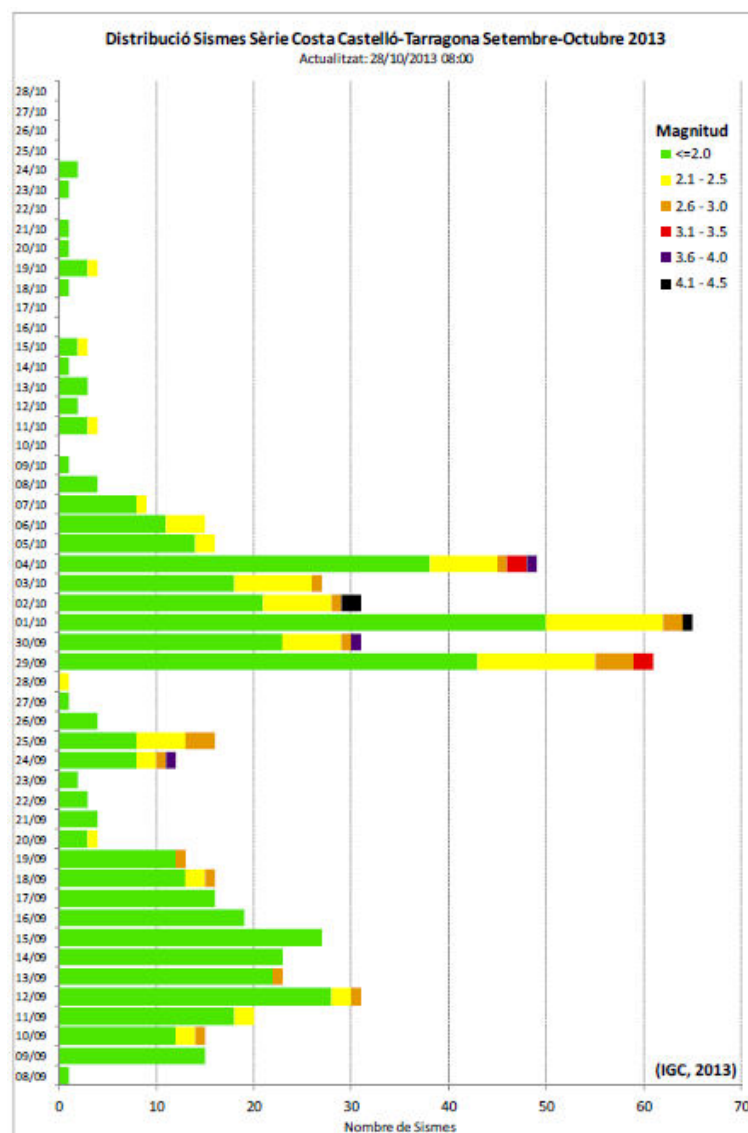


Figure 9: Histogram of Castor's seismic sequence, showing the number of earthquakes per day and their magnitudes. Two separate phases can be distinguished in this sequence. The first one would last until September 19th, just two days after injections were stopped, and maximum magnitudes did not surpass M 3. After four days of almost no seismicity, the first felt earthquake took place on September 24th (M 3.7), and high levels of seismicity with three M 4 earthquakes were recorded during the two following weeks. Source: ICGC (2013).

The Castor earthquakes have a frequency distribution of a seismic swarm: The main events do not happen at the beginning and there is no significant difference between the maximum event and the other important events. The injection operations finished in between Sept. 16th and 17th, and after that the number of events decreased as expected. But, on September 24th, the seismicity increased again, the strongest segment of the sequence taking place from Sept. 30th until October 4th. During the second phase (the sequence is usually divided in two phases, during and after injections) 8 events with magnitude equal or greater than M_L 3.5 were recorded. IGME (2013), state that the first phase corresponds to induced seismicity (according to low maximum values and distribution of its occurrence) with seismicity frequency decreasing since the end of the injection activities, something that was also noted by ICGC (2013). The second phase is, according to the same document, a case of triggered seismicity, with characteristics of a seismic swarm (Figure 10).

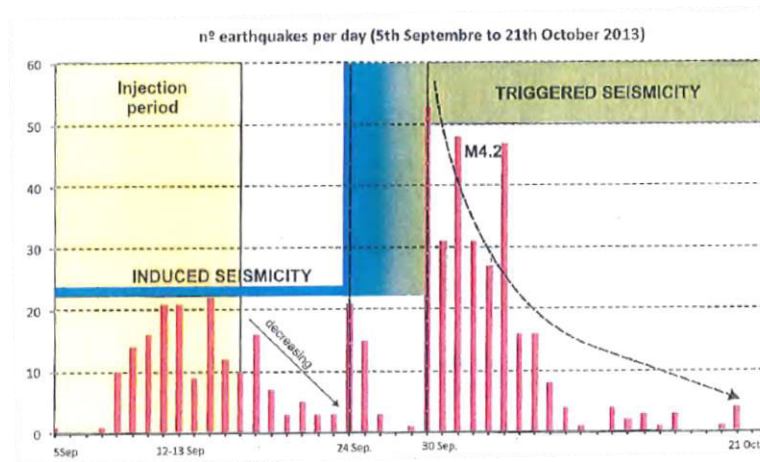


Figure 10: Castor seismic sequence. Source: IGME (2013).

The distinction in between the two phases can also be addressed by studying the Gutenberg-Richter law (GR law hereafter) of the Castor sequence. The Gutenberg-Richter law is named after its authors, who published it in 1944. It shows the relation between the frequency of earthquakes and its size, and can be modeled using the equation $\log(N) = a - bM$. N is the number of events of at least magnitude M , and a and b are the parameters to adjust. The first makes reference to the total seismicity rate of the region, whereas the second considers the relation between small and large earthquakes. The higher the b -value, the higher the number of low-magnitude earthquakes compared to bigger ones (further insight in chapter 6).

According to IGME (2013), during the first phase the b -value tends to 1.4 (high proportion of low magnitude earthquakes), whereas the adjust results in a value of around 0.8 for the second phase, closer to what is expected in tectonic processes (b -value around 1.0). Cesca et al. (2014), note that this change in the b -value may suggest a change in stresses but also a change in the dominant focal mechanism. IGME (2013), highlight the fact that the second phase indicates the presence of faults in the region which can produce earthquakes with bigger sizes than what was expected for induced earthquakes.

Although no numerical modeling and/or quantification of introduced perturbations is yet published (chapter 7 aims at quantifying the influence of a triggering mechanism), all

evidences seem to support the fact that the Castor swarm would have never taken place if no UGS activity had been performed. Both temporal and spatial correlation with gas injections, and change of seismicity regime in the area are indicators that seismicity was man-induced. IGN (2013), affirm that natural seismicity was accelerated by the gas injections, and ICGC (2013), conclude that the seismicity was probably induced or triggered by the injection. Nevertheless, the references used in this part also indicate that further studies, together with more accurate locations of the earthquakes and complete Escal UGS operation data, are necessary to make definitive statements.

3.3.2 Injection activities and seismicity

The total volume of gas in the reservoir at the end of the injection was around $1\text{E}+08\text{ m}^3$, and the seismicity was closely related in time with the third injection stage (September 2nd to 17th). During this phase, introduced the volume increment was of $8\text{E}+6\text{ Nm}^3$ (Normal cubic meters) per day. The injected volume in the third stage augmented notably compared to stages 1 & 2, as well as the rate of injection (IGME, 2013; SGC, 2014).

Using the wellhead pressure values from the third injection stage in the observation wells, Hall diagrams¹⁴ (Mihcakan et al., 2005) were plotted. The results in the three wells were similar, with two breaks appearing on September 5th and 13th. Still, the correlation was made each time for a particular well, and as noted in the reference document, it would be more reliable a relation of total pressure values. These values unfortunately, were not provided (IGME, 2013).

Temporal analyses of pressures on each observation well were also completed. The pressure curves for the analyzed wells show sudden pressure drops just at the time of earthquakes, which provide evidence of the proximity between the seismic source and the wells. In addition, most of the drops cause a permanent reduction of pressure in the well, while if farther apart the drop would be transient and not that high. The observed drops had a maximum value of 0.1bar.

The episodes with magnitudes greater than 2.0 were relocated by IGN (2013), who report that all of them took place SE of the Castor platform (between 2 and 4 km deep). Although the depth error may be substantial, the seismicity seems to have taken place from the top of the Amposta Chalk to the Montsia limestone. A general view of the absolute locations (before relocating) is presented in Figure 11 according to Cesca et al. (2014). However, a recent study by Gaite et al. (2016) places most of the events centered or NW of the platform, with greater hypocentral depths (most of them between 5 and 8 km beneath the seabed), and displaying a NW-SE alignment (Figure 12).

¹⁴The Hall diagram relates injected volume per day with pressure. As a result of induced seismicity studies, it has been observed that when the curve is truncated, induced seismicity takes place (EPA, 2012).

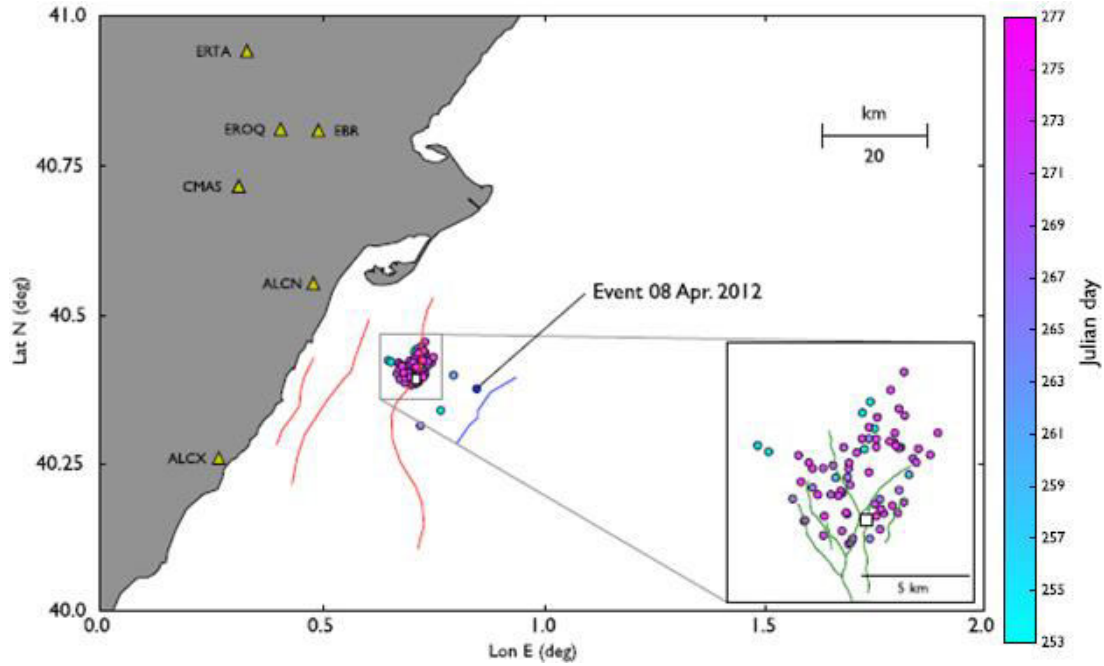


Figure 11: Absolute location results for the largest events in the sequence, and faults in the epicentral area. Circles: epicentral locations, with colour corresponding to the timescale on the right side; the prior 2012 April 8 event is also shown. White square: location of the Castor platform. Coloured lines: faults in the proximity of the injection site (faults further away are omitted). In the largest map, the rough locations of the Amposta fault strands (redlines) and a different mapped fault (blue line) are plotted according to Garcia-Mayordomo et al.(2012). The small panel shows a more detailed view of the epicentral region: more detailed digitalized faults are shown (green lines), according to Geostock (2010). These include the Eastern Amposta fault, striking NNE–SSW below the platform, different steep subparallel faults striking NW–SE on the NW side of the Amposta fault, and few subfaults on the opposite side of the Amposta fault striking NE–SW but with different dip angles. Source: Cesca et al. (2014).

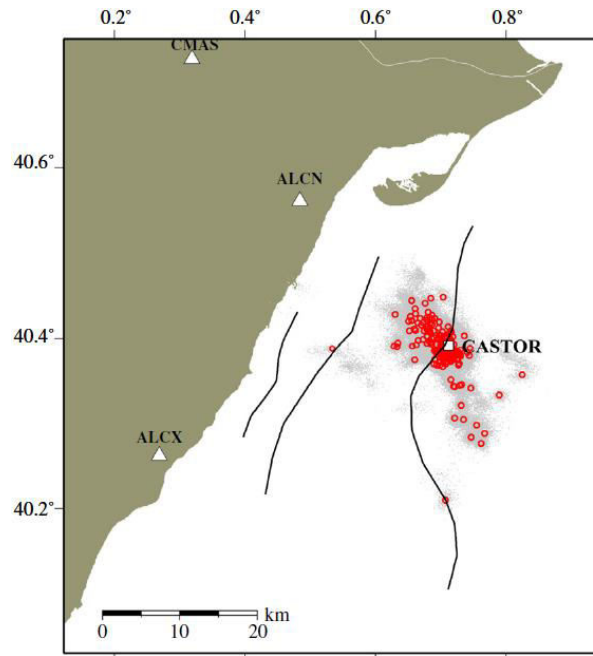


Figure 12: Locations obtained using the 3D shear wave velocity model developed in Gaite et al. (2016). Faults are plotted according to Garcia-Mayordomo et al. (2012). Source: Gaite et al. (2016).

IGME (2013), affirm that the distribution of the seismic sequence (orientation and depth) seems to relate with the named Castor Fault, at the E of the Castor platform, which had not

been detected or considered in any of the other studies. The focal mechanisms of the 8 strongest events (from M_w 3.5 above) calculated by Frontera et al. (2013), and IGN (2013), show a strike slip mechanism with some normal component. They provide a nodal plane (037/67 SE) which agrees with the main trace of the Castor Fault. However, their conducted mechanical compatibility analysis show that the compatible nodal planes are the ones with NW-SE direction (130/80 SW), which could agree with observed interruptions of direction NW-SE in the Castor Fault. Cesca et al. (2014), also report two possible nodal planes either involving a low-dip failure striking more or less parallel to the Eastern Amposta Fault, but dipping to the other side (SE), or a system of nearly vertical faults with orientation NW-SE (which accords to what is documented in IGME, 2013).

The similitude of focal mechanisms suggests that it was the same fault plane that slipped in each one of the events; hence, the local perturbation due to gas injections was affecting the same fault plane repeatedly. However, the nature of the seismic sequence, which shows a swarm-like display, would advocate for the dynamic interaction of various faults instead of the activation of only one fault, which is consistent with the fragmented nature of the IGME's (2013) Castor Fault (geologically, a fault should be understood as a fault zone, and not a line). The Castor Fault estimated total rupture area is of 5.76 km², thus the maximum possible magnitude related to its total surface rupture would be around M_w 4.8, based on Wells and Coppersmith (1984).

The seismic sequence, as accepted at the moment, is probably consequence of induced seismicity and afterwards, of triggered seismicity. The Amposta Oriental Fault, which is regarded to be the largest in the area, does not seem to have had any importance in terms of the observed seismicity (ICGC, 2013; IGME, 2013; Cesca et al., 2014). However, given its dimensions (potentially capable of hosting at least a M_w 5.9 event based on IGME, 2013, or M_w 6.6 based on Garcia-Mayordomo et al., 2015) further detailed studies should be performed in the region, in particular to improve the 3D knowledge of the main fault plane.

3.4 Preliminary review of potentially present destabilizing factors

Up to here, the state of the art in relation to the Castor UGS and the seismic sequence has been presented. Here, the principal mechanisms that could have caused seismicity (if it was indeed induced or triggered) as well as other aspects that remain unsolved or unclear are discussed shortly. The reader should bear in mind that this part is only based on previous seismological information (before locating any earthquake or proceeding with further calculations); its purpose is to present the main questions that arise in relation to this case of study, and help the reader understand the organization of the following chapters. As well, it will be useful as an evaluation tool to see up to which extent these points can be better explained afterwards.

3.4.1 Seismic activity triggers

Batchelor et al. (2007), affirm that the reservoir is supported by an aquifer which provides an active water drive and consequently helps hydrocarbon recovery. A reservoir of this

kind, as known in the oil industry, remains stable in terms of pressure after the injection of fluids (in this case with storage objectives). The reason is that water contained in the reservoir is displaced after the injection of another fluid and so, pressure in the reservoir should not experience relevant changes (e.g. Muskat, 1981).

As documented by IGME (2013), and noted in part 3.3, the third injection phase drastically increased both the injection rate¹⁵ and the total volumes injected per day. It was also the longest (September 2nd to 17th), and according to their descriptions it reached a maximum injection increment of 8E+6 Nm³ in a day, 3.2 times the analogue in phase 2. This corresponds to a 220 % of increment; EPA (2012), notes that injection rates should never exceed by more than 50 % those of the previous injection stage. The total injected volume at the end of phase 3 (approximately 1 E+8 Nm³) was around 3.5 times the total injected volume at the end of phase 2 (SGC, 2014).

Unfortunately, seismicity started in coincidence with a certain value of the total volume in the reservoir, and after having increased the injection rate. The sudden increase in injection rate and total volumes was probably founded on the type of reservoir, which behaves differently when compared to a volumetric one. As noted before, in a reservoir of this kind the pressure cannot augment rapidly. Instead, the pressure increase grows steadily only due to the total injected volume, which implies that pore pressure is a function of the total injected volume. This is the case expected at $t \gg t_0$ in any reservoir, as shown in Equation (6), see NRC (2012), where the final pore pressure is proportional to the injected volume.

$$p \cong \frac{V}{\pi R^2 H S} = \frac{V}{V_T S} \quad (6)$$

Where:

p	Large time pore pressure
V	Total injected volume
R	Radius of a disc-shaped reservoir
H	Reservoir thickness
S	Storage coefficient. Depends on rock porosity, and fluid and rock compressibility.
V_T	Reservoir shape volume

This means that indeed, an increment of pore pressure had to take place because of the injection. The question is whether these values were high enough within the reservoir to cause fault slip, and/or if this values could have been transmitted to other faults to trigger seismicity nearby. Actually, Escal UGS always stated that maximum reached pressure values (7-8 bar at the reservoir's top, and 2 bar in the aquifer itself) were substantially below the estimated threshold, set at 49 bar (Castor's Geology and Geophysics day held at the Association of Geologists of Catalonia, 2014).

¹⁵ESCAL UGS has stated that the IGME's report is full of inconsistencies; In fact, injection rates and volumes could have been misinterpreted (e.g. Berbis, 2015, in *el Periodico* newspaper online). The author has included IGME's data because it is the only source of information regarding the alleged seismicity-triggering third injection phase, but it should be treated carefully.

At the same time, this increase in pore pressure influences poroelastic stress changes. Just to provide a qualitative approach, and according to what has been seen in chapter 2, in a normal faulting regime (which could be the case near the Castor UGS) the Mohr's circle shrinks during injection, thus it is not necessarily destabilizing. But, as noted by various authors (e.g. Santarelli, 1998), stress path coefficient γ_h tends to be smaller during repressurization of a reservoir (UGS activities) than during depletion, thus leading to higher shear stresses and not so secure stress paths during injection. Combined with an increase in pore pressure, any state worsens as effective stresses are reduced.

In addition to the earlier inducing mechanisms, previous earthquakes could also have acted as triggers (e.g. by static stress transfer, see chapter 7) since they can destabilize certain faults. Thus, it is logical to think that conditions after injection were less stable than before it was performed. Based on data reported, other triggering mechanisms should be of less importance.

3.4.2 Geological unknowns

Another comment should be made in relation to the high karst permeability supposed by Escal UGS, which might not be as high as stated (SGC, 2014). As far as the author is concerned, permeability and porosity of the reservoir rock was low, although increased due to karstification, with creation of secondary porosity and permeability (Seeman et al., 1990; Bachelor et al., 2007). This is important as a reduction in the permeability results in an increase of the characteristic pressure and so, the pore pressure (NRC, 2012). It seems that not even the company responsible for the dynamic model of the Castor UGS had access to specific data in order to validate it, as written in the Watercraft Capital Prospectus (2013), and noted by geologist Josep Giner in SGC (2014).

Another aspect of great interest is the sealing capacity of the rock, especially in horizontal terms. No public information has been provided as to what extent the seal formation is laterally effective for gas, a much lighter fluid than heavy oil which was the original fluid in the reservoir. This has been noted in documents such as ICGC (2013), because of the threat that possible gas leaks pose to nearby faults. It is not likely that unnoticed gas leaks were produced, but once again the operating company has never made it clear why this could not have happened, based on geological reasons.

As for the literature published in relation to the topic, the fault plane accepted to have contributed to the largest earthquakes agrees in dip and orientation with the named Castor fault area. In accordance with IGME (2013), the Castor fault had not been described by GLJ Associates Ltd. or Geostock (consultancies hired by Escal UGS) when they studied the seismic 3D data. If that plane existed before the injections, it is at least unexpected that the operators did not notice it. Cesca et al. (2014), on the other hand, concluded that an East-dipping fault located eastwards of the main structure was compatible with Focal mechanisms solutions and background stress.

3.5 Seismicity's origin: A case of triggered seismicity¹⁶?

New fractures cannot be created unless pressure reaches the magnitude of the minimum principal stress (S_3 ; in strike-slip or normal faulting regimes corresponding to the minimum horizontal stress, S_h). This is assumed to be the lower limit, in processes such as hydraulic fracturing, to be able to fracture rock (Haring et al., 2008). Because of the UGS' nature, a project in which rock fracturing is not intended, it seems logical to assume that the value of S_h was never reached in the area (this is also stated by R. del Potro in Torres and Valles, 2015). Indeed, a plane capable of hosting $M > 4$ events could never have been generated by the injections while working at pressures way below threshold, as repeatedly reported by Escal UGS.

Induced seismicity, usually corresponding to low-magnitude events, can either take place by rock fracturing, or by pre-existing faults slipping (Haring et al., 2008; Baisch et al., 2009). Induced seismicity is bound, by definition, to be a consequence of the perturbation introduced in the reservoir being the main and/or only cause of fault slip. According to literature, this type of seismicity probably corresponded to the first phase of the sequence (compare part 3.3), but it was most likely not for the second.

The fact that the strongest earthquakes could not have been induced (directly) relies on various observations: Time delay between the halting of injections and the strongest shakes (various days / few weeks), impossibility of generating new fractures at the reported working pressures, magnitude of the perturbations being much smaller than the regional stresses, b value of the second part of the seismic sequence closer to what is expected for tectonic earthquakes, and the relationship between the energy introduced to the system (injections) and the energy released by the earthquakes. These facts come up in the different parts of this work and will be evaluated pertinently.

Because of what has been noted above, it has been suggested that, if not induced, the strongest earthquakes could have been triggered by the injections. That is to say, accumulated deformation along the causing fault had to be almost at slip levels, as the contribution of injections in terms of stress was just a fraction of the *in-situ* stress. ICGC (2013) and IGME (2013), support this hypothesis, although they cannot confirm it because of a lack of excluding evidences regarding the other possibilities. Cesca et al. (2014), reach the same conclusion. Before proceeding with further analysis in the following chapters, some insight regarding the energy relationship is provided, as it is fast forward to quantify and allows a first degree assessment.

A simplified calculation to determine the energy introduced to the system (E_{int}) has been performed. The goal is to compare it to the total seismic energy, in order to obtain the ratio between them, such as it has been done in Baisch et al. (2009) or in annex C (deeper analysis is provided there). By reasons of availability of information, the method used to calculate the E_{int} assumes isothermal conditions and obtains energy as a result of the variation of the pressure and volume in the reservoir (BU, 1999). Calculation parameters (volume balance, temperature of the reservoir and compressibility factor of the gas) were

¹⁶Triggered and induced seismicity are distinguished in this part, and refer to different types of man-generated seismicity.

obtained from Seeman et al. (1990), Batchelor et al. (2007), IGME (2013), Castor's Geology and Geophysics day held at the Association of Geologists of Catalonia (2014) and SGC (2014). The calculation is fully explained in annex C, as well as the basis for this discussion

Figure 13 depicts the result. It is seen that the E_{int} (around $6.2 \text{ E}+13 \text{ J}$) is just a fraction (6‰) of the total energy of the earthquakes (Seismic Moment, M_o , of $8.4 \text{ E}+15 \text{ J}$, see Figure 13, left), but greater than the energy released as seismic waves (E_{sis}). The value obtained by Escal UGS in relation to the E_{int} was around $2 \text{ E}+13$ (Castor's Geology and Geophysics day held at the Association of Geologists of Catalonia, 2014), probably due to unknown differences in initial and final volumes considered. They consider the total seismic moment of the earthquakes to be of $1.46 \text{ E}+16$, but as now published by the IGN (catalogue downloaded on November 2015 with coordinates 40.2° to 40.6° N and 0.5° to 0.9° E ; <http://www.ign.es/ign/layoutIn/sismoFormularioCatalogo.do>), the total M_o of the sequence should be of $8.4 \text{ E}+15 \text{ J}$.

If we compare the E_{int} with the M_o , it turns out that the first only represents a 2‰ of the M_o (in Figure 13, right, the value is 6‰ due to the differences indicated before). This can, indeed, serve as an initial hypothesis to say that the perturbations set up in the reservoir were minimal and just accelerated the process a determinate Δt , something which agrees with the triggered seismicity assumption.

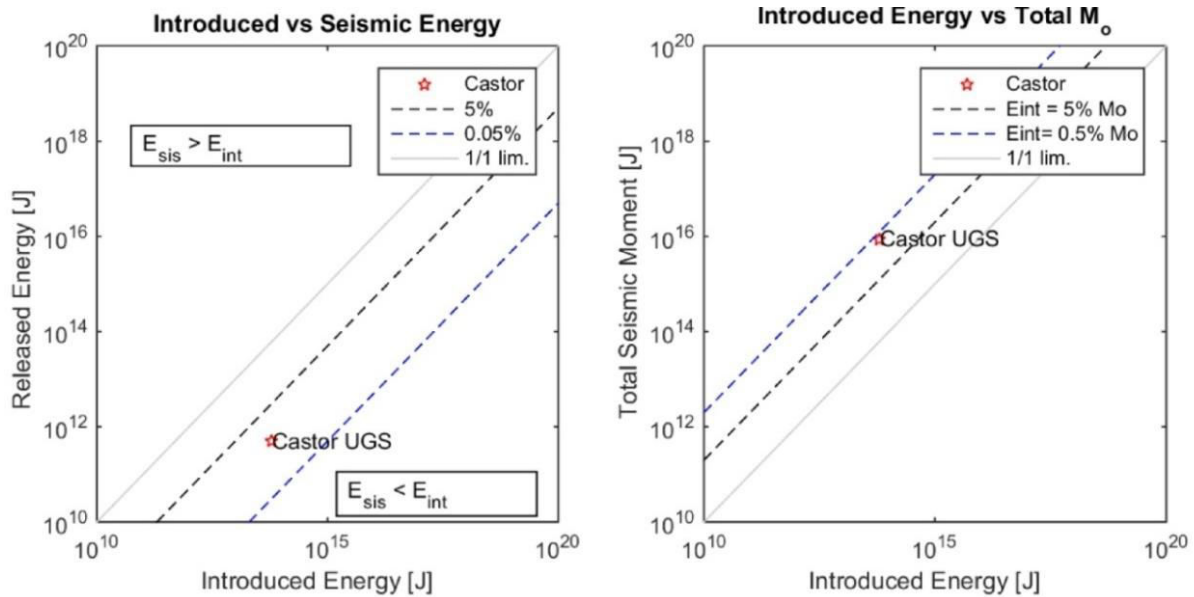


Figure 13: Top: Energy released by seismic waves compared to energy introduced to the system. 5% and 0.05% limits, as well as 1 to 1 limits are shown. Bottom: Total energy of the earthquakes (Seismic Moment) compared to energy introduced to the system.

However, if Figure 13 (left) is explored, perspective may change. Following Baisch et al. (2009), no evidence for an uncontrolled process (triggered seismicity) would be found from this graph point of view. This can be justified as it follows: Based on information from Figure 13 (left), a relevant indicator for triggered seismicity to have taken place would be E_{sis} being greater than E_{int} . As a lower bound of the earthquakes' energy (McGarr, 1999), man-contribution would hardly be the main cause if E_{sis} were already higher than the E_{int} (which is in turn an upper bound of the real energy acting in situ, as there is a great loss associated with friction). That is not the case.

The fact is, that even if this kind of relations have been used and proven useful in previous studies (Baisch et al., 2009, McGarr, 2002) results in annex C revealed that most of the concerning man-generated seismicity cases will most likely fall in an "undefined" region, such as the Castor case plotted in the figure. This is, E_{int} will be higher than E_{sis} , but lower than the M_0 . For such cases, the graphs in Figure 13 do not provide enough evidence to say if the events undergoing study were triggered or induced. Furthermore, it seems reasonable to say that the energy relationship should be carefully treated and only used as a preliminary or additional tool when assessing man-caused seismicity.

3.6 Approach of the present study

The three main unsolved aspects of Castor's case, from a scientific point of view, are:

1. Seismicity's location (hosting faults)
2. The current state of known faults after the seismic sequence (closer or not to failure)
3. Origin of the earthquakes (natural, induced or triggered)

When earthquake location on itself is not precise enough to assign an earthquake to a certain fault, a further effort which involves integrating all seismological and geomechanical sources of information may provide more clues; this process should help evaluating the first and second points, and here it combines focal mechanisms solutions and the study of one of the previously described physical mechanisms of induced seismicity, as well as its variation on the fault planes. Particularly, static stress changes by nearby earthquakes (as the sequence builds up) can be assessed.

In order to provide solid evidence regarding the origin of seismicity and after the studies made up to now, the logical step would be integrating all factors affecting faults' stability in a hydro-mechanical coupled model with the aim of studying how they vary and are transmitted in time (the most important trigger being the excess pore pressure). In this sense, for induced seismicity to be the case, the observed earthquakes should be possible to reproduce. The initial perturbation is supposed to be the injected volume, and a 3D finite element software should be able to cope with it. For starters, this process needs, as an input, very well constrained information regarding faults in the environment (which is currently not the case), as well as its geology, reservoir, and data concerning the gas injection procedure. None of these were available, so this alternative is out of scope here.

Consequently, this study aims at providing new constraints regarding the stress state of known faults in the area after the seismic sequence, and the quantification will be made by calculating the following:

1. Stress changes in neighboring faults. For instance, evaluating Coulomb stress changes (CSC; see chapter 7). It should be noted that this is a simplistic approach and does not account for complex interactions between migrating fluids, pore pressures, faults interaction and hydraulic connectivity.
2. Acceleration of recurrence times of characteristic earthquakes, as a consequence of 1.

To be able to achieve this task, a seismotectonic model has to be built. Seismological information will be examined in order to better constrain and improve knowledge on the seismic sequence (chapters 4, 5 and 6). On the other hand, available information on faults in the area will be compiled (references), and the simplified model will be introduced into a software which allows calculating CSC (chapter 7). Hence, information on the mapped faults' stress evolution and final state will be obtained. As indicated before, the considered mechanism that generates the stress change is the earthquake itself, which results in a static stress variation in the neighboring medium.

This procedure should allow evaluating which faults were more likely to have hosted the earthquakes, as well as the acceleration of the seismic cycle due to the considered trigger. In spite of the fact that this study does not have the tools to make a deep analysis on seismicity's origin, the combination of the frequency-magnitude distribution and the analysis of stress static stress changes could provide some insight on the topic. A scheme of the described approach can be seen in Figure 14.

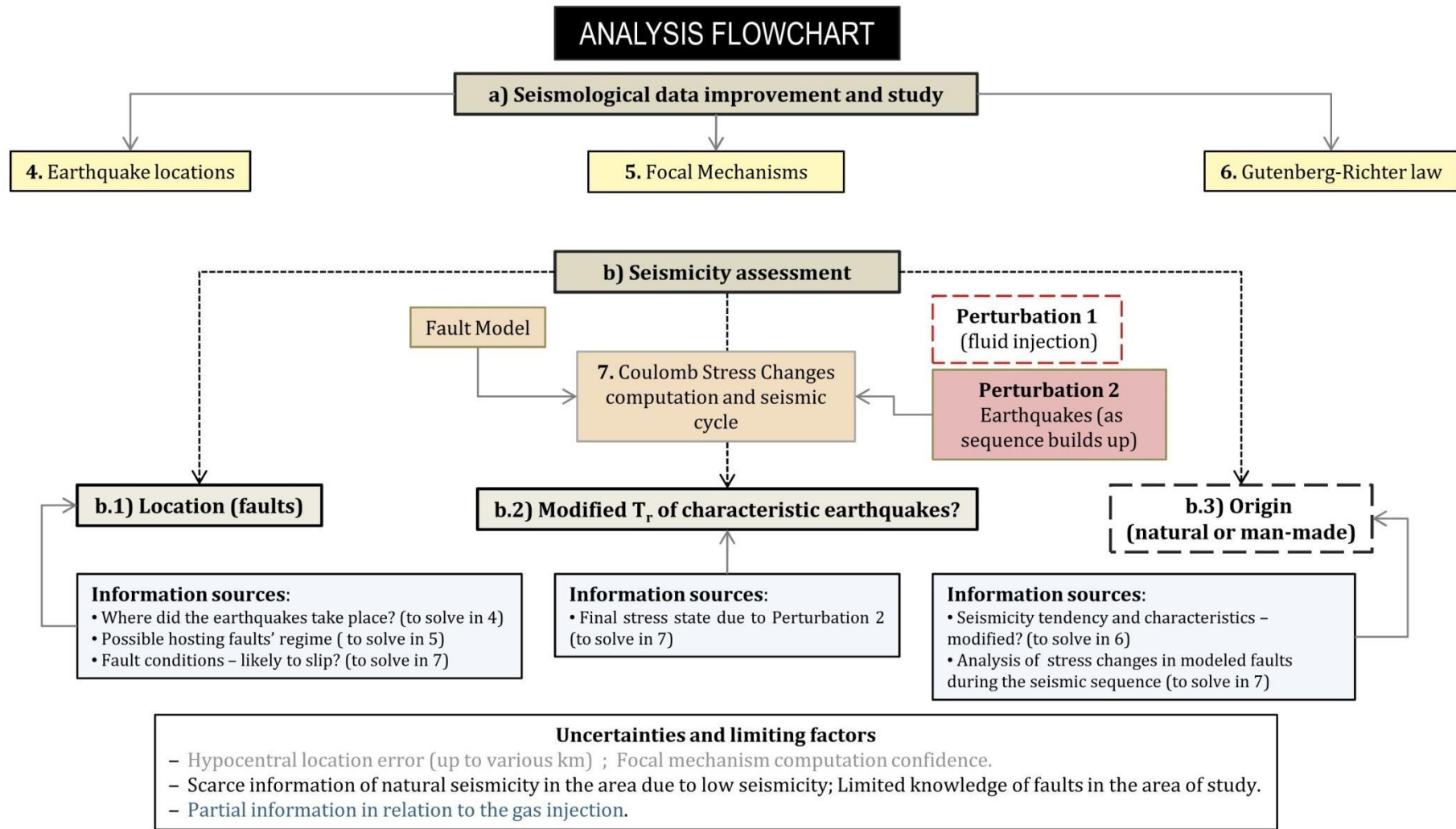


Figure 14: Workflow to reach objectives a) and b), the latter subdivided into b.1, b.2 and b.3, according to the unknown aspects from a scientific point of view. The numbers in the yellow (seismological topic) and light brown (geological - geomechanical topic) filled rectangles refer to chapter numeration. Discontinuously contoured boxes indicate that data input or methodology was insufficient to include (red) or properly assess them (black). In the uncertainties box, grey refers to errors that involve both the method applied and input data, black refers to limiting factors associated with current knowledge, and blue indicates that more information is known but was not available to the author.

4. HYPOCENTRAL LOCATIONS

This chapter exposes the method applied, input data and obtained results of the earthquake location process. Also, an assessment in relation to known geological structures in the area and the anthropogenic seismicity conjecture is provided. This last evaluation should be read along with the one provided in chapter 5 (focal mechanisms), as they complement each other.

4.1 Location method

4.1.1 Overview of location methods

A general overview on earthquake epicentral and hypocentral location accuracy and methods is provided in Husen and Hardebeck (2010). Overall, methods for locating an earthquake can be linearized or non-linearized (direct search) based. The first use partial derivatives as well as matrix inversion, with the main advantage of being computationally cheap and providing reliable results for well-constrained locations. Direct-search methods (e.g. Lomax et al., 2001), on the other hand, are computationally more expensive but are not dependent on the accuracy of the initial guess, and therefore work better for poorly-constrained locations. Both methods, which locate earthquakes one at a time, provide an absolute location (hypocenter located in a fixed geographic system and time base).

However, there are cases where it is interesting to locate not only one event, but a determinate set. For example, when spatiotemporal clustering is observed, such as in earthquakes taking place along a rupture that propagates over the entire fault area, or when there is interest in knowing the aftershock's location in relation to the main shock. In these cases, a set of earthquakes, such as the Castor swarm, can be located “together”. In literature this is referred as Joint Hypocenter Determination (JHD) as in Douglas (1967).

These methods can use seismic phase's arrivals (equally to single event location) or waveform misfits at detection points and thus, locations are absolute. Though, in a study of a seismic sequence earthquake locations precision relative to each other is really important, and relative location methods have been developed. These can be relative to a main event (master-event technique), such as in Deichmann and Garcia Fernandez (1992), or relative to each other (double difference, DD), as in Waldhauser and Ellsworth (2000).

Because location methods are differently oriented and make different assumptions, the selection of an earthquake catalogue will be based on the objectives of the pertinent seismic study. First, how each catalogue has been obtained has to be taken into account (goal and shortcomings); and second, error sources have to be considered (both random and systematic).

Single event location catalogs are more adequate to compare locations with other spatial structures, such as mapped faults. However, in order to sharpen clustered seismicity and infer on precise fault geometry, a relative location technique of a set of events is preferable. Therefore, the ideal approach for this study would be applying both an

absolute and a relative location method. However, by reasons of time and multiple objectives, events have been single-located, using an absolute location method (see 4.1.2).

4.1.2 HYPOCENTER routine

All earthquakes in the catalogue used in this study (newly-located, re-located and those just acquired) have been located using the program HYPOCENTER (Lienert and Havskov, 1995; hereafter HYC), which was originally released by Lienert et al. (1986), and afterwards revised to improve limitations derived from its predecessors (HYPO71, HYPOINVERSE, etc).

HYC was coded in FORTRAN77 and it implements the IASPEI91 software (Buland and Chapman, 1983; Kennett and Engdahl, 1991) to compute global travel times. It is a single-event absolute location method, linearized based, and Figure 15 shows a flowchart with the main computational steps taken by the program; these are afterwards explained in the text, but the reader is referred to Lienert and Havskov (1995), for further explanation and worked out equations.

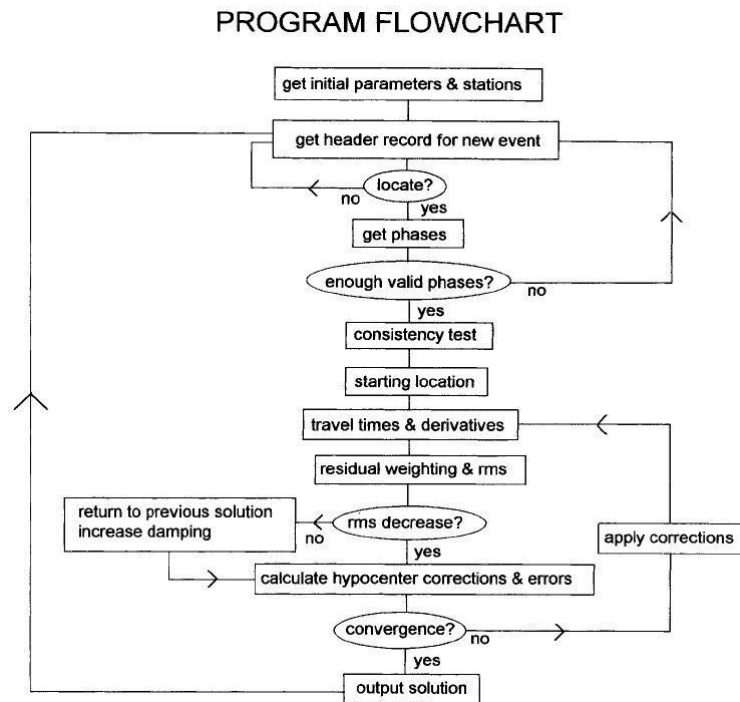


Figure 15: HYPOCENTER routine flowchart. Extracted from Lienert and Havskov (1995).

Input, output and first phase-picking check

The program reads Havskov's (1990) NORDIC input format (*.nor*), and writes an output in the same format which contains the determined hypocenter and its residuals. Therefore, this output can act as a detailed information source of each earthquake's hypocenter. A detailed *print* file is also provided, with computational steps' information. An example of each one can be seen in annex D.1.

As a first approach, data are examined for certainly bad arrivals. The first step consists in testing (at each station) that secondary phases occur after their primary phases (e.g. S arrives after P). After that, arrival time differences for analogous phases at couples of next-

to stations are tested to be less than the computed travel times amid them (as in Johnson, 1979).

Starting location, travel times and elevation correction

In order to avoid problems which usually affect iterative location programs (e.g. Buland, 1976), HYC uses four different approaches which will provide four starting locations. They are obtained using the next assumptions:

- a) The apparent velocity and azimuth of a plane wave is calculated using similar phases at different stations. The calculation is based on linear regression on the arrival times as a function of horizontal station coordinates.
- b) Approximate distances can be calculated using different phase picks at the same station; then, the program computes the intersection of pairs and uses distances to obtain an initial location.
- c) The intersection of two azimuths (which can be obtained from three-component stations) at different stations, as well as a single azimuth and a multi-phase picking.
- d) Time differences from depth phases multiplied by a user-specified constant are used to provide the starting depth.

Then, the starting location is the one with lower Root Mean Square Error (RMS) of its Travel Time Residuals (TTR). TTR are weighted with a slight modification of the method in Anderson (1982), which solves the problem of residual weight biasing due to a single large positive or negative outlier.

For this case, a layered model was specified by the user (see part 4.1.3), and it allows the determination of P_b , P_g , P_n , etc. arrival times when these are specified by the user. In this work, because of events' magnitudes and experience of the author in phase-picking, P-wave and S-wave arrival at each station were determined without specifying phase subtype. Therefore, the program assumes that it is the first phase having the same first letter (e.g. at our scale, P is P_g at short distances and P_n at larger distances). The layered velocity model is also used to calculate the station elevation corrections.

Hypocentral corrections

HYC applies the adaptively-damped least squares algorithm from Lienert et al. (1986). Equation (7) shows the computation of n travel TTR:

$$\delta t_i = t_i - T_i - t_0 \quad (7)$$

In (7), t_i is the i th arrival time (from phase picking), T_i is the calculated travel time (model), and t_0 the origin time of the earthquake. The final weight assigned to each travel time is the product of the user-specified weight and the residual and distance weights. To compute the least-squares hypocentral corrections (Δt_0 ; longitude, Δx_1 ; latitude, Δx_2 ; depth, Δx_3) the sum of the squared weighted differences is minimized (Equation (8)):

$$S^2 = \sum_{i=1}^n w_i^2 \Delta t_i^2 \quad (8)$$

The weighted means are subtracted to the residuals and partial derivatives to *center* them, which improves numerical stability and assumes that Δt_0 is independent of latitude, longitude and depth.

Hypocentral errors

The dimensions of the error ellipsoid ($\delta x_1, \delta x_2, \delta x_3$) are obtained from least-squares error analysis (e.g., Flinn, 1965). Variance of travel time residuals (s^2) is estimated from the squared sum of the weighted time residuals, using Equation (9):

$$s^2 = \frac{S^2}{(n - m)} \quad (9)$$

In Equation (9), $n-m$ correspond to the degrees of freedom of the F-distribution, $F\alpha(m, n - m)$. For a full solution, $m = 4$. Variance includes arrival times' errors as well as errors in the assumed velocity model (systematic), the latter not included in the error ellipsoid. HYC calculates the error in the origin time considering a confidence interval which is equal to the one in the arrival times.

The horizontal and vertical errors, estimated from the hypocentral parameter covariance matrix (C_{ij}), are obtained as in Equation (10) and (11):

$$e_h = \sqrt{(C_{11}^2 + C_{22}^2)} \quad (10)$$

$$e_z = \sqrt{C_{33}^2} \quad (11)$$

4.1.3 Input parameters

HYC works with two input files. On one hand, phase data needed to perform a location is stored in the input *.nor* file, the header line of which contains basically the origin time, approximate latitude, longitude and depth, and magnitudes. As well, the parameter file containing other calculation specifications and the location of each seismic station whose data is stored has to be inserted (*stationX.hyp*). See annex D.1 and D.2 for file examples and Lienert (1994), for further information.

In this study, the maximum depth was set to 70 km, while the starting-depth to iterate was left at 5 km. For local events, a distance weighting (w_d) is also computed (Equation (12)), in order to give more importance to phase pickings at closer stations.

$$w_d = \frac{x_{far} - \Delta}{x_{far} - x_{near}} \quad (12)$$

Where:

x_{far}	Distance st-ep for which the w_d is 0. Set at 400 km
x_{near}	Distance st-ep for which the w_d is 1. Set at 5 km
Δ	Epicentral distance (km)

Velocity model

All earthquake locations were performed using a 1D flat layer velocity model, which was adapted to the Valencia Gulf (VG model from now on). This model was based on Diaz and Gallart (2009), after an analysis of the Moho depth variation from the Catalan-Valencian

coast to the Balearic Promontory was carried out, and had already been used by ICGC (2013), and Tapia (2013). It is shown in Table 2.

Table 2: VG model specifications. The flat layer assumption considers constant values in any point inside the layer. Source: ICGC (2013).

Valencia Gulf 1D model			
Layer	Top depth [km]	Vp [km/s]	Vp/Vs
1	0	5.2	1.75
2	5	6.0	
3	13	6.4	
4	22	7.9	

Tapia (2013), studied the differences between the VG model and the Catalan 1D model, which is normally used to locate events in the Catalan area, for a group of 7 earthquakes corresponding to Castor’s seismic sequence. In her analysis, Tapia (2013), used NonLinLoc (Lomax et al., 2000) instead of HYC, but her findings revealed that the VG model was more appropriate for those earthquakes. Using the Catalan 1D model, obtained depths were around 20 km, much deeper than what is to be expected if they were induced earthquakes. On the other hand, the VG model, much more constrained around the epicentral area, proved to be better: Depths were much shallower, and residuals and PDF¹⁷ comparison showed substantially improvement. Epicenter values were very similar.

The only disadvantage in using the VG model is that stations located further onshore, such as the ones in the Pyrenees, do not benefit from it. The crust is much deeper at these locations and so, there is always an error between the theoretical travel times that HYC calculates, and manual phase pickings. But, taking into account that closer stations visibly get an advantage from the adapted one, locations are substantially improved.

Recently, Gaite et al. (2016), published a new paper, when locations had already been completed in this work. They use a new 3D model derived from surface-wave ambient noise tomography, and they are able to estimate the phase and group speed of Rayleigh waves. They implement it in the NonLinLoc, which they employ to locate their earthquake dataset. That new model was not considered here, although their results will be taken into account in the discussion.

4.2 Event data

4.2.1 Data selection

The ICGC had already located all events reported to have $M_L \geq 2.5$ (*pub* dataset hereafter). The *new* locations performed correspond to a set of 50 events ($2.2 \leq M_L \leq 2.4$, plus 2 with $M_L 2.1$, magnitudes by IGN), which have been located using the available waveforms in the ICGC (see Figure 16 for the complete seismic network). These events will be hereafter referred to as the *loc* dataset. Figure 17 shows the workflow exemplifying the events-to-locate selection process.

¹⁷The Probability Density Function is a parameter provided by NonLinLoc, but not available when using HYC.

4. Hypocentral locations

The first step consisted in defining an area in which to select the events of interest, which finally ranged from longitudes 0 to 1.5 ° E and latitudes 40 to 40.7 ° N (Figure 16). After that, all events which had taken place in September or October 2013 inside the defined rectangle were downloaded from the IGN seismic catalogue (last accessed March 2016, available at <http://www.ign.es/ign/layoutIn/sismoFormularioCatalogo.do>), by whom they had already been located. And then, the magnitude range was defined, in order to obtain a representative subset. The signal to noise ratio for events with magnitudes lower than 2.2 made it unadvisable to perform locations for them using HYC (see 4.1.2).

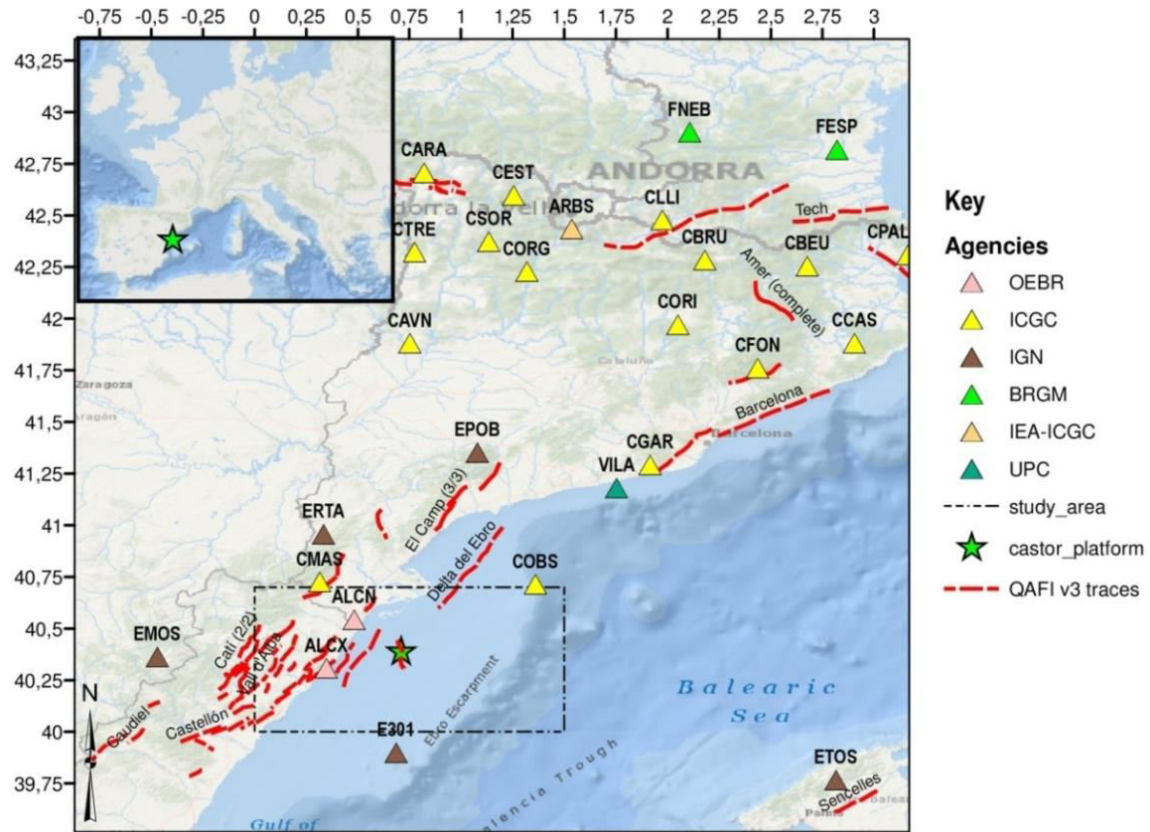


Figure 16: Catalan seismic network and main stations around the Castor platform. ALCN and ALCX waveforms were not available for the dataset located here (*loc*), nor E301 (Columbrete; since it became permanent named ECOL), which was installed during the seismic sequence. Study area shows the region in which earthquakes were selected. Red discontinuous traces indicate Quaternary Active Faults of Iberia (QAFI; IGME, 2015a), and Castor Platform is also plotted.

The date and time of each event, acquired from the IGN, was used to select the matching events (detected and stored in the ICGC database), which were the ones manually located as part of this work. The ICGC already had some automatic and manual locations, but both were disesteemed (the automatic because of very low confidence and the manual due to having been located using a non-adapted velocity model).

ICGC's event information is acquired in Group of Seismic Experts (GSE) format (see Dost et al., 2012, for further information). All location solutions performed here (*loc* dataset) are shown in annex D.3, as well as the list of each earthquake in the *loc* and *pub* datasets. The seismic network list (only with stations whose data was used here) is provided in annex D.4.

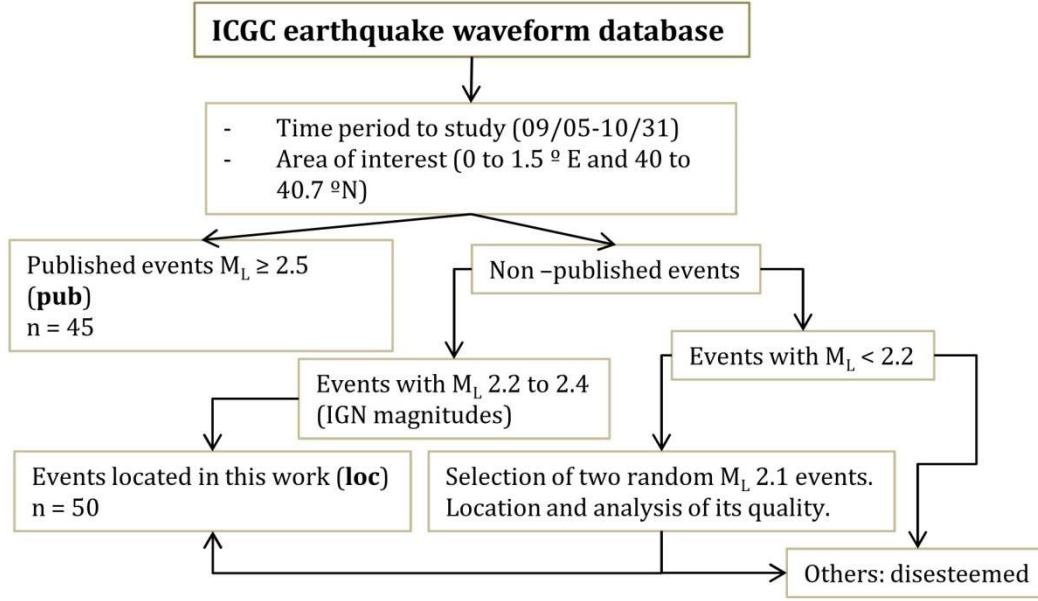


Figure 17: Schematic dataset selection workflow.

4.2.2 Data treatment: Posido v1.5.15

Posido v1.5.15 software, which runs on a user-friendly interface in Windows OS, was used in order to load the waveforms and locate the earthquakes. When phase arrival times have been picked by the user, the software initializes HYC routine so as to obtain a location, provided that a solution converging with data exists.

The main capabilities of Posido, regularly used at the ICGC in order to perform routine locations, are summarized below:

- Storing earthquake data catalogues
- For each seismic event, all waveforms available can be viewed and modified by the user.
- Locating earthquakes using either HYC or HYPOINVERSE. Multiple solutions, using for example different velocity models, can be saved.
- Calculating magnitudes, or assigning already known magnitudes to certain events.
- Seismic risk assessment (not treated here).

Phase picking and hypocentral location

For each event to be located, the process starts with the selection of the event from the database. Available waveforms (as obtained by seismic stations of the network) are automatically ready to be displayed.

In order to prevent the low frequency noise to interfere with time arrival measurement, data needs to be filtered. For the *loc* dataset, most locations were filtered with a 4th order 2 Hz high-pass filter, as the frequency content of the earthquake signal at the distances of study is mostly in this range. For those earthquakes with especially poor signal to noise ratio, a 10 Hz high-pass filter was applied. Baseline is corrected automatically by Posido.

Next, phase arrival times can be picked. Figure 18 and Figure 19 show P and S wave pickings at CMAS station for the September 9th, 05:37:42 (M_L 2.1), and October 1st,

03:32:45 (M_L 4.2) respectively. Both signals are equally filtered and distance station-epicenter difference does not have influence in worsening the first one; however, any reader with a minimum seismology experience will note how selecting precise possible phase arrivals in Figure 18 (see P wave picking) is not an easy task. This was the case for a considerable number of *loc* earthquakes, as magnitudes were smaller than 2.5.

Once all desired phases have been selected for each station, the user can initialize HYC routine and obtain a location. Then, Posido opens a new window (Figure 20) with location parameters and the result, so that the user can decide whether to keep it or perform a new one. Usually, for small earthquakes the first solution is not good enough (too high residuals). If that is the case, an iterative procedure where the user unselects phases with higher residuals, and/or picks new ones and performs a new location starts. This part can be time-consuming as, for small earthquakes such as the ones studied here, the described routine needs to be repeated many times, for each episode aimed to be located.

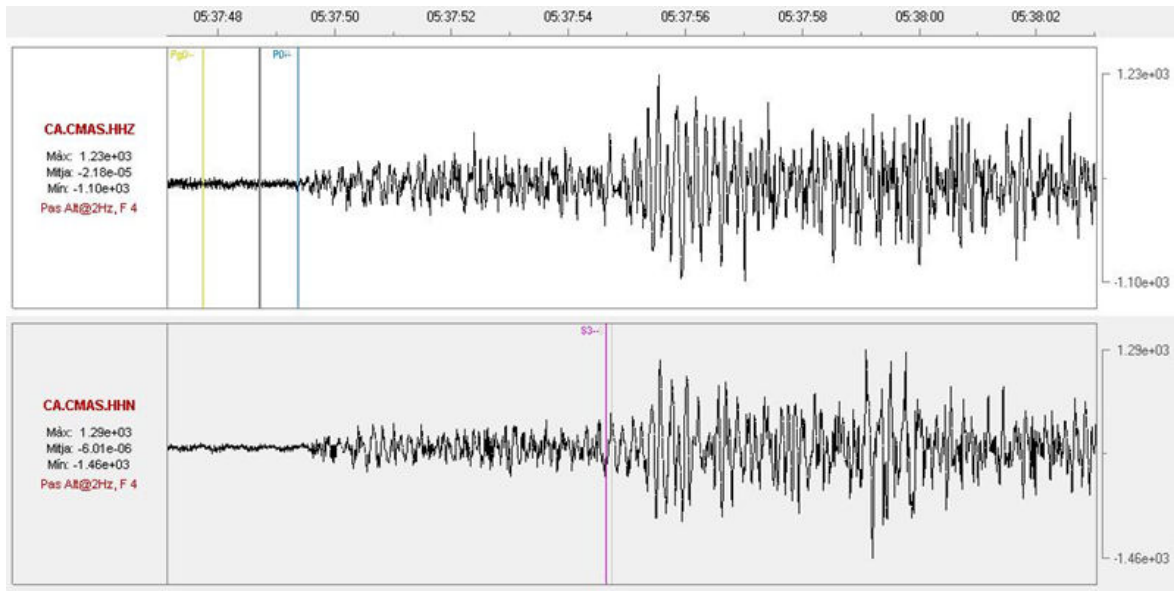


Figure 18: CMAS Z, N and E components' waveform showing the M_L 2.1 of September 9th 05:37:42. The blue vertical line is the P wave, while pink corresponds to the S. Light green shows other phase picks not considered (obviously, just one arrival time of each phase-type can be used).

4. Hypocentral locations

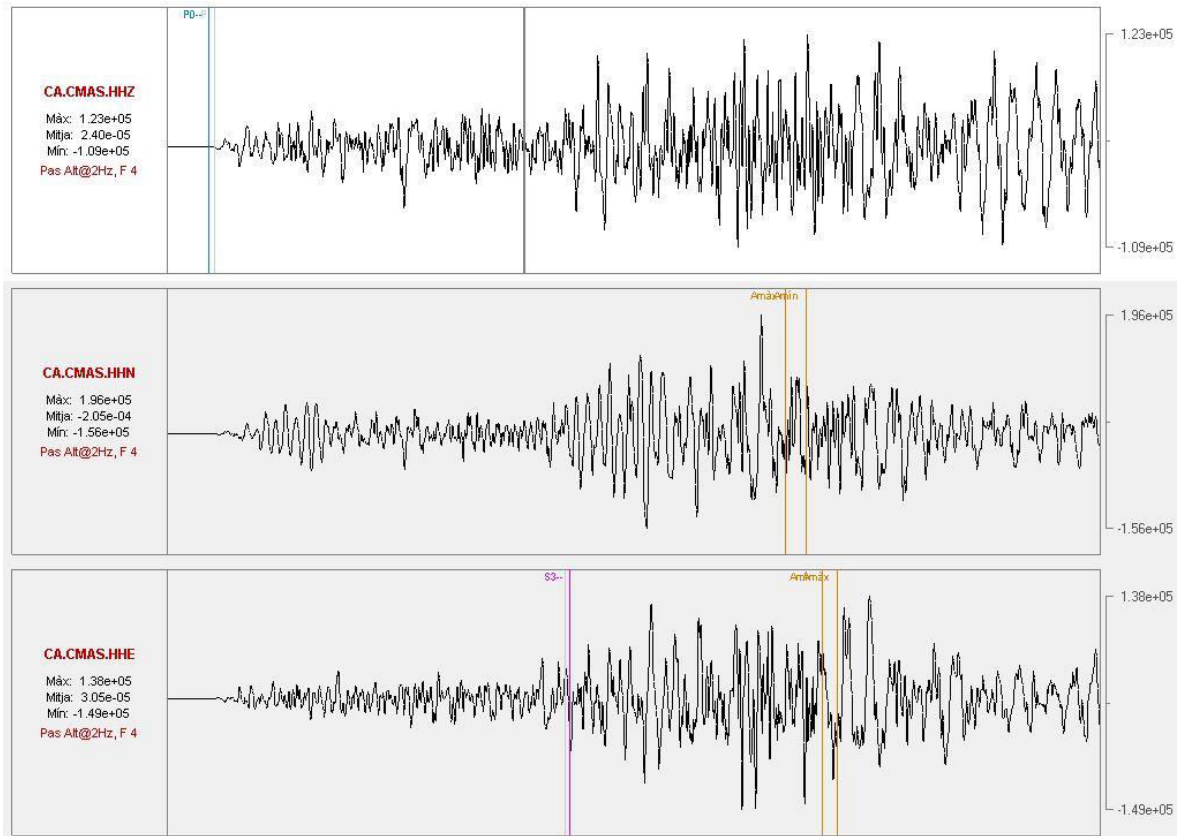


Figure 19: CMAS Z, N and E components' waveform showing the M_L 4.2 of October 1st 03:32:45. Apart from the P and S wave, light brown shows amplitude picks of the S wave, which are used to calculate the magnitude.

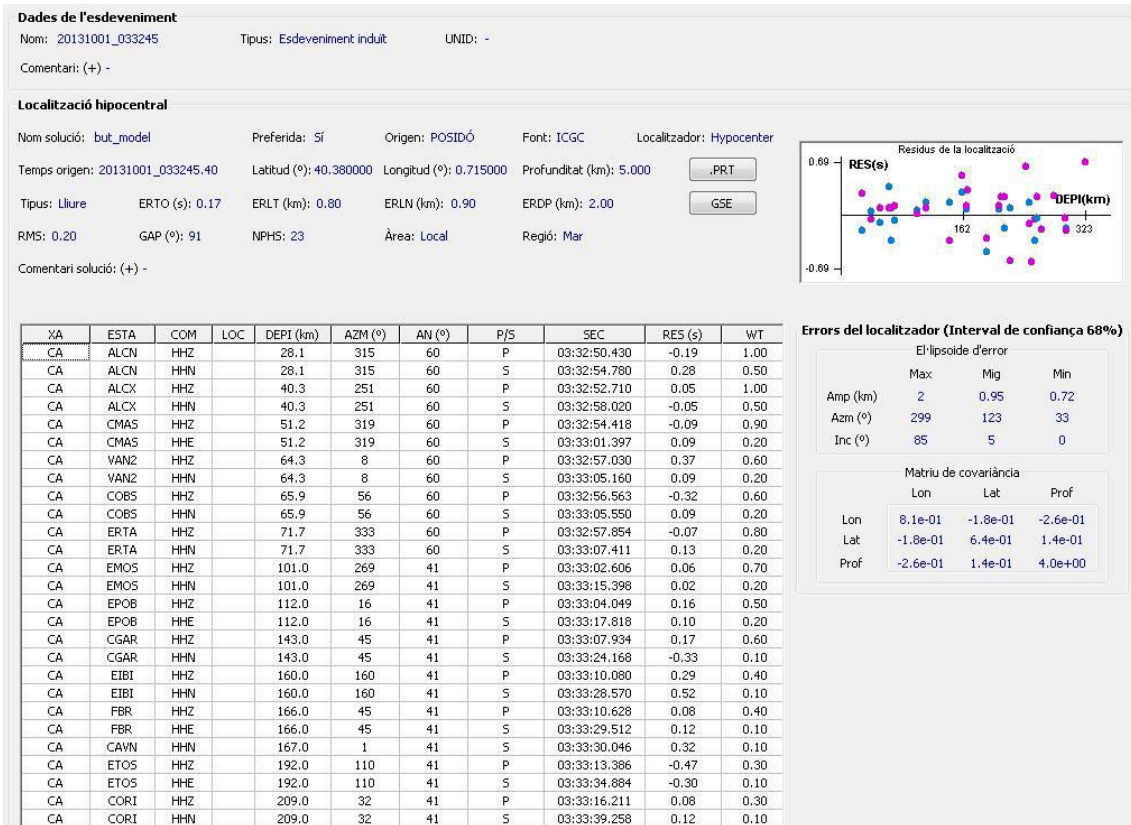


Figure 20: Location result as shown in Posido (event of M_L 4.2 occurred on October 1st 03:32:45).

Magnitude calculation

Magnitudes are calculated just after a location has been made. The instrumental response is corrected applying a filter, and the obtained output simulates that of a Wood-Anderson seismometer. Once the new waveform is displayed, maximum S-wave peak-to-peak amplitudes, for both horizontal components, can be determined at each station where an S-wave arrival time has been picked. The user decides whether to select a peak-to-peak value, and which one to select, for each channel available (Figure 21). The M_L is calculated following Equation (13):

$$M_{L_channel} = \log_{10} \left(\frac{App}{2} \right) + [-\log_{10}(A_0)]_{channel} \quad (13)$$

In Equation (13), App is the peak-to-peak amplitude in mm, and $[-\log_{10}(A_0)]_{channel}$ is an approximation of the attenuation of seismic waves due to epicentral distance. The attenuation values follow the law by Richter (1935).

After magnitudes at each channel have been computed, the magnitude of the event is the median of all values. As with locations, *new* magnitudes calculated here correspond to those events whose locations had not been published before by the ICGC (loc dataset). Figure 22 shows the result window for the event of October 1st, 03:32:45 (M_L 4.2).

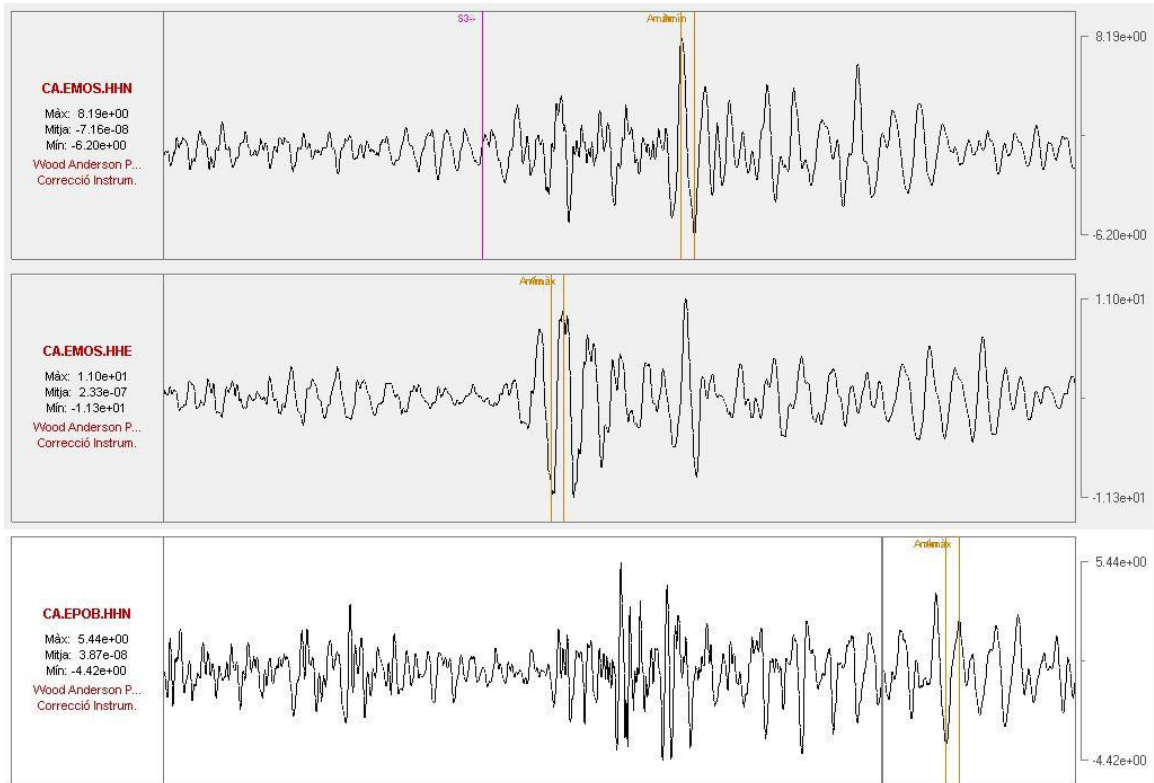


Figure 21: Wood-Anderson seismogram response for a certain earthquake. Light brown represents the maximum peak to peak amplitudes of the S wave.

4. Hypocentral locations

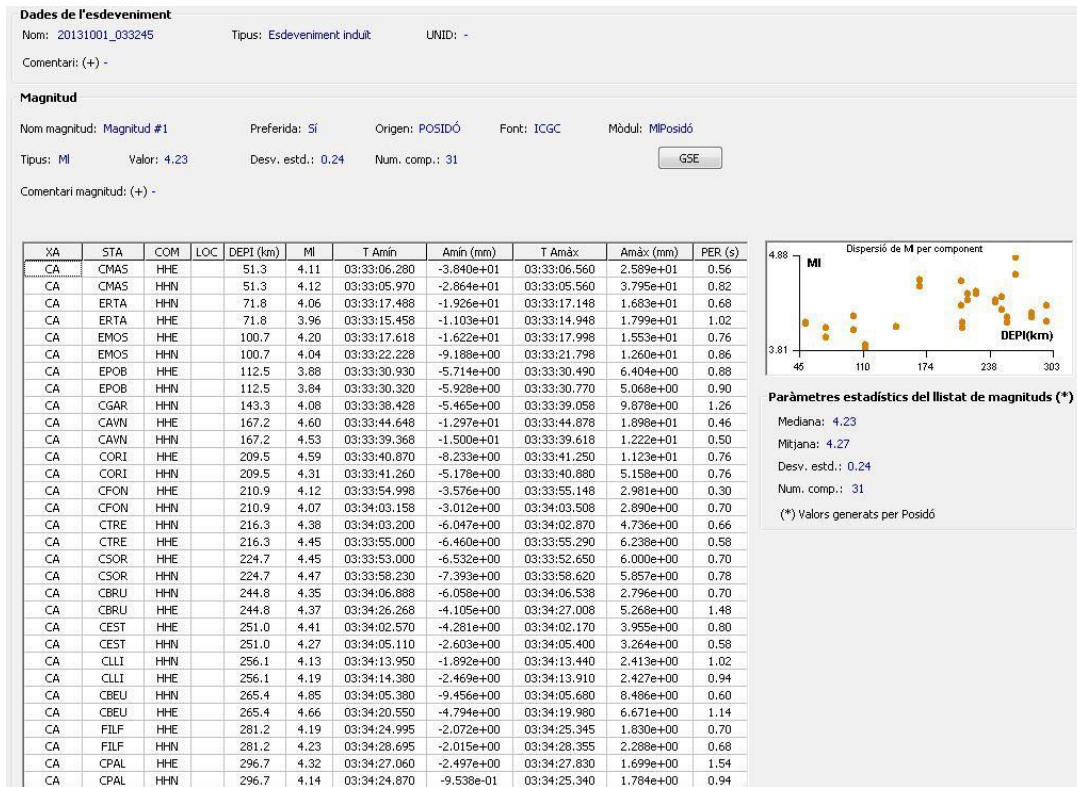


Figure 22: Magnitude result window as shown in Posidó event of M_L 4.2 occurred on October 1st 03:32:45.

4.2.3 Data conditions and quality of the locations

Given the seismic network distribution and small magnitudes, locating earthquakes in the Castor area has been a challenge on itself. As it will be further discussed in part 3.3, location quality relies, mainly, on a combination of the following factors:

- Minimum distance (between the closest station and the hypocenter).
- Gap (maximum angle separating two adjacent seismic stations, usually given in °. The angle is measured at the epicenter).
- Number of used seismic phases
- RMS

All 4 parameters are individual for each event. However, for an earthquake swarm in which all earthquakes are clustered, a) and b) are not likely to differ from one event to another. On the other hand, c) and d) are especially particular (they depend on how well the calculated travel times adjust with the picked arrivals). Regarding the *loc* dataset, minimum distance is above 30 km for all events, while gap is usually above 200 °. Thus, locating any earthquake but especially those below M 2.5 becomes a demanding subject.

4.3 Location results

4.3.1 Hypocentral locations

Figure 23 shows the epicentral locations of earthquakes (a total of 95, of which 50 are those of the *loc* dataset, and the rest are the *pub* events) and its depth distribution. It can be seen that most of the events are clustered at the left-center of the plot (in between 0.66

4. Hypocentral locations

and 0.73° of longitude and 40.35 and 40.4° of latitude; this gives an area of roughly 7.5 km^2 , where seismicity levels were higher. Depths are in between 0 and 9 km , with a clear majority of events in between 1 and 5 km deep.

The A-B profile in Figure 23, which indicates the main alignment direction of seismicity, can be seen in Figure 24. The profile is presented as it would be seen by an observer looking at it from the SW. Locations and depths agree with expected results, which were a concentrated cluster of shallow events, near injection-depth. It is interesting to note that average depth for published events (*pub*) is, at 2.57 km , notably shallower than the one obtained for this-work's located events (*loc*), which is 4.39 km . Under the assumption of induced seismicity, most of the events should be expected at near-reservoir depth. Based on available references, it is in between 1.7 and 2.5 km deep (e.g. IGME, 2013); Then, this difference in average depths could already be showing that locations of *loc* events, of smaller magnitudes, are subject to larger error.

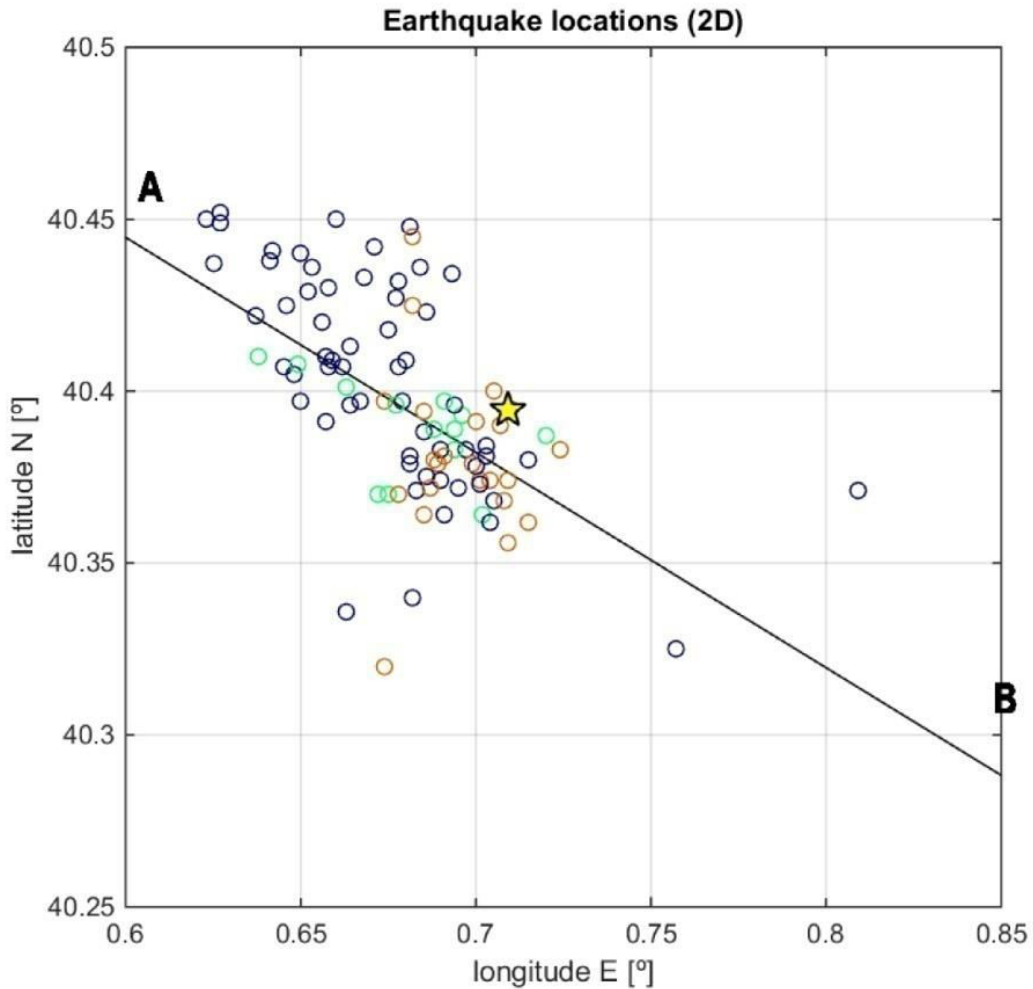


Figure 23: Earthquake locations with main alignment direction. Light brown indicates shallower than 1.5 km , green between 1.5 and 2.5 (reservoir depths) and blue deeper than 2.5 . The yellow star indicates the platform location.

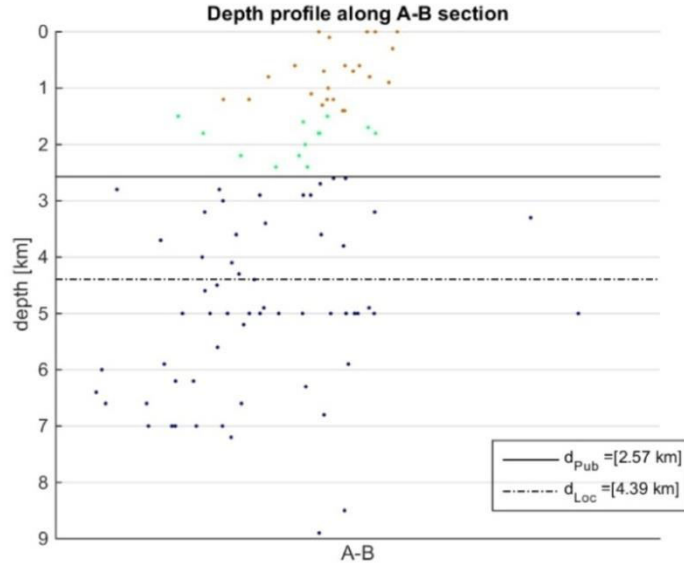


Figure 24: Depth distribution along the A-B profile.

Location parameters and error

Gaps with respect to magnitude and number of phases used in the location are shown in Figure 25, and the two datasets are easily distinguished. It is logical that, the more the number of phases used, the lower the gap. As more number of phases indicates also more stations, the gap is then cut down. Also, it has to be said that ALCN and ALCX waveforms were not available for the loc dataset, which explains part of the big differences. Gap values are below 100 ° for most *pub* events, but they increase up to more than twice this value when it comes to loc events.

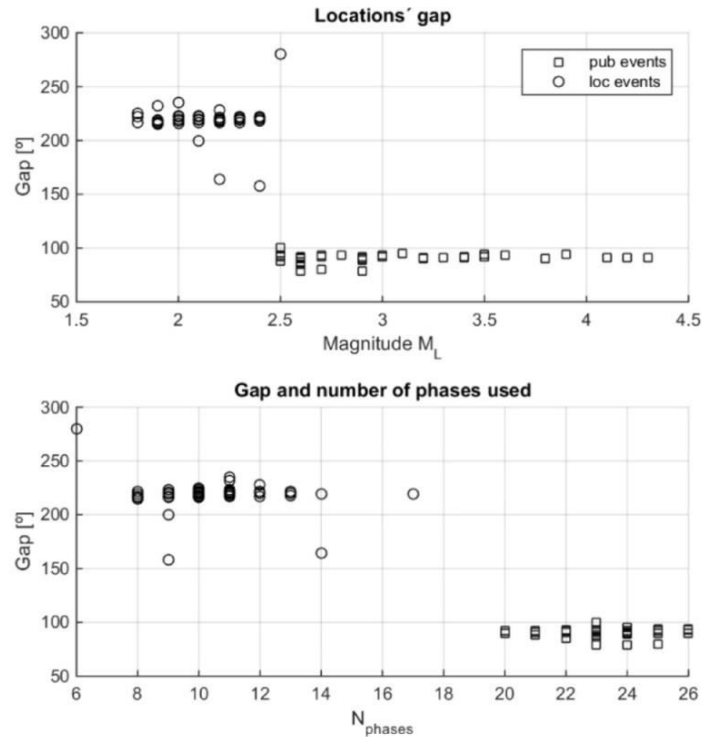


Figure 25: Gap as a function of magnitudes and number of phases used, for each location. Note how it inversely relates with the number of phases used.

The number of phases against the magnitude is shown in Figure 26. Two groups of events can easily be distinguished, one above 20 phase readings (*pub*) and the other with 17 or less (*loc*). One of the restrictions to “accept” a location was set to a maximum residual of 1s (could be a little higher for the furthest stations of the network, at more than 200 km, see Figure 27). With this bound, around 11 phase readings on average were used to locate *loc* events, which is half of those for *pub* events.

For each location, maximum residual plotting (Figure 27) indicates that there are a few events (up to M_L 3.2) with at least one residual above 1. Although it is true that upper-magnitude events do not have high residuals, there are also quite a remarkable number of locations for low-magnitude events with equally low residuals. This indicates that residual (on itself) is only a measure of how well each phase picking has been adjusted, but does not give information regarding how exact (e.g. how *true*) the locations really are.

In fact, it is rather the RMS that globally addresses the quality of the adjustment; it depends on how adequately data fits with the layered model. Results can be seen in Figure 28; as much as it refers to how precise phase pickings are in relation to the calculation made by HYC, a low RMS does not necessarily mean that it is a good location. An extreme case would be an adjustment for only three S and P phases, which would, almost certainly, return a very low RMS; however, the location would be far from true. That being said, for better-constrained events we also expect lower RMS values, as it is shown in Figure 28. Figure 29 compares the RMS against minimum epicentral distance station-event. The reader will note that those locations with at least one station at 40 km or less from the epicenter have a maximum RMS of 0.3; above this value, RMS started to grow for the studied group of events (*pub* and *loc*).

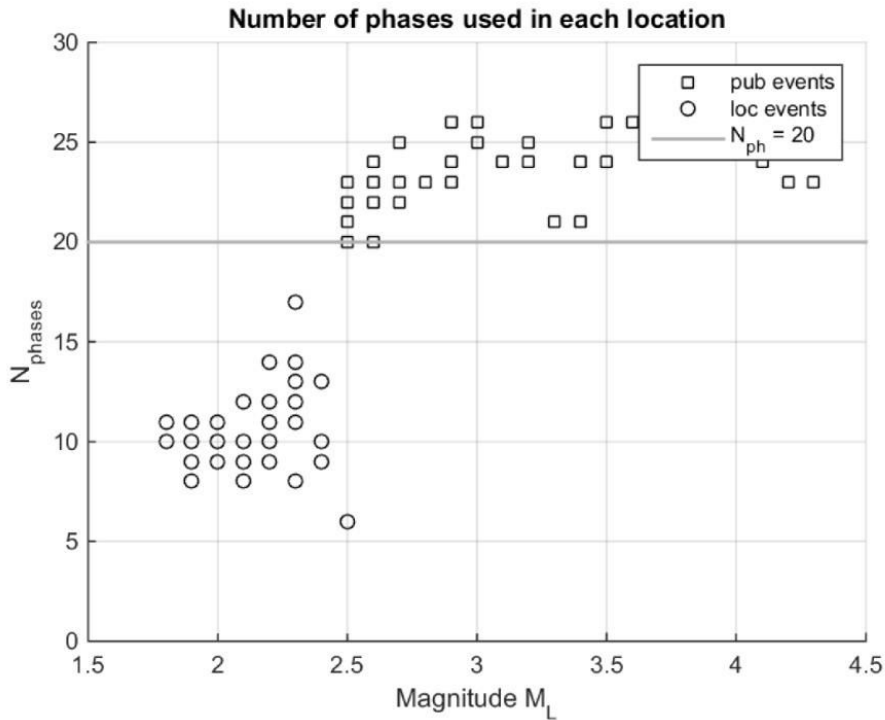


Figure 26: Number of phases vs. Magnitude in each single location. Grey line indicates the minimum number of phases used in *pub* events' locations.

4. Hypocentral locations

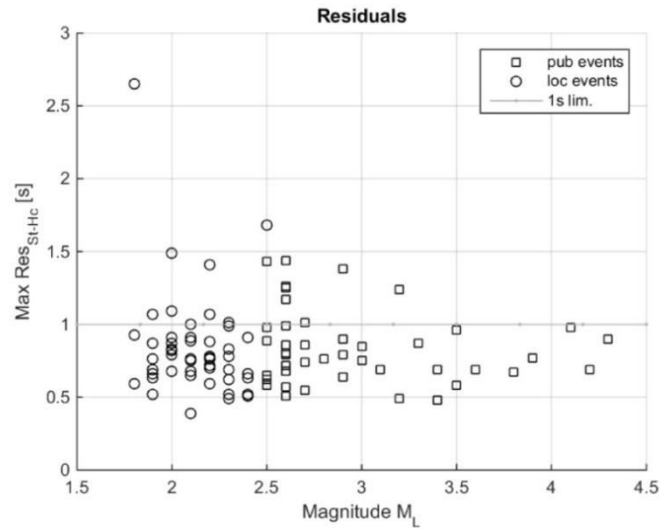


Figure 27: Maximum residual (station-hypocenter) vs. magnitude for each location.

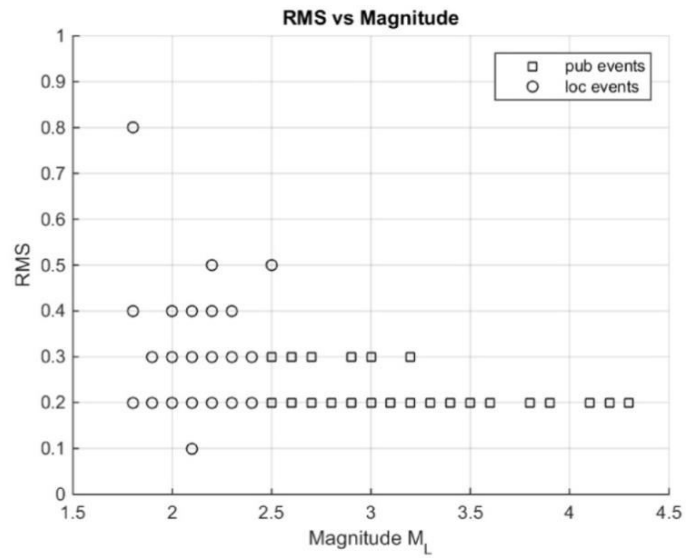


Figure 28: RMS of each location vs. magnitude.

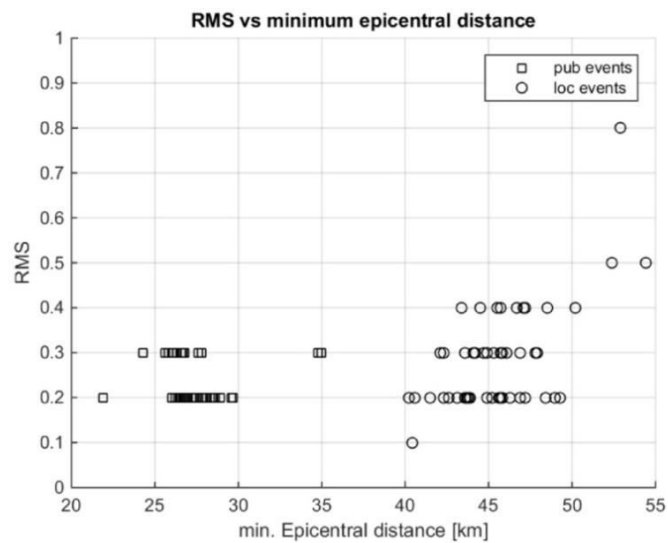


Figure 29: RMS vs. minimum epicentral distance. It can be seen how for those locations with the nearest station at 40 km or farther, RMS starts to increase.

4. Hypocentral locations

Figure 30 depicts the vector composition of horizontal error (with respect to the magnitude) which was evaluated as shown in Equation (14). The error was composed to obtain a better distinction between both groups of events, those with magnitudes equal or larger to 2.5 (*pub*) and those smaller (*loc*). Whereas for *pub* events the Er_h is always below 2 km, the average for *loc* events is more than twice this value (5.11 km).

$$Er_h = \sqrt{er_{lon}^2 + er_{lat}^2} \quad (14)$$

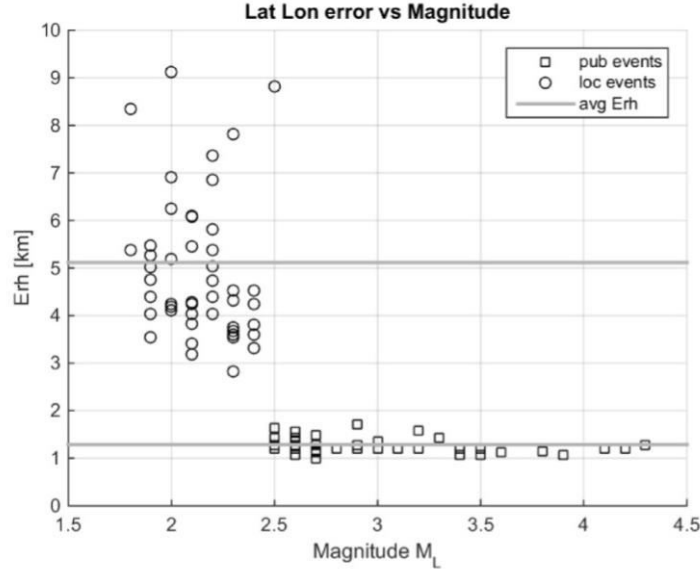


Figure 30: Horizontal error and magnitudes. Clearly, *pub* events (ML 2.5 and above) are more reliably located.

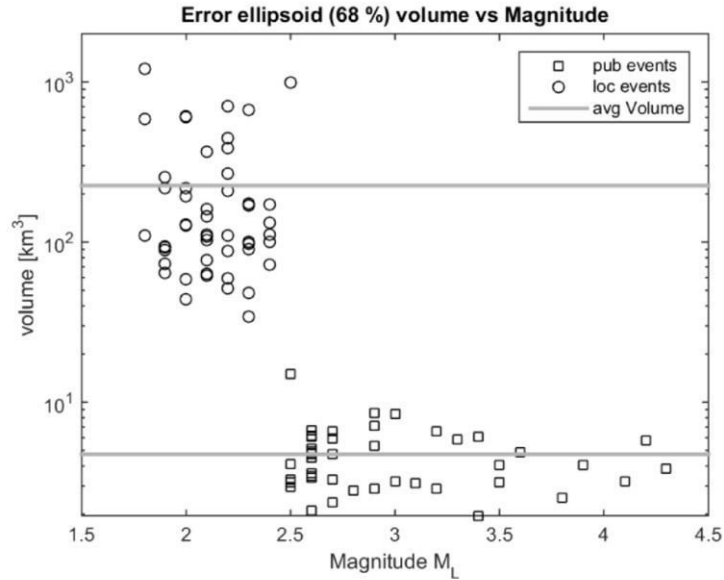


Figure 31: Volume of the error ellipsoids vs. magnitude.

The volume of the error ellipsoid (Figure 31, shown vs. magnitude), evaluated as in Equation (15), is also used for this purpose. The three semiaxes (a , b and c in Equation (15)) are obtained from the diagonalization of the covariance matrix, which is calculated by HYC.

As it takes into account the 3 dimensions of the space (a, b and c semiaxes) the difference between the *pub* and *loc* events is even bigger. The ellipsoids are shown in Figure 32 and Figure 33. Depth is the less well constrained dimension, a problem worsened by a lack of close stations. Locations of the *loc* dataset are subject to larger error, something that could be anticipated before reaching this point. The question is if this error is too much for such a study, something to be discussed in part 4.4 and following chapters.

$$V = \frac{4}{3}\pi abc \quad (15)$$

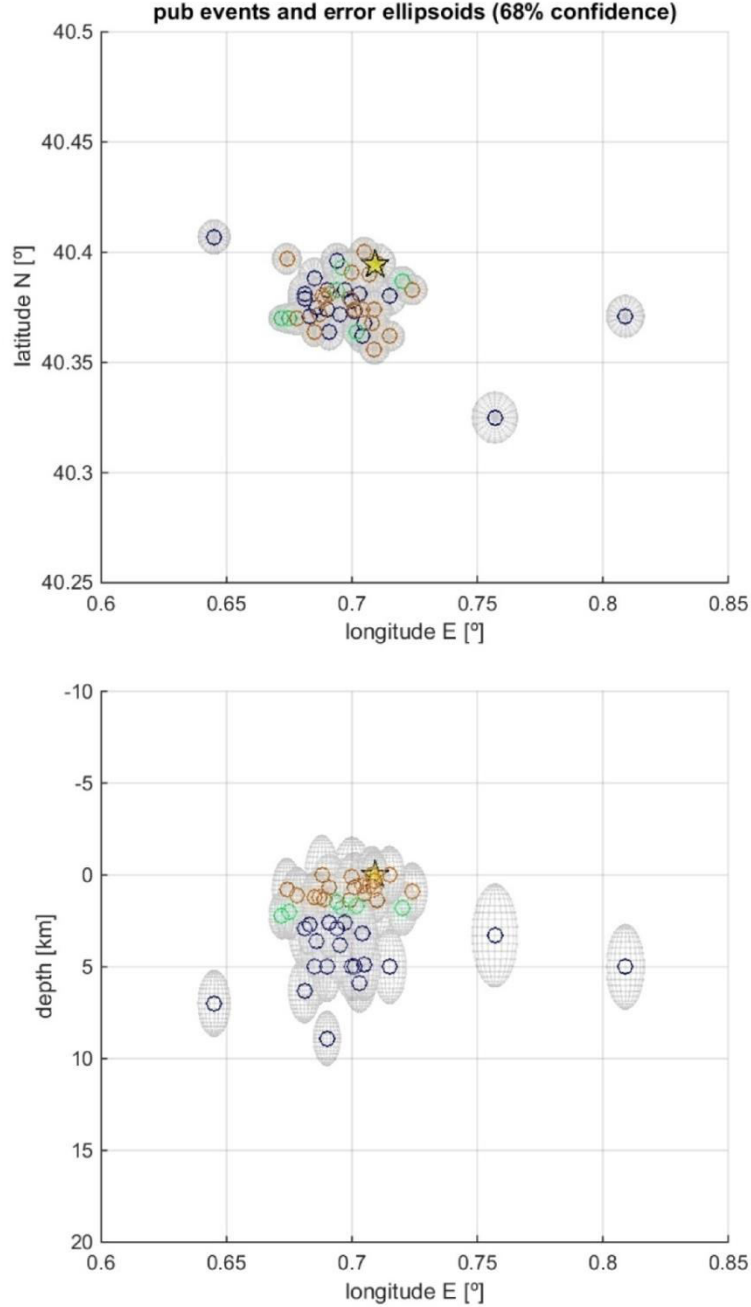


Figure 32: Error ellipsoids (*pub* dataset) displayed on the horizontal (above) and on an E-W depth profile. The yellow star represents the Castor Platform. Negative depths (height above surface) do not have physical meaning, but they are needed to show the whole error ellipsoids.

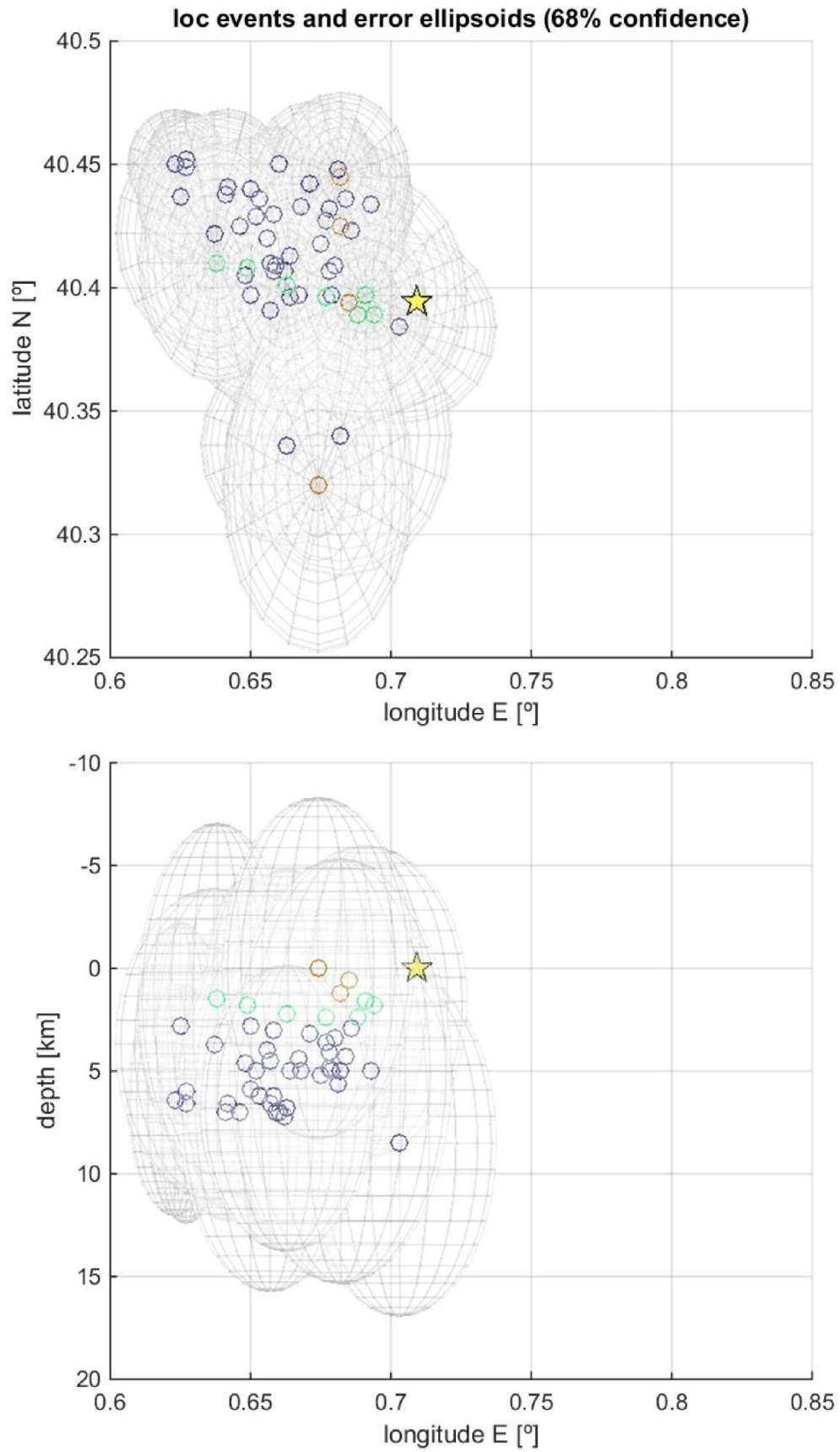


Figure 33: Error ellipsoids (*loc* dataset) displayed on the horizontal (above) and on an E-W depth profile. The yellow star represents the Castor Platform. Negative depths (height above surface) do not have physical meaning, but they are needed to show the whole error ellipsoids.

4.3.2 Magnitude analysis

Figure 34 shows how depth and magnitudes are related. For magnitudes greater than 3, practically no events deeper than 6 km occur, whereas smaller events ($M < 2.5$) are more distributed in between 0 and 9 km. Probably, this is related to smaller events being subject to larger errors, rather than happening at greater or more disperse depths. In fact, due to larger earthquakes' location being more trustworthy, it is most likely that most episodes happened in between 0 and 6 km under the surface.

Because of the new magnitude determinations after locating each event, magnitudes can differ up to 0.4 units from the original value. That is the reason why even if the smallest events to locate had at least M 2.1 (magnitude given by the IGN), some of them have magnitudes of 1.8 after the locations performed here (IGN use 5 different magnitudes, depending on the data sources and earthquake size; the reader is referred to <http://www.ign.es/ign/head/sismoTipoMagnitud.do> for additional information).

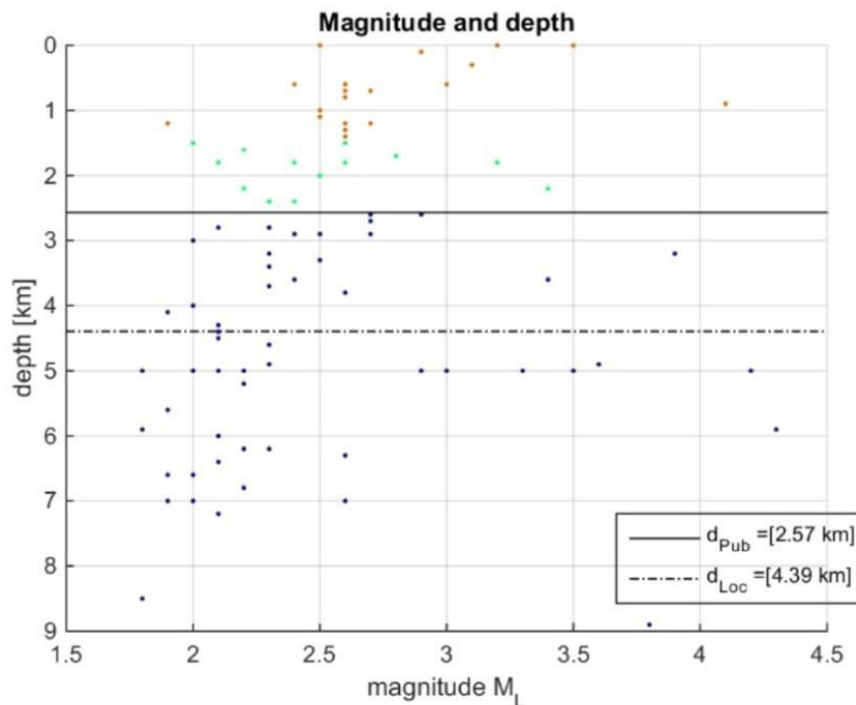


Figure 34: Depth and magnitude comparison. Horizontal lines indicate average depths of the *pub* and *loc* datasets, respectively.

A quick view of the quality in the magnitude determination can be seen in Figure 35; it shows that number of components used for each magnitude determination increases with magnitude of the event (more phase-pickings available). On the other hand, standard deviation is for most of the events between 0.2 and 0.4, without any particular relation with magnitude. Really low standard deviations (below 0.2) are only obtained if a small number of components are used; once again, low dispersion of data is not a synonym of a good determination.

Finally, a comparison of the IGN magnitudes and ICGC (*pub* and *loc*) obtained magnitudes is provided in Figure 36. The relation is given by Equation (16). Dispersion is very low for magnitudes higher than 2.5, but below that value it increases notably. ICGC's standard

4. Hypocentral locations

deviations for events with IGN M_L 2.4, 2.3 and 2.2 is respectively 0.197, 0.088 and 0.183, with a maximum of 0.4 magnitude units of difference.

$$M_{L_ICGC} = 1.091M_{L_IGN} - 0.288 \quad (16)$$

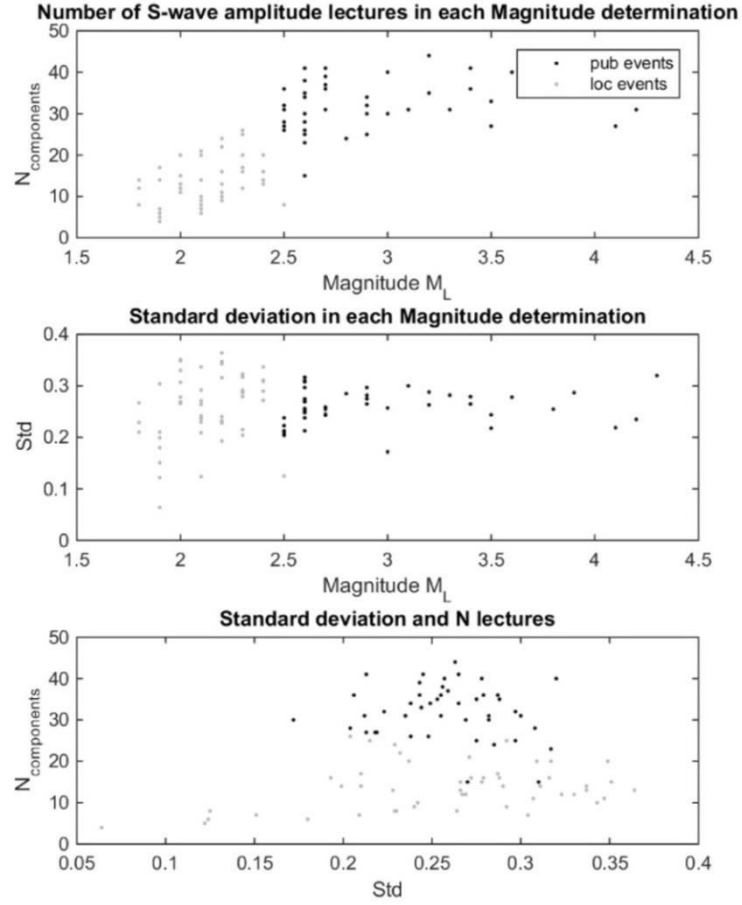


Figure 35: Primary magnitude determination parameters, plotted against magnitude and against each other. Note that while standard deviation does not vary, the number of components is systematically higher for the *pub* dataset.

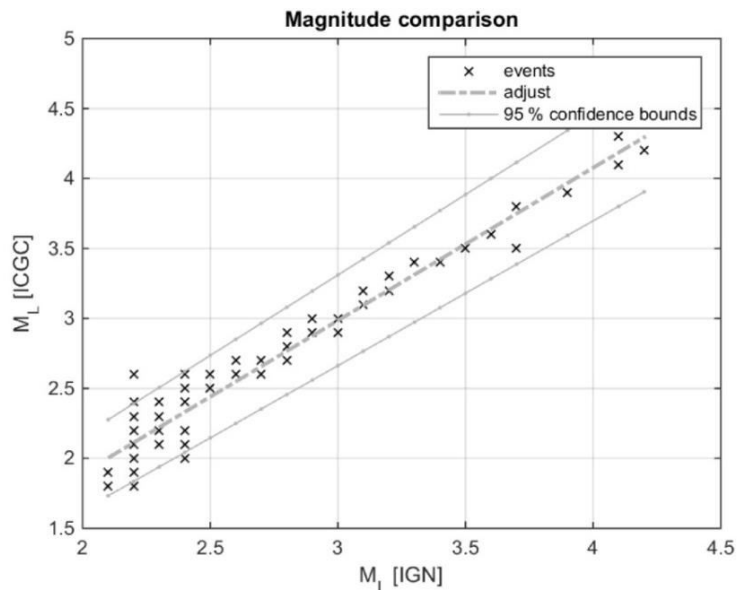


Figure 36: Magnitude comparison. The line adjust is the one in Equation (16).

4.4 Discussion: Interpretation of obtained locations. Implications for Castor's anthropogenic seismicity assumption

The cloud of events shown in Figure 37 displays an approximate distribution NW-SE of earthquake foci. It could indicate information about the activated fault system, but could as well be displaying location uncertainties due to seismic network distribution (Cesca et al., 2014); In fact, the error ellipsoids have shown that uncertainty level of those locations cannot be dismissed, and the *real* alignment of seismicity could be different.

Cesca et al. (2014), relocated a set of 73 events above mbLg 2 using the waveform stacking approach by Grigoli et al. (2013 a,b), as well as an average velocity model obtained from the CRUST 2.0 database. They determined an orientation of seismicity SSW-NNE, which differs from the one derived from the *pub* and *loc* datasets studied here (compare Figure 23 and Figure 37 with Figure 38, which is repeated from Figure 11 to ease comparison). However, the other reference study by Gaite et al. (2016), obtained an alignment much closer to the one shown in Figure 37.

The map in Figure 37 aims at providing a better overview of earthquake locations, together with mapped faults in the area. Most events are near these faults and those with larger magnitudes are located around them. Information regarding faults around the Castor platform was obtained from IGME (2013), and Cesca et al. (2014), whose information source was Geostock (2010). The subparallel WNW-ESE oriented faults' system are the Montsia West faults (at least Montsia West 2, 3 and 7, from south to north). The eastern fault (East 2), dipping towards NW, could be related to the Ampolla fault system, which is reported to merge with the main fault at depth (IGME, 2013).

4.4.1 Depth analysis

In order to obtain further insight on seismicity distribution and its relation with faults in the area, a schematic 3D model of the area was developed (an explanation, the Matlab code and the 3D figure is provided in annex E). Faults were first geo-referenced from those in Cesca et al. (2014), and afterwards extrapolated at depth using the information provided by IGME (2013), who describe fault lengths, widths and dips. The author aims at adding a vertical dimension to the map in Figure 37, as well as obtaining a schematic model of the area surrounding the reservoir.

The result can be seen in Figure 39, Figure 40 and Figure 41, which are horizontal slices of the model, to which neighboring depth quakes from *loc* and *pub* datasets were added. In Figure 39, the reader will note that most of the events are centered on the faults, and well clustered. Figure 40 and Figure 41, which are deeper slices, reveal a more dispersed seismicity, which distributes around a larger area. Based on information in IGME (2013), most of the faults would not reach depths of 3 km, and that is the reason why they are not shown in Figure 41. This last figure depicts a slight alignment along NW-SE and, comparing all three figures, seismicity seems to increase towards the W with depth. This agrees with most mapped faults dipping towards the SW or NW, depending on their strike.

4. Hypocentral locations

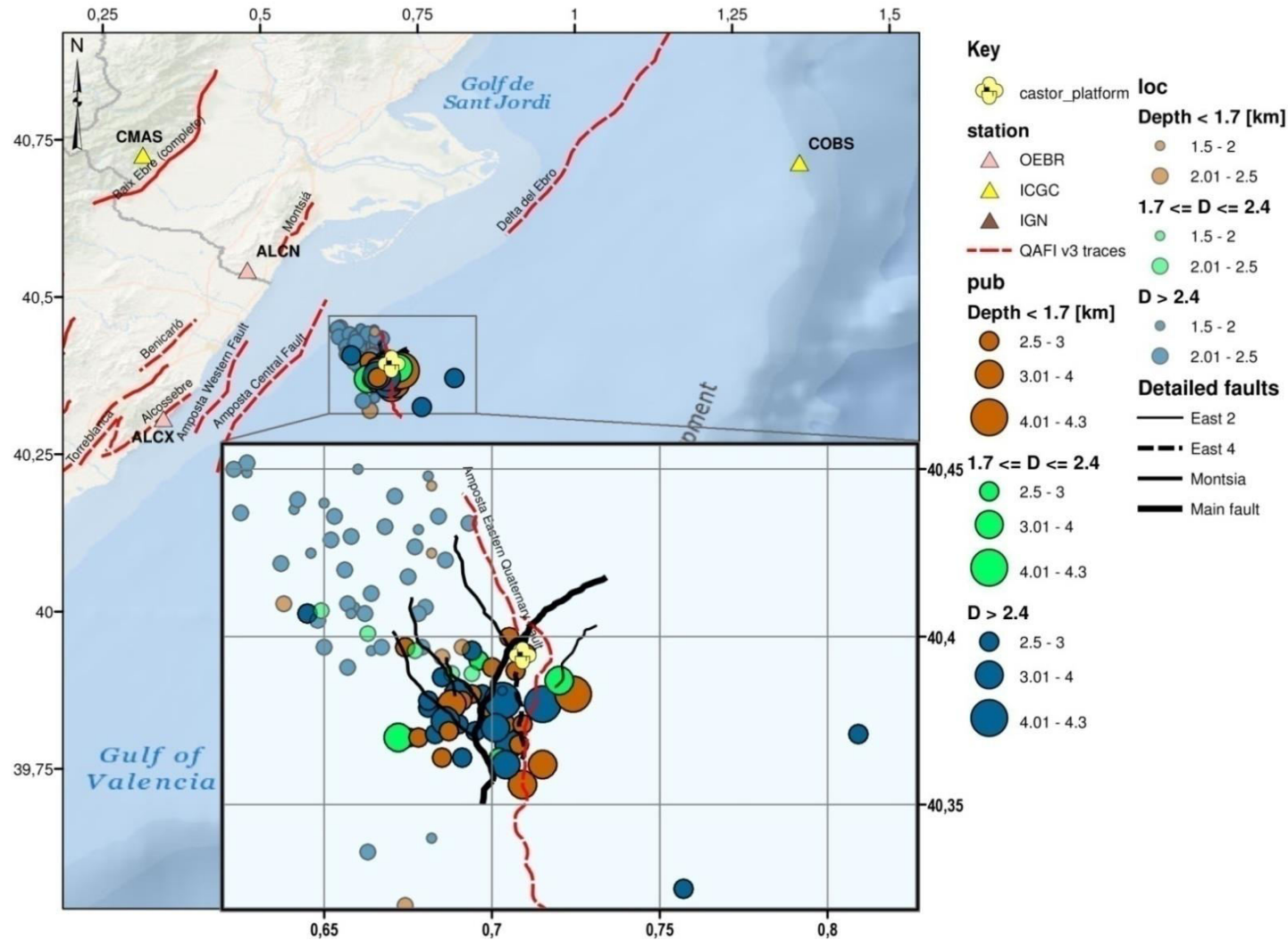


Figure 37: Earthquake locations. Seismic stations are plotted in different color depending on the agency to which they belong. The detailed fault system in the zoom view (black lines) is shown at an approximate depth of 1.7 km, near the reservoir top, and according to Cesca et al. (2014). The Amposta Eastern trace from the QAFI v3 (the composition of Montsia W7, Montsia W7B and Amposta South, see chapter 2 and annex A.4 for further information) is plotted near surface depth. Latitudes and longitudes are shown in degrees.

4. Hypocentral locations

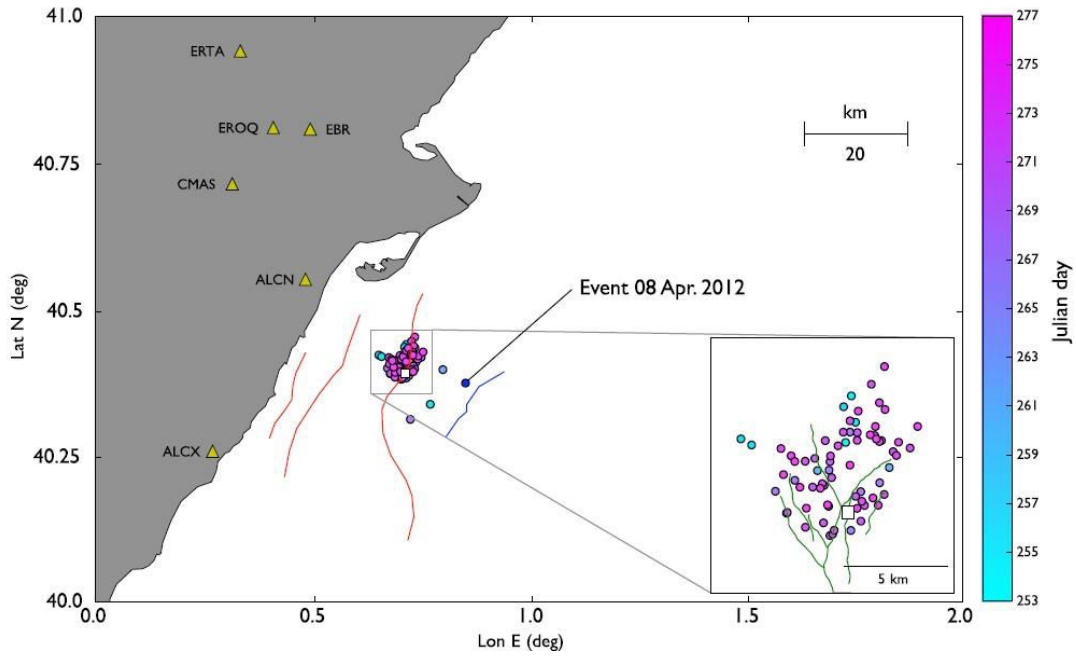


Figure 38: Absolute location results for the largest events in the sequence without using the seismic station COBS, according to Cesca et al. (2014). The red fault traces in the largest map are plotted based on Garcia-Mayordomo et al. (2012), whereas the green ones in the zoom accord to Geostock (2010). Source: Cesca et al. (2014).

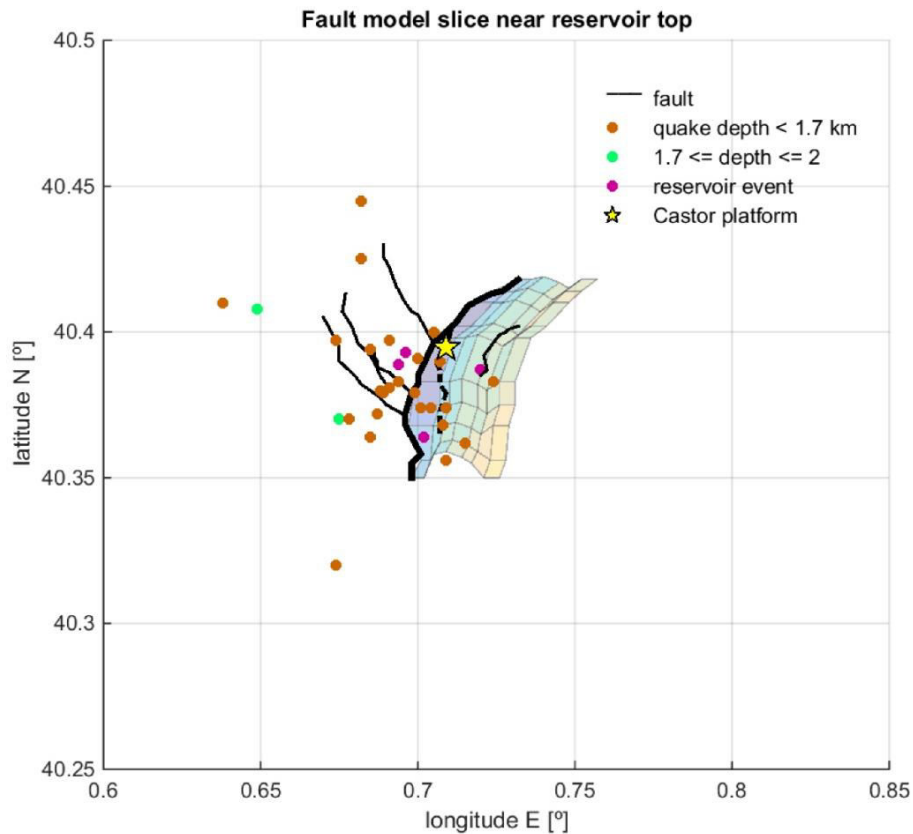


Figure 39: Fault model slice at depth 1.7 km. Earthquakes' color accords to Figure 37 apart from those in purple, which are the ones which happened inside or just around the boundaries of the reservoir. The main and East 4 faults are represented using thicker and discontinuous lines, respectively. The East 4 fault is the only one dipping towards the East. All earthquakes shallower than 2 km are shown, as well as a simple reservoir surface approximation. While faults dip to the W, the reservoir plunges to the E (review figure 8).

4. Hypocentral locations

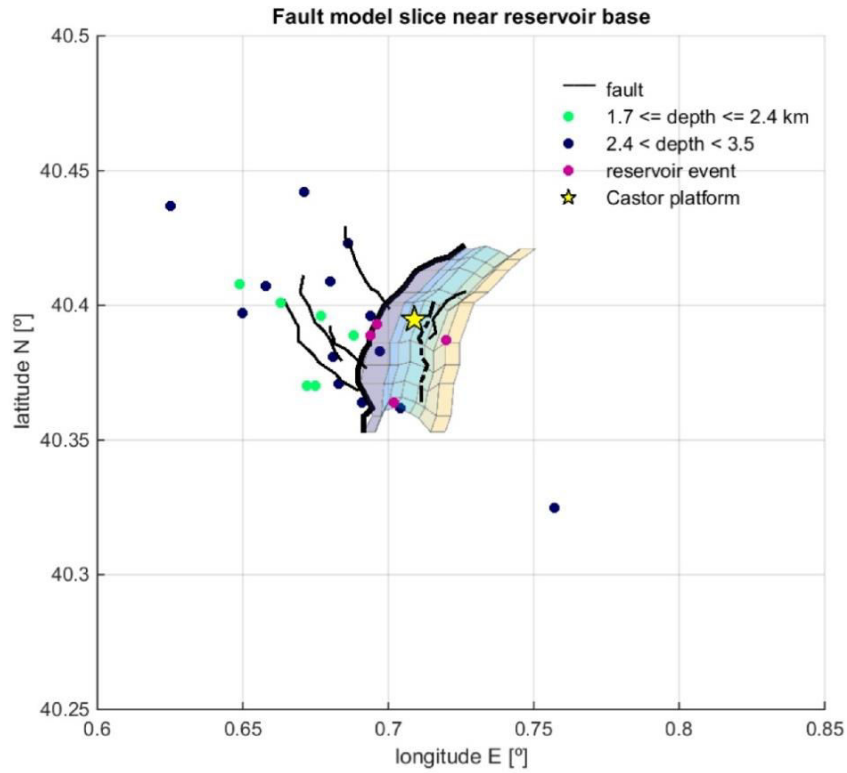


Figure 40: Fault model slice near reservoir base depth (around 2.5 km deep) . Earthquakes' color accords to Figure 37 apart from those in purple, which are the ones which happened inside or just around the boundaries of the reservoir. The main fault is represented using a thicker line. The rough base of the reservoir is shown, as well as those events in between 1.7 and 3.5 km deep.

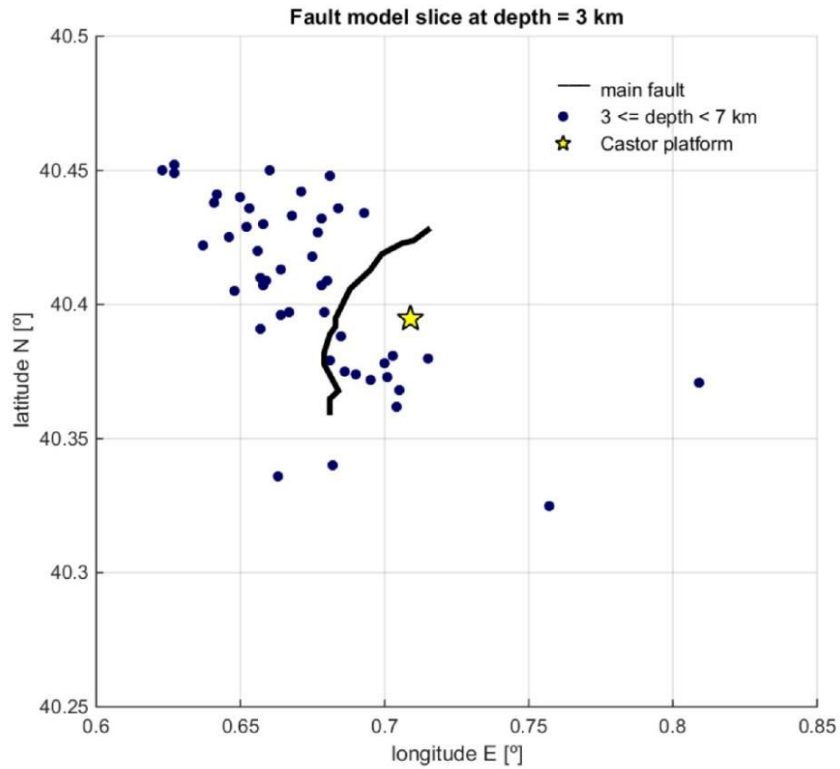


Figure 41: Fault model slice at an approximate depth of 3 km. Earthquakes' color accords to Figure 37, and earthquakes between 3 and 7 km are shown.

Due to earthquakes' dispersion and location errors discussed up to here, assigning the earthquakes to one or another fault does not seem feasible, but seismicity seems to have spatially developed on a quite logical way, especially regarding strikes and dips of faults in the area.

Bearing that in mind, two facts can be highlighted from the analysis of these figures. Firstly, most of the earthquakes are deeper than the "known with evidence" mapped faults' base, which is around 3 km. This could mean that depth of the performed locations is biased (mainly because of an absence of close stations), that main faults in the area extend further deep, or even that unknown faults are present (Gaite et al., 2016). Indeed, all could be possible at the same time as one being true does not exclude the other. And secondly, most hypocenters are located towards the NW and around the Montsia fault system, which would be the one most likely to have been activated if a systematic hypocentral depth error is assumed. Still, the cloud is too disperse to exclude the other faults yet, but information regarding constraints between observed seismicity and activated faults will be provided in the following chapters.

4.4.3 Spatiotemporal evolution of seismicity

Figure 42 shows earthquakes' epicenters and time of occurrence. From the plan view, the reader will note that earthquakes seem to expand inwards, to the center of the cloud, as time passes. Cold colors show the first events of the sequence, and they are more disperse. The fact that magnitudes, in general, are also smaller for first events hinders interpretation, as smaller events have bigger uncertainty in their locations; however, it could be that seismicity was clustering as time passed, because of a concentration of stress perturbation at that point.

Figure 43 depicts the histogram for the studied datasets (*pub* and *loc*). Four phases have been distinguished here in order to provide a better understanding of the seismicity tendency with time. Phase 1 lasts until September 17th (end of the injections), and has a total of 21 events for which magnitudes never exceeded 3. Phase 2 is short, and after a few days where it seemed as if seismicity had been controlled, its limit is defined by the M 3.6 of September 24th. The third phase is the one with the strongest events (3 earthquakes above M 4). Finally, the fourth phase starts after the last day with earthquakes above M 3. This four-phase distinction has been made in order to better assess the spatial development with time; seismicity change and evolution will be further discussed in chapter 6.

So, how did the events in the four phases presented before distribute so that the result is the one shown in Figure 42? Figure 44 illustrates it, and although having a dataset with more events would be preferable, it seems that seismicity evolved as it was inferred before, forming an earthquake cloud which clustered as time went by.

4. Hypocentral locations

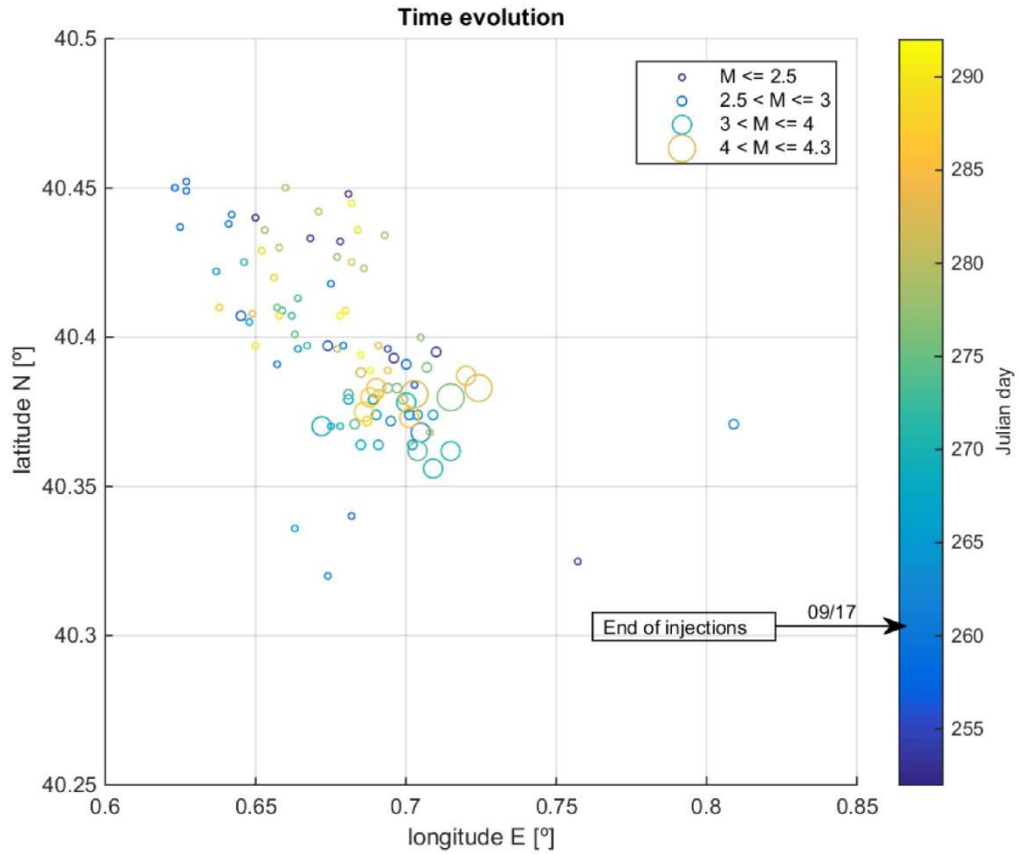


Figure 42: Time evolution of all earthquakes from the *pub* and *loc* datasets. Plan view, size of circles indicates magnitude according to figure legend and color indicates time according to colorbar.

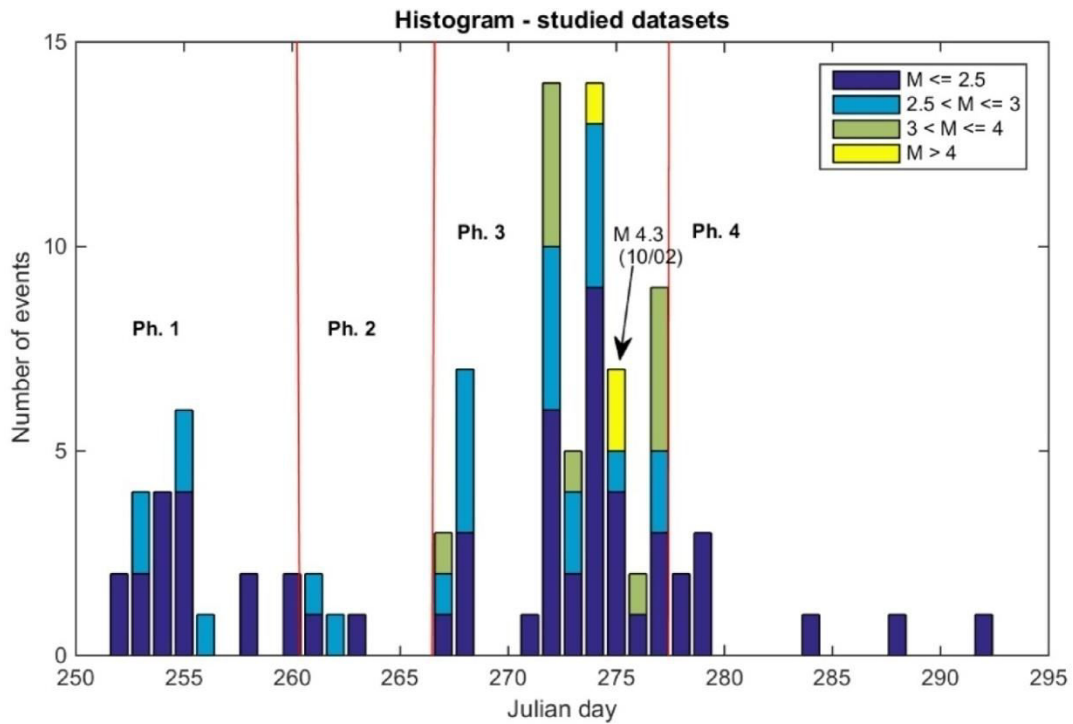


Figure 43: Histogram of the *pub* and *loc* datasets divided in four phases. The first one refers to the swarm during injections. The second one comprises a decreasing of seismicity after injections were stopped. The third phase includes the days with strongest shaking (up to M 4.3), and the fourth is the gradual return to base levels.

4. Hypocentral locations

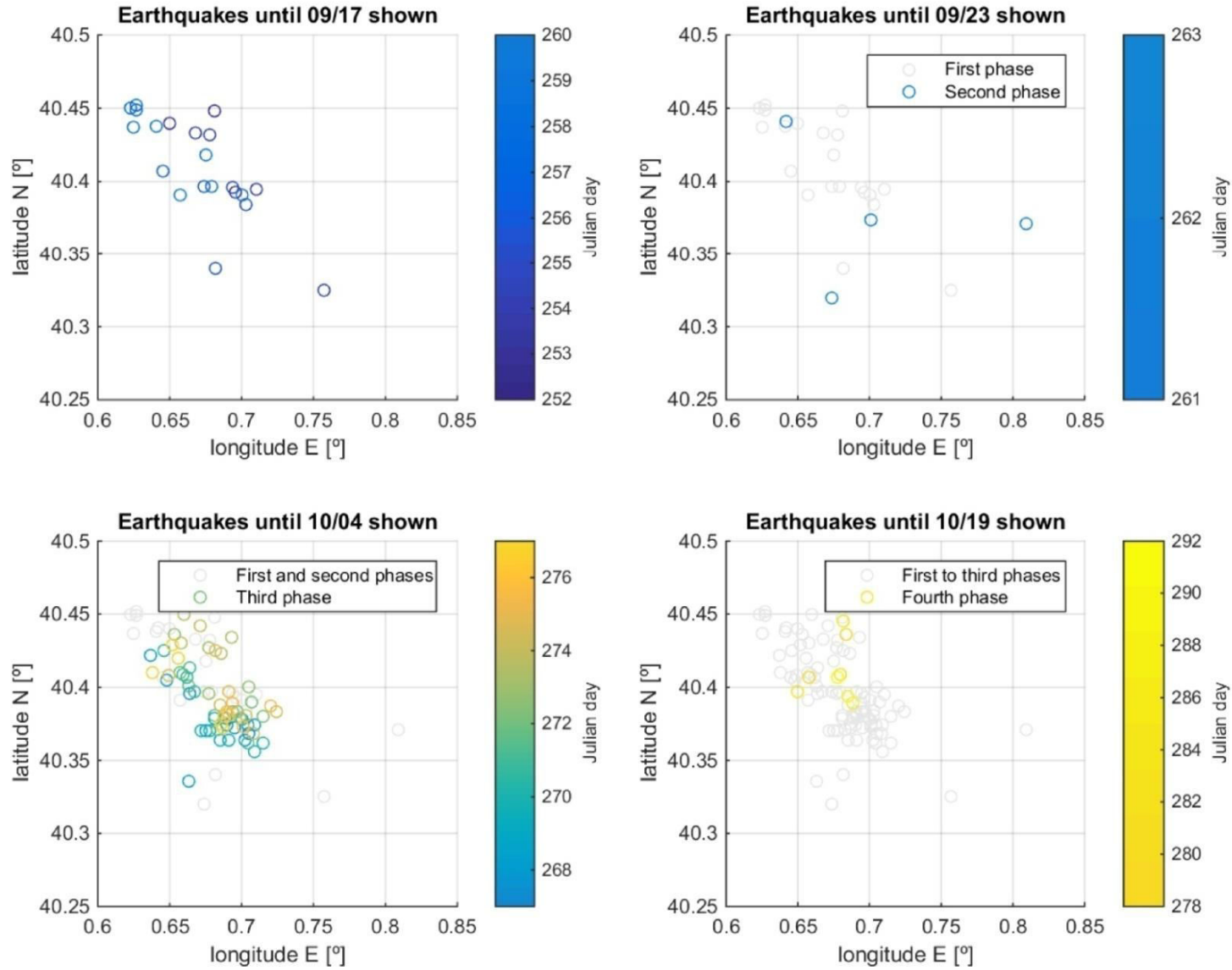


Figure 44: Plan view of the earthquakes in each of the four phases described in the text. Here, the focus is plenty on time and location, so size of the earthquakes is not distinguished.

Therefore, the author suggests the following statements regarding each phase, as working hypotheses:

1. Injections take place and so earthquakes happen at those points with higher injection influence (small but localized pore pressures). Energy released is small and it is a direct reflex of the introduced perturbations, which generate slight and recurrent fault slips. The perturbation influence should expand outwards (as time passes) during this phase. These first earthquakes could be linked with induced seismicity.
2. No external energy is introduced to the system (injections stop), but recurrent earthquakes take place because of the previous perturbation. Earthquakes would naturally diminish with time (this is observed until September 23rd). Nevertheless, stress has concentrated at certain points, where weak zones (faults) are likely to slip if a certain threshold is surpassed (see Figure 1, chapter 2). The stress concentration adding to the dominating regional stress is partly due to gas injections (external perturbation), and partly because of other triggers, such as the earthquakes that took place before September 23rd. As the perturbations migrate, the process is no longer controlled by any external activity, nor possible to predict (without an adequate numerical model simulating the activity that took place in the area).
3. When certain stress levels are reached, faults slip, and size of the earthquakes is controlled by the fault area along which rupture can propagate. This does not mean that all the fault surface slips, but the stressed part; the main earthquakes in this sequence, around M 4, imply dislocations of around 5 cm along rupture surfaces of the order of 0.5-1 km² (according to Wells and Coppersmith, 1994). Fault orientation could also have played an important role in the behavior of rupture (e.g. Gischig, 2015). The sequence is self feed back, probably a result of hydromechanical coupling within the fault network, with previous injections and earthquakes acting as triggers in a stress regime dominated by the background stress, and hence seismicity would be triggered.
4. Even considering that the system is feed back, enough energy is released as a result of the earthquakes; the amount of stress on faults diminishes, and so does seismicity.

Unfortunately, at the moment this statements are only based on observations (e.g. no perturbation has been quantified), and no conclusions can be drawn yet. Analysis of coupled phenomena in a detailed and well constrained model would be best to see if it is possible to reproduce the earthquake sequence. If this was managed, it would provide security to any statement, in the sense that they would be based on the application of fundamental concepts of rock mechanics, fluid dynamics and porous media behavior. Such an approximation is out of scope here, but parts 6 and 7 will provide further insight on the topic of seismicity's nature and quantification of stress transfer between faults, and some comments will be added in relation to the points presented above.

Experience should have taught us that observations, when not supported by strong theoretical background, are of dangerous nature. This comment is just to clarify that, at this point, the path leading to understanding Castor's case may have slightly smoothed, but the puzzle is far from solved. Up to here, the only conclusion that can be drawn from

calculations is that seismicity could agree, or at least be coherent, given the morphology of known faults in the area and considering the three dimensions of the space. Yet, questions regarding which and how these faults were activated, as well as the operator's influence in the earthquakes, remain unsolved. They will be addressed next.

5. MOMENT TENSOR

This chapter exposes the calculation of the moment tensor and the derivation of focal mechanisms (FM from now on), as well as an interpretation of the results which follows the structure in chapter 4. The final discussion of the results (part 5.4) complements the one in 4.4.

5.1 Method

5.1.1 Introduction

The formulation using the Seismic Moment Tensor (SMT) simplifies obtaining the earthquake source parameters. Usually, the processes that result from slip along a fault are modeled as *double couples*¹⁸, which consist of 4 forces. A general representation of various seismic sources can be obtained by combining various force couples into the SMT. Essentially, the moment tensor is the expression of the movement on a fault, comprising nine sets of two vectors (Aki and Richards, 1980; Stein and Wyssession, 2009; USGS earthquake glossary, see <http://earthquake.usgs.gov/learn/glossary/?term=moment%20tensor>).

Figure 45 shows an example of a left lateral strike slip fault, and the associated double couple. While the M_{yx} couple is intuitive because of the slip movement, the M_{xy} is not; however, in order to prevent net torque on the fault it has to be included. Due to this double couple nature, if the slip was right lateral on the x-z plane, the body forces would remain equal. As a result, the solution of a double couple FM will always provide two planes (fault plane and auxiliary).

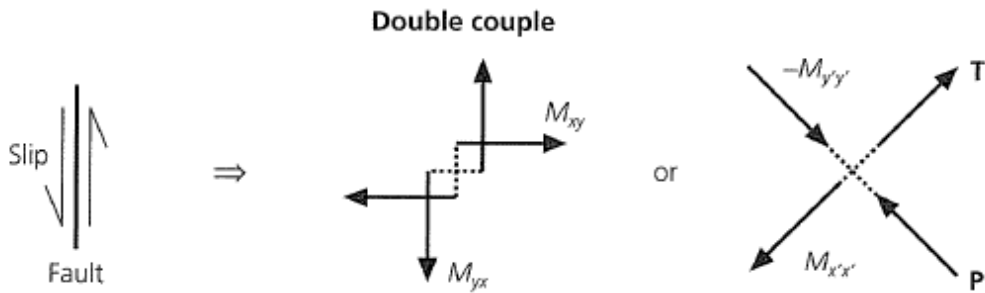


Figure 45: Strike slip fault and body force descriptions of the double couple. Each force couple can be formed by two forces offset a determinate distance (left double couple, generates torque) or dipoles (right, does not introduce torque). Modified from Stein and Wyssession (2009).

The magnitude of the equivalent body forces is M_0 , and if M_{yx} and M_{xy} are unit vector couples, the expression in (17) can be written:

$$SMT = M_0(M_{xy} + M_{yx}) \quad (17)$$

¹⁸ A force couple is a pair of forces which act together, and the concept is similar to that of electromagnetic dipoles. Source: Stein and Wyssession (2009).

Thus, the SMT is a mathematical way to approximate rupture, and it represents both fault geometry (using the different components) and size (using the scalar moment M_0). As a rank 2 tensor, it has a total of 9 components and 6 are independent.

For example, the earthquake in Figure 45 (left) can be approximated using the SMT as shown in Equation (18), considering that fault and slip directions are oriented neatly to the coordinate system. If not, the tensor would appear more complicated, but the concept is the same.

$$SMT = \begin{pmatrix} 0 & M_0 & 0 \\ M_0 & 0 & 0 \\ 0 & 0 & 0 \end{pmatrix} = M_0 \begin{pmatrix} 0 & 1 & 0 \\ 1 & 0 & 0 \\ 0 & 0 & 0 \end{pmatrix} \quad (18)$$

As an indication to Equation (18); the trace of the tensor is always 0 for pure double couple sources, as the slip vector lies in the fault plane and is perpendicular to the vector normal to the plane. A nonzero trace indicates volume change.

Once the SMT is determined, fault geometry can be deduced and the FM obtained (typically represented as a beachball plot). The process is based on linear algebra regarding vector transformations; the eigenvectors of the SMT are parallel to the T (tension), P (compression) and null axes. After that, strike, dip and rake can be determined. The interested reader is referred to Stein and Wysession (2009), to obtain a more detailed view on the topic.

As noted before, any FM solution provides 2 possible fault planes which are perpendicular; *a priori*, distinguishing which one is the rightful is not viable and because of that, other strategies may come into play. Ideally, gathering information of mapped faults in the area of interest should be enough to discriminate between them.

5.1.2 FMNEAR routine

Seismic waves' radiation patterns, which are seen on seismograms, correspond to a determinate FM. The process to obtain the FM solution consists on inverting the waveform and obtaining the double couple of forces, whose information is contained in the SMT. Such a thing can be done thanks to the linear relationship between ground motion and the components of the SMT, which allows obtaining the latter via linear inversion.

To do so, FMNEAR (Delouis, 2014) was used. It was coded as to obtain a program which could use near-source records efficiently, even for large earthquakes. Hence, the source can be modeled with a finite length (taking into account its spatial extension), rather than just a point, for magnitudes above M_w 5.5. Kuge (2003), applied a similar method for earthquakes up to M_w 6.8. To do this, a distribution of point sources along a linear finite fault can be studied.

Essentially, the routine implemented consists in choosing various fault planes and obtaining their theoretical waveforms, which are then compared with the real waveform. The most similar to the objective waveform has a FM equal (or more similar) to that of the studied earthquake. The program steps are summarized henceforth, but the reader is remitted to the original article (Delouis, 2014), whose structure has been maintained, for deeper understanding. Here, the FMNEAR webservice (Delouis, Gerakis, Deschamps, Geoazur/Observatoire de la Côte d'Azur) has been used in order to obtain the FM for the

earthquakes of interest (available at http://source.unice.fr:8080/FMNEAR_website/fmnear.html; last accessed June 21st 2016).

Data input and processing

The hypocenter and a first estimate of the earthquake magnitude are needed as input values. Depth may be less constrained, but the final FM depends on the initial estimate, as it will be latter explained.

Processing of data includes baseline correction, picking the initial P wave arrival, integrating twice the acceleration signal to obtain displacement, and applying a time shift, window, filter and decimation:

- Time shift is performed to be independent of the absolute time and to align the observed signals with synthetic ones.
- Windowing use is to determine the time range for which waveform inversion has to be calculated. It is related with the f_{\min} (low-cut frequency) of the filter.
- Filtering is an essential process applied to maintain all essential frequencies of the studied signal and at the same time avoid the others (noise). Low frequencies emitted by the rupture, in strong motion records, want to be kept, and it might be difficult to obtain them without too much noise (see Delouis, Charlety and Vallée, 2009).
- Decimation is important to obtain a reliable sampling rate that also allows a relatively fast computing time. In this method the signals are sampled to $(1/f_{\max})$.

Determination of the FM parameters (Strike, Dip and Rake)

A linear finite source model is inverted to test each fault plane (nodal planes defined by strike, dip and rake). Linear finite source models are considered as a series of uneven point sources, spaced according to magnitude. Rupture lengths are determined based on Wells and Coppersmith (1994), and the longitude of the line measures twice the according rupture length. This is done to explore unilateral ruptures, as well as bilateral ones.

A local moment rate Source Time Function (STF) is evaluated for each point source, where onset rupture time and rake angle are calculated. The STF is based on overlapping isosceles triangles whose amplitudes are inverted in order to use a simulated annealing algorithm¹⁹ (this process is carried out for finite fault sources; the events' magnitudes in this study did not require such an approach). The minimization of the RMS on the waveforms is used as the convergence norm. The inversion is made for all tested fault planes, and the procedure is taken from Delouis et al. (2002).

Searches and source depth

The grid search is carried out in two steps. The first (coarse search) consists in testing 24 fault planes (12 different FMs). 8 FMs are dip-slips and 4 strike-slips. The strike, dip and central rake values tested are shown in Figure 46, and they allow fast coverage of the whole parameter space.

¹⁹A Simulated Annealing (SA) is a probabilistic technique, used to approximate the global optimum of a determinate function.

Depth is evaluated after this first step. Seven different depth values are tested, the range depending on initial depth, and the final value is selected based on the RMS misfit. Finally, four different values around the one with the lower misfit are tested, and the depth value is defined. After that, the coarse grid search (step 1) is done again with the final depth, and step 2 maintains this depth value.

A more detailed exploration is done in the second step (fine search), around the best solutions (a dip-slip and a strike-slip) previously obtained as a result of the coarse search. The strike is varied $\pm 20^\circ$, and then dips of 15, 30, 45, 60 and 70° are tested for the dip slip case, whereas 60, 75 and 90° are assessed for the strike-slip. Finally the strike is moved by $\pm 5^\circ$, and the dip varied by ± 5 and $\pm 10^\circ$. For each substep, every new exploration is performed with the best solution previously found as input.

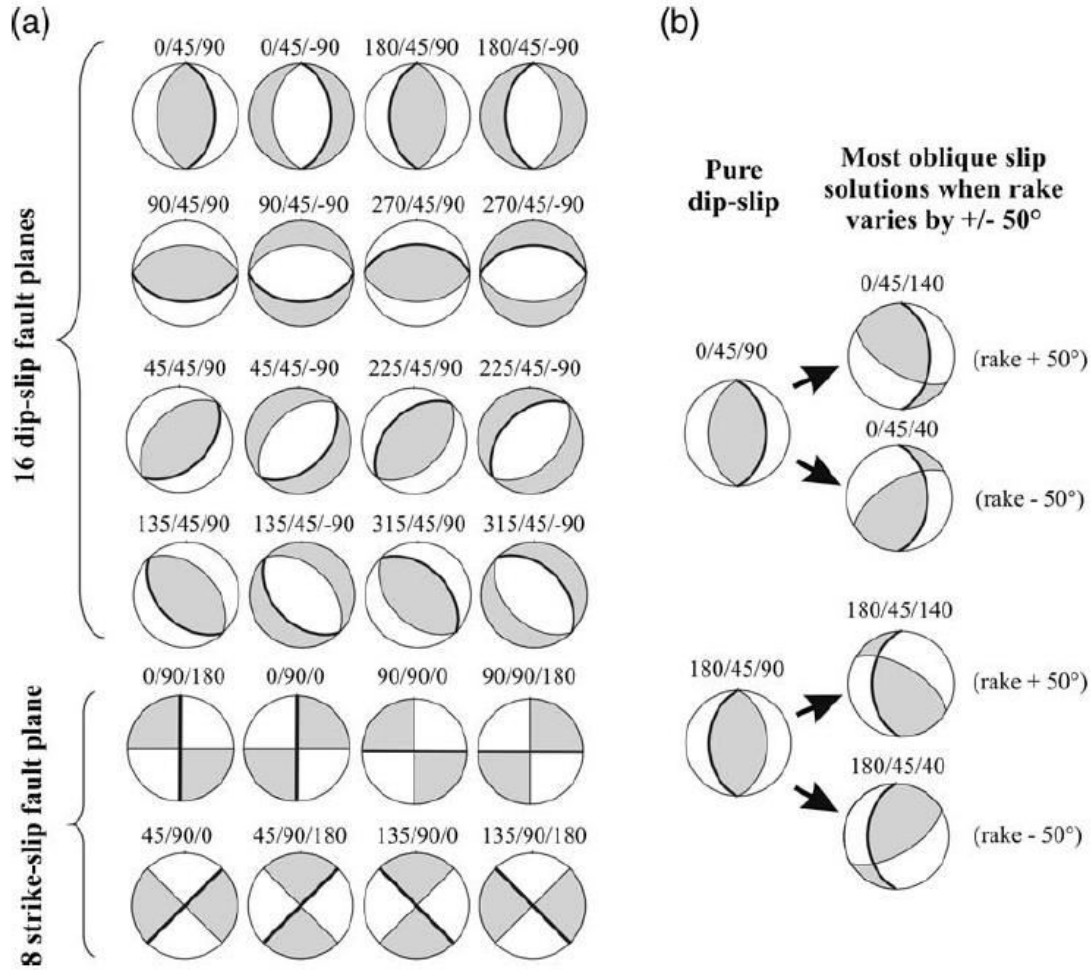


Figure 46: (a) The 24 fault planes tested in the coarse search, with strike, dip and central rake values tested. (b) exploration of obliquity in the focal mechanisms when the rake is modified to $\pm 50^\circ$ around the central value. In (a) and (b), the fault plane is represented by a heavier black line. Extracted from Delouis (2014).

The rake is also tested ($\pm 30^\circ$) around the best value previously found, each time a new strike and dip are tested. Each rupture plane is stored with their corresponding normalized RMS misfit function (see Equation (19)), which will then be used to compute a confidence index. The computed and recorded signals can be realigned, using a maximum time shift which depends on hypocentral distance.

$$RMS = \sqrt{\frac{\sum w(obs - cal)^2}{\sum w(obs)^2}} \quad (19)$$

In equation (19), \sum is the sum over all waveform's data points, *obs* and *cal* are the observed and calculated amplitudes, and *w* is a weight factor in between 0 and 1.

Error treatment

Station components with poorly matching waveforms are discarded. To do that, successive thresholds in RMS misfit are considered, and components with misfit values above the evaluated threshold (0.999, 0.96, 0.85 and 0.65 depending on the stage of the process) are discarded.

An error of few kilometers in an evaluated epicenter location would cause relevant variations in the travel path azimuth to the closer stations. As earthquake locations usually have errors of this magnitude, a progressive reduction in weight for stations closer than 20 km is implemented (Equation (20)). The minimum weight assigned is 0.1.

$$w = \left(\frac{d_{epi}}{20} \right)^2 \quad (20)$$

Quality of the inversion

The quality of the results is studied using two different indicators:

- 1) Intrinsic quality of the waveform modeling (RMS misfit and visual comparison).
- 2) Confidence Index (CI), defined by Delouis (2014), as “an empirical indicator of the quality and uniqueness of the solution”. To obtain it, the distance between the FM with the lower RMS misfit function (which is the best solution) and all other focal solutions explored during the coarse and fine searches is computed. The routine calculates the distance between two FM as the sum of the absolute value of the differences in the theoretical amplitude of the P wave, as predicted by the two mechanisms, divided by the number of points that sample the focal hemisphere (distance in between 0 and 1). After that, the difference in RMS between the best solution and the others is evaluated, and the CI is low when a small RMS difference is associated with a large distance between FMs. In contrast, it is high if no solutions with similar RMS and distant FMs are found. In addition, the more the number of components used, the higher the CI.

Generally speaking, a FM can be considered “trustworthy” when the CI is above 70 % (its values ranging from 0 to 100 %). Finally, the user can compare the obtained FM and M_w as well as moment distribution along strike, with already published source models (not implemented in the FMNEAR).

5.2 Event data

5.2.1 Data selection

Frontera et al. (2013), calculated the FMs for the largest 8 events (M_L 3.5, 3.5, 3.6, 3.7, 3.9, 4.1, 4.2, 4.3), using the first obtained locations for the earthquakes as there was a need for obtaining information as soon as possible. Apart from recalculating those FMs, this part had the goal of seeing down to which magnitude value reliable FMs could be obtained, using Delouis' (2014) FMNEAR. Unfortunately, due to poor quality in the waveforms and locations (low magnitudes and big gaps being the main factors), no reliable FMs for events with $M < 3.5$ could be obtained despite the efforts made.

In order to compute the FMs two different velocity models have been used, the first one being a global default model, and the second a slight modification of the Valencia Gulf model presented in Table 2 (see 4.1.3). Therefore, FMs presented here reach a minimum of M_L 3.5 and correspond to the 8 largest events of the seismic sequence. They have been obtained for the definitive locations²⁰ (those in the *pub* dataset), and using two different models in order to compare and examine differences.

5.2.2 Velocity models

FMNEAR webservice uses by default a general four layered model, introduced to provide reliable results for worldwide earthquakes. The parameters of the model are summarized in Table 3.

As well as computing focal mechanisms with the default model, they were also calculated using a modified VG model, which is shown in Table 4, henceforth called Castor model. As FMNEAR relies on a depth-increasing density, the VG model in Table 2 (see 4.1.3) was adapted to agree with it. The goal was seeing if remarkable differences were obtained because of an adapted model or, on the other hand, whether the routine is not highly dependent on it.

Table 3: FMNEAR webservice speed model. Q_p , Q_s are the seismic attenuation coefficients (Higher Q means lower attenuation).

Default model						
Layer	Thickness [km]	V_p [km/s]	V_s [km/s]	Density [kg/cm ³]	Q_p	Q_s
1	0.6	3.3	1.75	2	200	100
2	1.4	4.5	2.6	2.3	350	175
3	3	5.5	3.18	2.5	500	250
4	25	6.5	3.75	2.9	600	300
Mantle	-	8.1	4.68	3.3	1000	500

Table 4: Castor velocity model. Q_p and Q_s are the seismic attenuation coefficients (Higher Q means lower attenuation).

Castor model						
Layer	Thickness [km]	V_p [km/s]	V_s [km/s]	Density [kg/cm ³]	Q_p	Q_s
1	5	5.2	2.97	2.5	400	200

²⁰The grid search algorithm depends on the input location, which makes it important to be able to obtain well constrained locations.

5. Moment tensor

2	13	6.0	3.43	2.7	550	275
3	22	6.4	3.66	2.8	600	300
Mantle	-	7.9	4.51	3.3	1000	500

5.3 Results

In view of small magnitudes of the studied events, achieving reliable FMs is not an easy task. FMNEAR webservice has proven to be useful and fast, usually taking no longer than 9 - 11 minutes to find a FM solution for the magnitude range of study and amount of data introduced. That being said, the process until a solution with $CI \geq 70\%$ was found was not simple, especially for events with $M < 4$. Numerous changes regarding which waveforms not to use, changing input depths (up to hypocentral depth ± 4 km), and locking or not locking them had to be introduced; each change had to be done independently for each event, which in the end resulted in a time-consuming process. In spite of that, solutions are provided in Table 5 and Table 6.

5. Moment tensor

Table 5: FMs solutions summary table – default model. Sorted by input magnitude (highest to lowest). Solutions obtained by Frontera et al. (2013), IGN (2013) and Cesca et al. (2014) are also shown to ease comparison. Frontera's et al. (2013) solutions were obtained using the same method (FMNEAR) and model (default).

Default model																	
Earthquake location data					FM computation and result										Previous studies		
Date - time UTC	Lat. (°)N	Lon. (°)E	Depth (km)	M _L	Input depth (km)	FM depth (km)	Strike (°)	Dip (°)	Rake (°)	RMS	Conf. Index (%)	Comp. used	M _w	Beach ball plot	Frontera et al. (2013)	IGN (web catalog)	Cesca et al. (2014)
2013/10/02 23:06:50	40.381	0.703	5.9	4.3	3	5	135.0	90.0	-154.8	0.572	87	31	4.2				
2013/10/01 03:32:45	40.38	0.715	5	4.2	8	11	135.0	70.0	-164.6	0.5	88	24	4.1				
2013/10/02 23:29:29	40.383	0.724	0.9	4.1	5	6	40.0	65.0	8.8	0.6	74	26.0	4.0				
2013/09/30 02:21:17	40.362	0.704	3.2	3.9	4	8	140.0	65.0	-142.5	0.6	83	32	3.9				
2013/10/04 08:49:48	40.383	0.69	8.9	3.8	5	8	45.0	60.0	-9.5	0.5	82	18.0	3.7				
2013/09/24 00:21:50	40.368	0.705	4.9	3.6	4	5	135.0	85.0	-144.4	0.539	83	13	3.6			Not available	
2013/10/04 09:55:20	40.373	0.701	5	3.5	3	3	130.0	85.0	-157.6	0.5	79	10.0	3.6				
2013/09/29 22:15:48	40.362	0.715	0	3.5	5	8	130.0	85.0	-169.9	0.6	84	28.0	3.6				

5. Moment tensor

Table 6: FMs solutions summary table – Castor model. According to other indications given for the previous table.

Castor model																		
Earthquake location data					FM computation and result											Previous studies		
Date - time UTC	Latitude (°)	Longitude (°)	Depth (km)	M _L	Input depth (km)	FM depth (km)	Strike (°)	Dip (°)	Rake (°)	RMS	CI (%)	Comp. used	M _w	Beach plot	ball	Frontera et al. (2013)	IGN (web catalog)	Cesca et al. (2014)
2013/10/02 23:06:50	40.381	0.703	5.9	4.3	2	3	130	90	-135.2	0.52	87	19	4.2					
2013/10/01 03:32:45	40.38	0.715	5	4.2	10	9	40	70	17.1	0.57	78	19	4.1					
2013/10/02 23:29:29	40.383	0.724	0.9	4.1	5	6	115	70	158.7	0.518	84	21	3.9					
2013/09/30 02:21:17	40.362	0.704	3.2	3.9	3	4	130	70	-171.6	0.514	81	17	3.9					
2013/10/04 08:49:48	40.383	0.69	8.9	3.8	8	8	135	70	167.3	0.678	75	24	3.7					
2013/09/24 00:21:50	40.368	0.705	4.9	3.6	6	2	220	85	-5.8	0.658	78	20	3.5				Not available	
2013/10/04 09:55:20	40.373	0.701	5	3.5	6	6	220	80	-3.6	0.557	86	14	3.5					
2013/09/29 22:15:48	40.362	0.715	0	3.5	1	8	230	80	12.9	0.638	75	26	3.6					

5.3.1 Focal mechanism solutions

As depicted by the *beach ball* diagrams in Table 5 and Table 6, the events correspond to strike-slip mechanisms, and some of the FMs also show some normal component. Further information on the topic of the FM computation is provided in annex F, which shows the waveform adjust and location map for each of the 16 computed FM solutions.

Compared with the solutions obtained by Frontera et al. (2013), they appear to be, essentially, the same faulting mechanism; plane orientations are as well similar, and not major differences are appreciable at first sight between the solutions of one or the other model. These findings suggest that, considering waveforms are the same, slight location differences result in also slight FM differences. As well, the default velocity model is probably well constrained for earthquakes in the area of study, as FMs are fundamentally the same when the Castor model is used.

5.3.2 Nodal plane orientation, dip and depth

Mostly, nodal planes for the calculated FMs can be grouped in two different families, one is NE-SW and the other is NW-SE to WNW-ESE (Figure 47). Frontera et al. (2013), IGN (2013), and Cesca et al. (2014), obtained similar orientations (compare Table 5 and Table 6). Given known faults in the area, NE and SE orientations could be equally possible. Both families show sub-vertical to steep fault planes, roughly ranging from 90 to 60 ° as illustrated in Figure 47.

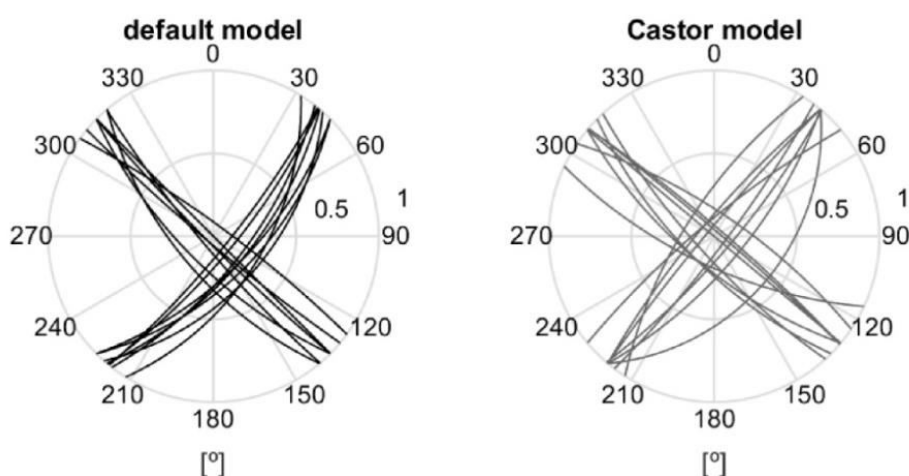


Figure 47: Cyclographic projections of nodal planes on a polar sphere. 0.5 and 1 indicate dips of 45 and 0° respectively.

A depth study is depicted in Figure 48 and Figure 49, which allows saying the following in regard to the studied dataset with FMNEAR's webservice:

- Obtained FMs' depths range from 3 to 8 km (except for one event at 11 km), and none of the two models used results in systematically higher or lower depth values.
- Input and output depths differ up to 7km, usually existing a difference smaller than 3 km.

- FMs would suggest vaguely deeper events than what was found during the earthquake location process. These results are supported by those in Gaité et al. (2016) but not by those in Cesca et al. (2014).

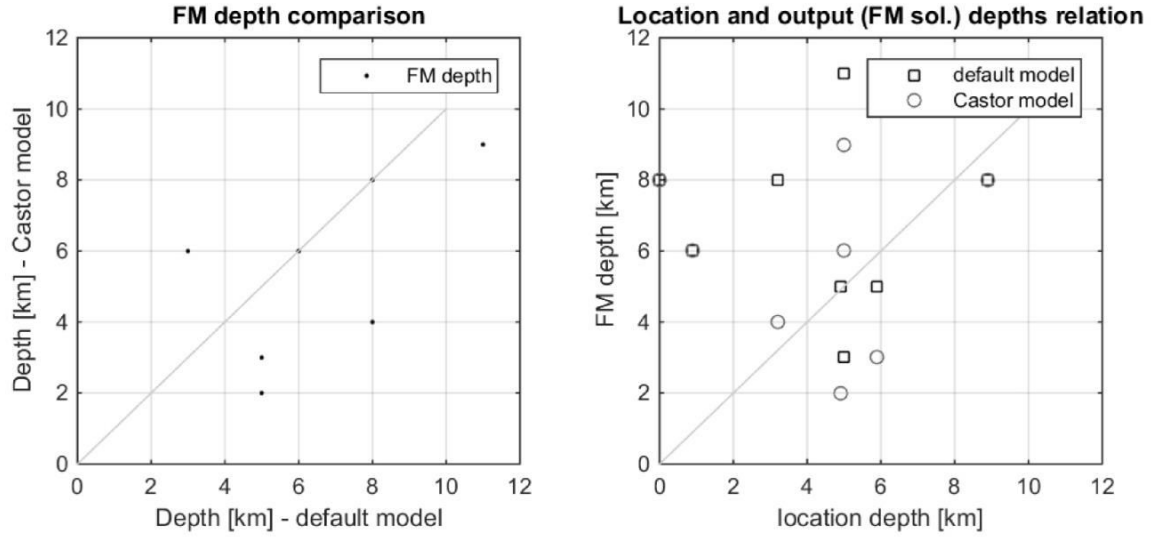


Figure 48: Left: FM solution depth for each of the 8 events, considering the default or the Castor model. Right: FM solution depth compared to input (location) depth.

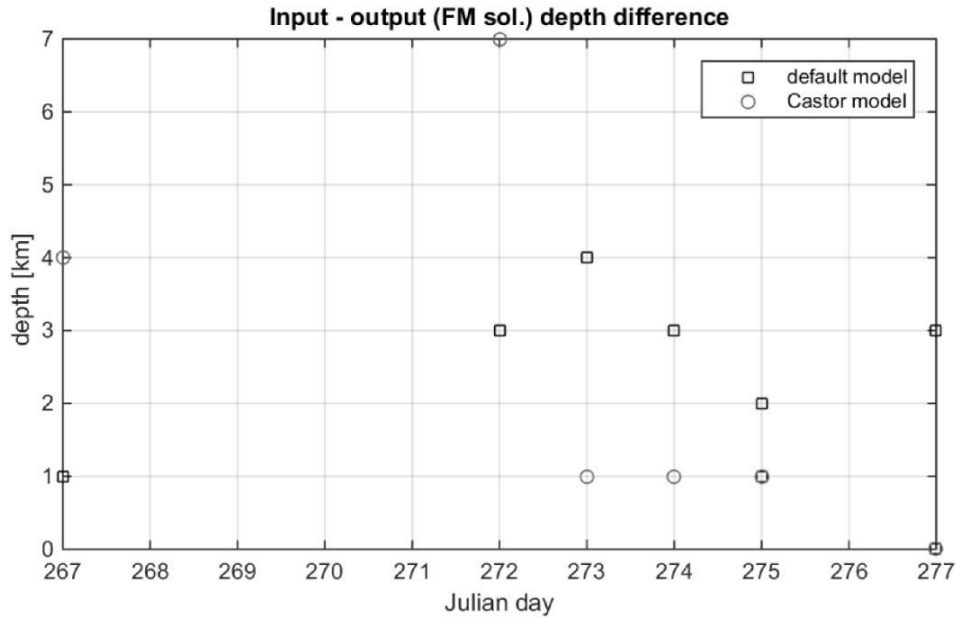


Figure 49: Depth difference between input (location) and output (FM).

5.3.3 Magnitudes

Figure 50 compares input M_L with output FM's M_w (magnitude values are always referred in the text as a number with one decimal, but they are computed with two decimals). It can be noted that FM's magnitude is usually of lower value than the input magnitude, although for events with $M_L < 3.9$ they are really similar. The maximum difference is of 0.2 units for the M_L 4.1 of October the 2nd, when the Castor model was used to calculate the FM. For the M_L range which is under study here (3.5 to 4.3), M_w should be almost equal to input M_L (Hanks and Kanamori, 1979; Kanamori, 1983), which accords to observations in Figure 50.

For this dataset, M_L and M_w can be related with the expressions (21) and (22), which were obtained using the default and Castor model solutions respectively. Differences are almost inexistent between the two.

$$M_w = 0.733M_L + 0.996 \quad (21)$$

$$M_w = 0.735M_L + 0.950 \quad (22)$$

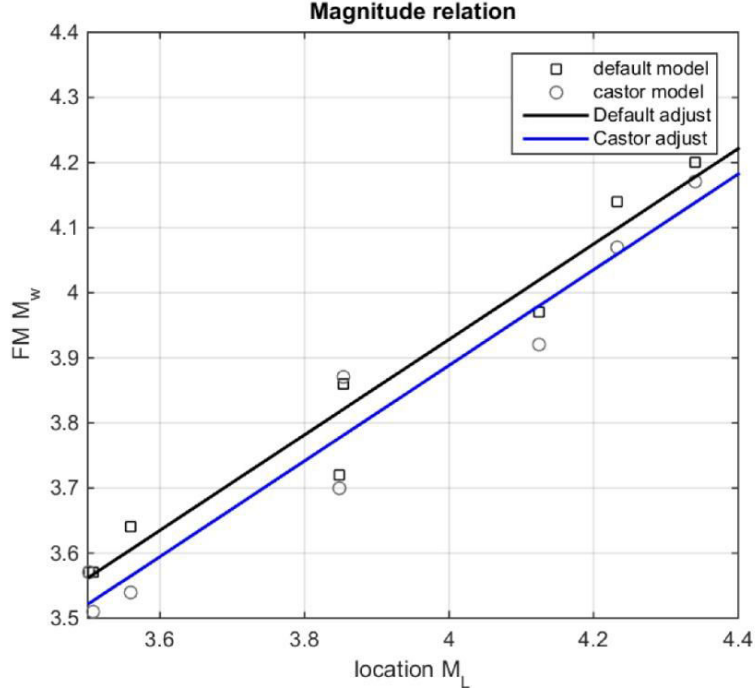


Figure 50: M_L - M_w comparison and adjust.

5.3.4 Quality assessment

When FMs are found using FMNEAR, the CI should be regarded as the most truthful indicator of its quality. At the same time, both the RMS and number of components are implemented in the CI calculation and it should be possible to find existing correlations between them. And, as the bigger the event the better the signal to noise ratio, it is also expected that higher CIs are obtained for the largest events of the sequence. This analysis is shown in Figure 51.

Considering that the RMS misfit is an intrinsic error evaluation parameter, it is logical to think that the CI, even if it comprises more factors, will be inversely related with RMS. Figure 51 (above) shows that this assumption is true on a general line as solutions with higher RMS have lower CI.

Magnitudes and number of components do not provide equally clear correlations. In Figure 51 (middle), even if the highest CI is achieved for one of the strongest events, the same can be said for the lowest CI. In fact, not even a dimly positive correlation can be observed for these solutions. As magnitude values and differences between the 8 events are small, it is acceptable that CI does not scale with magnitude.

Figure 51 (below) shows that not because there is an increase in the number of components used, should the CI be higher. The highest CIs are in fact acquired when a

relatively high number of components can be used and, at the same time, RMS is low and no solutions with similar RMS and distant FMs exist (explained in part 5.1.2). When a very high number of components is used, RMS increases and therefore CI cannot have super-high values, which explains why solutions using more than 25 components do not have the highest CI (this can be said for this dataset, but this value of 25 should not be extrapolated to other cases).

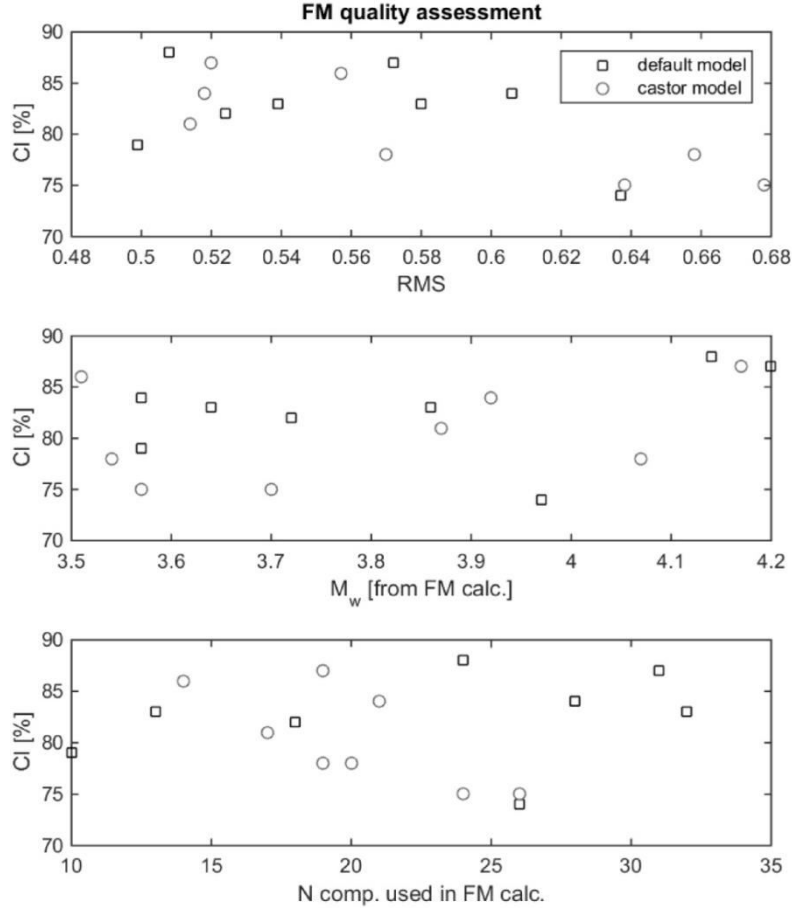


Figure 51: Quality analysis for solutions obtained using both models.

5.3.5 Model assessment

Up to here, results using one or the other model have been described and investigated together. From the quality assessment in the previous part, no clear differences are seen between them, which makes it difficult to state if the adapted (Castor) model was better than the default one. As a matter of fact, Figure 47 shows that even if orientations are the same, dipping direction is systematically the same for each of the two families when using the default model, but not when using the Castor model. As well, the process of changing input parameters in order to obtain a CI 70%+ solution proved more difficult for the Castor model.

As FMNEAR routine uses waveforms from all input stations and most of them are far from the Castor nearby coast, it is possible that using the Castor model is rather a disadvantage. Then, most reliable solutions would be those obtained with the "global" model. Nevertheless, as solutions are similar and this statement would require further study and time, both model solutions will be considered in the following part.

5.4 Discussion: Tectonic interpretation. Implications in relation to Castor's anthropogenic seismicity assumption

FMs solutions are contextualized in Figure 52. Locations are the same using one or the other velocity model, as location of the epicenter is an input parameter. However, input and output depths do not necessarily have to be equal, as it has been seen in 5.3.2. It is important to note that when the default model was used, solutions for most events indicated strike slip with some normal-dip slips (represented in blue in Figure 52 right); on the other hand, those for the Castor model are almost pure strike slip mechanisms (rakes really close to 0 or ± 180).

Solutions are at first sight a little discouraging, in the sense that all faults in the area are described as pure normal faults (e.g. Perea, 2006, Garcia-Mayordomo et al., 2012; IGME, 2013). However, solutions seem robust enough as all FMs solutions in previous studies had some strike-slip component, which could indicate relevant background stress changes in the quaternary. Essentially, solutions specify the activation of a NW-SE or NE-SW fault (see Figure 52 and Figure 53), and because both orientations are present in the area no immediate discrimination can be made. In Figure 53, note that as strike is shown and it depends on dipping direction, Castor model solutions have 4 different strikes instead of two (Compare with Figure 47). Nonetheless, if dips are taken into account both the Main and the Ampolla fault should be discarded, as they dip towards NW and obtained solutions indicate east dipping for the NE-SW oriented planes.

Supplementary information regarding plane dips is shown in Figure 54, which plots dip against FM depth. Although subvertical planes exist for all depths, the steepest ones correspond to the shallowest FMs (ellipse in the figure) and the less inclined ones (55 to 65 °) do not exist for solutions shallower than 5 km. This could accord with the described listric morphologies as in IGME (2013); however, values indicate remarkably steeper planes, and the tendency is not very clear.

The fact that most of the events occur with a similar mechanism could be representative of the activation of the same fault plane repeatedly or various planes with similar orientations. This is the case for the Montsia fault system (W2, W3, W7), which accords both in orientation and dip direction to the systematically repeated plane of roughly 135/70-80 SW, although they would not be that steep according to descriptions. The other possible fault plane, striking to the NE, is less steep (40-50°). Cesca et al. (2014), obtained remarkably lower dips for this NE oriented family, and stated that they could agree with a fault identified by Seeman et al. (1990), roughly parallel to the sedimentary stratification near the reservoir (see Figure 8 in chapter 3). In Figure 52, this fault could agree with the East 4 fault strand, according to Geostock's (2010), nomenclature.

In case it were one of the known ones, the activated fault(s) should have been one of the two previously described families; as well, the fact that the Main Fault would not have been activated is confirmed. However, the precise identity of the hosting fault(s) remains unknown.

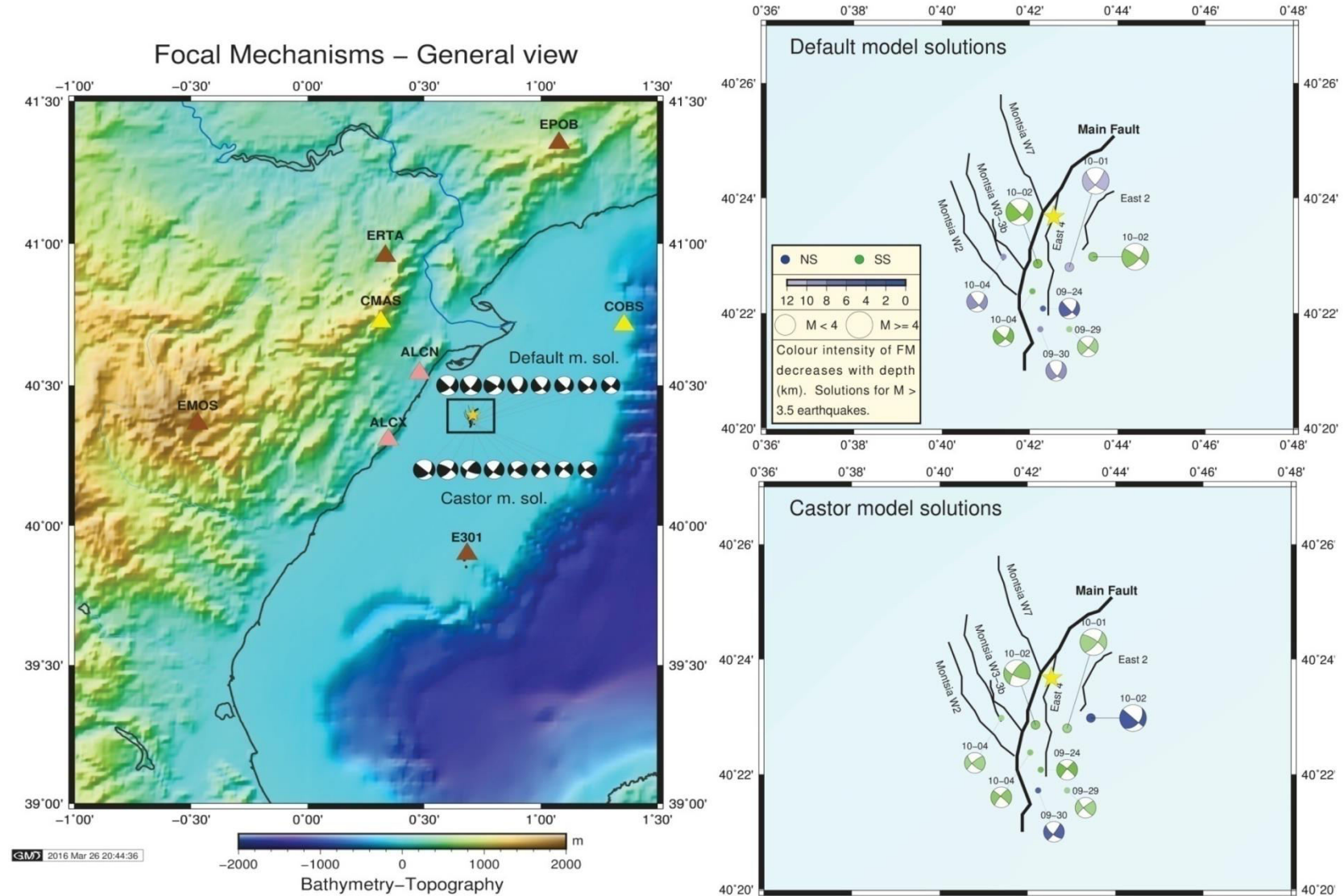


Figure 52: Left: General map of the area with FM solutions. Seismic station colors accord to Figure 16 (chapter4). The black rectangle shows the rough zoomed area. Right: Solutions using the default or Castor model in a detailed map of the Amposta E fault system, plotted near reservoir top depth. The yellow star represents the Castor Platform. In the legend, NS (Normal-Strike slip) is used for those solutions whose rake indicates relevant normal component, whereas SS is used for the others (strike slip).

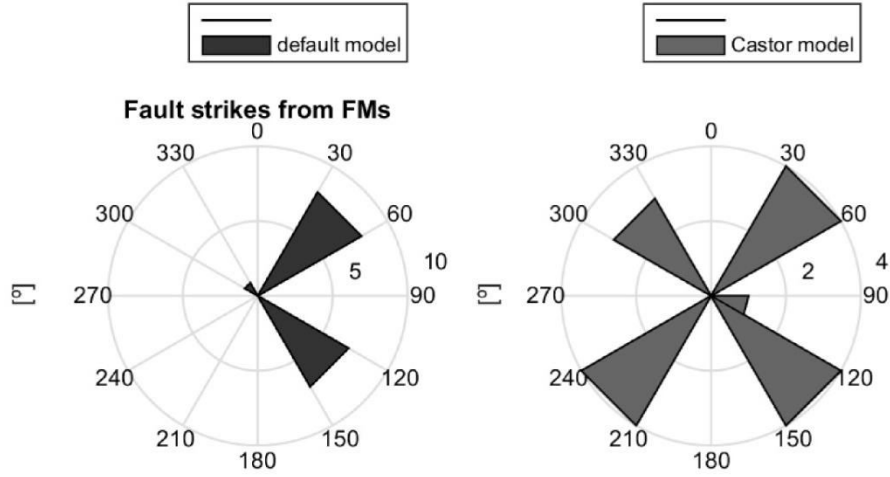


Figure 53: Rose diagram highlighting nodal plane orientations.

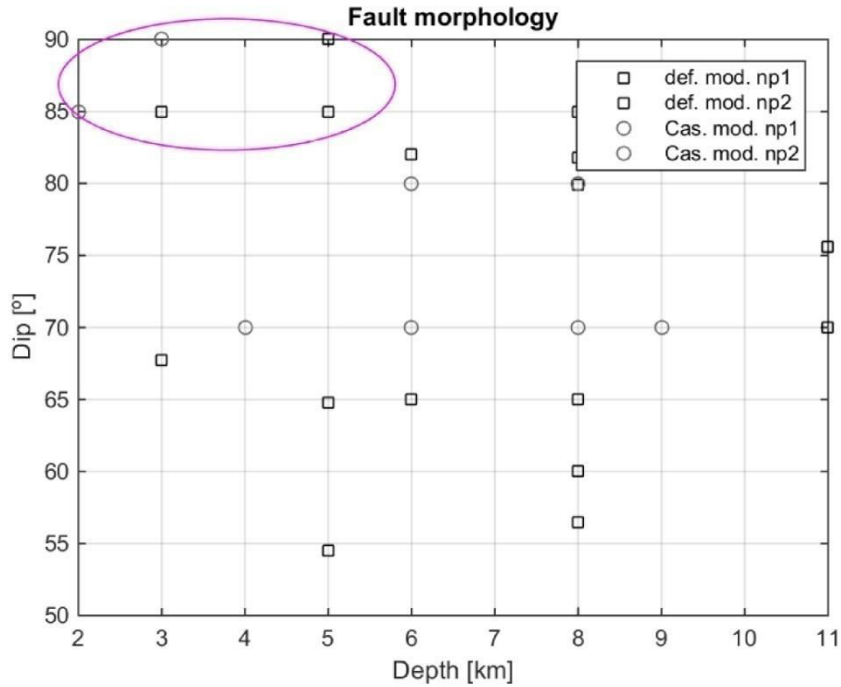


Figure 54: Dip and depth of each FM (note that for each FM there are two different nodal planes). The ellipse highlights the steepest planes.

FMs and injection-derived seismicity

Up to now, it has been seen that earthquakes agreed in space and time with the last injection phase. However, FM solutions suggest deeper events than what was expected, although it is true that depth is subjected to bigger imprecision and the studied events are shallow. Then, found fault planes could agree with those existing in the area and two main scenarios open up (The Castor fault in IGME, 2013, is not considered because of the reasons explained in 4.4.1). First, the rupture of a steep NW-SE oriented fault(s), and second, the activation of a low dipping NE-SW structure(s). The problem is that knowing which is the one that *actually* happened cannot be said here, and the fact that (some) events could have happened on deeper unknown faults should be taken into account as well.

Another difficulty is that recognizing how rupture differed from previous natural earthquakes in the area is not attainable, as no available FMs are found in the IGN Moment Tensor Catalog. The fact that solutions have a predominant strike-slip component (and considering that these solutions are correct on a general context after the comparison with previous studies) makes it possible that one or more of the following conditions are met:

1. The described normal faults in the area are no longer behaving as pure normal faults, due to regional stress state.
2. Other faults, or further fault traces are present in the area (most likely), and they hosted part of the earthquakes (unknown).
3. Injections altered stress conditions on local areas in fault planes and slip took place with a different direction of what would be expected given faults' nature in the area. Or, injections altered stress conditions on local areas in fault planes and slip took place because of this modification, but according to governing stress.

Condition 1 can be explored via the World Stress Map (Heidbach et al., 2008), which shows a direction of maximum horizontal stress (S_H) about 10° NNE (plate is under oblique collision in the northwestern Mediterranean area), and both normal and strike slip faulting regimes appear at a certain distance from the Castor platform (e.g. Schindler et al., 1998). Cesca et al. (2014), assumed a least compressive stress (S_h) striking 100° and an intermediate vertical stress (S_v). This stress regime ($S_H > S_v > S_h$) gives as a result strike-slip ruptures, which makes it logical to think that, even if faults are described as normal based on seismic profile interpretation, they will now slip according to governing stress.

Condition 2 should always be considered as there is no security that the geological model of the area represents reality. It could be aggravated here because this study did not have the best sources of information regarding geology. But, as matters stand today and based on available literature, it could also be possible that geological complexity was underestimated in the Castor UGS project.

Condition 3 takes into account the induced seismicity assumption. Two main processes can be considered here, as causative mechanisms of earthquakes by injection. The first is hydraulic fracturing, which takes place when the tensile strength of the rock is surpassed. For this to happen, fluid pressure has to reach the value of the S_{min} , and when such conditions are met, new fractures can open. Because of the Castor UGS' emplacement (reservoir with an active water drive), and accounting for maximum overpressure values, which never exceeded 0.8 MPa (the maximum secure threshold would have been set at 4.9 MPa, as stated by IIE, 2013), this does not seem possible.

Another issue in relation to condition 3 is the pore pressure change. Even if it were not high enough to open new fractures, the increase in fluid pressure would have diminished shear strength on hydraulically connected faults. As reported by Cesca et al. (2014), this kind of mechanism, controlled by fluid diffusion, should expand outwards with time, something that was not observed (see chapter 4); Also, this process is usually slow (various days), and earthquakes that take place just after the injection at various kilometers of distance cannot be controlled by it. But the fact that rupture takes place according to governing stress (regional stress), as fluid pressure change modifies fault's shear strength, but not the shear stress acting on it, and that this process can be combined

with other earthquake triggering effects, such as previous earthquakes, would fit with observations (triggered seismicity). Thus, pore pressure increase is most likely to have partially influenced seismicity.

After what has been seen, it seems that fluid injection would, at least, have helped seismicity develop, even if it was not the main cause and/or the strongest events were no longer caused by activity within the reservoir. In order to properly state up to which level seismicity was influenced by injections, modeling of stress perturbation should be carried out, as it was previously indicated. Even if it does not seem very probable, the possibility that seismicity was natural or rather triggered because of solid stresses which were already present before the UGS activity (for example from the exploitation of the Amposta field when it was producing oil) cannot be excluded. Further discussion forthcoming in the next chapters.

6. STATISTIC ANALYSIS OF SEISMICITY: THE FREQUENCY-MAGNITUDE RELATION

This chapter focuses on providing further insight on the evolution of seismicity. The Gutenberg-Richter law (GR law), also called Frequency-Magnitude Relation (FMR), is probably the most complete option to display earthquake occurrences (e.g. McGuire, 2004). The law was first proposed by Ishimoto and Iida (1939), and Gutenberg and Richter (1944), and it notes (Equation (23)):

$$\log_{10} N(M) = a - bM \quad (23)$$

M is a determinate magnitude value, and a and b are constants for a determinate dataset. The first is referred to the total seismicity of an area, while b indicates the (negative) slope of the curve, and therefore the relationship between large M events and small M events. Then, N is the expected number of events of at least magnitude M , for the time frame of the dataset. Usually the result is given in N events per year.

6.1 Method

6.1.1 GR law determination

Using the logarithm relationship in Equation (24), Equation (23) can be re-written as in Equation (25). Even if that expression is perhaps less known, it is probably more used in topics such as seismic hazard analysis. It is introduced here as both λ and β will be used hereafter.

$$\log_{10} x = \frac{\ln(x)}{\ln(10)} \quad (24)$$

$$N(M) = e^{(\delta - \beta M)} = \lambda e^{-\beta M} \quad (25)$$

Where:

$$\delta = \ln(10) a$$

$$\beta = \ln(10) b$$

$$\lambda = 10^a \quad \text{Total activity rate (number of } M \geq 0 \text{ earthquakes per time unit)}$$

Truncated FMR

In the application of the FMR, there are two implicit aspects that should be recalled. Firstly, events are independent (this requires a catalog which has been cleaned of repeated events, aftershocks, earthquakes of different origin, etc). And secondly, the seismic network cannot detect all earthquakes; hence, a minimum magnitude (Magnitude of Completeness, M_c or M_0) has to be defined (e.g. Palacios et al., 2006), as a lower limit above which all events should have been recorded.

The value of the M_c depends on the characteristics and distribution of the available seismic network, and will vary from one location to another. In this study, the approach to

determine M_0 follows the maximum-curvature (MAXC) method described in Wiemer and Wyss (2000). Briefly, it consists in defining the point of maximum curvature by means of the maximum value of the first derivative of the FMR curve. As indicated by Woessner and Wiemer (2005), the procedure is equal to the magnitude bin with higher number of events in the non-cumulative FMR.

Then, for a lower bound, Equation (25) becomes Equation (26):

$$N(M) = \lambda_0 e^{-\beta(M-M_0)} \quad (26)$$

Where:

$$\begin{aligned} \lambda_0 &= 10^a && \text{Activity rate (number of } M \geq M_0 \text{ earthquakes per time unit)} \\ e^{-\beta(M-M_0)} &= G(M) && \text{Complementary cumulative function} \end{aligned}$$

And the Probability Density Function (PDF), of the $G(M)$, which will be used later and is usually expressed as $f(x)$, is noted in Equation (27):

$$f(M) = \int_{M_0}^{\infty} G(M) dM = \beta e^{-\beta(M-M_0)} \quad (27)$$

To the fact of an existing M_c , one has to add that for most seismic studies, it is felt that the seismotectonic area of analysis cannot generate magnitudes above M_{\max} (the maximum magnitude on the earthquake catalog), and because of that an upper truncation needs to be introduced. The simplest way to incorporate the upper bound is truncating and renormalizing the PDF, and then Equation (26) can be rewritten as Equation (28):

$$N(M) = \lambda_0 [1 - k + k e^{-\beta(M-M_0)}] \quad (28)$$

Where:

$$\begin{aligned} k &= [1 - e^{-\beta(M-M_0)}]^{-1} \\ M_0 &\leq M \leq M_{\max} \end{aligned}$$

Equation (28) expresses the double-truncated FMR in a seismic source. Some authors have suggested truncating the Cumulative Distribution Function (CDF) instead of the normalized PDF, but in general, the approach described in the previous equations is the applied one (see McGuire, 2004, for further details).

Fitting the FMR

In order to properly fit the truncated FMR various methods can be applied. The first option arising, as it is computationally fast and simple, is a regression analysis using the Least Squares method (LSE). However, the following inconveniences when using a regression analysis (LSE) have been cited in literature so as to avoid using it (e.g. Felzer, 2006; McGuire, 2004):

- Disrupts the fact of independent observations (lower magnitude events should not be influenced by earthquakes observed at higher magnitudes).
- Observations do not follow a Gaussian distribution (as it is assumed in the LSE), but Poissonian.
- LSE is excessively influenced by the largest earthquakes, and assumes that the error on each datapoint is equal.

Because of that, it is most recommended to use Maximum Likelihood Estimation method (MLE) in order to approximate λ_0 and β , as recommended by the previously cited references. Next, a brief overview of the method in order to obtain an expression which allows the estimation will be presented. The text is based on Myung (2002), McGuire (2004), and Zivot (2009). The reader is nevertheless referred to Casella and Berger (2002), or DeGroot and Schervish (2011), for additional consistency on the subject.

For a set of values of a certain parameter, the PDF shows that some function values are more probable than others. In other words, the PDF (shown in Equation (27) regarding the lower-truncated FMR) provides information on which values are more likely to be obtained given a certain defined parameters. In our case however, accounting for a determinate earthquake catalog, the inverse problem needs to be solved. The function values are known (number of earthquakes in each magnitude range, $N_i(M)$), and the function parameters (β, λ_0) need to be found, considering a sample of n values (number of magnitude subsets).

Let N_1, \dots, N_n be a determinate sample with a PDF expressed as $f(N_i|\omega)$, where ω is a $(k \times 1)$ vector of parameters (in our case $k = 2$). In order to solve the inverse problem, the likelihood function can be defined if the roles of the data vector N and parameter vector ω are reversed (Equation (29)):

$$L(\omega|N) = f(N|\omega) \quad (29)$$

Thus, the likelihood function expresses the unnormalized probability of a parameter vector, given a certain dataset. Knowing that the Joint Density (JD) of the trial can be expressed as the product of the marginal densities (Equation (30)):

$$f(N_1, \dots, N_n|\omega) = f(N_1|\omega) \cdot \dots \cdot f(N_n|\omega) = \prod_{i=1}^n f(N_i|\omega) \quad (30)$$

Which, considering that N values are discrete random variables, results immediately in Equation (31), after the definition given in (29):

$$L(\omega|N) = \prod_{i=1}^n f(N_i|\omega) \quad (31)$$

Therefore, for the case of study, and taking into account Equation (27) which is the non-upper-bounded $G(M)$'s PDF (in most cases it is sufficient to work with this one, as it will be indicated afterwards), the likelihood function for β will be given by Equation (32):

$$L(\beta|N) = \prod_{i=1}^n \beta e^{-\beta(M_i - M_0)} \quad (32)$$

If Equation (32) is maximized as in Equation (33), then solving for β gives the expression in (34):

$$\frac{d[L(\beta)]}{d\beta} = 0 \quad (33)$$

$$\beta = (\bar{M} - M_0)^{-1} \quad (34)$$

This simple expression allows obtaining β in a very straightforward way. If the upper-bound magnitude (M_{\max}) is considered, then the expression for β needs to be solved iteratively (35). This expression is obtained with the same procedure as shown in (32) to (34), but with the pertinent double-truncated expression. However, for the earthquake catalog of study (and most cases), M_{\max} is more than 2 units the value of M_0 ; then, solution in (34) gives practically the same value as if the upper bound expression for β is solved (Equation (35))

$$\frac{1}{\beta} = \bar{M} - M_0 + \frac{(M_{\max} - M_0)e^{-\beta(M_{\max} - M_0)}}{1 - e^{-\beta(M_{\max} - M_0)}} \quad (35)$$

On the other hand, the maximum likelihood function for λ_0 (activity rate) is shown in equation (36). A Poissonian distribution of earthquakes is assumed (successive events are independent in time), for z existing events during a time t . And when equation (36) is maximized, as in (33) but now with respect to λ , the result in equation (37) is obtained.

$$L(\lambda_0|z) = \frac{(\lambda_0 t)^z e^{-\lambda_0 t}}{z!} \quad (36)$$

$$\lambda_0 = z \cdot t^{-1} \quad (37)$$

It is seen that, with Equation (34) and (37), obtaining the FMR is quite simple. The difficulty lays in achieving a complete earthquake catalog and sampling the total number of events over a high enough number of bins (small magnitude range of each subset).

For this study, in which the interest was also on the method itself, both the LSE and MLE were tested, and their differences will be presented in the results.

6.1.2 b value evaluation on the context of induced seismicity

This approach found its motivation in the paper by Eaton and Maghsoudi (2015), and was applied with the goal of obtaining further insight on the topic of the FMR and its time evolution. The outcome can be read in part 6.5.

Introduction

GR law calculations of earthquake catalogs related to Hydraulic Fracture (HF) operations (usual procedure to enhance permeability in wells, during Enhanced Geothermal System, EGS, development or advanced oil recovery among others) have resulted in systematically higher b values, which are close to 2 (e.g. Oates et al., 2013), than the estimated for most active fault systems (0.7 to 1.2).

Eaton and Maghsoudi (2015), explore various causes which may be responsible for the larger b values of such catalogues. They consider incorrectly scaling of the instrument's response, incomplete catalogues, superposition of two or more distinct populations (different b values), magnitude saturation due to instrumentation and FMR revealing preferred scaling.

As noted before, the possibility that the full catalogue contains microseismic²¹ magnitudes which are scale-variant is explored, as it is already suggested by Kagan (2010), in his tapered GR distribution. The question is that microseismic FMRs could reflect

²¹Microseismic events are generally regarded in the literature as those with $M \leq 2$.

observations near the maximum potential magnitude that can be produced by the hosting phenomenon, but no further. Then, a reduction of the parameter to values close to unity could account for changes from a scale-dependant brittle deformation process to the activation of scale-invariant faults (for the considered spatial scales).

Despite the fact that the b parameter might not be the best choice for characterizing magnitude distributions in certain cases (e.g. small size of microseismic catalogues), the study concludes that:

- Indeed, higher b values in microseismic catalogues could be linked with fundamental differences of rupture behavior in HF processes and natural fault activations, resulting in different scaling characteristics.
- The high $\sim 2b$ values, together with observations of negative deviation of the cumulative GR-law from the FMR's line of best fit, show evidences that when dealing with microseismic magnitudes, seismic moments are not scale-invariant.
- The abrupt drop in the b parameter to expected values for active fault systems (close to unity) would represent fault activation.

Accounting for Castor's case (mostly broadband seismic stations and no remarkably-high proportion of micro-earthquakes, as all of them which were detected have $M > 0$), and supposing a complete enough catalog (more than 200 events, see part 6.2, which is the minimum estimated in the article to obtain trustworthy estimates), the FMR scaling is revealed as the most likely cause for such difference (provided it exists) in the named b values.

Next, the FMR relationship variation (with focus on the b parameter) will be studied for Castor's earthquakes. The reader should nevertheless note that the author has no information regarding if (due to the stated high permeability) and/or how the wells were stimulated, but it has already been acknowledged that no HF took place in the area. In addition, studies such as Eaton and Maghsoudi (2015), are usually referred to really clustered events (hundreds of meters) which have been located with site surface and downhole sensors. Surely, the total amount of earthquakes in the Castor reservoir neighboring was much higher than the acquired catalogue (closest station being ALCX at an epicentral distance of 20-30 km for most of the events).

Implementation of the method

Time-variance of the FMR is computed using the LSE as explained in 6.1.1, using a moving window containing 100 events. The overlap with the previous window when it is shifted is 50 %. It starts at $t = 0$ (day of the first earthquake of the catalog) including the first 100 events and then it is slid until the last 100 events are comprised. The b parameter evolution is studied taking into account the standard error interval. In this case, the decision of using less than 200 events on each computation was almost forced due to the total amount of earthquakes in the catalog (see 6.2).

6.2 Earthquake catalog

The catalog to fit the FMR comprises events from September 5th to October 29th, and it is available via the IGN web (see annex G). All events from the minimum to the maximum magnitude recorded are of interest, and the area of study ranged from latitudes 40.2 to 40.6 °N and longitudes 0.5 to 0.9 °E. As really small magnitude values are present (below M_L 1.5), the area chosen in chapter 4 was readjusted to the reservoir surroundings to avoid including events which had no relation with the UGS seismicity.

Finally, the catalog includes a total of 548 seismic events, with a minimum magnitude of M_L 0.7. All magnitudes reported are M_L , except for 5 of the main events, whose magnitudes are reported in M_w . No conversion was applied to that 5 values as their differences are expected to be minor in the magnitude range between 3.5 and 4.2, and the FMR fitting has been applied supposing all magnitudes are M_L . The decision not to convert all values to M_w is taken in order to avoid introducing larger error.

6.3 Natural seismicity in the area

The area's natural seismicity is low (IGN, 2013), being one of the less active in the Iberian peninsula (Figure 55). The Castor UGS is placed in the north-western zone 27, for which the relative hazard is qualified to be low by IGME (2015), although it is noted that homogeneity and size of the dataset are scarce. The assumed b value for natural seismicity is 0.89 (IGN-UPM, 2013), but it is indicated that it could not be computed due to insufficient data and the b parameter reported is that of the northern zone 23.

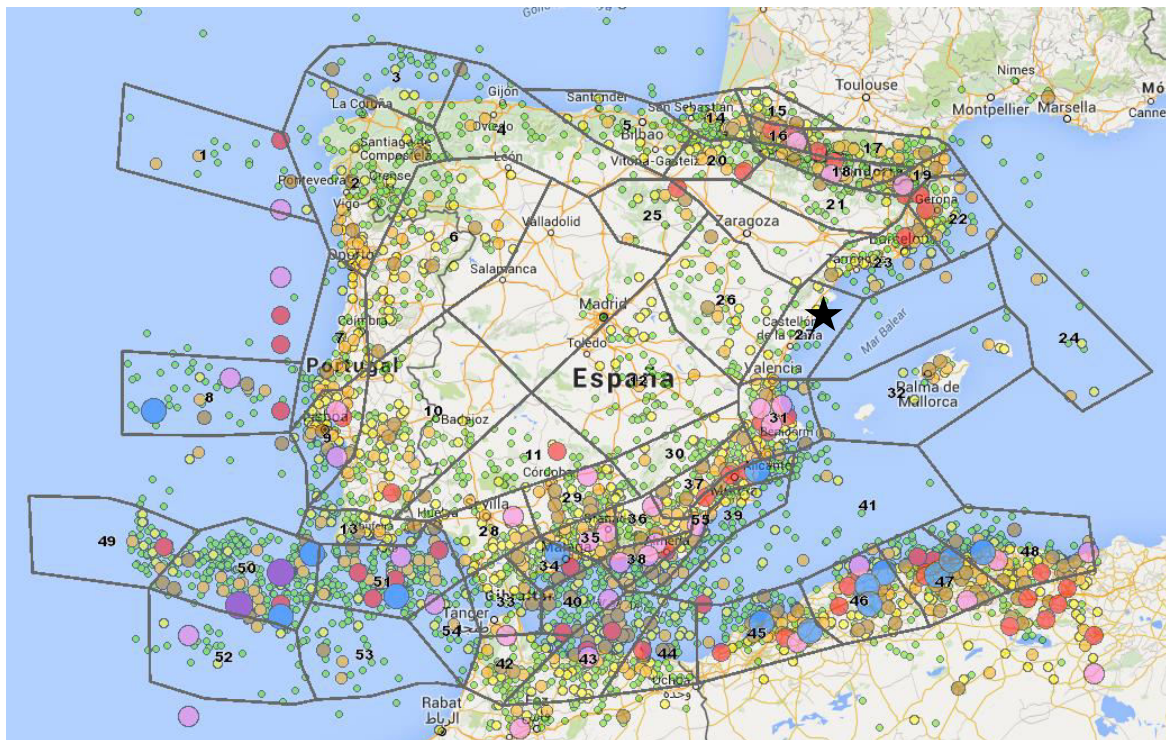


Figure 55: Seismogenic zonation of the Iberian peninsula and its seismicity. The black star shows the platform location. Modified from the ZESIS database (IGME, 2015b).

6.4 Results

Fitting results can be observed in Table 7 and Figure 56. The value of the a parameter is of little interest here as it only refers to the productivity, and therefore attention is paid to the other parameter, b . Magnitude bins were created each 0.25 magnitude units, using the magnitude value in the middle to represent them (e.g. in between M 1.75 and 2.0, 1.875 was used).

The strict M_c via the MAXC estimation was 1.875, although the value used to fit the FMR was M_c 2.125 (maximum frequency bin + 1). The decision was taken to avoid underestimation (see Woessner and Wiemer, 2005), which could account for obtained fitting results being more reasonable with the indicated higher value. The M_c using IGN's catalogue had previously been estimated to be around 2 in this zone (Gonzalez, in preparation). Standard deviations (Table 7) are only provided in the case of the LSE fit, as for the MLE the parameters were calculated analytically from expressions (34) and (37), and no standard errors were obtained.

Table 7: Values of the b parameter of the GR law and differences according to analysis group and method used. The standard deviation is also indicated for the LSE case.

FMR fit	Whole sequence		Phase 1		Phase 2	
	LSE	MLE	LSE	MLE	LSE	MLE
b	1.06 ± 0.055	0.95	1.61 ± 0.067	1.55	0.94 ± 0.056	0.87

Regarding the b parameter, it is about 0.05 - 0.1 units smaller when using the MLE, thus it can be said that the differences are minimum. The obtained values are really close to those already reported by Cesca et al. (2014), though their catalogue was that of the Ebre Observatory, which contained almost twice the events. It can be seen that the b value is about 1.0 for the whole sequence. However, when events are separated into those occurring during injections (until September 17th) and afterwards, a remarkable difference exists, as it drops from 1.55 to 0.87 (really close to what is expected for natural seismicity in the area).

As seen in Figure 56 (right), the adjust for the second phase of the sequence underestimates the frequencies for events with magnitudes greater than 3.5. Something similar can be said for the adjust of the whole sequence, which takes into account the strongest events as well (Figure 56, left). A similar observation led to the development of the characteristic earthquake theory, which suggests that faults tend to generate essentially the same maximum size events with a fairly narrow range near that maximum; it directly implies that a linear extrapolation of the GR law from smaller magnitudes underestimates the occurrence of great (characteristic) events (Schwartz et al., 1981; Schwartz and Coppersmith, 1984).

As well, the drop in the b value (from phase 1 to phase 2) coincides with an important increase in the seismic moment release (Figure 57). A change in the b parameter has been related to a (potential) change in stresses, or in the dominant focal mechanism (Schorlemmer et al., 2005), and to fault activation (Maxwell et al., 2010); recently, it was noted that it could be indicating a change from brittle deformation processes which are scale dependent to the activation of an essentially scale invariant slip system (Eaton and Maghsoudi, 2015). It should be taken into account that the named scale invariant fracture

does not consider the characteristic earthquake hypothesis (based on which the linear relationship would be lost again near the maximum magnitude). This is logical regarding induced events, which are assumed to be far from the fault potential maximum. Their implications on this case will be discussed next.

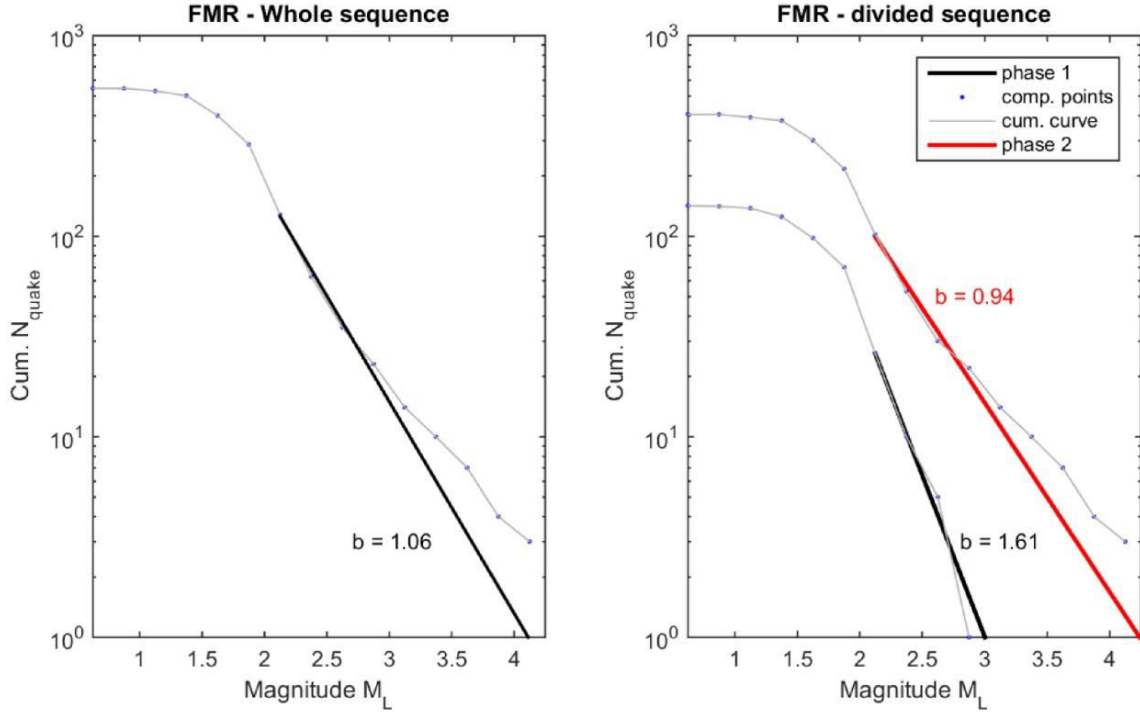


Figure 56: Cumulative FMR. Blue dots and grey lines show the observed distribution, while the black and red lines indicate the fit (LSE) to the GR distribution and the value of the b parameter. On the right panel, the sequence is divided between the events up to the last day of injections (phase 1), and events afterwards (phase 2).

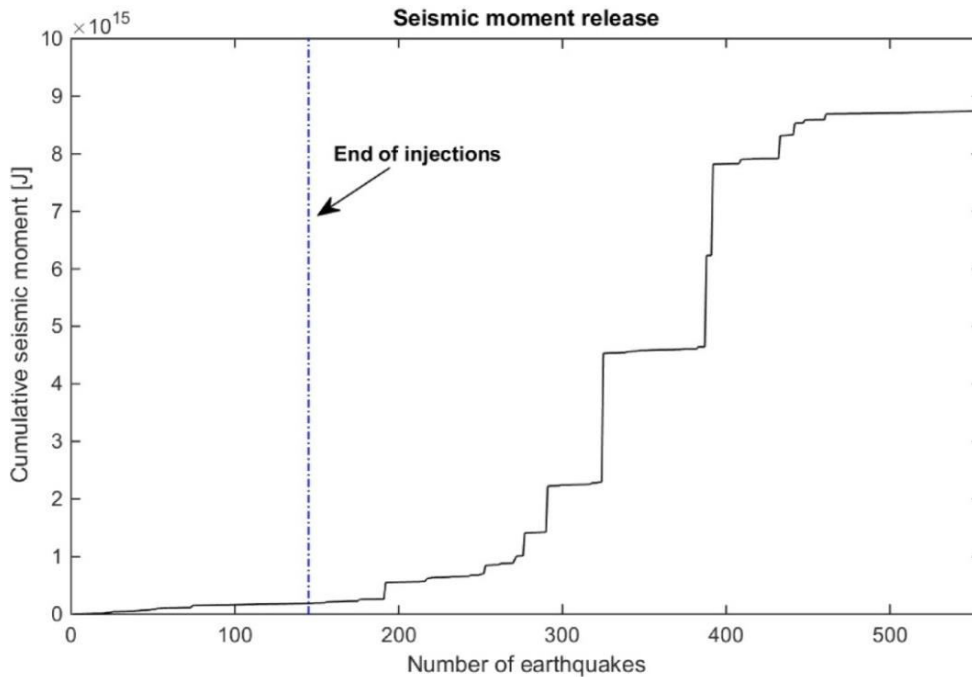


Figure 57: Cumulative seismic moment release of the earthquakes, as obtained from the IGN catalogue.

6.5 Discussion: FMR and the b parameter. Implications for the anthropogenic seismicity assumption

Further insight on the variation of the b parameter is presented in Figure 58. At least two drops are observed, which could be related to the phenomena noted before. Analysis from FMs provides information which allows stating that faulting type associated with the main shakes did not change in between September 24th and October 4th, but no other FM have been computed outside that time span. Therefore, information regarding the slip type before September 24th remains unidentified.

Some significant stress changes could have been introduced in the unknown faults where the earthquakes took place, allegedly during injection activity. Note that the term "significant", does not necessarily mean large on a global scale, just large enough to change equilibrium conditions on a fault (further information coming up on next chapter). The first drop shown in Figure 58 is probably related to the main causing faults' activation (note dates, and compare with values obtained in Figure 56), and clearly different in nature to the prior events, whose fitting returned much higher b values (higher than what should be expected for natural tectonic activity, roughly from 0.7-1.2); but, values are as well below what is usually observed in induced seismicity monitoring (e.g. during HF activities), which revolves around 2. As well, magnitudes were larger than those monitored in controlled HF operations ($M_L 2.9$ was already detected on September 13th).

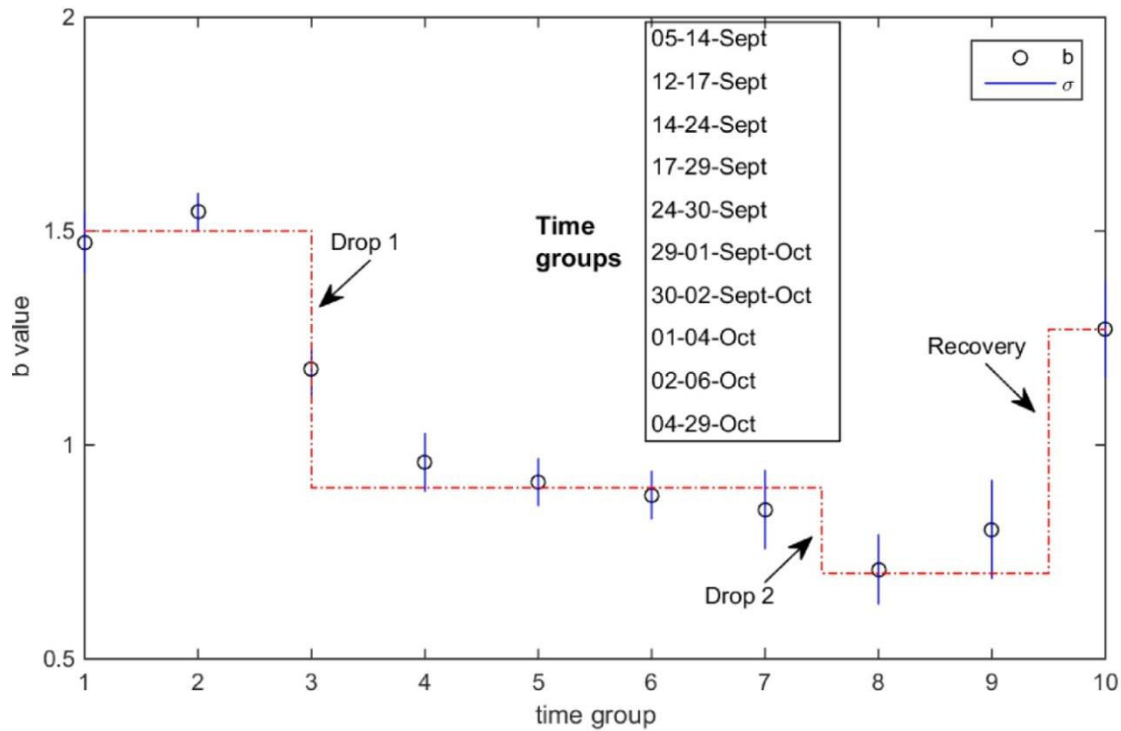


Figure 58: Moving-window calculation of b parameter for the studied catalog, divided according to indications in the figure. The central b value and standard deviations are shown according to indications, as obtained using the LSE. The red discontinuous line represents the tempting interpretation, with two significant drops. In between groups 2 (September 12th to 17th) and 4 (September 17th to 29th) the parameter value falls from 1.55 to 0.95, whereas between 7 (September 30th to October 2nd) and 8 (October 2nd to 4th) changes from 0.85 to 0.7.

On the other hand, the second drop is more diffuse and achieved after a progressive diminution when the moving-window calculation of the parameter is carried out. A possible explanation for this decrease of the b parameter is an increase in the differential stress as the end of the seismic cycle approaches (Smith, 1981; Lei et al., 2004), as the b parameter has already been referred to as an inverse stressmeter of the crust (Schorlemmer et al., 2005). That second drop, either sudden as pictured in Figure 58, or progressive (following the tendency from time group 4), reaches the lowest value of this series at the precise time window which comprises the greatest seismic moment release (October 1st to 4th), so it accords with the hypothesis explained earlier in this paragraph. As well, it would be consistent when the characteristic earthquake hypothesis is taken into account.

Based on the discussion above, the following evolution of the b parameter and its motives are proposed:

1. Seismic activity composed mostly of microseisms is initiated, after a perturbation unbalances the system. A particular fault(s) yield to small shear over stresses in a recurrent way, which means high productivity with few earthquakes above M 2 (high b value).
2. The equilibrium on some larger fracture system is removed, as a consequence of various unidentified triggers. This activation produces larger earthquakes and accounts for the observed drop in the b parameter.
3. The b value falls progressively towards the end of the seismic cycle, possibly as a result of higher differential stresses on the earthquake-causative structures, thus indicating that the main dynamic fracture is about to take place. In this case the limit would be at b around 0.8.
4. The foremost moment release is produced, when the b parameter reaches its lowest values. Hence, the frequency of occurrence of the main event would be underestimated if a linear relationship of the GR law is assumed after the first stress drop.
5. Once seismic cycle is restarted (lower differential stresses at its beginning), the b value returns to a higher value found to be slightly higher than 1. It accords with expected values in normal or strike-slip faulting regimes (Schorlemmer et al., 2005), although it is higher than the value reported for natural seismicity in the area.

The performed retrospective analysis provides new evidence as to why real time monitoring of the statistical behavior of seismicity, and particularly of the b parameter, could indeed be a powerful tool to estimate geo-hazard proximity when dealing with seismicity inducing activities (e.g. Eaton and Maghsoudi, 2015).

The unavoidable question that follows is what happens with the induced (by the gas injections) seismicity assumption. It had been pointed out before in literature (e.g. ICGC, 2013; IGME, 2013; Cesca et al., 2014; Gonzalez, 2014) that the first phase was probably induced seismicity. Given the results in Figure 56 and Figure 58, as well as the time history evolution of seismicity, which rapidly decreased the days following the halt in injections (chapter 4), it is the easiest conclusion to reach. Up to date, no natural seismicity with these b values has been reported. As well, the responsible phenomena for the strongest

earthquakes, after seismic activity reactivated, seem to be different. Yet, the b value for the first phase is clearly lower than what has been reported for induced events in HF experiments, and some moderate events (up to $M \sim 3$) had already occurred before injections stopped. Thus, characterizing the first phase might not be as straightforward.

Moreover, while the GR law allows for characterizing seismicity, it does not give proof in relation to the role played by the responsible perturbation(s). The concern being on the second phase of the seismic sequence (as it has been seen that relatively small perturbations can trigger large earthquakes), it should be investigated up to which point the man-introduced triggers (mainly fluid overpressures and stress changes due to the supposedly induced earthquakes) could have caused the tremors. The study should be focused in calculating injection fluid pressures as well as their diffusion through connected networks and rock matrix. At least, the stress change due to shear deformation caused by the previous earthquakes ought to be added to the analysis; the sum can be done by computing Coulomb stress changes on planes of interest, and analysis of variation of recurrence times of characteristic earthquakes (Baisch et al., 2009).

On the subject of fluid overpressures and with tensile fracture being discarded, the key aspect is the transmission of these pressures, as low values can already destabilize faults. This involves knowing hydraulic connectivity along the whole fracture network, and was not attempted here. Chapter 7 will explore the case regarding static stress transfer due to the 8 main events; the previous earthquakes (at least hundreds, with $M < 3.5$) are not taken into account due to the inability to associate them to a precise fault plane (see chapter 4).

7. EARTHQUAKE STATIC STRESS TRANSFER

The theory of self-organized criticality (e.g. Bak and Tang, 1989), presupposes that all areas in the brittle crust are stressed near failure levels. In this context, and as introduced in chapter 2, earthquakes can trigger other seismic events (e.g. King et al., 1994; Hardebeck et al., 1998; Steacy et al., 2005; TNO, 2014), even if the perturbation is small. Static earthquake triggering can be understood as the result of a fault slip which translates into strain in the neighboring regions. Due to medium confinement, the consequence is a stress perturbation which can bring other faults to slip conditions; in other words, the seismic cycle may be accelerated.

In this chapter, the author assumes that the reader is familiar with an engineering comprehension of stress and strain. These two concepts are essential when dealing with engineering problems involving changing conditions in the studied medium due to some introduced perturbation. The advantages of working with an elastic assumption remain on its simplicity; particularly, the linearity of the relations allows a much simpler conceptual understanding of the process and obtained results.

Today's computation capabilities make it no longer possible to justify simpler assumptions in terms of calculation ease. But, elastic calculations need fewer input parameters, which helps in reducing the associated error. Thus it is a powerful tool for poorly constrained studies in which uncertainty is high, provided the required conditions are met.

7.1 Fundamental concepts

The author does not intend to cover the topic of stress and strain relationships nor the theory of elasticity, for which numerous references are available (e.g. Hooke, 1676; Timoshenko & Goodier, 1934; Schofield & Wroth, 1968; Malvern, 1969; Gere, 2004; Prat, 2006). This part should just provide a specific introduction to the most important concepts and equations in relation to the performed analysis.

7.1.1 Stress and strain

The general elastic constitutive law, which relates stress and strain, can be expressed as in Equation (38) :

$$\sigma_{ij} = E_{ijkl}\varepsilon_{kl} \quad (38)$$

Both the stress and strain tensor (σ_{ij} and ε_{kl} respectively) are symmetric, which means that only 6 independent components exist ($\sigma_{ij} = \sigma_{ji}$; $\varepsilon_{kl} = \varepsilon_{lk}$). As a result, the rigidity matrix E_{ijkl} can have, at most, 36 different constants. However, the usually assumed cases are:

- Orthotropy (3 symmetry planes): 9 different constants.
- Transversal anisotropy (one symmetry axis): 5 different constants.
- Isotropy (three symmetry axes): 2 different constants.

The relation between stress and strain in isotropic conditions can be expressed using the well- known Hooke's law, as shown in Equation (39).

$$\sigma_{ij} = \lambda \varepsilon_{kk} \delta_{ij} + 2\mu \varepsilon_{ij} \quad (39)$$

Where δ_{ij} is the identity tensor, and λ and μ are the Lamé parameters. These can be related to Young's modulus (E) and Poisson's ratio (ν) the following way (see Prat, 2006, for further explanation):

$$E = \frac{\mu(3\lambda + 2\mu)}{\lambda + \mu}; \quad \nu = \frac{\lambda}{2(\lambda + \mu)}$$

The engineering notation for each component of stress and strain is shown in Table 8, together with the tensor equivalence, and Figure 59 shows the usual representation of triaxial stress.

Table 8: Stress and strain notations.

Notation	Engineering	Tensor
Stress	$\sigma_x \sigma_y \sigma_z \tau_{yz} \tau_{xz} \tau_{xy}$	$\sigma_{11} \sigma_{22} \sigma_{33} \sigma_{23} \sigma_{13} \sigma_{12}$
Strain	$\varepsilon_x \varepsilon_y \varepsilon_z \gamma_{yz} \gamma_{xz} \gamma_{xy}$	$\varepsilon_{11} \varepsilon_{22} \varepsilon_{33} \varepsilon_{23} \varepsilon_{13} \varepsilon_{12}$

It is worth noting that, unlike for stress, when considering strain the difference is big between both notations, as shear components in engineering notation are twice those of tensor notation. A good review on the topic of notations is provided by Lagace (2001).

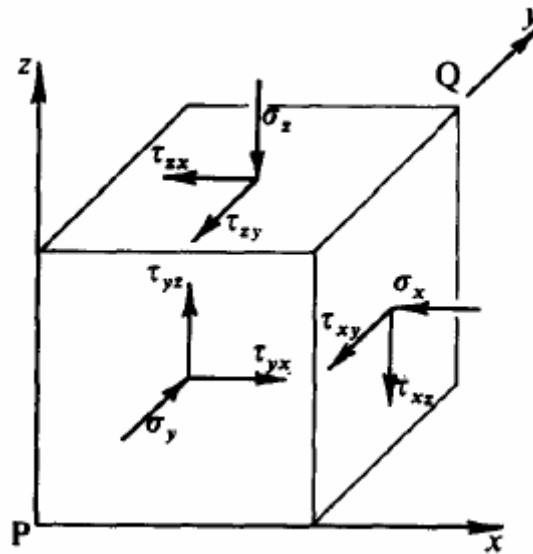


Figure 59: Stresses on a cube, using engineering notation. Source: Schofield and Wroth (1968).

7.1.2 Stress on a plane

Consider now Figure 60. The representation is two-dimensional, which is used because plane stress equations are much simpler to deal with, but also because failure conditions on a fault plane are inherently two dimensional (King et al., 1994).

In order to study failure conditions on a plane, stresses acting on it have to be determined. Forgetting for now about the principal stresses, the normal and shear stresses on the failure plane of interest (σ_β and τ_β) can be computed using a simple transformation, which allows obtaining the stresses on the x_1 and y_1 axes (parallel and normal to the failure plane) given a certain stress state defined on the original axes (x, y).

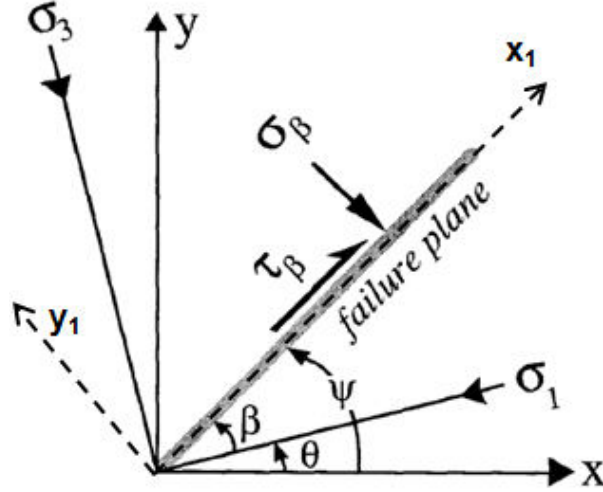


Figure 60: Axis system, principal stresses (σ_1 and σ_3) and a failure plane. Modified from King et al. (1994).

These transformations of plane stress are usually exemplified in courses of mechanics of materials (see Gere, 2004, or Zabatsky, 2007; specific insight in Schoenball, 2014). The calculation procedure is detailed on annex H, and the resulting equations are given below in matrix form:

$$\begin{pmatrix} \sigma_{x1} \\ \sigma_{y1} \\ \tau_{x1y1} \end{pmatrix} = \begin{bmatrix} \cos^2 \psi & \sin^2 \psi & 2 \sin \psi \cos \psi \\ \sin^2 \psi & \cos^2 \psi & -2 \sin \psi \cos \psi \\ -\sin \psi \cos \psi & \sin \psi \cos \psi & \cos^2 \psi - \sin^2 \psi \end{bmatrix} \begin{pmatrix} \sigma_x \\ \sigma_y \\ \tau_{xy} \end{pmatrix} \quad (40)$$

According to axes shown in Figure 60, σ_{y1} is σ_β , and $\tau_{x1y1} = \tau_{y1x1} = \tau_\beta$.

7.1.3 Principal angles

Taking into account a few trigonometric identities, the first and third equations resulting from (40), which allow obtaining σ_{x1} and τ_{x1y1} , can be rewritten the following way:

$$\sigma_{x1} = \frac{\sigma_x + \sigma_y}{2} + \frac{\sigma_x - \sigma_y}{2} \cos 2\psi + \tau_{xy} \sin 2\psi \quad (41)$$

$$\tau_{x1y1} = \frac{\sigma_y - \sigma_x}{2} \sin 2\psi + \tau_{xy} \cos 2\psi \quad (42)$$

To account for the principal stresses, which are the maximum and minimum normal stresses, the equation in (41) can be differentiated as shown in (43). The principal angle ψ_p (from now on noted as θ to accord with Figure 60) is the angle which defines them. There are two values of θ in the range $0-180^\circ$, which differ 90° and define the principal stresses (perpendicular to each other).

$$\frac{d\sigma_{y1}}{d\psi} = 0 \rightarrow \psi_p (= \theta) = \frac{1}{2} \tan^{-1} \left(\frac{2\tau_{xy}}{\sigma_x - \sigma_y} \right) \quad (43)$$

Once the orientations of the principal stresses are known, the angle between them and the plane of interest can be found (in Figure 60, β equals $\psi - \theta$). Consequently, the stress acting on the plane can also be expressed in terms of the principal stresses. If the angle between

σ_1 (major principal stress) and the failure plane is β , Equations (44) and (45) can be written. The complete procedure is detailed in annex H.

$$\sigma_\beta = \frac{\sigma_1 + \sigma_3}{2} - \frac{\sigma_1 - \sigma_3}{2} \cos 2\beta \quad (44)$$

$$\tau_\beta = \frac{\sigma_1 - \sigma_3}{2} \sin 2\beta \quad (45)$$

The maximum and minimum principal stresses are defined by the direction in which the normal stress components achieve the maximum and minimum values. Going back to the cube in Figure 59, shear components on all faces of the cube are 0 when these directions are considered. Thus, the two equations above are essentially the same as equations (41) and (42), just without the shear components (one sign changes, due to σ_b being σ_{y1}). The definition of principal stresses as those acting perpendicularly on planes with no shear stress can be noted as well using the Mohr's circle representation (Figure 61).

7.1.4 The Mohr-Coulomb failure criterion and Coulomb stress

Although various criteria have been used in order to express the failure conditions on rocks (e.g. Jaeger and Cook, 1979), the Mohr-Coulomb failure criterion is probably the more widely used (Equation (46), Figure 61). It has the advantage of being linear, which simplifies equations. However, under tensile conditions the relation proves to be inaccurate (Hudson & Harrison, 1997), and due to its definition it cannot account for the reduction of friction as stress increases.

$$\tau_\beta = c' + \mu \sigma'_\beta \quad (46)$$

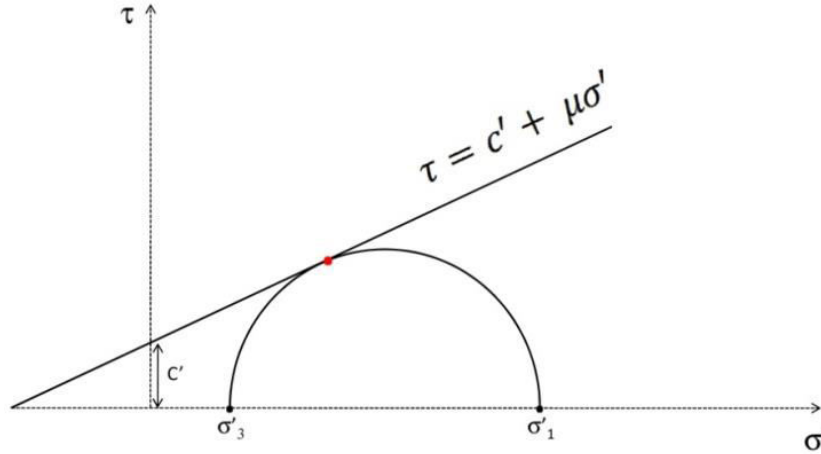


Figure 61: Schematic representation of the Mohr's circle, which stands for the stress conditions, and the Mohr-Coulomb failure envelope. The red dot marks the intersection of the circle and the failure envelope.

As seen in Equation (46), the failure condition, defined by τ (the maximum tolerable shear stress) depends on the effective normal stress on that plane (σ'), a friction coefficient (μ), and an effective cohesive term (c'). The β subindexes are maintained here to accord with Figure 60, although they need to be expressed in effective terms to be rigorous with the failure criterion. In rock mechanics, the cohesion can be understood as the initial asperities that need be broken before movement can start. Mathematically, it refers to the distance between the origin of coordinates and the point in which the straight line defined by the frictional term intersects the y axis.

The Coulomb failure function is shown in Equation (47). Coulomb stress (σ_f), can be understood from Equation (46) just by moving the frictional term to the left of the equal. Based on this criterion, failure will occur whenever the resultant value (which is the Coulomb stress) is higher than the available cohesion on the plane. Under a conservative assumption which considers that cohesion is 0, failure will be promoted if the shear stress is greater than the frictional term. Shear stress is always positive in this equation, thus positive Coulomb stress is destabilizing. Normal stress will be positive when the fault is unclamped and negative otherwise (Lin & Stein, 2004). Special attention needs to be paid when dealing with strike-slip faults, where normal stress will be chosen positive or negative depending on fault's potential direction of movement, which may be right or left-lateral (King et al., 1994).

$$\sigma_f = \tau_\beta - \mu\sigma'_\beta \quad (47)$$

Equation (47) can be now written by substituting the normal and shear stress by expressions (44) and (45), which yields:

$$\sigma_f = \frac{\sigma_1 - \sigma_3}{2} (\sin 2\beta - \mu \cos 2\beta) - \frac{\mu(\sigma_1 + \sigma_3)}{2} + \mu P_w \quad (48)$$

And, if Equation (48) is differentiated with respect to β , the angle at which the maximum Coulomb stress occurs can be found (equation (49)). It is seen that the orientation is only influenced by friction, and for a common value of $\mu = 0.6$, β is about 30° . Thus, for a vertical plane that slips laterally (strike slip fault), the optimal orientations are located at $\pm 30^\circ$ of the maximum horizontal stress (S_H), as in a strike-slip faulting regime, $S_H = S_1$ (note, once again, Figure 60).

$$\frac{d\sigma_f}{d\beta} = 0 \rightarrow \beta = \frac{1}{2} \tan^{-1} \left(\frac{1}{\mu} \right) \quad (49)$$

Let us consider now equation (47) again. To account for pore fluid pressure, the normal stress has been represented in terms of the effective normal stress. Another option to introduce the effect of the fluid is by means of the effective coefficient of friction, as in Equation (50):

$$\mu' = \mu(1 - B_k) \quad (50)$$

In the equation above, B_k is the Skempton's coefficient, which takes values in between 0 (no fluid) and 1 (if pore fluid pressure equals the normal stress acting on the plane), as shown in King et al. (1994), among others. Then equation (47) can be rewritten in the most commonly used form in studies of Coulomb stress transfer:

$$\sigma_f = \tau_\beta - \mu'\sigma_\beta \quad (51)$$

7.2 Method

The USGS freely provides the software package COULOMB (Toda et al., 2011), which allows calculating Coulomb Stress Changes (henceforth CSC) given a source fault and an observational fault's model (represented by strike, dip and rake and according to Aki &

Richards, 1980, convention, which is shown in Figure 62). The software uses the methodology summarized below in parts 7.2.1 through 7.2.3 to perform calculations, and has been widely used in research (e.g. King et al., 1994; Lin and Stein, 2004; Toda et al., 2005; Mukuhira et al., 2012; Sumy et al., 2014); it was utilized in this study as well.

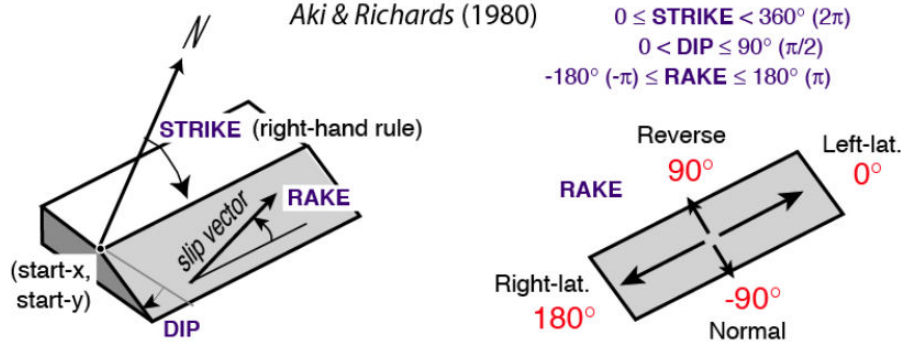


Figure 62: Convention used in focal mechanisms and Coulomb's software. Source: Toda et al., 2011.

7.2.1 Stress propagation

The calculations are made assuming a homogeneous elastic half-space. The first part of the calculation involves obtaining displacements at each point of the grid after the source fault slips. Strains are computed as the spatial derivatives of displacements. Okada (1992), provided analytical solutions both for source shear and tensile faults, characterized by point and finite rectangular models.

Okada's solutions and its derivation may be conceptually simple, but they are numerically demanding and extensive. The general form for the internal displacement field given a rectangular fault source in a half-space is shown in Equations (52) to (54). Nonetheless, the reader is referred to Okada (1992), for the complete set of equations and their applicability, as they are not repeated here.

$$u_x(x, y, z) = \frac{U}{2\pi} (u_1^A - \hat{u}_1^A + u_1^B + zu_1^C) \quad (52)$$

$$u_y(x, y, z) = \frac{U}{2\pi} (u_2^A - \hat{u}_2^A + u_2^B + zu_2^C) \cos \delta - (u_3^A - \hat{u}_3^A + u_3^B + zu_3^C) \sin \delta \quad (53)$$

$$u_z(x, y, z) = \frac{U}{2\pi} (u_2^A - \hat{u}_2^A + u_2^B - zu_2^C) \sin \delta + (u_3^A - \hat{u}_3^A + u_3^B - zu_3^C) \cos \delta \quad (54)$$

The source fault is at (0,0,-c) of the (x, y, z) coordinate system. Other parameters are (δ, L, W, U), which represent slip direction, length, width and net displacement respectively. u_i^j are functions to account for the x, y and z components (subindex i) which have 3 parts each (indicated by the superindex j). Each source fault type (strike-slip, dip slip and tensile) has its own functions.

Currently, Okada's solutions are already programmed in various packages coded using Matlab or Fortran, an example being the COULOMB software. This study used always rectangular source faults, with appropriate rakes from focal mechanism information, and net slip values according to fault's dimensions and magnitude of the source earthquake (see Madariaga, 1979, or Wells & Coppersmith, 1994, for further relations between fault's size, seismic moment and dislocation).

According to an isotropic medium hypothesis, all parameters needed to relate strains and stresses are E and ν or Lamé's λ and μ . Hence, stress can be obtained once strain has been computed, using the constitutive model in Equation (39).

7.2.2 Coulomb stress changes computation

As seen in part 5.1, Coulomb stress can be obtained in a quite straightforward way once the axes are defined adequately and for a two dimensional stress perturbation. Specifying a common axes system in which x and y are horizontal and faults are vertical, the scheme is direct:

1. From an input stress defined in (x, y) axes, which has only 3 independent components in two dimensions, the perpendicular and shear stress are resolved on the plane of interest (see Equations in(40)).
2. The Coulomb stress is calculated for a certain effective friction coefficient by applying Equation (51).

However, if strike-slip or dip-slip cases are involved in a triaxial stress state, the stress tensor grows up to 6 independent components, as in Figure 59. This means that, in order to transform stress from the old axes (input) to the new ones (fault plane), and following a scheme similar to the one in Equation (40), the transformation matrix now has 36 components. Considering a 3 axes system which is rotated, each old axis can be related to the new ones by the cosine of the angle in between them, thus in total 9 different elements appear (Figure 63 and Table 9).

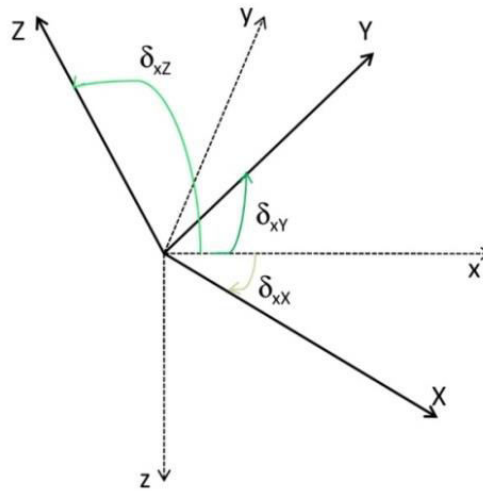


Figure 63: Scheme of two axes systems.

Table 9: Direction cosines (simplified notation) of the angles between the old and new axes.

Axes system	x	y	z
X	l_1	m_1	n_1
Y	l_2	m_2	n_2
Z	l_3	m_3	n_3

As stress are second order tensors (2 subscripts), they need not one, but two direction cosines for transformations. The transformation equations (e.g. Lagace, 2007; Zoback, 2007; Haftka, 2008) can be written in compact form using the direction cosines matrix

and its transposed matrix, as shown in Equation (55). This way the stress state on the new tridimensional axes system can be obtained, which allows applying Equation (51) to find the CSC.

$$[\sigma]^{New} = [t]^T [\sigma]^{Old} [t] \quad (55)$$

$$t = \begin{bmatrix} l_1 & l_2 & l_3 \\ m_1 & m_2 & m_3 \\ n_1 & n_2 & n_3 \end{bmatrix}$$

7.2.3 The role of the background stress

Up to here, the computation of CSC on an observation fault resulting from an event on the master fault has been explained. But how do we determine the optimal orientations for faults to slip? (from now on, Optimally Oriented Fault Planes are named OOFP).

Here is where the background (or regional) stress becomes important. Unlike the Coulomb stress change resolution on a plane, the determination of the OOFP needs the total stress tensor, as shown in Equation (56) where superindex r and q indicate regional and earthquake respectively (King et al., 1994). Then, the angle of the principal axes is derived using Equation (43), and the orientation of the OOFP is evaluated once β has been found (Equation (49)).

$$[\sigma]^{tot} = [\sigma]^r + [\sigma]^q \quad (56)$$

Depending on the type of fault of the OOFP of interest (pure strike, normal, thrust), the considerations to determine fault's strike and dip need to be adapted. This is due to regional (and principal) stresses which vary depending on faulting's regime (Table 10). Equations (57) to (59) shown below indicate how to solve each case. A pure fault assumption means that rakes are fixed to 0 or 180 for strike-slip, -90 for normal and 90 for thrust OOFP, according to the used convention (Figure 62).

Table 10: Relative magnitudes of the commonly assumed background stresses depending on the faulting regime. S_H and S_h are the maximum and minimum horizontal stresses, whereas S_v is the vertical.

Strike-slip regime	$S_{max} = S_H$	$S_{med} = S_v$	$S_{min} = S_h$
Normal regime	$S_{max} = S_v$	$S_{med} = S_H$	$S_{min} = S_h$
Thrust regime	$S_{max} = S_H$	$S_{med} = S_h$	$S_{min} = S_v$

$$\text{Strike-slip} \quad \text{strike} = \theta \pm \beta ; \text{dip} = 90^\circ \quad (57)$$

$$\text{Normal} \quad \text{strike} = \theta ; \text{dip} = 90 - \beta \quad (58)$$

$$\text{Thrust} \quad \text{strike} = 90 + \theta ; \text{dip} = \beta \quad (59)$$

Formulae (57) to (59) can be addressed as follows: For pure strike-slip faults, the dip is always assumed to be vertical. Strike is determined using both angles, as noted before when β was derived. In normal faulting environments, faults trend parallel to the S_H (e.g. Zoback, 2007), and the dip can be obtained as the complementary form of the angle between the S_{max} (which is vertical) and the fault plane (β). In thrust faulting regimes faults trend perpendicular to the S_H , and the dip is directly the angle between the S_{max} , which is now horizontal, and the fault plane.

In this work only pure cases of OOFB which accord to the regional stress have been evaluated (see part 7.2.6), which means that all cases can be solved based on the explanations and equations given above. Nevertheless, COULOMB offers the possibility of determining "absolute" OOFB (with unfixed dips and rakes). In this case, the algorithm is much more time-demanding as it searches over the entire focal sphere at each point of the grid (Toda et al., 2011), and was not examined here.

It should be noted that the derivations given above for θ , σ_f and β (Equations (43), (48) and (49)) considered plane stress, and accord to the directions defined by the (x,y) axes. If they are horizontal, and fault plane is vertical, the resolution is valid for a pure strike slip fault. When dip slip cases are involved (fault plane not dipping perpendicular to the x,y axes), the components σ_z , σ_{xz} and σ_{yz} cannot be ignored in order to calculate the orientations of the principal stresses. Moreover, in the tridimensional case the relative magnitude of the vertical and horizontal stress is essential as it controls whether dip-slip or strike-slip events take place (King et al., 1994). This is taken into account in COULOMB and in the developed program in next section.

7.2.4 Layered half-space

Okada's solutions implementation in COULOMB works assuming an homogeneous elastic half-space. However, crustal layering surely would introduce some changes in the Coulomb stress computation on planes. This may be especially important in large earthquakes which can transmit static stresses over important distances in the depth axis.

Wang et al. (2003), developed the Fortran programs EDGRN and EDCMP, which can work in a layered half space. They are currently compiled to work on Windows OS and may be freely downloaded from the GFZ Potsdam website at <http://www.gfz-potsdam.de/en/section/physics-of-earthquakes-and-volcanoes/data-products-services/downloads-software/> (last accessed April 2016). ED software allows unlimited layers and free layer width, and its results have solved numerical instabilities (e.g. Sato, 1971), as indicated by Wang (1999). Following the numerical Green's function approach, seismic event's elastic strains can be solved accounting for a layered half-space. The first program (EDGRN) computes the Green functions and the second (EDCMP) implements its values to compute displacements, strains and stresses at each point of the grid.

A part of this chapter's work was to be destined to compare both codes as well as investigating the differences between the layered (ED) results and the homogeneous (COULOMB) model results. In the end however, it was decided to perform calculations just with COULOMB to ease comprehension of the method and results. Moreover, the fact that Castor mapped faults and most of the earthquakes are located at depths shallower than 6-8 km, and that changes regarding V_p (P-wave velocity), V_s and specific weight in the first 10 km of crust are not significant (e.g. Diaz and Gallart, 2009; Tapia, 2013), made it the logical decision to take.

EDCMP to CSC

In spite of that choice, a Matlab code which works with both EDCMP's strain and stress output files to obtain CSC was built (it reproduces the process in part 7.2.2). The goal was obtaining a straightforward code whose output was comparable to COULOMB results, when it comes to mapping CSC at all points of the grid, and which could be used in other

local studies (ICGC). As well, it served the author as an evaluation tool in relation to the math involved. The program flowchart is shown in Figure 64, while the code is provided in Annex I. The program's functions were tested by comparing the CSC obtained by this code and the ones given by COULOMB.

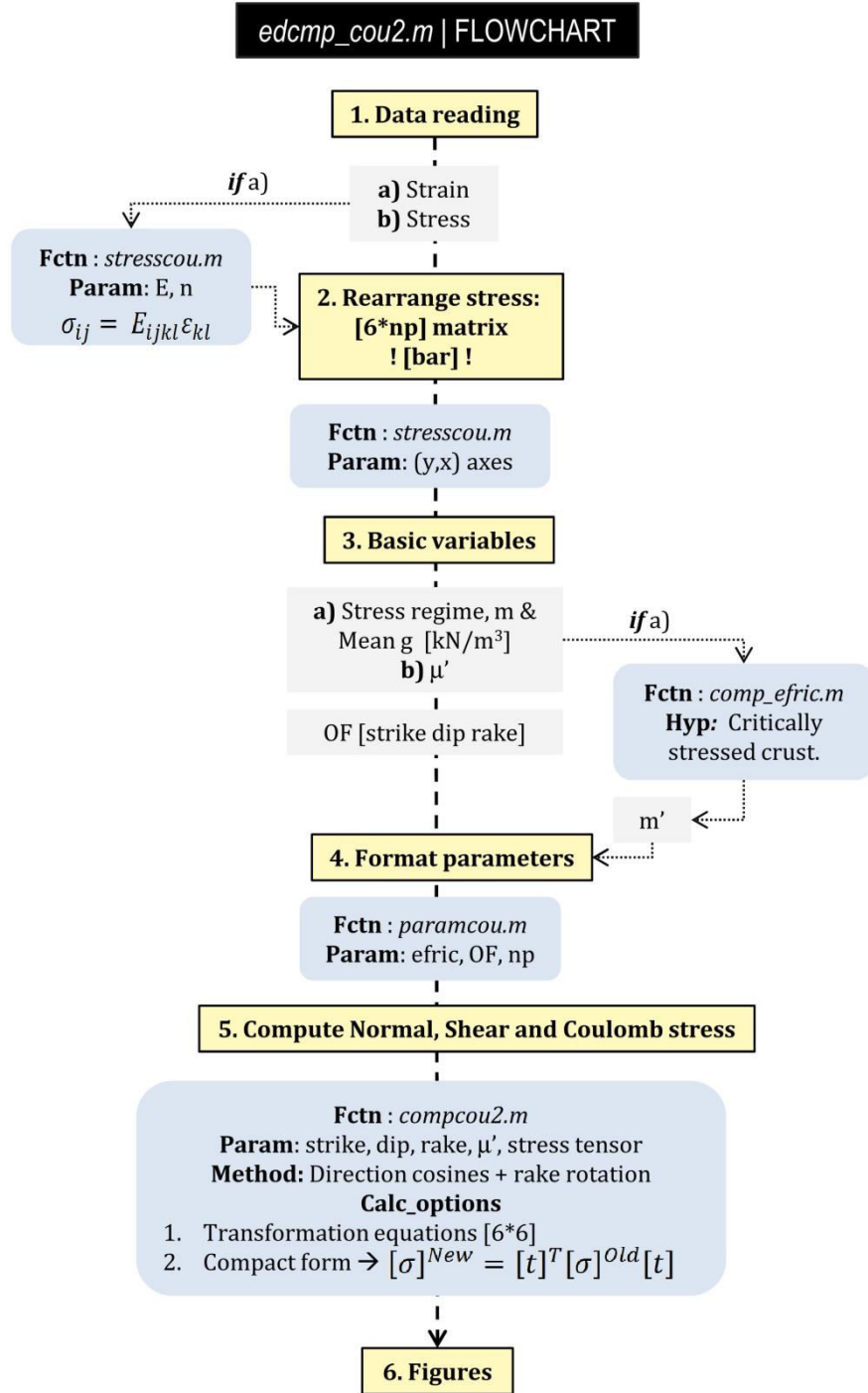


Figure 64: *edcmp_cou2.m* flowchart. Main steps are shown in yellow highlighted boxes. Subroutines and their input parameters or calculation basis are shown in light blue, while light grey shows user-defined parameters or information needed to compute CSC in function *compcou2.m*.

Therefore, it can be used once the strain or stress tensor at each point of the grid has been found (with EDCMP or any other software), so as to obtain a plan-view map of CSC according to observation faults strike, dip and rake, and for a given friction value.

7.2.5 Acceleration of the seismic cycle

CSC are considered in order to see whether a fault or an area is destabilized (positive values). Afterwards, precise values of CSC are used to quantify the acceleration of the seismic cycle (e.g. Harris, 2000; Baisch et al., 2009), as shown in Equation (60):

$$\delta_{cyc} = \frac{CSC}{\Delta\sigma} T_r \quad (60)$$

In order to compute the variation of the seismic cycle (time units), both the assumed stress drop ($\Delta\sigma$) and recurrence time (T_r) have to be estimated. Usually, the characteristic earthquake (Schwarz and Coppersmith, 1984) is used, as it is assumed to be the greatest earthquake that a particular fault can host. The size of the characteristic earthquake (M_w), provided the geometrical characteristics of the fault are known, can be estimated using the empirical relations by Wells & Coppersmith (1994).

Then, the T_r can be determined (e.g. Perea, 2006) as the ratio between the expected seismic moment, which can be obtained from the M_w using Hanks & Kanamori's (1979), relation, and the geologically assessed moment rate (see Wesnousky, 1986). The formulae needed can be seen in Equations (61) to (63). In Equation (62), A is the area of the fault, G is the shear modulus, which can be estimated for an elastic medium assuming E and ν , and SR is the slip rate.

$$M_o^e = 10^{1.5(M_w+10.7)} [dyn \cdot cm] \quad (61)$$

$$M_o^g = A \cdot G \cdot SR \quad (62)$$

$$T_r = \frac{M_o^e}{M_o^g} \quad (63)$$

Due to slip rates only having been reported for the main fault (Amposta East), the T_r of characteristic earthquakes in the other structures have not been attempted to calculate. The studies which reported slip rates, such as Perea (2006), and Garcia-Mayordomo et al. (2015), also calculated the T_r of the Eastern Amposta fault, obtaining important differences. Here, CSC have been computed on a simplified model (rectangular faults), in which the main fault's input data (annex E, chapter 4) was significantly different from Perea (2006), and slightly different from Garcia-Mayordomo et al. (2015). Therefore, the T_r of the characteristic earthquake was recalculated.

On the other hand, the earthquake stress drop²² can be calculated as shown in Equation (64), by relating the average strain change ($\frac{\Delta u}{L}$) to the static stress drop using Hooke's law (Lay and Wallace, 1995).

$$\Delta\sigma = C \cdot G \left(\frac{\Delta u}{L} \right) = C \left(\frac{M_o}{Rupt. Area \cdot L} \right) \quad (64)$$

$$C (strike slip) = \left(\frac{2}{\pi} \right) ; C (dip slip) = \left[\frac{4(\lambda + \nu)}{\pi(\lambda + 2\nu)} \right]$$

²²The stress drop can be defined as: "the difference between the state of stress at a point on the fault before and after rupture". Source: Lay and Wallace (1995).

7.2.6 Parameter selection

Thanks to the basis of keeping assumptions simple, the needed base parameters to perform the calculations described in this chapter is not very high (except for part 7.2.5). However, some of them are subject to important uncertainties; an effort has been made to constrain them as much as possible, as well as involving likely ranges more than just one value, and Table 11 summarizes the choices made.

Table 11: Parameter selection and variations in order to compute Coulomb stress changes and acceleration of the seismic cycle.

Parameter	Unit	Range	Source & Method
Young's modulus (E)	Pa	8E+10	Usual value (Toda et al., 2011)
Poisson ratio (ν)	Unitless	0.25	Usual value (Toda et al., 2011)
Effective friction (μ')	Unitless	0.2-0.6	a) From μ , γ_r and stress regime (Zoback, 2007). b) Recommended values (King et al., 1994; Hardebeck et al., 1998; Sumy et al., 2014)
Regional stress regime	-	Strike slip to normal	FM solutions (this study; Frontera et al., 2013; IGN, 2013; Cesca et al., 2014) and fault's description (IGME, 2013)
Regional stress orientation	$^\circ$	$S_H = 23 \pm 9$ $S_h = S_H + 90$ $S_v = \text{vertical}$	Schindler et al. (1998), Heidbach et al. (2008), Cesca et al. (2014)
Regional stress magnitude ($z = 1.7$ km)	Bar	S_1 : 411-391 S_2 : 391-371 S_3 : 248-241	Critically stressed crust and frictional equations (Jaeger and Cook, 1979; Zoback, 2007). Water table negligible.
Source faults: strike, dip, rake, geometry and net slip	-	-	Strike, dip and rake from FM solutions in this study. Rectangular geometry ($L=1\text{km} = 2w$). Net slip to accord with Magnitude of the event, for a given geometry (e.g. Aki and Richards, 2002)
Castor faults (receiver): strike, dip, rake and geometry	-	-	Strike from Geostock (2010) in Cesca et al. (2014). Dip and depth dimensions from IGME (2013). Rake to accord with FM-derived stress regime.
Main fault rupture area (RA)	Km ²	70-2.75	From dimensions in the derived model, accounting for curvature (max value). Wells & Coppersmith (1994) otherwise.
Main fault Moment magnitude (M_w)	Dimensionless	6.0-4.5	From RA (Wells & Coppersmith, 1994)
Shear modulus (G)	Pa	3.2E+10	According to E , n
Main fault slip rate (SR)	mm/y	0.04-0.63	Perea (2006), Garcia-Mayordomo et al. (2015),
Stress drop ($\Delta\sigma$)	Bar	10-30	Calculated for strike and dip slip (Lay and Wallace, 1995). Likely range (Baisch et al., 2009) considered as well.

Apart from the program *Edcmp_cou2.m*, Annex I provides the coda developed to generate both the source and observation faults models for CSC calculations (see annex E as well), and to compute the acceleration of the seismic cycle. A COULOMB input file is provided too.

7.3 Results

This study computes CSC due to the 8 largest events of the Castor seismic sequence (M_w 3.6 to 4.2), for which FM solutions have been obtained (solutions using FMNEAR's default model have been used, see chapter 5). An input plane is needed for calculations performed. The location of these events, numbered in chronological order, can be seen in Figure 65:

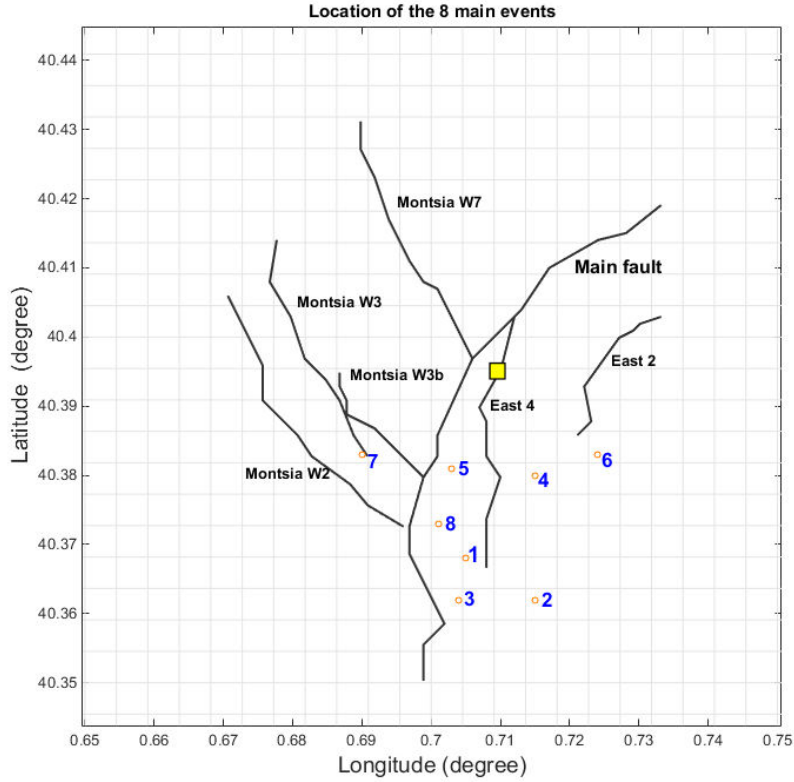


Figure 65: Location of the 8 strongest events of the seismic sequence, numbered in chronological order (first to last). Fault's trace at an approximate depth of 1.7 km is also depicted (according to Geostock, 2010), as well as the Castor platform location (yellow square).

7.3.1 Coulomb stress change on the source fault planes

The first part of the analysis involves an study of how static stress was transmitted onto the causative fault planes. The first assumption to be made is choosing between the two nodal planes of each FM solution. This study, based on earthquake static stress transfer as a potential trigger of seismicity, assumed that the causative fault plane was the one with higher CSC. This means that after each earthquake, the CSC was checked on both nodal planes of the next earthquake in the sequence, and the one with greater values was chosen as the hosting plane of that next event. With the same assumption, the first event's nodal plane was selected as the one which caused greater CSC on planes obtained for the second event. Results can be seen in Figure 66.

All earthquakes but one (09/30), had positive CSC on their nodal planes before they occurred. Due to normal stress being mostly added to shear stress, given that faults are essentially strike slips with determinate rakes, a high effective friction value (0.6) has been used to plot the figure, although changes were not significant.

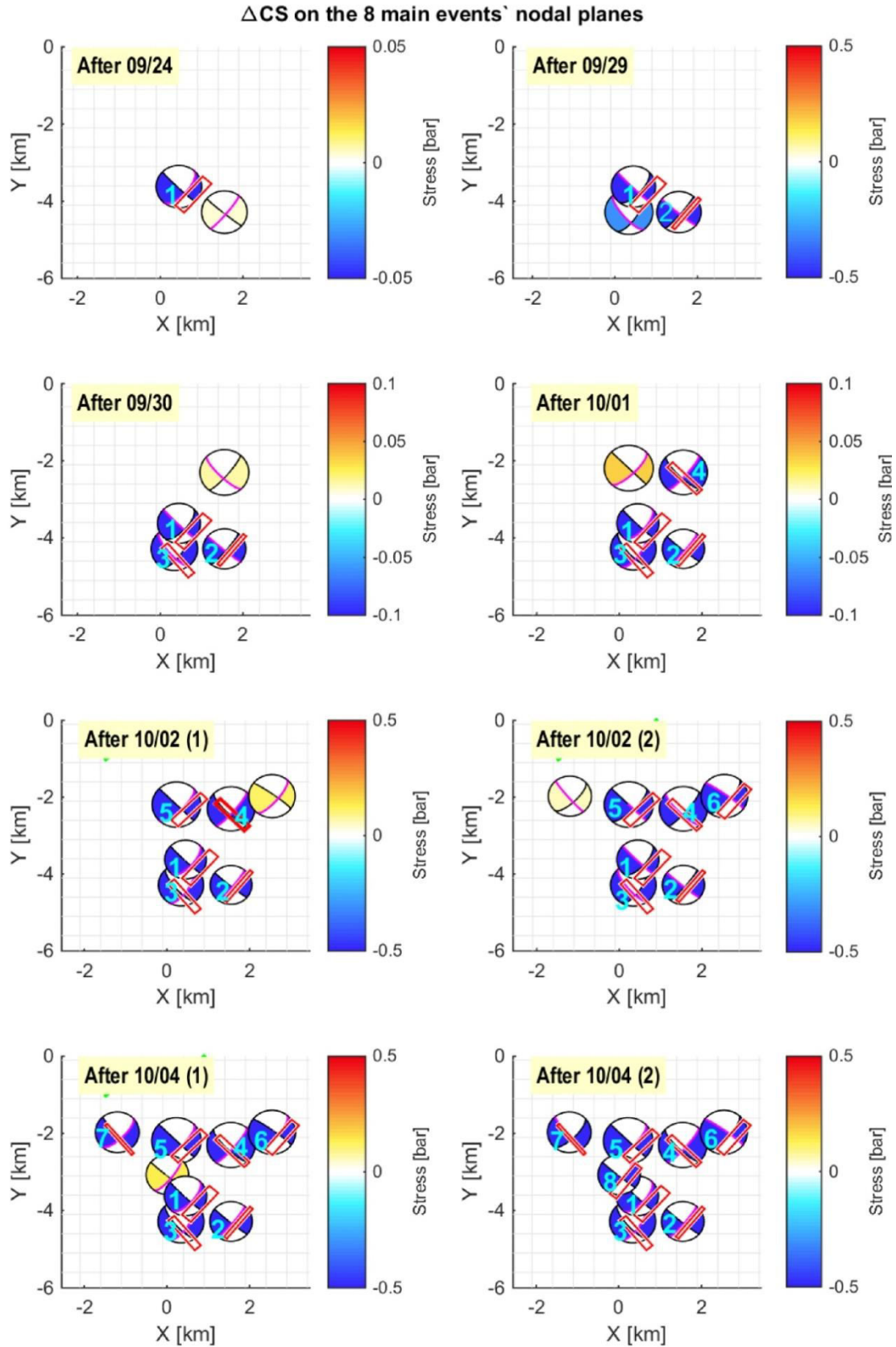


Figure 66: Coulomb stress resolved on the nodal planes. Each subplot shows the CSC due to the nodal plane of the previous earthquake slipping, on both the nodal planes of the old and the upcoming event. Past nodal planes are shown as red rectangles, whereas the new ones are directly represented onto the beach ball plot (pink line). The last subplot shows as well the faults' trace at a depth of 1.7 km, to better picture locations. Note that colorbar changes scale as sequence evolves. $\mu' = 0.6$.

Figure 67 and Figure 68 are time series on the same fault planes discussed above (modeled in COULOMB using one patch for each one), but allow a better comprehension of the variation of Coulomb stress in terms of quantity. They have been plotted for $\mu' = 0.4$ (usually assumed value, e.g. King et al., 1994; Hardebeck et al., 1998) and $\mu' = 0.6$ respectively, and as the reader will note, changes are small. As faults are modeled with the generally assumed dimensions for a M_w 4 earthquake (which means that all fault patch moves with the associated slip), stress drops after each event on the corresponding planes are much greater than any positive CSC contribution on them.

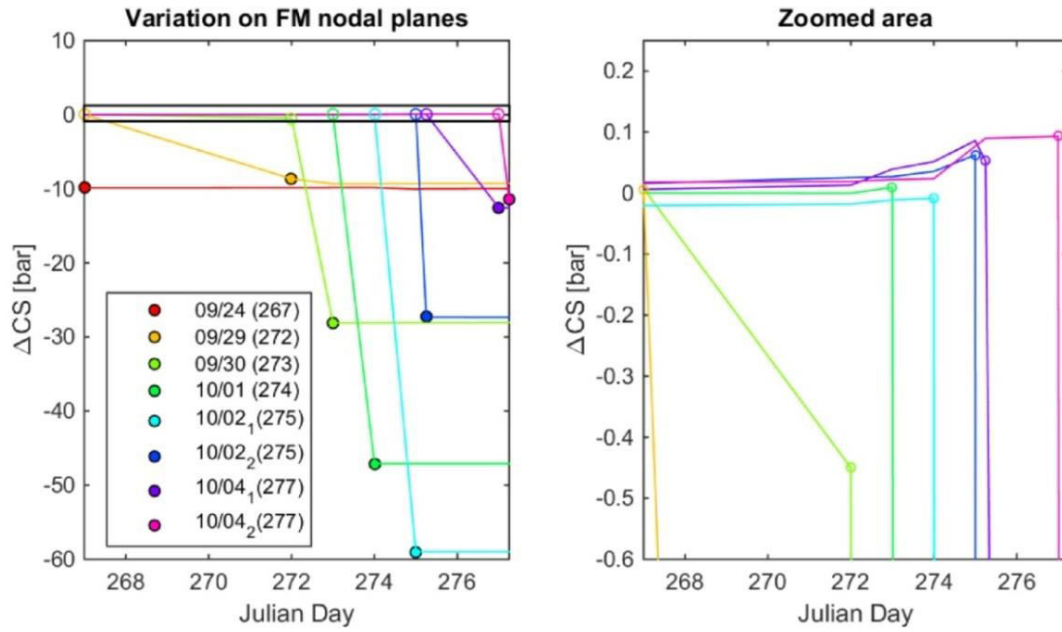


Figure 67: Time series of CSC on the source fault planes. Each line color represents one different plane, with empty circle markers being the state before the quake and filled markers afterwards. The black box in the left subplot limits the zoomed area on the right. $\mu' = 0.4$.

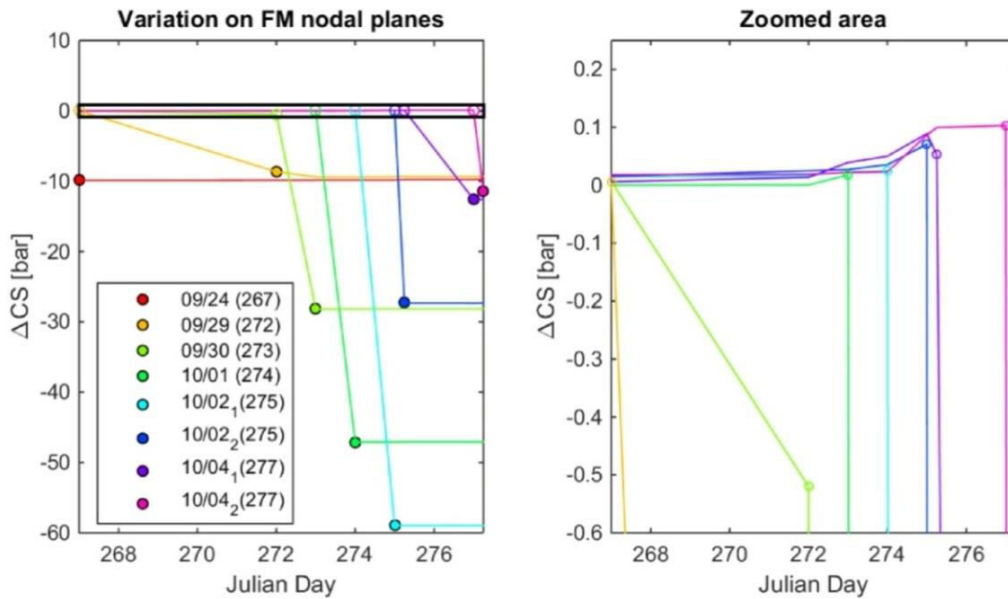


Figure 68: Time series of CSC on the source fault planes. $\mu' = 0.6$.

The zoomed area allows viewing the positive CSC. Except for the event of 09/30 and the first of 10/04, this latter having a slight decrease of Coulomb stress on it before slipping, all other planes slipped not only when CSC were positive, but when it was at its peak. However, values are small (maximum around 0.1 bar). Even if events are really close in terms of horizontal distance, their depth difference can be as big as 6 km (see chapter 5), which influences CSC to be minor. As FM solutions rely on depth and their confidence was found to be satisfactory, this parameter has not been varied because the FM solution would not be valid anymore.

7.3.2 Coulomb stress change on the mapped fault planes

As well, the evolution of CSC has been studied on the mapped fault planes (see annex E and I). Figure 69 shows the variation on faults modeled as single patches, while Figure 70 shows the variation on each fault subdivided into an appropriate number of patches according to its size. Figure 71 depicts the final state (after the 8 main events) on the fault planes. The figures are plotted for a common μ' of 0.4, but the results for other friction values, as well as CSC evolution on the fault plane model, can be seen in annex J. The source faults (the ones slipping), are the ones derived from FM solutions and the analysis in the previous part (7.3.1).

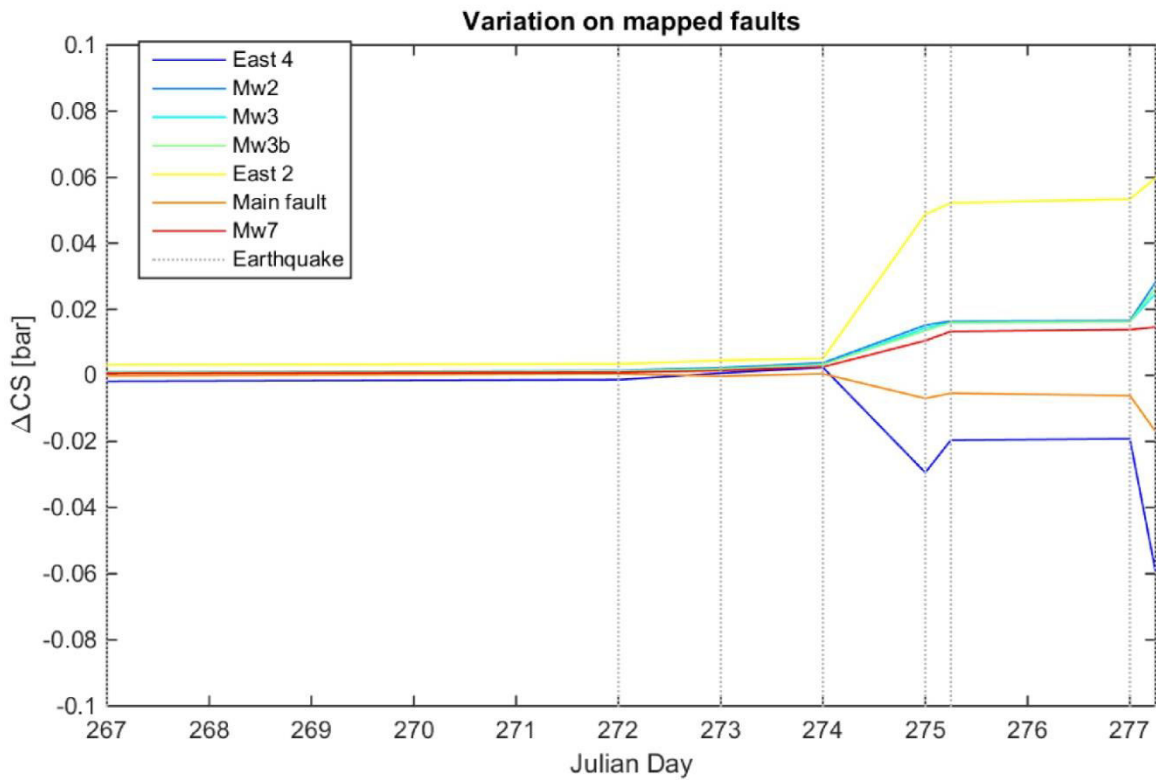


Figure 69: Time series of CSC on the receiver fault planes. The discontinuous vertical lines indicate the occurrence of an earthquake (note that days 267 and 277 also have earthquakes). Colors are used to better distinct faults, and do not accord with CS being positive or negative (which is represented on the vertical scale). $\mu' = 0.4$.

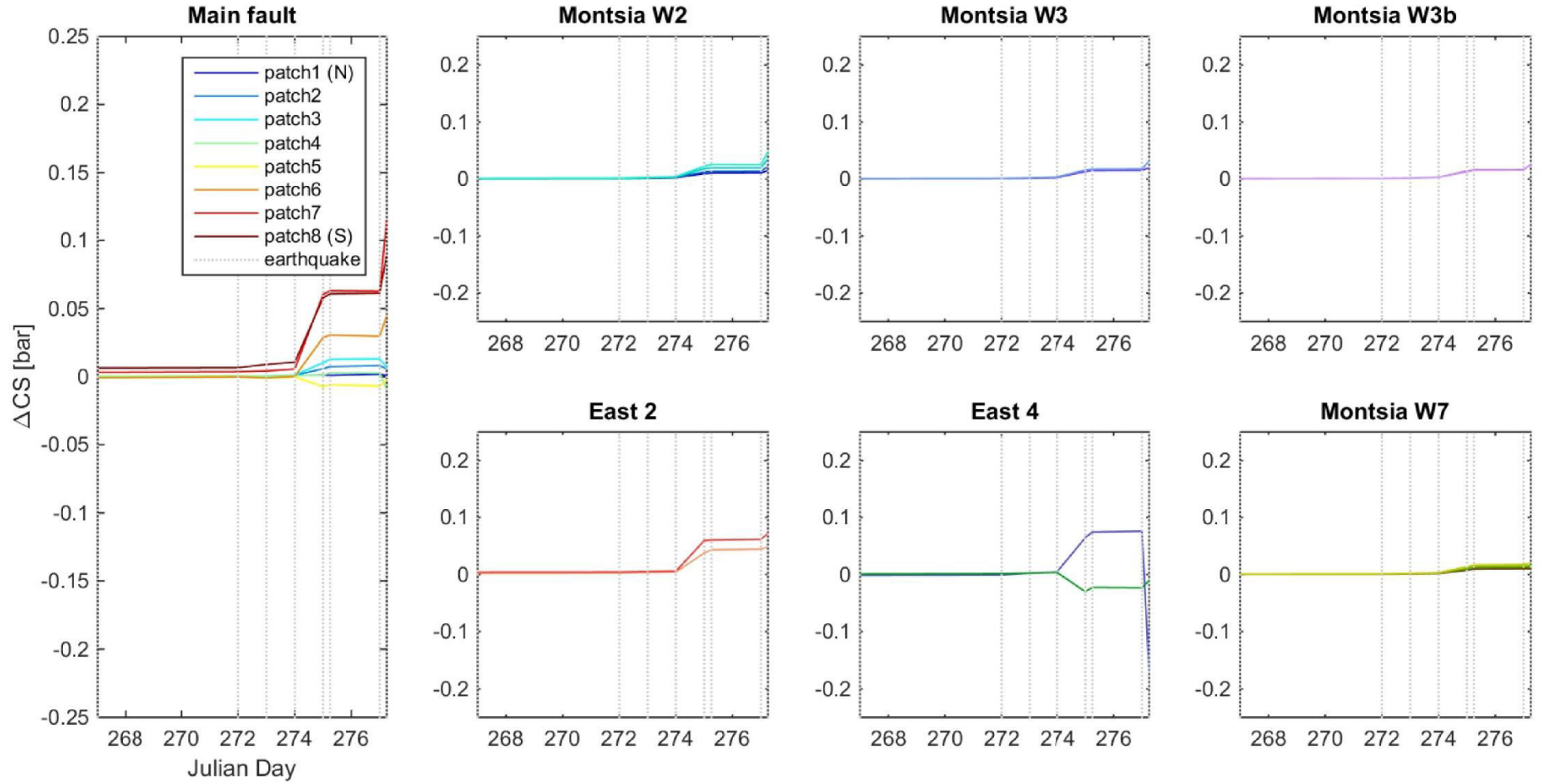


Figure 70: Time series of CSC on the receiver fault planes, divided each one into various patches. $\mu' = 0.4$.

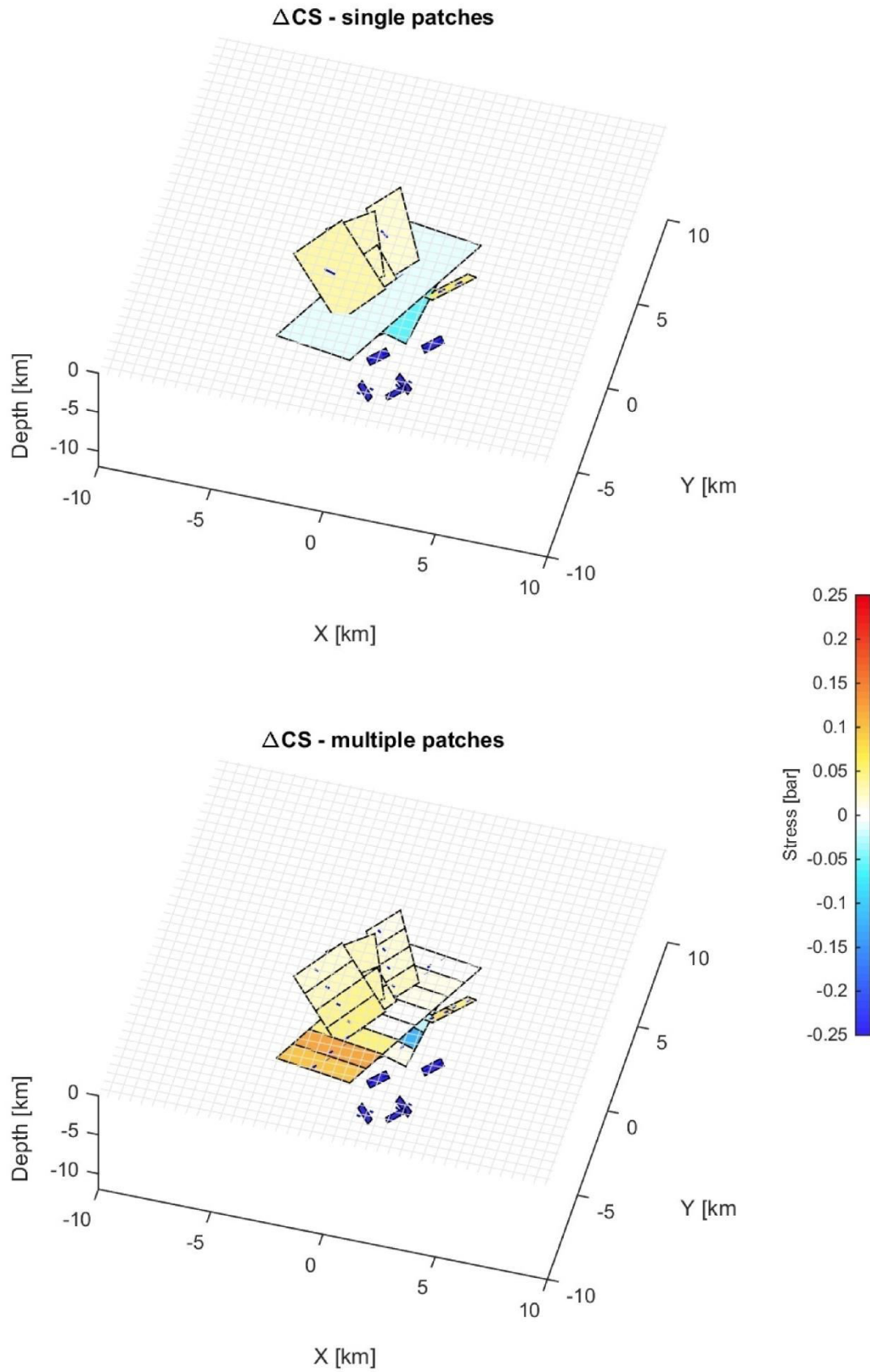


Figure 71: CSC on modeled fault planes, using single patches (above), and multiple patches (below). Deeper dark blue patches are the source faults, corresponding to those in Figure 66. $\mu' = 0.4$. The orientation of the plot view was chosen so that all faults were visible, although no perfect solution which shows all fault areas at once is possible.

Rake of mapped faults has been inferred from FM information (see in Table 11), which involves the governing stress. The value used is the average of the rakes obtained for the FM solutions (faults are assumed to move as strike-slips with some normal component), and the nodal plane closer to fault strike is selected (both were tested for the main fault, and the one in which higher values of CSC were computed was finally used; see annex J.2). Even if mapped faults are described as normal, here it was considered that faults would behave as partial strike slips, according to current background stress.

CSC are calculated on the central coordinate of each fault patch, which accounts for the differences observed between the single and multiple patch models. When faults are small or the stress increment very homogeneous, subdividing patches is not as important as here. The main fault, being the largest, is the one which registers more variation (from near-zero negative CSC using a single patch, to near 0.1 bar positive CSC).

Both the minimum and maximum CSC are found after the 8 main events have taken place. Regarding positive CSC, it can be seen that stresses add up to each other as the sequence goes by. The main shock (10/02, 23:06:50 UTC) and the last one (10/04) are two events contributing more. This is due to size for the first one, and due to depth (3 km) for the second one. Mapped faults' knowledge does not reach depths beyond 3 km, so distance event-fault increases further deep. Higher CSC are found on the southern patches of the main fault, with a maximum value of 0.12 bar (see Figure 70 and Figure 71). The assumed rake value is really close to the optimal one for this patch strike and dip. Results were not very sensitive to effective friction changes.

7.3.3 Optimally oriented faults

In parts 7.3.1 to 7.3.2, CSC have been studied on precise fault planes and, as explained before, for such calculation the background stress is not relevant. However, CSC can also be studied on OOF, for which the regional stress is needed. Two different stress regimes with varying orientations of the S_H have been considered as indicated in Table 11, in order to study optimal strike-slip orientations as well as optimal normal faults (see 7.2.3). The magnitudes of the stress regime are calculated under the assumption of a critically stressed crust, and frictional equations are derived assuming a Mohr-Coulomb failure criterion (see Zoback, 2007).

Figure 72 shows the results at a depth of 1.7 km, after the 8 main events. It can be seen that the CSC are always below 0.2 bar, and that for a strike slip regime the worst assumption (higher CSC) is the first one (strike = 9°). The orientations of the OOF are also shown, which strike at approximately $\pm 30^\circ$ from the S_H orientation according to what was explained in the theory. At this depth, it can be said that OOF do not receive much higher CSC than the mapped ones. It has to be noted that in line with the hypotheses made, the effective friction should be smaller than 0.6. If the stress magnitudes and P_w are known, it can just be estimated as in Equation (65):

$$\mu' = \frac{\mu(\sigma - P_w)}{\sigma} \quad (65)$$

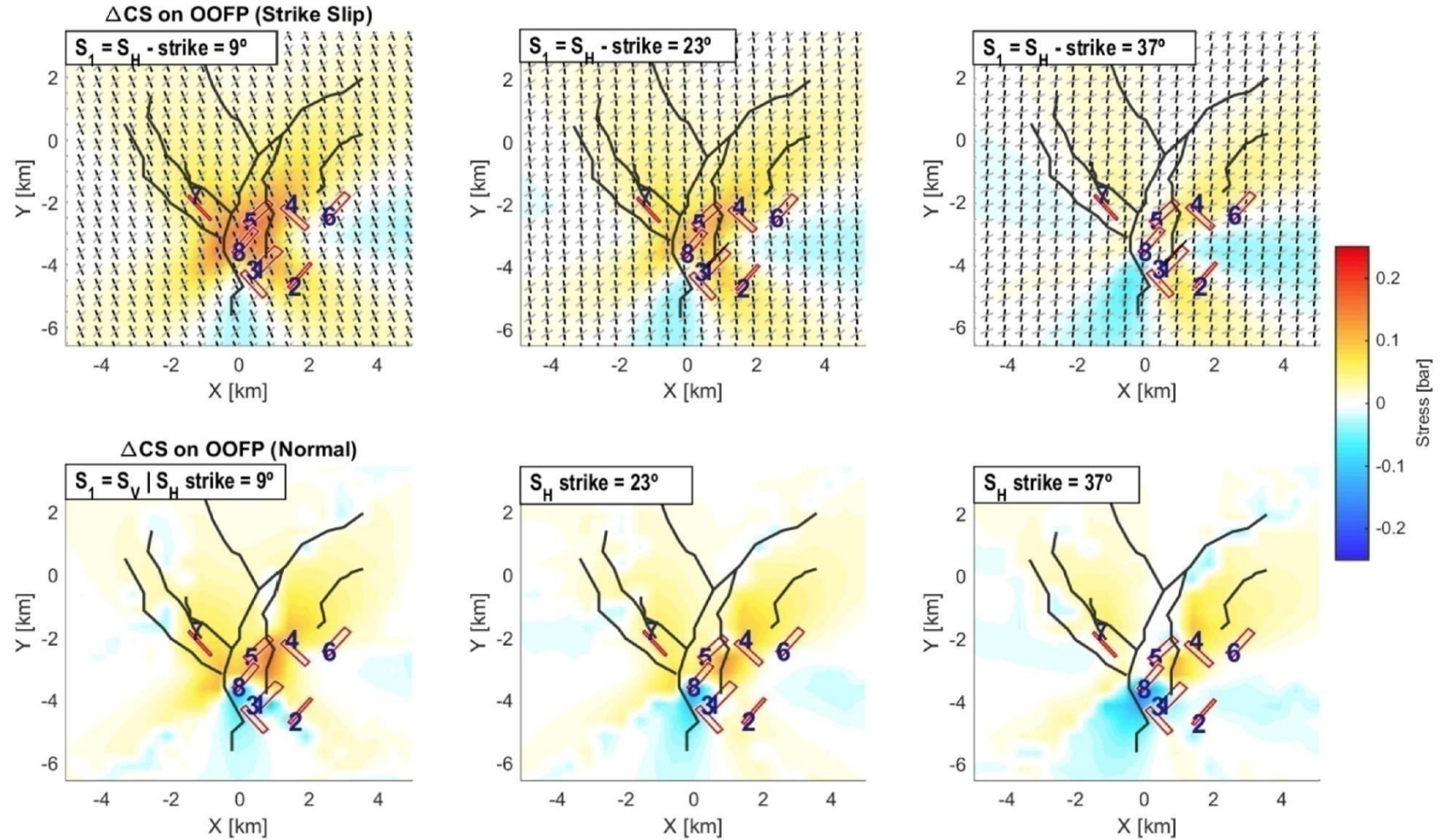


Figure 72: Coulomb stress changes computed at each point of the grid for a fixed depth of 1.7 km, where the fault traces (main black lines) are plotted. S_H strike is varied from 9 to 37° ($S_h = S_H + 90$). The three panels above show as well the OOF (strike-slip) orientations, left lateral in grey and right lateral in black. Red rectangles represent the hosting planes, although they are deeper than the map plot. $\mu' = 0.6$.

Accounting for $\mu = 0.6$, the two extreme values of σ (σ_1 and σ_3), and hydrostatic pressure, μ' ranges in between 0.19 and 0.35, which is close to what is obtained using Equation (50) with B_k 0.5 to 0.7. However, given fault orientations, assuming higher values is conservative (higher CSC are found), that is why 0.4 or 0.6 is usually taken to plot figures. In any case, μ' relevance has proven to be quite low in this study.

Figure 73 depicts the results at depth = 5 km. Note that the stress scale has augmented an order of magnitude, due to earthquake location proximity. The CSC are mostly of negative nature as hosting faults have released stress. The effective friction change influence is minor, and the panorama is vaguely worse for a normal regime supposition.

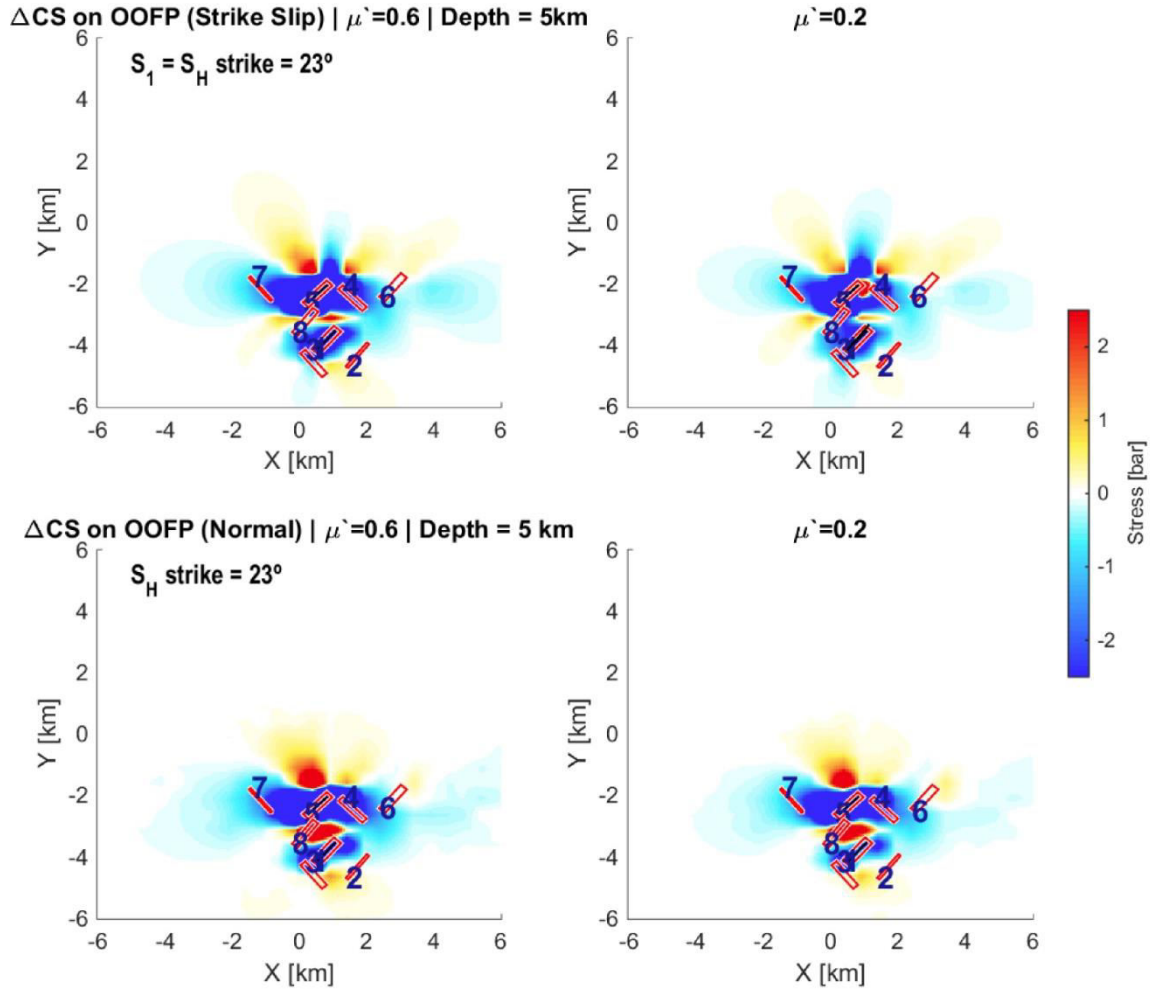


Figure 73: Coulomb stress changes computed at each point of the grid for a fixed depth of 5.0 km, according to figure indications.

To complete the analysis, two cross sections were created (Figure 74). The first one, across the Montsia system, was computed for observation faults with strike, dip and rake equal to the average of that of the Montsia faults, roughly 135, 50, -150. On the other hand, the C-D profile cuts across the main and east faults, and in this case it is assumed that they will move as strike slips, due to differences in between them which made it unadvisable to average values. The magnitudes of the CSC increase with depth, as most of the earthquakes took place in between 5 and 8 km below the surface. Fault parts which could potentially

have been left with larger Coulomb stress are those at greater depths. The figure is plotted for $\mu' = 0.6$ according to the comments made before.

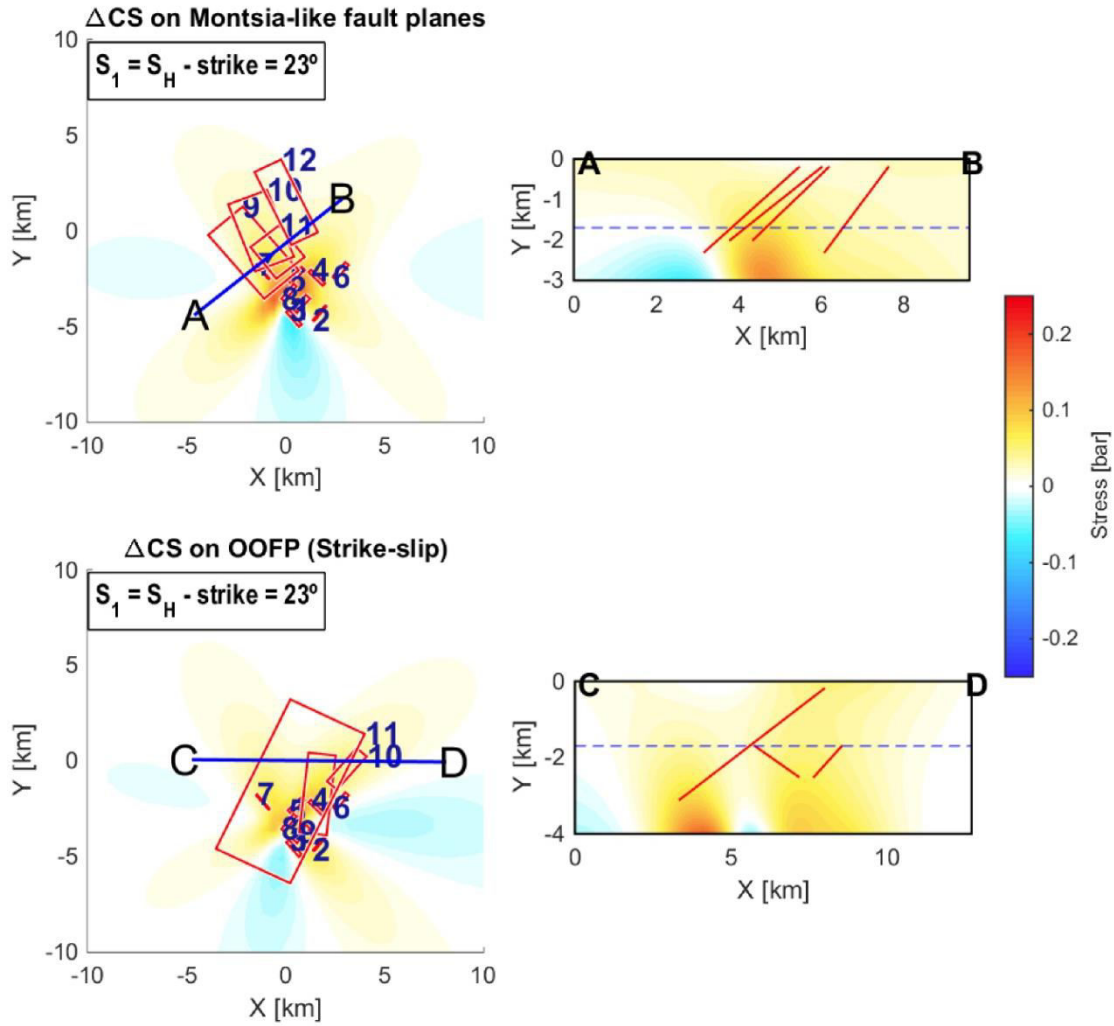


Figure 74: Coulomb stress changes resolved on cross sections indicated in the left panels. The map view is plotted at the depth indicated by the discontinuous line. $\mu' = 0.6$.

7.3.4 Acceleration of the seismic cycle on the main fault

The variations of recurrence times on the main fault are also calculated. They are only computed on the main fault, due to the reasons indicated below:

1. Maximum CSC on the other planes were clearly smaller.
2. It is the structure which can potentially host the greatest earthquake in the area, thus the most important in terms of seismic hazard.
3. Data such as slip rates can only be found in literature for the main fault.

Three different earthquake cases are studied (M_w 6.0, 5.0 and 4.5). The maximum magnitude corresponds to the characteristic magnitude, determined from a hypothetical case where rupture takes place over the entire fault area. The maximum expected magnitude is lower than the M_w 6.6 reported by Garcia-Mayordomo et al. (2015), but it does not significantly affect the results as the computed stress drop would be similar.

Results are shown in Table 12 and Table 13. The advantage of showing results in % (Table 12) of the acceleration is that the computation of recurrence times, which introduce notable uncertainty, is not required (CSC are directly divided by the earthquake stress drop, see Equation (60)). In fact, the selected stress drop values which are not calculation-derived (*min* and *max* in Table 12 and Table 13) are the lower and upper value of a range of small stress drops (Kanamori and Anderson, 1975), which is, once again, a conservative assumption (already indicated in Baisch et al., 2009).

The maximum accelerations (%) are respectively 0.38, 1.14 and 1.1, resolved considering the mean CSC on the fault in the case of the M_w 6.0, while for the others it is assumed that the most stressed area breaks and the maximum CSC is selected. But, even considering the maximum CSC, the seismic cycle would not have been accelerated more than 1.4 % for the maximum assumed event.

The computation of the T_r as shown in part 7.2.5 needs the slip rate on the fault. According to slip rate values given by authors in Table 11, three different return periods (whose mean and standard deviation, SD, is indicated in Table 13) were computed for each case (see annex I). The mean value of the T_r was the one used in calculations. "Accelerated years" out of the recurrence time helps in stating that the influence of CSC seems to be, at most, of second order.

Table 12: Acceleration of the seismic cycle (%), assuming three different magnitude cases and two effective friction values, and according to stress drops indicated in the table. *ss* and *ds* in the stress drop boxes refer to strike slip and dip slip respectively, while *min* and *max* are the assumed threshold values.

δ_{cyc} (%)	$M_w = 6.0$		$M_w = 5.0$			$M_w = 4.5$		
	$\mu' = 0.4$	$\mu' = 0.6$	$\Delta\sigma$ [bar]	$\mu' = 0.4$	$\mu' = 0.6$	$\Delta\sigma$ [bar]	$\mu' = 0.4$	$\mu' = 0.6$
$\Delta\sigma$ [bar]								
21.8 (ss)	0.145	0.174	12.1 (ss)	0.96	1.14	12.5 (ss)	0.93	1.10
29.1 (ds)	0.109	0.130						
10 (min)	0.316	0.379	16.1 (ds)	0.72	0.85	16.6 (ds)	0.70	0.83
30 (max)	0.105	0.127						

Table 13: Acceleration of the seismic cycle (years), assuming three different magnitude cases, according to stress drops and T_r indicated in the table. Note that Standard Deviation (SD) is higher than the $T_r \cdot \mu' = 0.4$.

δ_{cyc} (y)	$M_w = 6.0$	$M_w = 5.0$		$M_w = 4.5$	
	$T_r=5675$ y $SD = 6898$	$\Delta\sigma$ [bar]	$T_r= 1300$ y $SD = 1584$	$\Delta\sigma$ [bar]	$T_r=410$ y $SD = 911$
$\Delta\sigma$ [bar]					
21.8 (ss)	8.2	12.1 (ss)	12.5	12.5 (ss)	3.8
29.1 (ds)	6.2				
10 (min)	17.9	16.1 (ds)	9.4	16.6 (ds)	2.9
30 (max)	6.0				

7.4 Discussion: Coulomb stress variations and the occurrence of earthquakes in the case of study

The analysis performed in this chapter was conducted to evaluate both the influence of static stress transfer during the main events of the seismic sequence, and the stress state on faults after the last $M_w \geq 3.5$ shock. Positive CSC are nearly inexistent until the M_w 4.2 main shock (10/02), at a depth of approximately 5 km, occurred (Figure 69 and Figure 70). Afterwards, only the M_w 3.7 (10/04), whose FM was solved for a depth of 3 km, contributed in increasing CSC in a relevant way. Although it has to be noted that if FM solutions had been obtained at shallower depths the CSC could have been greater, it is not likely that this was the case, at least for most of them. A recent study by Gaite et al. (2016), which elaborated a more detailed 3D velocity model to locate the earthquakes, supports this fact; most of the events they located occurred at depths greater than 5 km.

The occurrence of any of the 8 studied events on one of the mapped fault planes (Castor faults, here used as receiver faults only) seems improbable except for the last one; when accounting for static stress transfer as a trigger and considering the locations and FM solutions obtained, the M_w 3.6 of 10/04 could indeed have taken place on one of the mapped faults. The main fault was clearly discarded from the beginning due to the obtained nodal planes, and the discussion was whether the Montsia system or some of the eastern faults could have been activated.

Cesca et al., (2014), who obtained shallower focal depths, already pointed out towards the East-dipping fault (here named East 4) as the one with higher probability to have hosted some of the events, although no quantification was made. CSC on that fault have proven to be near 0.1 bar positive just before the last event (Figure 70), which occurs on a nodal plane with very similar orientation and depth, and then they clearly fall. Instead, the other fault planes register very small to small but growing CSC, which are at their the highest after the 8 events, at least on most of the modeled patches.

Based on the numbers reported, CSC could have triggered the last earthquake on an east-dipping fault at around 2-3 km beneath the Castor platform, which accords with the herein named East 4. They were most likely not responsible for any of the others. The fact that critically stressed faults can slip with the minimum perturbation means that if some of the earthquakes had been located at shallower depths, evidence could have been found for some other main events to have happened at one of the Montsia or eastern faults. This introduces important uncertainty in terms of relating CSC and the main events in the sequence, as depth is the worst resolved spatial dimension due to seismic network distribution and distance. Despite that, its impact in the long-term seismic hazard is almost certainly low, as will be explained below.

The remaining positive CSC have been studied on the main fault, in order to quantify their influence in the future seismic events. It has been seen that the acceleration of the seismic cycle due to resolved CSC is fairly small. Considering the maximum calculated values, slightly above 0.1 bar, accelerations never exceed the 1 %. On the account of the calculated stress drops, the CSC would have to be an order of magnitude greater (around 1 bar) to start influencing recurrence times in a more relevant way (e.g. 10 %). In terms of the

maximum earthquake considered, that value has to be doubled to obtain the same acceleration, and it should be remembered that such values ought to be achieved along the whole rupture area, which is highly improbable. The analysis performed at 5 km of depth (Figure 73) supports this argument, as positive CSC are particularly localized, and a calculation using source and observation faults at the same depths was also considered to prove it (see annex J.3).

Consequently, seismic cycle concerning future earthquakes could have been accelerated to some extent for low to moderate earthquakes up to M_w 5.0. For greater events, the influence of CSC as a result of the 8 main events is irrelevant. Bearing in mind minimum hypocentral distances to coast (20-30 km), any $M_w < 5.0$ earthquake would hardly pose a risk for population.

No further risk-related study has been made on the source planes (derived from FM), as they represent unknown faults. Moreover, given the dimensions used and their stress state after the considered earthquakes, they should have been left far from failing again. Conversely, positive CSC on most of the causative fault planes just before they slipped, as seen in Figure 66 to Figure 68, means that CSC, especially after the first $M > 4$ event, could have acted as (partial) triggers on them.

8. FINAL REMARKS

8.1 Integrated discussion

While the aspects directly related to each chapter analysis have already been discussed in the proper place, a joint discussion of the key features on a general context had not been done beforehand. The argumentation that follows should be able to cope with the main worked topics.

Locations obtained here for a set of 95 events pointed out towards deeper fault sources than the currently known fault planes, especially after FM solutions were computed for the main events. This accords with the recently published paper by Gaite et al. (2016), whose authors reach a similar conclusion, but not with Cesca's et al. (2014) locations, who constantly obtained depths of 1-3 km (near reservoir). Induced seismicity caused by fluid overpressures should be expected (at least at the beginning) around the point of injection, and then expand outwards, something that has been addressed to as the *Kaiser* effect, in studies such as Baisch et al. (2009).

However, the obtained spatiotemporal clustering of earthquakes, as shown in Figure 42 and Figure 44 (page 58), indicates a different evolution. In fact, the first events of the sequence, which are also of smaller magnitudes, are located farther from the injection point than the main ones. Given the ellipsoid errors in the performed locations, it is obvious that some bias could be present, and particularly, the general cloud is probably shifted to the NW. This is observed when comparing locations with results obtained by Gaite et al. (2016), and it is due to the location method applied and network distribution. For epicenters located outside the network and when important gaps are present, it has been observed that they are systematically brought closer (in this case to the NW; Fajula and Romeu, 2016). In terms of depth, the comparison with Gaite et al. (2016), gives more confidence to foci being deeper than the reservoir bottom.

The aforesaid deeper foci supposition inherently yields that should the events be induced, transmissivity of an unknown fracture network beneath the reservoir is high. In fact, the system could be closer to failure at depth and that is why most of the seismic events took place there. This accords as well with fault's laterally limiting the reservoir being seals, as pressure increments would have been transmitted to other points. While it is the gas that was injected at certain overpressures and that remained at the top of the storage cavity because of its lighter specific weight, as it entered the reservoir it would have driven present water deep below; its displacement could have induced shear on deeper structures. Not only that accords with the observed deep seismicity, but it also is coherent given a top-sealed (stratigraphic trap) and laterally impervious (structural trap) reservoir.

Deeper existing structures in the area had already been inferred from deep seismic reflection profiles, which showed evidence of faults up to the deep-upper crust (Roca and Guimera, 1992; Gallart et al., 1995; Verges and Sabat, 1999). Nevertheless, the fact that small-magnitude events could have taken place at shallower depths, at least based on

error ellipsoids obtained here, should not be ruled out. If that were true, it would allow an interpretation in which seismicity migrated towards deeper sources with time (larger earthquakes are much better constrained in terms of depth), where most of the large earthquakes took place.

According to induced seismicity's definition, its nucleation and size are controlled by the introduced perturbation (controlled process), which consequently constrains the energy output (and hence the magnitude) of the resulting event. Given the introduced volumes (roughly $1\text{E}+8 \text{ Nm}^3$), and maximum overpressures (8 bar according to Gonzalez, 2014), the potentially greatest induced earthquakes can be constrained by relating the energy introduced to the system and the seismic moment. In that sense, if we assume the introduced energy to have been $6.2\text{E}+13 \text{ J}$ (see chapter 3), the maximum potentially induced moment release would be of $M \sim 3$. Such an earthquake would most probably never be felt at 20-30 km (where the nearest population nuclei were settled) from the source point. If the neighboring known faults are assumed to isolate the reservoir, and therefore the introduced perturbation cannot interact with (read trigger seismicity) other earthquake-hosting structures, the resulting induced seismic hazard while operating at the reported pressures should be very low.

Nevertheless, felt earthquakes up to M_w 4.2 (net slip of around 6cm on a fault plane of 2 km^2 , following Wells and Coppersmith, 1994) took place, which means that something in the previous comments is missing so as to accord with reality. The fact is that once earthquakes started taking place and planes slip, additional perturbations (to that of the fluid overpressure) entered the system (static and dynamic stress changes at least). The problem once seismicity has started is that equilibrium has been broken, and an uncontrolled process may occur (triggered seismicity).

Consistent with Escal UGS (2014), the upper pressure threshold for fault activation had been set at 49 bar (the security margin for hydraulic fracture in the upper seal was larger). Thinking in terms of a Mohr-Coulomb failure envelope, this means that studied faults could not slip unless the effective normal stresses were reduced by that amount. However, as it was indicated before, it was just with $1/7$ of that value and a relatively small volume of injected gas that the earthquakes came about. This relates particularly well with uncontrolled processes (triggered earthquakes) in the sense that the amount of energy introduced does not constrain the energy output, which responds to the amount of elastic strain accumulated during the previous seismic cycle, which might last for thousands of years. If not only the excess pore pressures, but also other triggers such as the static stress transfer (compare chapter 7) by the foreshocks are considered, the total perturbation can trigger a larger earthquake. In literature, stress changes as little as 0.1 bar have been repeatedly reported to influence the locations where aftershocks occur (e.g. Baisch et al., 2009; Mulargia and Bizzarri, 2014).

As reported in chapter 7, Coulomb Stress Changes (CSC) up to 0.1 bar were computed on the source planes derived from FM solutions. The calculations were made considering static stress transfer by the main events which struck before the objective event only. Hence, taking other triggers into account it is coherent to believe that values could have added up to some tenths of bar on certain planes. In a critically stressed crust which relies on earthquakes as a mechanism of self-equilibrium (e.g. Bak and Tang, 1989), it is

presupposed that all structures are about to fail, which is what almost certainly happened in the Castor case. Among the mechanisms that triggered those earthquakes, CSC probably played a partial role. Fluid pressure (diffused from the injection point) could have been the other trigger involved, and a maximum of 8 bar would have resulted in values unlikely bigger than 1 bar where ruptures took place, once loss by friction, diffusion and other phenomena are introduced. When compared with the stress drop, the man-introduced perturbation (pore pressure increase) should have been minimum.

As matters stand, the author does not consider it likely either that an increment of 8 bar induced the first part of the sequence. It seems more reasonable that the earthquakes were triggered as well, meaning that smaller sources were already close to failure. This could be supported by the following facts:

- the b parameter, while higher than normal, never achieved values of ~ 2 , which are found when induced seismicity takes place (e.g. Eaton et al., 2014a).
- The reported overpressures (external perturbation) are low to very low when compared with other injection projects, such as those generating HF (e.g. Baisch et al. 2009), and it was well below the threshold set by the operators.
- The total introduced energy is already an order of magnitude lower than seismic moment release during the first phase of the sequence ($2E+14$ J up to September 17th based on IGN's catalog; see chapter 3).
- When seismicity is responding to fluid pressure diffusion it is usually slow (various days), and earthquakes taking place just after injections (first phase of the sequence) at various kilometers of distance cannot be controlled by it (e.g. Cesca et al., 2014; Nevertheless it has to be noted that hypocentral location uncertainty is too high to ensure this statement)

As indicated above, the b value during injections was smaller than when repetitive shear or tensile fracture is responding to pressurized fluid migration (at the required values, which are much higher than 8 bar), but could be reflecting scale-limiting behavior on critically stressed fractures as well. This last statement is rational when linked with the second part of the sequence, which involved a larger-scale fault system (consistently lower b value over the entire magnitude range, as proposed by Eaton and Maghsoudi, 2015, but not necessarily constant either; see chapter 6).

Nonetheless, the question regarding the origin of seismicity should be answered with a quantitative analysis of gas-injection induced seismicity in the Castor UGS (probably, numerical 3D coupled model required). Unlike for the second part of the sequence, where it could have played a partial role, it is not likely that the static stress transfer due to the initial events ($M < 3$) affected the development of seismicity.

What part of liability should therefore be attributed to Escal UGS? After this study's understanding of the process, the clue is on the first earthquakes, the foreshocks, because the second part of the sequence was fundamentally controlled by the natural stress state; faults in the area were really close to failure, and a slight modification was enough to release all the stored energy. In addition, it is unlikely that gas injections up to September 17th, 2013, influenced in a relevant way recurrence times of future characteristic earthquakes in the area. This is because the fluid overpressure at the rupture point would

hardly be relevant when compared with the earthquake stress drop (see chapter 7 for further background).

Still, even if the introduced perturbation was minimum and no evidence of induced seismicity is found, what cannot be argued is that the stress state was modified. After the published literature and the poor control that we seem to have over seismicity, no stress modification in areas with known active fault systems should be done, except when all relevant geological information is acknowledged and the related geo-hazard can be handled. Even if the distinction is made for scientific purposes, both triggered (by a man-introduced perturbation) and induced events have an anthropogenic origin, and therefore, they would not have happened at the time without human intervention.

8.2 Conclusions

- An absolute exact location of the studied earthquakes, given the existent seismic network and the selected computation method, is not possible. But, there is evidence to think that the earthquakes could have taken place on deeper sources than the reservoir bottom, which remain unknown.
- Although normal in the past, current faults in the area should slip basically as strike slips with some normal component, as indicated by FM solutions (the actual earthquakes reflect the present stress state).
- The b parameter might be a good ally when dealing with potentially earthquake-inducing activities. It can provide valuable magnitude knowledge and its real time monitoring can help in identifying the proximity of major ruptures. Nevertheless, it should be taken as a complementary resource.
- One of the mapped faults, an ESE dipping structure herein named East 4 might have caused part of the earthquakes; A NE-SW striking feature which dips to the east is consistent with FM solutions (left lateral strike slip) and well oriented in relation to the actual stress field.
- Computed CSC on mapped faults seem to point out towards the mentioned East-dipping fault as a causative fault, and based on magnitudes achieved, the CSC could have acted as a partial trigger in the sequence.
- Montsia faults, as mapped here, do not seem to accord with FM results (the NW-SE striking nodal plane is almost vertical) nor with a rupture based on resolved CSC, which would be at its highest after all the considered events.
- The influence of CSC on the main fault, when it comes to characteristic earthquakes in the area, is negligible. It is likely that what is reckoned to be the main causative mechanism (pore pressure increase), did not accelerate it in a relevant way either (very low reported overpressures). Because of that, the seismic cycle regarding future earthquakes is assumed to follow its natural path without having been significantly disturbed.
- The studied seismic sequence did not significantly vary the earthquake hazard parameters, but that does not mean that seismic hazard is negligible. Known structures are already capable of hosting moderate to strong earthquakes which could be damaging.
- It remains to be proven whether any seismicity was actually induced in the area. The company's responsibility in the earthquakes as particular phenomena should be discussed once a quantitative study dealing with injections and induced seismicity at a time is made (numerical modeling). But, looking at the bigger picture, Castor UGS was already known to be capable of triggering seismic events (Ugalde, 2005), and involved a poorly informed country in relation to seismic hazard.
- When complex processes are under way, no assumptions should be made until a quantitative model that represents reality is achieved, thanks to applying fundamental concepts based on the theory. Descriptions or empirical observations, by themselves, do not imply knowledge (see Alonso et al., 2010, or Puzrin et al., 2010).

8.3 Recommendations on the context of fluid injection activities

The following points represent important aspects that should always be double checked when dealing with projects of this kind, and have been elaborated from the study made, as well as from the cited references. However, the note on existing doubts in the Castor Project written by University of Barcelona's geologist J. Giner must be highlighted here (see SGC, 2014), as well as the document by EPA (2012).

This part does not intend to be exhaustive nor a guide for UGS projects, but to highlight important and rather logical aspects that, based on reported cases, have not always been followed.

8.3.1 Geological model

As results based on incorrect data will never represent reality, it is coherent to state that any subsoil activity has to be based on a truthful geological model. In the context of interest, it is now not irrational to think that geo-hazard was underestimated, and some of the points that follow might hold part of the key.

- Behavior of an ancient oil reservoir supported by an aquifer with a powerful water drive might be difficult to characterize. Not only the water, but also important quantities of movable oil might be present, whose response may be uncertain, but ought to be taken into account.
- A layer might seal oil, but be incapable of sealing gas at the same time. Gas is a much lighter fluid, and therefore its pressurized migration is much more difficult to control. If gas is to be injected on an oil reservoir, clear evidence has to be found in relation to the ability of the corresponding seals to avoid gas moving.
- A deep stratigraphic and structural characterization must be done in order to properly assess storage/extraction capacity, and associated risks.
- On all scales, an according geo-mechanical analysis of the rock itself should be completed. Clear threshold values, when it comes to maximum pressures or stored volumes allowable, have to be determined.
- An exhaustive analysis of present faults in the zone of interest must be conducted. The fact that the larger structures are already known does not exclude it, as smaller structures might modify its behavior once equilibrium is broken.
- Even when the best methods are applied, room for a certain level of uncertainty should always be left. Geological risk usually involves too many processes to be able to mind-control the whole of them. In that sense, it is always recommended to simplify as much as possible in order to obtain a representative model which allows understanding the key aspects of the medium. Simplifying correctly is extremely difficult, but it is usually the only way to deal properly with a project of this kind.

8.3.2 Operation practice

- The primary control parameters (total injected volume and injection ratios) which are in command of the change of fluid pressure in the storage space, need to be

real time monitored and escalate prudently (see EPA, 2012, for explicit indications).

- Injection procedure has to be adapted to the geo-mechanical properties of the rock. If they can cope with economic requirements, then the project is doable. In contrast, if they are not, another alternative must be explored.
- Potential earthquake triggering mechanisms (among the ones indicated in chapter 2) should be considered according to the project, and the operation procedure must be evaluated in line with them.

8.3.3 Other aspects

- A seismic hazard analysis, integrating all possible triggers and outcomes, should never be dismissed.
- Precise and exact locations of earthquakes ought to be obtained. The first step, even before any activity starts, is ensuring a properly distributed seismic network near the injection point. In an offshore facility such as the Castor platform, installing Ocean Bottom Seismometers (OBS) is advised.
- Real time monitoring of seismicity should always be carried out (spatial distribution, analysis of frequency and magnitudes, pattern, etc)
- Acting protocols, such as the named *traffic light* system (e.g. EPA, 2012; IGME, 2013) must be set up. The acting plan has to be up to date not only to advance to further stages of the project, but also when it comes to dealing with unwanted or even unexpected phenomena, which unluckily, have proven to be quite usual.

8.4 The Castor's case: Future prospects to be expected

The Castor UGS, as presented by Escal UGS and supported by the Spanish government, should have been the largest UGS in Spain. Such a facility (whose cost surpassed 1300 million €, as indicated by SGC, 2014, but which could become 4 times more expensive as Spanish citizens pay for it, based on Gonzalez, 2014) had to go through a massive administrative procedure, obtaining more than 40 permits in order make it happen. Even with ecologists' and local authorities' opposition and, as seismicity denoted, dubious placement chosen for the UGS, such an investment is not likely to be ended unless all evidence advocates for it.

As matters stand, the Castor is on hibernation phase (guarded by a new company, ENAGAS) , and despite what was indicated in the previous paragraph it does not seem probable that the plant is re-opened; in fact, it is difficult to foresee which may be the key factor to take a final decision, but the named MIT study under way will be crucial to deciding whether further injections can take place from a technical point of view. However, it has to be noted that any project of this kind has to overcome administrative and social acceptance issues as well, which, given the experienced seismicity, is undoubtedly going to be a challenge for the company.

9. REFERENCES

ACS. (2007). Press release "Acuerdo entre Eurogas, ACS y Enagás sobre el Proyecto Castor de Almacenamiento". [Retrieved October 2015], available at:

<<http://www.grupoacs.com/index.php/es/c/saladeprensa/1/63>>

Adushkin, V.V., V.N. Rodionov, S. Turuntnev, and A.E. Yodin. (2000). Seismicity in the Oil Field. *Oilfield Review*, Summer, pp. 2-17.

Aki, K., & Richards, P. G. (1980). *Quantitive Seismology: Theory and Methods*. University Science Books. 700pp.

Alonso, E. E., Pinyol, N. M., & Puzrin, A. M. (2010). *Geomechanics of failures. Advanced topics*. Springer Science & Business Media.

Anderson, K. R. (1982). Robust earthquake location using M-estimates. *Physics of the Earth and Planetary Interiors*, 30(2), 119-130.

Baisch, S., D. Carbon, U. Dannwolf, B. Delacou, M. Devaux, F. Dunand, R. Jung, M. Koller, C. Martin, and M.Sartori. (2009). Deep heat mining basel: seismic risk analysis, *SERIANEX Group, Departement für Wirtschaft, Soziales und Umwelt des Kantons Basel-Stadt, Basel*.

Bak, P., & Tang, C. (1989). Earthquakes as a self-organized critical phenomenon. *J. geophys. Res*, 94(15), 635-15.

Bary, A., Crotogino, F., Prevedel, B., Berger, H., Brown, K., Frantz, J., & Ren, N. (2002). Storing natural gas underground. *Oilfield Review*, 14(2), 2-17.

Batchelor, J. A., Sherley, B., Klepacki, D., Lewis, R., & Jensen, R. E. (2007). Validating the integrity of the Amposta structure for gas storage offshore Spain. In *Offshore Europe*. Society of Petroleum Engineers.

Belcher, S. (2004). The Basics of Underground Natural Gas Storage. Energy Information Administration, Department of Energy, Washington DC. (U.S.).

Berbís, S. (2015/11/23). El Observatori de l'Ebre aconsejó parar la inyección de gas al Castor al iniciarse los seísmos. *El periódico*. [Retrieved from (last visit 2016/05/20)]:

<<http://www.elperiodico.com/es/noticias/medio-ambiente/observatori-lebre-aconsejo-parar-inyeccion-gas-castor-iniciarse-los-seismos-4696550>>

BU- Boston University. (1999). The first law of thermodynamics. [Retrieved November 2015], available at:

<<http://physics.bu.edu/~duffy/py105/Firstlaw.html>>

Bourne, S. J., K. Maron, S. J. Oates, and G. Mueller. (2006). Monitoring Reservoir Deformation on Land—Evidence for fault re-activation from microseismic, InSAR, and GPS Data. Extended Abstracts E026 presented at 68th EAGE Conference/SPE EUROPEC 2006, Vienna, Austria, 12–15, June.

Buland, R. (1976). The mechanics of locating earthquakes. *Bulletin of the Seismological Society of America*, 66(1), 173-187.

9. References

- Buland, R., & Chapman, C. H. (1983). The computation of seismic travel times. *Bulletin of the Seismological Society of America*, 73(5), 1271-1302.
- Casella, G., & Berger, R. L. (2002). *Statistical inference* (Vol. 2). Pacific Grove, CA: Duxbury. 200pp.
- Castor's Geology and Geophysics day held at the Association of Geologists of Catalonia. (2014). Jornada Geologia y Geofísica del Proyecto Castor. Implicacions de Risc. Col·legi de Geòlegs de Catalunya. Barcelona (Catalunya). [Last accessed 2016/03/20] available at (in Spanish):
- <<http://www.youtube.com/watch?v=D4ct7rsBB1A>>
<<http://www.youtube.com/watch?v=w1MAYT3CPnE>>
<<http://www.youtube.com/watch?v=58UoyOia6r0>>
<<http://www.youtube.com/watch?v=fAJ2uB5GkEM>>
<<http://www.youtube.com/watch?v=H72F40YuZIU>>
- Cesca, S., Dost, B. & Oth, A. (2013a). Preface to the special issue "Triggered and induced seismicity: probabilities and discrimination", *J. Seismol.*, 17(1), 1-4.
- Cesca, S., Grigoli, F., Heimann, S., González, Á., Buforn, E., Maghsoudi, S., & Dahm, T. (2014). The 2013 September-October seismic sequence offshore Spain: a case of seismicity triggered by gas injection?. *Geophysical Journal International*, 198(2), 941-953.
- CNIG. (2013). Actualización de mapas de peligrosidad sísmica de España 2012. [Revised version Oct. 2015]. [Retrieved October 2015]. Available at:
- <<http://www.ign.es/ign/layoutIn/sismoListadoMapasSismicos.do>>
- DeGroot, M. H., & Schervish, M. J. (2011). *Probability and statistics* (4thed.). Boston, MA: Addison-Wesley. 912pp.
- Deichmann, N., & Garcia-Fernandez, M. (1992). Rupture geometry from high-precision relative hypocentre locations of micro earthquake clusters. *Geophysical Journal International*, 110(3), 501-517.
- Delouis, B. (2014). FMNEAR: Determination of focal mechanism and first estimate of rupture directivity using near-source records and a linear distribution of point sources. *Bulletin of the Seismological Society of America*.
- Delouis, B., Charlety, J., & Vallée, M. (2009). A method for rapid determination of moment magnitude M_w for moderate to large earthquakes from the near-field spectra of strong-motion records (MWSYNTH). *Bulletin of the Seismological Society of America*, 99(3), 1827-1840.
- Delouis, B., Giardini, D., Lundgren, P., & Salichon, J. (2002). Joint inversion of InSAR, GPS, teleseismic, and strong-motion data for the spatial and temporal distribution of earthquake slip: Application to the 1999 Izmit mainshock. *Bulletin of the Seismological Society of America*, 92(1), 278-299.
- Del Potro, R., & Diez, M. (2015). Induced Seismicity in Underground Gas Storage-The Case of Castor, Offshore NE Spain. In *77th EAGE Conference and Exhibition-Workshops*.
- Díaz, J., & Gallart, J. (2009). Crustal structure beneath the Iberian Peninsula and surrounding waters: A new compilation of deep seismic sounding results. *Physics of the Earth and Planetary Interiors*, 173(1), 181-190.

9. References

- Dieterich, J. H., Richards-Dinger, K. B., & Kroll, K. A. (2015). Modeling injection-induced seismicity with the physics-based earthquake simulator RSQSim. *Seismological Research Letters*, 86(4), 1102-1109.
- Dost, B., Zednik, J., Havskov, J., Willemann, R., & Bormann, P. (2012). Seismic Data Formats, Archival and Exchange. Published online by GFZ Potsdam. Available at [last accessed 2016/06/10]:
<<http://gfzpublic.gfz-potsdam.de/pubman/item/escidoc:4321>>
- Douglas, A. (1967). Joint epicentre determination. *Nature*, 215, 47-48.
- Eaton, D. W., & Maghsoudi, S. (2015). 2b... or not 2b? Interpreting magnitude distributions from microseismic catalogs. *First Break*, 33(10), 79-86.
- Ellsworth, W. L. (2013). Injection-induced earthquakes. *Science*, 341(6142), 1225-1229.
- EPA - Environmental Protection Agency U.S. (2012). Minimizing and managing potential impacts of induced seismicity from class II injection wells. Washington, DC: Underground Injection Control National Technical Workgroup.
- Escal UGS. (2014). Almacenamiento subterráneo de gas natural CASTOR. Conference at Col·legi d'Enginyers Industrials de Catalunya [2014/01/20]. Last accessed 2016/06/21, available at:
<www.eic.cat/gfe7docs/13763.pdf>
- Escal UGS. (2015). The Castor Project. [Retrieved October 2015] available at:
<www.proyectocastor.com>
- Fajula, A. & Romeu, N. (2016). Valoració del sistema de Determinació Automàtica de Sismes locals, DAS, i del Teleavís, Període 2015, Informe intern ICGC.
- Felzer, K. R. (2006). Calculating the Gutenberg-Richter b value. In *AGU Fall Meeting Abstracts* (Vol. 1, p. 08).
- Flinn, E. A. (1965). Confidence regions and error determinations for seismic event location. *Reviews of Geophysics*, 3(1), 157-185.
- Foh, S., M. Novil, E. Rockar, and P. Randolph. (1979). *Underground Hydrogen Storage Final Report*. Brookhaven National Laboratories, Upton, NY.
- Fontboté, J. M., Guimerà, J., Roca, E., Sàbat, F., Santanach, P., & Fernández-Ortigosa, F. (1990). The Cenozoic geodynamic evolution of the Valencia trough (western Mediterranean). *Revista de la Sociedad Geológica de España*, 3(2), 7-18.
- Frontera, T., Goula, X., Olivera, C. (2013). Càlcul del tensor moment dels sismes de la crisi de la costa de Tarragona i Castelló de Setembre i Octubre de 2013. Institut Cartogràfic i Geològic de Catalunya, Barcelona.
- Gaite, B., Ugalde, A., Villaseñor, A., & Blanch, E. (2016). Improving the location of induced earthquakes associated with an underground gas storage in the Gulf of Valencia (Spain). *Physics of the Earth and Planetary Interiors*, 254, 46-59.
- Gallart, J., Vidal, N., Estévez, A., Pous, J., Sàbat, F., Santisteban, C., & Suriñach, E. (1995). The ESCI-Valencia Trough vertical reflection experiment: a seismic image of the crust from the NE Iberian Peninsula to the Western Mediterranean. *Rev Soc Geol Espana*, 8(4), 405-415.

9. References

- García-Mayordomo, J., Insua-Arévalo, J. M., Martínez-Díaz, J. J., Jiménez-Díaz, A., Martín-Banda, R., Martín-Alfageme, S., & Masana, E. (2012). The Quaternary Active Faults Database of Iberia (QAFI v. 2.0)/La Base de Datos de Fallas Activas en el Cuaternario de Iberia (QAFI v. 2.0). *Journal of Iberian Geology*, 38(1), 285.
- García-Mayordomo, J. (2015) Amposta Eastern Quaternary Fault: ME004. In: Quaternary Active Faults Database of Iberia v.3.0 - November 2015 (García-Mayordomo et al., eds.), IGME, Madrid.
- Geertsma, J. (1973). Land subsidence above compacting oil and gas reservoirs, *J. Petrol. Tech.*, 25, 734–744.
- Geostock. (2010). Castor underground storage facility—seismic interpretation study—contribution to the static model. ESCAL internal report.
- Gere, J. M. (2004). *Mechanics of Materials* (7thed.). Thomson Brooks, Cole. 1045pp.
- Ghassemi, A., Tarasovs, S., & Cheng, A. D. (2007). A 3-D study of the effects of thermo mechanical loads on fracture slip in enhanced geothermal reservoirs. *International Journal of Rock Mechanics and Mining Sciences*, 44(8), 1132-1148.
- Gischig, V. S. (2015). Rupture propagation behavior and the largest possible earthquake induced by fluid injection into deep reservoirs. *Geophysical Research Letters*, 42(18), 7420-7428.
- Gonzalez, A. (2014). Proyecto Castor. Relación de la secuencia sísmica con la inyección de gas. *Enseñanza de las ciencias de la Tierra*, 22(3), 298.
- Gonzalez, A. (Submitted 2016). The national Spanish earthquake catalogue: Evolution, precision and completeness.
- Grasso, J.-R., and Wittlinger. (1990). 10 years of seismic monitoring over a gas field area, *Bulletin of the Seismological Society of America* 80: 450-473.
- Grigoli, F., Cesca, S., Vassallo, M., & Dahm, T. (2013a). Automated seismic event location by travel-time stacking: An application to mining induced seismicity. *Seismological Research Letters*, 84(4), 666-677.
- Grigoli, F., Cesca, S., Amoroso, O., Emolo, A., Zollo, A., & Dahm, T. (2013b). Automated seismic event location by waveform coherence analysis. *Geophysical Journal International*, ggt477.
- Gutenberg, B., & Richter, C. F. (1944). Frequency of earthquakes in California. *Bulletin of the Seismological Society of America*, 34(4), 185-188.
- Haftka, R. (2008). Transformations of Stress in Applied elasticity and advanced mechanics of solids, University of Florida. [Last accessed 2016/06/18], available at:
<<http://www2.mae.ufl.edu/haftka/adv-elast/lectures/Section2-4.pdf>>
- Hanks, T. C., and Kanamori, H. (1979). A moment magnitude scale, *Journal of Geophysical Research*, 84, 5, 2348 - 2350, 9B0059, doi:10.1029/JB084iB05p02348.
- Hardebeck, J. L., Nazareth, J. J., & Hauksson, E. (1998). The static stress change triggering model: Constraints from two southern California aftershock sequences. *Journal of Geophysical Research B*, 103(B10), 24427-24437.
- Harris, R. A. (2000). Earthquake stress triggers, stress shadows, and seismic hazard. *Current Science*, 79(9), 1215-1225.

9. References

- Havskov, J. (1990). Replace the HYPO71 format. *Bulletin of the Seismological Society of America*, 80(4), 1043-1045.
- Häring, M. O., Schanz, U., Ladner, F., & Dyer, B. C. (2008). Characterisation of the Basel 1 enhanced geothermal system. *Geothermics*, 37(5), 469-495.
- Healy JH, Rubey WW, Griggs DT, Raleigh CB. (1968). The Denver Earthquakes. *Science*, 161(3848):1301-1310.
- Heidbach, O., Tingay, M., Barth, A., Reinecker, J., Kurfeß, D., & Müller, B. (2008). The world stress map database release 2008, doi: 10.1594/GFZ.WSM. Rel2008.
- Hooke, R. (1676). *Description of Helioscopes, and some other Instruments*, London (UK).
- Hudson, J.A. & Harrison, J.P. (1997). *Engineering rock mechanics*. Pergamon (Elsevier), Oxford (UK). 444 pp.
- Husen, S., & Hardebeck, J.L. (2010). Earthquake location accuracy. Community Online Resource for Statistical Seismicity Analysis, doi:10.5078/corssa-55815573. Available at [last accessed 2016/06/10]:
<<http://www.corssa.org>>
- ICGC.(2013). Anàlisi de la informació geològica, geofísica i sismològica disponible sobre l'antic camp petrolífer d'Amposta i el projecte Castor, en relació a la sismicitat induïda que va tenir lloc durant els mesos de setembre i octubre de 2013 i recomanacions per a possibles noves operacions. Generalitat de Catalunya, Barcelona, Spain.
- ICGC. (2015). *Butlletí Sismològic 2013*. Departament de Territori i Sostenibilitat, Generalitat de Catalunya. Barcelona (Catalunya).
- IGME (2012). QAFI: Quaternary Active Faults Database of Iberia. [Retrieved November 2015]. Available at:
<<http://info.igme.es/qafi/#>>
- IGME. (2013). Informe geológico sobre la crisis sísmica relacionada con el almacén subterráneo de gas denominado Castor (Castellón, noreste de España). Ministerio de Economía y Competitividad, Madrid (Spain).
- IGME (2015a). QAFI v.3: Quaternary Active Faults Database of Iberia. [Last Accessed 2016/03/05], from IGME web site:
<<http://info.igme.es/QAFI>>
- IGME. (2015b). ZESIS: Base de Datos de Zonas Sismogénicas de la Península Ibérica y territorios de influencia para el cálculo de la peligrosidad sísmica en España. Available at [last 2016/06/10]:
<<http://info.igme.es/zesis>>
- IGN. (2013). Informe sobre la actividad sísmica en el golfo de Valencia. Ministerio de Fomento, Madrid (Spain).
- IGN-UPM (2013) Actualización de Mapas de Peligrosidad Sísmica de España 2012. Centro Nacional de Información Geográfica, Madrid, 267 pp.

9. References

IIE, Instituto de la Ingeniería en España. (2013). El proyecto Castor, en espera de encontrar las causas y prever las consecuencias. [Last accessed 2016/03/27]. Available at:

<http://www.iies.es/El-proyecto-Castor-en-espera-de-encontrar-las-causas-y-prever-las-consecuencias_a3229.html>

Ishimoto, M., & Iida, K. (1939). Observations of earthquakes registered with the microseismograph constructed recently. *Bull. Earthq. Res. Inst*, 17, 443-478.

Jaeger, J. C., Cook, N. G. (1979). *Fundamentals of rock mechanics*. Chapman and Hall. 593pp.

Jaeger, J. C., Cook, N. G., & Zimmerman, R. (2007). *Fundamentals of rock mechanics*. John Wiley & Sons. 505pp.

Johnson, C. E. (1979). I. *CEDAR--an approach to the computer automation of short-period local seismic networks*. II. *Seismotectonics of the Imperial Valley of southern California* (Doctoral dissertation, California Institute of Technology).

Kagan, Y. Y. (2010). Earthquake size distribution: Power-law with exponent?. *Tectonophysics*, 490(1), 103-114.

Kanamori, H. (1983). Magnitude scale and quantification of earthquakes. *Tectonophysics*, 93(3-4), 185-199.

Kanamori, H., & Anderson, D. L. (1975). Theoretical basis of some empirical relations in seismology. *Bulletin of the Seismological Society of America*, 65(5), 1073-1095.

Kennett, B. L. N., & Engdahl, E. R. (1991). Traveltimes for global earthquake location and phase identification. *Geophysical Journal International*, 105(2), 429-465.

Kerr, R. (2012). Learning how to NOT make your own earthquakes. *Science* 335: 1436-1437.

King, G. C. P., Stein, R. S., and J. Lin. (1994). Static Stress Changes and the Triggering of Earthquakes. *Bull. Seism. Soc. Amer.*, 84(3), 935-953.

Kim, W. Y. (2013). Induced seismicity associated with fluid injection into a deep well in Youngstown, Ohio. *Journal of Geophysical Research: Solid Earth*, 118(7), 3506-3518.

Klose, C. D. (2013). Mechanical and statistical evidence of the causality of human-made mass shifts on the Earth's upper crust and the occurrence of earthquakes. *J. Seismolog.*, 17, 109-135.

Kraaijpoel, D., Nieuwland, D., Wassing, B. & Dost, B. (2012). Induced seismicity at the underground gas storage facility in the Netherlands, in *Proceedings of the EGU General Assembly 2012*, April 27, Geophys. Res. Abstr., Vol. 14, EGU2012-132982.

Kuge, K. (2003). Source modeling using strong-motion waveforms: toward automated determination of earthquake fault planes and moment-release distributions. *Bulletin of the Seismological Society of America*, 93(2), 639-654.

Lagace, P.A. (2001). Review of language of stress/strain analysis. Structural mechanics, unit 3, MIT open courseware. [Last accessed 2016/06/15], available at:

<<http://ocw.mit.edu/courses/aeronautics-and-astronautics/16-20-structural-mechanics-fall-2002/lecture-notes/unit3.pdf>>

9. References

- Lagace, P.A. (2007). Stress and Strain Transformations, MIT open courseware. Last accessed [2016/06/15] available at:
<<http://web.mit.edu/16.unified/www/FALL/materials/Lectures/M2.4-Unified08.pdf>>
- Lay, T., & Wallace, T. C. (1995). *Modern global seismology* (Vol. 58). Academic press. 521pp.
- Lei, X., Masuda, K., Nishizawa, O., Jouniaux, L., Liu, L., Ma, W., ... & Kusunose, K. (2004). Detailed analysis of acoustic emission activity during catastrophic fracture of faults in rock. *Journal of Structural Geology*, 26(2), 247-258.
- Lienert, B. R. (1994). HYPOCENTER 3.2-A Computer Program for Locating Earthquakes Locally. *Regionally and Globally, Hawaii Institute of Geophysics & Planetology, Honolulu*.
- Lienert, B. R., Berg, E., & Frazer, L. N. (1986). HYPOCENTER: An earthquake location method using centered, scaled, and adaptively damped least squares. *Bulletin of the Seismological Society of America*, 76(3), 771-783.
- Lienert, B. R., & Havskov, J. (1995). A computer program for locating earthquakes both locally and globally. *Seismological Research Letters*, 66(5), 26-36.
- Lin, J., & Stein, R. S. (2004). Stress triggering in thrust and subduction earthquakes and stress interaction between the southern San Andreas and nearby thrust and strike-slip faults. *Journal of Geophysical Research: Solid Earth*, 109(B2).
- Lomax, A., Virieux, J., Volant, P., & Berge-Thierry, C. (2000). Probabilistic earthquake location in 3D and layered models. In *Advances in seismic event location* (pp. 101-134). Springer Netherlands.
- Lomax, A., Zollo, A., Capuano, P., & Virieux, J. (2001). Precise, absolute earthquake location under Somma-Vesuvius volcano using a new three-dimensional velocity model. *Geophysical Journal International*, 146(2), 313-331.
- Lord, A. S. (2009). Overview of geologic storage of natural gas with an emphasis on assessing the feasibility of storing hydrogen. SAND2009-5878, Sandia National Laboratory, Albuquerque, NM.
- Madariaga, R. (1979). On the relation between seismic moment and stress drop in the presence of stress and strength heterogeneity. *J. geophys. Res.*, 84(B5), 2243-2250.
- Malvern, L. E. (1969). *Introduction to the Mechanics of a Continuous Medium* (No Monograph).
- Martinez del Olmo, W., & Esteban, M. (1983). Paleokarst development. *Carbonate Depositional Environments*, 93-95.
- Maxwell, S. C., Jones, M., Parker, R., Leaney, S., Mack, M., Dorvall, D., & Hammermaster, K. (2010, June). Fault activation during hydraulic fracturing. In *72nd EAGE Conference and Exhibition incorporating SPE EUROPEC 2010*.
- McGarr, A. (1991). On a possible connection between three major earthquakes in California and oil production. *Bulletin of the Seismological Society of America* 81(3): 948-970.
- McGarr, A. (1999). On relating apparent stress to the stress causing earthquake fault slip. *Journal of Geophysical Research: Solid Earth*, 104(B2), 3003-3011.
- McGarr, D. Simpson, L. Seeber. (2002). Case histories of induced and triggered seismicity. *International Handbook of Earthquake and Engineering Seismology*, Academic Press, Waltham, MA, 8(40).

9. References

- McGarr, A. (2014). Maximum magnitude earthquakes induced by fluid injection. *J. Geophys. Res. Solid Earth*, 119, 1008–1019, doi:10.1002/2013JB010597.
- McGuire, R. (2004). Seismic Hazard and Risk Analysis, Earthquake Engineering Research Institute, Oakland, California.
- Merten, R. (2006). Petroleum exploration and production in Spain. *Zeitschrift der Deutschen Gesellschaft für Geowissenschaften*, 157(4), 717-732.
- Mihcakan, I. M., Altinay, E. I., & Kasap, I. (2005). The Hall Plot Analysis of a Water Injection Test Affected by Geothermal Reservoir Response. In *Proceedings World Geothermal Congress*.
- Mucciarelli, M., & Priolo, E. (2013). Monitoring induced seismicity from underground gas storage: first steps in Italy. In *EGU General Assembly Conference Abstracts* (Vol. 15, p. 12375).
- Mulders, FMM. (2003). Modeling of stress development and fault slip in and around a producing gas reservoir. Technical University of Delft.
- Muskat, M. (1981). *Physical principles of oil production*. Springer, Berlin (Germany). 922 pp.
- Mukuhira, Y., Asanuma, H., & Haring, M. (2012). Correlation between the coulomb stress and occurrence of the large induced seismicity at Basel, Switzerland in 2006.
- Mulargia, F., & Bizzarri, A. (2014). Anthropogenic triggering of large earthquakes. *Scientific reports*, 4.
- Myung, I. J. (2003). Tutorial on maximum likelihood estimation. *Journal of mathematical Psychology*, 47(1), 90-100.
- National Research Council (NRC; US). (2012). Committee on Induced Seismicity Potential in Energy Technologies. *Induced Seismicity Potential in Energy Technologies*. National Academies Press.
- Oates, S. J., Vogelaar, A., Herber, R., & Winsor, J. (2013). On the relationship between levels of seismicity and pump parameters in a hydraulic fracturing job. In *4th EAGE Passive Seismic Workshop*.
- Okada, Y. (1992). Internal deformation due to shear and tensile faults in a half-space. *Bulletin of the Seismological Society of America*, 82(2), 1018-1040.
- Orlic B, Wassing BBT, Geel CR. (2013). Field Scale Geomechanical Modeling for Prediction of Fault Stability During Underground Gas Storage Operations in a Depleted Gas Field in the Netherlands.
- Palacios, P., Molina, I., & Segovia, M. (2006). The Gutenberg–Richter Law: assumptions, limitations and interpretations. *Statistics in Volcanology. Special Publications of IAVCEI*, 1, 115-127.
- PB-KBB Inc. (1998). *Advanced Underground Gas Storage Concepts Refrigerated-Mined Cavern Storage: Final Report*. PB-KBB Inc, Houston, TX.
- Perea, H. (2006): Falles actives i perillositat sísmica al marge nord-occidental del solc de València (Active faults and seismic hazard in the northwestern margin of the València trough). Ph.D. Thesis, Universitat de Barcelona, 382 p.
- Playà, E., Travé, A., Caja, M. A., Salas, R., & Martín-Martín, J. D. (2010). Diagenesis of the Amposta offshore oil reservoir (Amposta Marino C2 well, Lower Cretaceous, Valencia Trough, Spain). *Geofluids*, 10(3), 314-333.

9. References

- Plotnikova, L.M., Nurtaev BS, Grasso JR, Matasova LM, Bossu R. (1996). *The character and extent of seismic deformation in the focal zone of gazli earthquakes of 1976 and 1984, $M > 7.0$* . Knoll P and Kowalle G, editors. Birkhauser Basel. 377 p.
- Prat, P. (2006). *Ecuaciones constitutivas. Elasticidad y Plasticidad*. Departament d'Enginyeria del Terreny, Cartogràfica i Geofísica, Universitat Politècnica de Catalunya. Barcelona (Spain). [Last accessed 2016/06/18], available at:
<https://portal.camins.upc.edu/materials_guia/250131/2012/Elasticitat-Plasticitat.pdf>
- Pratt, W.E., and D.W. Johnson, 1926. Local subsidence of the Goose Creek oil field (Texas). *Bulletin of the Seismological Society of America* 34(7): 577-590.
- Priolo, E., Romanelli, M., Linares, M. P., Garbin, M., Peruzza, L., Romano, M. A., & Fabris, P. (2015). Seismic monitoring of an underground natural gas storage facility: The Collalto Seismic Network. *Seismological Research Letters*, 86(1), 109-123.
- Puzrin, A. M., Alonso, E. E., & Pinyol, N. M. (2010). *Geomechanics of failures*. Springer Science & Business Media. 245pp.
- Richter, C. (1935). An Instrumental Earthquake Magnitude Scale, *Bull. Seism. Soc. Am.*, 25(1), 1-32.
- Roca, E., & Guimerà, J. (1992). The Neogene structure of the eastern Iberian margin: structural constraints on the crustal evolution of the Valencia trough (western Mediterranean). *Tectonophysics*, 203(1), 203-218.
- Roger, A. M. & Lee, W. H. K. (1976). Seismic study of earthquakes in the Lake Mead, Nevada-Arizona region. *Bull. of the Seis. Soc. of America*. 66(5), 1657-1681.
- Romano, M.A., Peruzza, L., Priolo, E., Garbin, M., Picotti, V., Guido, F.L. & Ponza, A. (2015). Preliminary imaging of active faults in the Montello-Collalto area (Southeastern Alps, Italy) by a high-sensitivity seismometric network. *6th International INQUA Meeting on Paleoseismology, Active Tectonics and Archaeoseismology*, 19-24 April 2015, Pescara, Fucino Basin, Italy.
- Santarelli, F. J., Tronvoll, J. T., Svennekjaier, M., Skeie, H., Henriksen, R., & Bratli, R. K. (1998). Reservoir stress path: the depletion and the rebound. In *SPE/ISRM Rock Mechanics in Petroleum Engineering*. Society of Petroleum Engineers.
- Sato, R. (1971). Crustal deformation due to dislocation in a multi-layered medium. *Journal of Physics of the Earth*, 19(1), 31-46.
- Schindler, A., Jurado, M. J., & Müller, B. (1998). Stress orientation and tectonic regime in the northwestern Valencia Trough from borehole data. *Tectonophysics*, 300(1), 63-77.
- Schoenball, M. (2014). *Evolution of stress and seismicity in fractured geothermal reservoirs*. Ph.D. thesis, Karlsruher Instituts für Technologie (Germany).
- Schofield, A. N., & Wroth, C. P. (1968). *Critical state soil mechanics*. McGraw-Hill, London. 228pp.
- Scholz, C. H. (2002). *The mechanics of earthquakes and faulting*. Cambridge University Press, Cambridge (UK). 504 pp.
- Schorlemmer, D., Wiemer, S., & Wyss, M. (2005). Variations in earthquake-size distribution across different stress regimes. *Nature*, 437(7058), 539-542.

9. References

- Schwartz, D. P., K. J. Coppersmith, F. H. Swan III, P. Somerville, and W. U. Savage. (1981). Characteristic earthquakes on intraplate normal faults (abstract), *Earthquake Notes*, 52, 71.
- Schwartz, D. P., & Coppersmith, K. J. (1984). Fault behavior and characteristic earthquakes: Examples from the Wasatch and San Andreas fault zones. *Journal of Geophysical Research: Solid Earth*, 89(B7), 5681-5698.
- Seeman, U.; Pumpin, V.F. and Casson, N. (1990). Amposta Field. AAPG. Structural Traps II: Traps Associated with Tectonic Faulting. Pages 1-20. *The American Association of Petroleum Geologists*, Special Volumes.
- Segall, P. (1989). Earthquakes triggered by fluid extraction. *Geology*, 17, 942-946.
- Segall P., & Fitzgerald SD. (1998). A note on induced stress changes in hydrocarbon and geothermal reservoirs. *Tectonophysics* 289:117.
- Segall, P., Grasso, J. R., & Mossop, A. (1994). Poroelastic stressing and induced seismicity near the Lacq gas field, southwestern France. *Journal of Geophysical Research: Solid Earth*, 99(B8), 15423-15438.
- Simpson, D.W. (1976). Seismicity Changes associated with reservoir loading. *Engineering Geology* 10, 123-150, p.123.
- SGC - Síndic de Greuges de Catalunya. (2014). Informe sobre el projecte Castor. Barcelona (Catalunya).
- Smith, W. D. (1981). The b-value as an earthquake precursor. *Nature*, 289, 136-139.
- Soltanzadeh, H., & Hawkes, C. D. (2008). Semi-analytical models for stress change and fault reactivation induced by reservoir production and injection. *Journal of Petroleum Science and Engineering*, 60(2), 71-85.
- Steady, S., Gombert, J., & Cocco, M. (2005). Introduction to special section: Stress transfer, earthquake triggering, and time-dependent seismic hazard. *Journal of Geophysical Research: Solid Earth*, 110(B5).
- Stein, R. S. (1999). The role of stress transfer in earthquake occurrence. *Nature*, 402(6762), 605-609.
- Stein, S., & Wysession, M. (2009). *An introduction to seismology, earthquakes, and earth structure*. John Wiley & Sons. 498pp.
- Suckale, J. (2009). Induced seismicity in hydrocarbon fields. *Advances in geophysics*, 51, 55-106.
- Sumy, D. F., Cochran, E. S., Keranen, K. M., Wei, M., & Abers, G. A. (2014). Observations of static Coulomb stress triggering of the November 2011 M5.7 Oklahoma earthquake sequence. *Journal of Geophysical Research: Solid Earth*, 119(3), 1904-1923.
- Talwani, P. (1997). On the nature of reservoir-induced seismicity. In *Seismicity Associated with Mines, Reservoirs and Fluid Injections* (pp. 473-492). Birkhäuser Basel.
- Tapia, M. (2013). Localitzacions hipocentrals amb mètode no linial (NONLINLOC): Comparativa amb HYPOCENTER i diferents models de velocitat. Internal report to ICGC and LEGEF.
- Timoshenko, S. P., & Goodier, J. N. (1934). *Theory of Elasticity*. United Engineering Trustees. Inc., USA.

9. References

- TNO (Netherlands Organisation for Applied Scientific Research). (2014). Literature review on Injection-Related Induced Seismicity and its relevance to Nitrogen injection. Anonymous report. Commissioned by Nederlandse Aardolie Maatschappij B.V., Assen (NED).
- Toda, S., Stein, R. S., Richards-Dinger, K., & Bozkurt, S. B. (2005). Forecasting the evolution of seismicity in southern California: Animations built on earthquake stress transfer. *Journal of Geophysical Research: Solid Earth*, 110(B5).
- Toda, S., Stein, R. S., Sevilgen, V., & Lin, J. (2011). *Coulomb 3.3 graphic-rich deformation and stress-change software for earthquake, tectonic, and volcano research and teaching-user guide* (No. 2011-1060). US Geological Survey.
- Torres, S. & Vallès, R. (2015). Castor, un negoci rodó? [Documentary]. Televisió de Catalunya (tv3), 30 minuts. Barcelona (Catalunya). Available at [in Catalan; last accessed 2016/06/10]:
- <<http://www.tv3.cat/videos/5433692>>
- Ugalde, A. (2005). Evaluación de Impacto Ambiental. In Almacenamiento subterráneo de gas natural Amposta (Permiso Castor, Tarragona). Ebro Observatory (Spain). CSIC-URL.
- Universidad de Alicante. (2013). Informe sobre la actividad sísmica al sureste de Vinaroz. Unidad de Registro Sismológico, Universidad de Alicante, Alicante (Spain).
- UNECE (2013). *Study on underground gas storage in Europe and Central Asia*. Technical report, United Nations Economic Commission for Europe.
- Utsu, T., & Ogata, Y. (1995). The centenary of the Omori formula for a decay law of aftershock activity. *Journal of Physics of the Earth*, 43(1), 1-33.
- Van Eijs, R.M.H.E., F.M.M. Mulders, M. Nepveu, C.J. Kenter, and B.C. Scheffers. (2006). Correlation between hydrocarbon reservoir properties and induced seismicity in the Netherlands. *Engineering Geology* 84: 99-111.
- Van Wees, J. D., Buijze, L., Van Thienen-Visser, K., Nepveu, M., Wassing, B. B. T., Orlic, B., & Fokker, P. A. (2014). Geomechanics response and induced seismicity during gas field depletion in the Netherlands. *Geothermics*, 52, 206-219.
- Van der Zee, W., Guises, R., Vossen, J. & Holland, M. (2011). Dynamic Geomechanical Modelling of the Bergermeer Underground Gas Storage, Netherlands. Baker Hughes, Houston (TX, U.S.).
- Vergés, J., & Sàbat, F. (1999). Constraints on the Neogene Mediterranean kinematic evolution along a 1000 km transect from Iberia to Africa. *Geological Society, London, Special Publications*, 156(1), 63-80.
- Wang, R. (1999). A simple orthonormalization method for stable and efficient computation of Green's functions. *Bulletin of the Seismological Society of America*, 89(3), 733-741.
- Wang, R., Martín, F. L., & Roth, F. (2003). Computation of deformation induced by earthquakes in a multi-layered elastic crust—FORTRAN programs EDGRN/EDCMP. *Computers & Geosciences*, 29(2), 195-207.
- Waldhauser, F., & Ellsworth, W. L. (2000). A double-difference earthquake location algorithm: Method and application to the northern Hayward fault, California. *Bulletin of the Seismological Society of America*, 90(6), 1353-1368.
- Watercraft Capital Prospectus. (2013). Castor Underground Gas Storage Concession.

9. References

- Wells, D. L., & Coppersmith, K. J. (1994). New empirical relationships among magnitude, rupture length, rupture width, rupture area, and surface displacement. *Bulletin of the seismological Society of America*, 84(4), 974-1002.
- Wesnousky, S. G. (1986). Earthquakes, Quaternary faults, and seismic hazard in California. *Journal of Geophysical Research: Solid Earth*, 91(B12), 12587-12631.
- Wiemer, S. & Wyss, M. (2000). Minimum magnitude of completeness in earthquake catalogs: Examples from Alaska, western United States and Japan. *Bull. Seismol. Soc. Am*, 90, 859-869.
- Woessner, J., & Wiemer, S. (2005). Assessing the quality of earthquake catalogues: Estimating the magnitude of completeness and its uncertainty. *Bulletin of the Seismological Society of America*, 95(2), 684-698.
- Zabatsky, A.B. (2007). Plane Stress Transformation Equations. Engineering Science, University of Oxford.[Last accessed 2016/06/18], available at:
<http://users.ox.ac.uk/~kneabz/Stress5_ht08.pdf>
- Zivot, E. (2009). Maximum likelihood estimation. MLE lectures, University of Washington (USA). [Last accessed 2016/04/01],available at:
<<http://faculty.washington.edu/ezivot/econ583/mleLectures.pdf>>
- Zoback, M. D. (2007). *Reservoir geomechanics: Earth stress and rock mechanics applied to exploration, production and wellbore stability*. Cambridge University Press, Cambridge, UK. 461pp.
- Zoback, M., and J. Zinke (2002), Production-induced normal faulting in the Valhall and Ekofisk oil fields, *Pure Appl. Geophys.*, 159, 403-420.

